

AFOSR-TR-89-1643

2

AD-A214 989

Final Report  
on  
Program to Study the  
Oxidation of Carbon-Carbon Composites  
and Coatings on these Materials

by  
J. Cullinan, J. Schaeffer, E. A. Gulbransen  
G. H. Meier and F. S. Pettit

Materials Science and Engineering Department  
University of Pittsburgh  
Pittsburgh, PA 15261

for

Grant No. AFOSR-86-0251  
Air Force Office of Scientific Research  
Bolling Air Force Base, DC20332-6448

September 30, 1989

DTIC  
ELECTE  
NOV 29 1989  
S B D

DISTRIBUTION STATEMENT A

Approved for public release;  
Distribution Unlimited

## REPORT DOCUMENTATION PAGE

1a. REPORT SECURITY CLASSIFICATION Unclassified		1b. RESTRICTIVE MARKINGS	
2a. SECURITY CLASSIFICATION AUTHORITY		3. DISTRIBUTION/AVAILABILITY OF REPORT  unlimited	
2b. DECLASSIFICATION/DOWNGRADING SCHEDULE		5. MONITORING ORGANIZATION REPORT NUMBER(S)  1643	
4. PERFORMING ORGANIZATION REPORT NUMBER(S)		7a. NAME OF MONITORING ORGANIZATION AFOSR	
6a. NAME OF PERFORMING ORGANIZATION Materials Science & Eng. Dept University of Pittsburgh	6b. OFFICE SYMBOL (If applicable)	7b. ADDRESS (City, State, and ZIP Code) Bolling AFB, D.C. 20332-6448	
8a. NAME OF FUNDING/SPONSORING ORGANIZATION AFOSR	8b. OFFICE SYMBOL (If applicable)	9. PROCUREMENT INSTRUMENT IDENTIFICATION NUMBER Grant No. AFOSR - 86 - 0251	
8c. ADDRESS (City, State, and ZIP Code) Bolling AFB, D.C. 20332-6448		10. SOURCE OF FUNDING NUMBERS	
		PROGRAM ELEMENT NO. 61102F	PROJECT NO. 2306
		TASK NO. A2	WORK UNIT ACCESSION NO.
11. TITLE (Include Security Classification) Program to Study the Oxidation of Carbon-Carbon Composites and Coatings on these Materials.			
12. PERSONAL AUTHOR(S) J. Cullinan, J. Schaeffer, E. A. Gulbransen, G. H. Meier, F. S. Pettit			
13a. TYPE OF REPORT Final Technical	13b. TIME COVERED FROM 7/15/86 TO 7/13/89	14. DATE OF REPORT (Year, Month, Day) September 30, 1989	15. PAGE COUNT 206
16. SUPPLEMENTARY NOTATION			
17. COSATI CODES		18. SUBJECT TERMS (Continue on reverse if necessary and identify by block number)	
FIELD	GROUP	SUB-GROUP	
19. ABSTRACT (Continue on reverse if necessary and identify by block number)			
<p>The oxidation of carbon-carbon composites and coatings on these composites in oxygen at temperatures between 300 to 1400°C has been investigated. State-of-the art systems have been characterized prior to the oxidation studies by using optical and scanning electron microscopy. It has been determined that uncoated carbon-carbon composites cannot be used at temperatures above about 400°C for extended periods of time because of oxidation. Oxidation does occur at temperatures below 400°C but at very low rates. Boron has not been found to be an effective inhibitor for carbon-carbon oxidation. Water vapor increased the oxidation rate of these uncoated composites at temperatures below about 600°C. Oxidation products involving boron were removed from these composites at temperatures above 600°C when water vapor was present in the gas. Coatings were useful in protecting carbon-carbon composites from oxidation under isothermal test conditions but these coatings failed under cyclic conditions. The factors leading to the failure of coatings on carbon-carbon composites are described.</p>			
20. DISTRIBUTION/AVAILABILITY OF ABSTRACT <input checked="" type="checkbox"/> UNCLASSIFIED/UNLIMITED <input type="checkbox"/> SAME AS RPT. <input type="checkbox"/> DTIC USERS		21. ABSTRACT SECURITY CLASSIFICATION Unclassified	
22a. NAME OF RESPONSIBLE INDIVIDUAL L. J. Shioler		22b. TELEPHONE (Include Area Code) 202-767-4933	22c. OFFICE SYMBOL NE

# ABSTRACT

The oxidation of carbon-carbon composites and coatings on these composites in oxygen at temperatures between 300 to 1400°C has been investigated. State-of-the-art systems have been characterized prior to the oxidation studies by using optical and scanning electron microscopy. It has been determined that uncoated carbon-carbon composites cannot be used at temperatures above about 400°C for extended periods of time because of oxidation. Oxidation does occur at temperatures below 400°C but at very low rates. Boron has not been found to be an effective inhibitor for carbon-carbon oxidation. Water vapor increased the oxidation rate of these uncoated composites at temperatures below about 600°C. Oxidation products involving boron were removed from these composites at temperatures above 600°C when water vapor was present in the gas. Coatings were useful in protecting carbon-carbon composites from oxidation under isothermal test conditions but these coatings failed under cyclic conditions. The factors leading to the failure of coatings on carbon-carbon composites are described.



Accession For	
NTIS GRA&I	<input checked="" type="checkbox"/>
DTIC TAB	<input type="checkbox"/>
Unannounced	<input type="checkbox"/>
Justification	
By	
Distribution/	
Availability Codes	
Dist	Avail and/or Special
A-1	

## TABLE OF CONTENTS

	Page
Abstract	
1.0 Introduction . . . . .	1
2.0 Carbon-Carbon Oxidation	
2.1 Carbon Oxidation . . . . .	4
2.2 Oxidation of Carbon-Carbon Composites . . . . .	7
2.3 Oxidation of Inhibited Carbon-Carbon . . . . .	8
2.4 Coatings for Carbon-Carbon Composites . . . . .	16
2.4.1 SiC Oxidation . . . . .	16
2.4.2 Coating Systems . . . . .	21
3.0 Experimental	
3.1 Sample Procurement . . . . .	27
3.2 Isothermal Oxidation . . . . .	29
3.3 Cyclic Oxidation . . . . .	31
3.4 Acoustic Emission . . . . .	31
3.5 BET Surface Area Measurements . . . . .	32
3.6 Density Measurements . . . . .	33
3.7 Metallography . . . . .	33
4.0 Results and Discussion	
4.1 Uncoated Carbon-Carbon Composites . . . . .	36
4.1.1 Initial Characterization . . . . .	36
4.1.2 Oxidation Kinetics in Dry Oxygen . . . . .	40
4.1.2.1 Stage 2 Oxidation Behavior . . . . .	41
4.1.2.2 Stage 3 Oxidation Behavior . . . . .	49
4.1.2.3 Structures of Carbon-Carbon . . . . .	51
4.1.3 Oxidation Kinetics in O <sub>2</sub> -H <sub>2</sub> O . . . . .	53
4.2 Coated Carbon-Carbon Composites . . . . .	56
4.2.1 Initial Characterization . . . . .	56
4.2.1.1 HP24 . . . . .	57
4.2.1.2 HP24/M185 . . . . .	59
4.2.1.3 HP24/BXC/RT42A/Glaze and /No Glaze . . . . .	60
4.2.2 Oxidation Kinetics of Coated Carbon-Carbon . . . . .	62
4.2.2.1 Isothermal Oxidation . . . . .	62
HP24 . . . . .	63
HP24/M185 . . . . .	67
HP24/BXC/RT42/No Glaze . . . . .	70
HP24/BXC/RT42/Glaze . . . . .	71
4.2.2.2 Cyclic Oxidation . . . . .	75
Results Obtained at 1125°C . . . . .	75
Results Obtained at 900°C . . . . .	78
Summary of Cyclic Oxidation Results . . . . .	81
4.2.2.3 Acoustic Emission . . . . .	82
4.2.2.4 Coating Recommendations . . . . .	83
HP24 . . . . .	83
HP24/M185 . . . . .	85
No Glaze and Glaze . . . . .	86



5.0 Conclusions . . . . . 88

6.0 References . . . . . 92

Appendix A

## 1.0 INTRODUCTION

Carbon-carbon composites (CCC) are being considered for aerospace applications because of their light weight and excellent mechanical properties. Depending upon the application<sup>(1)</sup>, carbon-carbon composites could be used for periods ranging from a few hours to a few thousand hours at temperatures in the interval between 600°C and 2200°C. A major problem in using such materials in oxidizing environments is that carbon reacts with oxygen forming gaseous carbon oxides. Two approaches are being examined to protect carbon-carbon composites in oxidizing environments, in particular, the use of inhibitors to slow the reaction rates, and the use of coatings where a barrier develops between the composite and gases which limits the reaction rate. It has been proposed that boron and phosphorus additives which form  $B_2O_3$  and  $P_2O_5$ , can inhibit the oxidation of carbon.<sup>(2)</sup> Furthermore, several protective coatings are being considered to prevent oxygen from reacting with carbon.<sup>(3,4)</sup> These coatings rely on the development of oxide films which provide protection by inhibiting oxygen diffusion. A typical coating under consideration is silicon carbide which upon oxidation forms a silica film that acts as a diffusion barrier. A problem arises in attempting to use coatings to protect carbon-carbon, since thermal expansion mismatch between the

composite and the coating causes the coating to crack. Frequently, composite systems contain additives which upon oxidation form liquids that can seal such cracks.<sup>(3)</sup>

Luthra <sup>(1)</sup> has compared the oxidation rates of some uninhibited carbon-carbon composites to calculated rates based upon gas phase diffusion and a surface reaction as rate-limiting steps (Figure 1). This comparison shows that the oxidation of carbon is limited by gas phase diffusion at temperatures above about 800°C and a surface reaction controls the rate at lower temperatures. The actual rates of oxidation are orders of magnitude greater than the acceptable rates for both short- and long-term applications at temperatures above 600°C. If carbon-carbon composites are to be used at temperatures above 600°C in oxidizing environments, coatings must be used. Moreover, in view of the sensitivity of coatings to cracking, the inhibition of the oxidation reaction must be examined, and utilized as effectively as possible.

Another problem encountered in using carbon-carbon composites arises from variability in fabricating these materials. For example, the SiC conversion layers often penetrate deeper through the matrix than through the fibers.<sup>(5)</sup> The effect of such variations in coating microstructure on coating performance has not been documented.

This program has been concerned with the oxidation of carbon-carbon composites (CCC) at temperatures between 300 and 1500°C. Inhibition effects, the influence of water vapor, and the behavior of relevant coatings have also been investigated. The approach utilized has consisted of thorough documentation of the as-processed materials using optical metallography, scanning electron microscopy (SEM), and transmission electron microscopy (TEM). Oxidation of uninhibited and inhibited carbon-carbon was studied in dry oxygen over a range of temperatures between 300 and 1300°C. The effect of water vapor on the oxidation of such materials was then studied. Finally, oxidation of coated specimens was examined at temperatures between 800 and 1500°C.

In the following sections of this report an assessment of the literature for carbon-carbon is presented. The experimental procedures are then described. In the results and discussion section the oxidation of carbon-carbon composites is documented and described, inhibition of the oxidation process and the effects of water vapor are explained, and coating degradation on carbon-carbon composites is documented along with the identification of coating characteristics which result in premature failure.

## 2.0 CARBON-CARBON OXIDATION

### 2.1 Carbon Oxidation Behavior

The oxidation of CCC and various forms of carbon has been the subject of many research studies. Reports indicate that at high temperatures ( $T > 800^{\circ}\text{C}$ ) the rate controlling step is oxygen diffusion through a boundary layer of reaction product.<sup>(6-8)</sup> At lower relative temperatures a surface reaction controls the oxidation rate.<sup>(7,9-11)</sup> Figure 1 shows this transition in rate controlling processes for CCC oxidation. The temperature at which this transition occurs is reported to be a function of the gas flow rate, gas pressure, sample size, surface area, and impurity content.<sup>(12,13)</sup> The oxidation of CCC should not differ extensively from that of various carbons.

The oxidation of carbon follows a normal Arrhenius type of relationship of the form:

$$\text{rate} = A \exp(-E/RT)$$

where A is a preexponential term; E is the experimental activation energy; R is the gas constant; and T is the absolute temperature. Typical values obtained for E in the chemical (surface) controlled temperature range are: 44 KCal/mol for graphite by Tyson<sup>(7)</sup>; 40 - 56 KCal/mol by Serpinet<sup>(14)</sup>; 41.5 KCal/mol for Rhee and Chang<sup>(15)</sup>; 42 KCal/mol

by Eyring and Blyholder<sup>(10)</sup>; and 39KCal/mol for spectroscopic carbon by Gulbransen.<sup>(16)</sup> The values for E in the diffusion controlled regime are about 1 KCal/mol.

The processes involved in the chemically-controlled regime have not been described precisely. Eyring and Blyholder<sup>(10)</sup> proposed that the desorption of CO(g), which has an activation energy of 40 kcal/mole was rate controlling. Gulbransen et. al.<sup>(9)</sup> proposed the adsorption of oxygen was rate controlling for thick specimens.

Wicke<sup>(17)</sup> classified the activation energy for the oxidation of carbon into three regimes described in terms of the oxygen concentration at the specimen surface. In the first regime, the oxygen concentration is the same over all the active surface of the sample. The activation energy obtained in this case is the true activation energy for the surface controlled reaction. The second regime is described by an oxygen concentration at the specimen surface which is less than that in the bulk gas. The activation energy in this case is 0.5 of the activation energy for a surface controlled reaction. In the third regime, gas diffusion through a boundary layer is controlling, i.e., the oxygen concentration is low at active surfaces. In this case the value for the activation energy is small, tending toward zero.

The oxidation rate of carbon changes with microstructure. Carbon occurs in many structures including: diamond, glassy, pyrolytic, and graphite. Generally, the more graphitic a carbon, the less reactive it tends to be. The total reaction rate, however, depends on impurities and pore structure.

Pore structure can influence the oxidation rate of carbon. Rienoso and Walker<sup>(18)</sup> found that a glassy carbon had an oxidation rate slower than that of a more graphitic pyrolytic carbon. The glassy carbon had no connected porosity so the active surface area remained constant during oxidation. The pyrolytic carbon had a connected network of porosity that caused the active surface area to increase with oxidation resulting in faster overall rates.

Impurities can also influence carbon oxidation.<sup>(13,15,18,19)</sup> Most elements catalyze the oxidation of carbon. The catalysts increase the oxidation by either an electron transfer mechanism or an oxygen transfer mechanism.<sup>(19)</sup> Notable exceptions are P and B without water. These two elements inhibit the oxidation of carbon. Figure 2<sup>(20)</sup> shows the effect that B can have on the oxidation of carbon.

The surface area to volume ratio of the carbon can affect the oxidation behavior by increasing the surface temperature as a result of the exothermic oxidation of the carbon. Gulbransen<sup>(12)</sup> calculated a 90°C temperature increase at the

surface for a sample at 1200°C and a surface area of 0.13 cm<sup>2</sup>. This sample size was small enough to avoid limiting the rate of reaction because of oxygen consumption, i.e., oxidation was controlled by a surface reaction.

Several authors have reported a change in surface area, usually an increase, with oxidation exposure.<sup>(12,15,18)</sup> If the surface area increases, the overall oxidation rate increases unless a correction is made. The surface area change also makes the observation of true oxidation rates difficult.

In summary, the oxidation of carbon has been extensively studied. The rate determining step for the oxidation process at temperatures below 600-800°C is a phase boundary reaction involving the adsorption-dissociation-desorption of oxygen molecules, CO, and CO<sub>2</sub>. At higher temperatures the rates are controlled by diffusion of oxygen, CO, and CO<sub>2</sub> through a gaseous boundary layer at the specimen surface.

## 2.2 Oxidation of Carbon-Carbon Composites

The constituents in a CCC do not oxidize at the same rate. At temperatures between 650 and 800°C the matrix carbon oxidizes faster than the more graphitic carbon fibers.<sup>(21,22)</sup> The oxidation apparently starts at the fiber/matrix interface, proceeds to the matrix and then the fibers.



The rate of oxidation for a CCC composite is reported to be higher than the rate for pyrolytic or amorphous carbon<sup>(12)</sup> and composites made from PAN fibers are more reactive than composites made from pitch fibers.<sup>(23)</sup> This lower reaction rate may be related to the more graphitic structure that can be attained in the pitch fibers.

The heat treatment temperatures used in the fabrication of a CCC can affect oxidation. The reason for the effect is unclear but may be related to retained impurities.<sup>(21,24,25)</sup>

Flow rate has been shown to affect the oxidation behavior of CCC.<sup>(24)</sup> Generally as the flow rate increases the oxidation rate also increases. Dependence of an oxidation rate on flow rate indicates that diffusion through a boundary layer is controlling.

Stresses on a sample during oxidation have also affected oxidation rates.<sup>(26,27)</sup> Compressive stresses have little or no affect on the oxidation, while tensile stresses open pores and microcracks, which accelerate oxidation.

### 2.3 Oxidation of Inhibited Carbon-Carbon

Boron and phosphorous have been added to CCC as inhibitors to slow the oxidation of carbon. Apparently oxides of these elements block active surface sites, slowing the phase boundary controlled oxidation process. The oxides

accomplish this without changing the activation energy of the process.<sup>(20)</sup>

Early inhibition studies were concerned primarily with the oxidation protection of nuclear reactor graphites. Workers<sup>(28-36)</sup> found that Cl, CCl<sub>4</sub>, POCl<sub>3</sub>, P<sub>2</sub>O<sub>5</sub>, and B<sub>4</sub>C slowed the reaction of carbon with oxygen. McKee<sup>(19)</sup> lists these substances and their derivatives as the only known inhibitors of the carbon oxidation reaction.

PhosphorusOxyChloride (POCl<sub>3</sub>) has been studied by several workers and several mechanisms have been proposed. Arthur and Bangham<sup>(35)</sup> suggest that POCl<sub>3</sub> may slow reactions between CO and O<sub>2</sub> since CO/CO<sub>2</sub> ratios are larger when the inhibitors are present. Wicke<sup>(17)</sup> on the other hand proposes that the inhibitor acts as a physical barrier between the oxygen and carbon. The physical barrier was thought to occur even though the concentration of POCl<sub>3</sub> was not large enough to create a monolayer on the surface.

Magne et. al.<sup>(33)</sup> studied the effects of phosphates on the oxidation of graphite. The phosphates had two effects on the reaction. One effect was the neutralization of catalytic impurities on the surface. The other effect was the decreased reactivity of carbon atoms by direct reaction with the phosphates. The authors state that the phosphates may not impede very potent catalysts like lead. These workers also

found that  $\text{CO}/\text{CO}_2$  ratios increased when inhibitors were present.

McKee<sup>(8)</sup> examined the morphology of  $\text{POCl}_3$ -inhibited single crystal graphite after oxidation. Earlier workers<sup>(37)</sup> had found that single crystal graphite oxidized at the edges of basal planes and at dislocations that emerged from the basal plane. The attack was shown by etch pits that had formed. McKee, however, did not observe etch pits on an inhibited sample at these sites at temperatures of up to  $200^\circ\text{C}$ . The strong adsorption of  $\text{POCl}_3$  at these sites was thought to block the oxidation process.

In a later study McKee<sup>(38)</sup> used various organophosphates to inhibit graphite powders. He found that a similar activation energy existed for the inhibited powder (48 KCal/mol) and the uninhibited powder. This suggested that the inhibitors blocked reactive surface sites.

Boron-based inhibitors have followed a similar evolution. Early workers found that B additives slowed the reaction of carbon with oxygen.<sup>(31,36)</sup> Woodley<sup>(31)</sup> did work on boronated graphite. The boron was added as boron carbide ( $\text{B}_4\text{C}$ ) to two grades of graphite, "black" and "grey". The black graphite exhibited increasing oxidation rates as a function of time at temperatures between  $500$  and  $800^\circ\text{C}$  similar to ordinary nuclear graphite. The grey graphite, however, exhibited a maximum in

oxidation rate with time followed by a decrease in rate. Woodley attributed this effect to the formation of more  $B_2O_3$  in the grey material as a result of a more uniform distribution of the carbide. The  $B_2O_3$  formed at rates slower than the oxidation of C into  $CO_2$ . The build-up of  $B_2O_3$  reduced surface areas 25 - 50% by filling pores and providing a physical barrier between reactants leading to inhibition. The activation energies for the oxidation reaction were between 31 and 38 KCal/mol. Woodley also found that B altered the  $CO/CO_2$  ratio such that little CO formed between 580 and 780°C.

Walker and Alldarice<sup>(36)</sup> studied the effect of B doping of graphite on oxidation kinetics. These workers observed a maximum in oxidation rate for doped and undoped samples at 1% burn off (ie. 1% of total weight of carbon is oxidized). The rate decayed into a steady state rate at 6% burn off ( $T=625^\circ C$ ,  $P_{O_2}=100$  Torr). Activation energies varied between 45 and 52 KCal/mol. Lower activation energies were associated with higher levels of doping. The authors attributed the reduction in oxidation rate of the doped samples to the blocking of active oxidation sites. The surface area as determined by BET exhibited a maximum at 10% burn off for the same conditions. For the undoped sample a constant value of surface area was observed after the maximum, while the doped sample exhibited a decrease in surface area.

The same authors examined the effect of water vapor on the oxidation of B doped graphite. Water vapor caused  $B_2O_3$  removal from external surfaces by the formation of volatile boric acids. No such effects were observed on internal surfaces.

The morphology of molten  $B_2O_3$  on single crystal graphite has been studied by Thomas<sup>(37)</sup> who found that the liquid  $B_2O_3$  had a globular form on the graphite surface but also filled hexagonal holes on the surface. As these underlying holes widen the liquid reverts to the globular form. Splitting of the boron oxide globules was seen to occur.

McKee<sup>(20)</sup> impregnated graphite powders with B-based solutions and heated them to convert the solutions to boron oxide. An addition of 2 weight percent boron oxide reduced oxidation by a factor of five at 800°C. Activation energies increased with  $B_2O_3$  additions from 46 to 51 KCal/mol. Organoboron compounds that wetted the graphite were the most effective inhibition solutions. These compounds resulted in finer dispersions of boron oxide in the graphite. Boron oxide was present in concentrations large enough to cover the entire surface, but did not, as evidenced by the constancy of activation energies. Instead,  $B_2O_3$  segregated to active oxidation sites. The preference of boron oxide to poison active sites was associated with the bonding of glassy  $(BO_3)_n$

groups to terminal carbon atoms. Oxidation in environments containing water vapor was not found to affect the inhibiting effects of boron. This observation may be the result of a large amount of  $B_2O_3$  on the specimen surface.

McKee<sup>(39)</sup> studied the effect of borate coatings on carbon-carbon composites (CCC). The samples used in the study consisted of polyacrylonitrile (PAN) fibers in a pyrolyzed pitch matrix. McKee also tested fibers without a matrix. A nonisothermal, linear temperature ( $10^\circ\text{C}/\text{min}$ ) rise, oxidation test was run on treated and untreated fibers in air. The untreated fibers lost weight significantly at  $450^\circ\text{C}$ . Treated fibers lost no weight until a temperature of  $1000^\circ\text{C}$  was obtained. Untreated CCC lost weight at  $500^\circ\text{C}$  while the treated CCC lost weight at  $1000^\circ\text{C}$ . Isothermal oxidation tests in air at  $1000^\circ\text{C}$  showed that impregnation of pores with borates in conjunction with borate coatings was the most effective way of protecting CCC from oxidation. The small weight losses observed in the test were attributed to the loss of boron oxide as a vapor species. Additions of water vapor to the air increased the weight loss as a result of the higher vapor pressures of hydrated boron oxides but still resulted in reduced oxidation rates. The eventual vaporization of the boron oxide coating in air and in air-water atmospheres led to the rapid gasification of the CCC. It was concluded that

coating CCC with  $B_2O_3$  could prevent oxidation at temperatures up to  $1000^\circ C$ . McKee pointed out that the ends of carbon fibers were poor in resistance to oxidation. Apparently the fibers oxidized at the ends and along the axes and undercut the boron oxide coating.

Ehrburger et. al.<sup>(4)</sup> studied the inhibition of CCC oxidation with boron oxide. The composite was made of exacrylic fibers (30%), pyrocarbon matrix(40%), and open porosity(30%). The inhibitor was added by converting orthoboric acid to boron oxide by heating in  $N_2$  at 973K. Electron microscopy revealed that a 1 hr. treatment resulted in the boron oxide forming as globules. Globular boron oxide exhibited unpredictable oxidation results. An alternative treatment for 61 hours resulted in the boron oxide uniformly covering surfaces with more reproducible oxidation results. Oxidation results were characterized in terms of an inhibition factor. The inhibition factor was the ratio of the oxidation rate of an untreated sample to the rate of an inhibited sample. The inhibition factor was found to increase with boron oxide content. The rate of increase, however, decreased after a 2 w/o (weight percent) boron oxide addition. The reductions in oxidation rate were explained in terms of the amount of boron oxide added to the composite. Additions up to 2 w/o were proposed to block active reaction sites.

Amounts greater than 2 w/o boron oxide resulted in a diffusion barrier that separated the reactants. The CO/CO<sub>2</sub> ratio for oxidation at 707°C was lower for inhibited samples and varied with the amount of burn off. In addition this ratio was lower for increased additions of B<sub>2</sub>O<sub>3</sub>. At a 10 w/o boron oxide addition the reacted gas was essentially CO<sub>2</sub>.

Wallouch and Hientz<sup>(40)</sup> experimented with a B-P-SiO<sub>2</sub> inhibitor which caused oxidation rates to decrease for samples tested at 500-800°C. This inhibition effect was more effective on fine grained graphites than coarse grained graphites. The reason for this difference was thought to be a reduction in more active surface area for the fine grained graphite which causes the preexponential term in the Arrhenius expression used to describe carbon oxidation to be decreased.

CCC have been fabricated with a chemical vapor infiltrated (C.V.I.) BN filler inhibition system<sup>(41)</sup> which provided oxidation resistance up to 1000°C if the porosity was maintained at low levels. Greater oxidation resistance was found for increased BN content. Christin et. al.<sup>(42)</sup> used SiC to obtain oxidation resistance. SiC was found to work only when the composite was fully densified. Rossignol et. al.<sup>(43)</sup> used TiC to inhibit carbon. TiC was less effective than SiC or BN.



The data available on the inhibition of carbon-carbon shows that there are two ways that the oxidation of carbon can be inhibited. One involves procedures where the rates of the chemical reaction (adsorption-dissociation-desorption) at the surface of carbon are decreased. The other approach involves the development of a barrier layer which separates the carbon from the gaseous reactants.

#### 2.4 Coatings for Carbon-Carbon Composites

CCC oxidize at high temperatures at catastrophic rates. The rates are such that untreated CCC cannot be used for long or short term applications.<sup>(1)</sup> Inhibition of CCC does not slow the rate of oxidation enough to use the composites at high temperature ( $T > 800^{\circ}\text{C}$ ). The use of CCC at high temperatures thus requires the use of a suitable coating. Coatings exposed to oxidizing environments at high temperature selectively oxidize elemental constituents to form a protective oxide scale. The protective scale acts as a transport barrier between the aggressive environment and the substrate. The scale is usually based on the slowly growing scales of  $\text{Al}_2\text{O}_3$ ,  $\text{SiO}_2$ , and  $\text{Cr}_2\text{O}_3$ .<sup>(44)</sup>

##### 2.4.1 SiC Oxidation

The current coatings used on CCC are usually based on Si. Silicon reacts with the carbon in low  $P_{O_2}$  environments to form silicon carbide, SiC. SiC is a polymorphic line compound that can have a wide range of Si and C thermodynamic activities.

Coatings of SiC on CCC are applied by vapor deposition processes. In a deposition process where Si is in excess the SiC has a Si activity of nearly 1.0. The other extreme is where carbon is in excess and the SiC has a carbon activity of nearly 1.0. SiC oxidizes very slowly as a result of the formation of  $SiO_2$ .<sup>(45)</sup> Many studies of the oxidation behavior of SiC have been published.<sup>(45-55)</sup> A brief review of some of this work is useful to better understand the behavior of SiC coated CCC.

The oxidation mechanisms of a nonoxide ceramic are more complicated than that for a pure metal because the oxidation of both components of such ceramics must be considered. In the case of SiC oxidation, Si reacts to form  $SiO_2$ , while the C can form CO or  $CO_2$  of various pressures. The oxidation kinetics of SiC are often parabolic with time indicating a diffusion controlled reaction. The rate controlling step is controversial and depends on the characteristics of the  $SiO_2$  that is formed. Some workers have found that the diffusion of oxygen in molecular form to the SiC/ $SiO_2$  interface is the rate controlling step.<sup>(47)</sup> Other workers<sup>(49,52)</sup> indicate that

desorption of CO from the SiC/SiO<sub>2</sub> interface controls the oxidation rate especially at higher temperatures.

Spear and Tressler<sup>(47)</sup> have studied the oxidation of green colored single crystal SiC. They found parabolic kinetics at 1200<T<1500°C in Po<sub>2</sub> > 0.001 atm. The activation energy for oxidation of (0001) Si faces of the SiC was between 53.3 and 71.2 KCal/mol. The energy for the (000 $\bar{1}$ ) C faces was 26.7 KCal/mol at 1200<T<1350 and 62.1 KCal/mol at T>1350°C. The experimental activation energies were in good agreement with the following kinetic equation:

$$J_{\text{oxidants}} (\text{in}) = mNB / 2 X_0$$

where J is the flux of oxidizing species diffusing via interstitials or vacancies; m is a stoichiometric constant that depends on the predominating product species (m=1 for C, m=3/2 for CO, m=2 for CO<sub>2</sub>); N is the number of oxide molecules in unit volume of SiO<sub>2</sub>; B is the parabolic rate constant; and X<sub>0</sub> is the SiO<sub>2</sub> scale thickness. Oxygen diffusion by an interstitial mechanism (molecular form) was believed to be the predominant diffusing species at low temperature. Ionic diffusion of oxygen via vacancies was believed to be the rate controlling step at low Po<sub>2</sub>.

The oxidation of SiC exhibits an active to passive transition. The transition occurs when SiC is exposed to environments with low Po<sub>2</sub>. The SiC upon oxidation may form

gaseous species like  $\text{SiO}_{(g)}$ , instead of the passivating  $\text{SiO}_2$ .<sup>(56)</sup> Oxidation under these former conditions is considered to be in the active regime. The passive regime refers to oxidizing conditions where  $\text{SiO}_2$  forms on the surface of the sample. Gulbransen et. al. studied this phenomena on bulk single crystal SiC.<sup>(45)</sup> They found that the transition is strongly dependent on partial pressure of oxygen and temperature. For example, they found that the transition from active to passive oxidation for SiC occurred at .01 Torr  $\text{O}_2$  at 1200°C; .075 Torr  $\text{O}_2$  at 1300°C; .1 Torr  $\text{O}_2$  at 1350°C; and .5 Torr  $\text{O}_2$  at 1400°C. The  $\text{SiO}_2$  that formed on SiC was amorphous at temperatures lower than 1300°C. Above 1300°C, the  $\text{SiO}_2$  formed as cristobalite.

Pultz<sup>(49)</sup> has also studied the passive-active transition in SiC. Pultz found that active oxidation could occur at cracks and other microstructural defects in the SiC.

Schiroky<sup>(55)</sup> has studied the oxidation of 100  $\mu\text{m}$  coatings of C.V.D. SiC on graphite. Tests were done at 1000 to 1800°C in air for times up to 10 hours. Schiroky observed bubble formation at  $T > 1650^\circ\text{C}$ . The bubbles are mostly  $\text{CO}_{(g)}$ , caused by reaction of the protective  $\text{SiO}_2$  layer with SiC. Beneath the bubbles, tunnel-like holes penetrated the entire  $\text{SiO}_2$  layer thickness. Active oxidation of the SiC was proposed to have caused the formation of these holes. The oxygen needed to

create the holes was thought to result from diffusion through the bubble membrane.

Singhal<sup>(52)</sup> found pores in the scales of oxidized hot-pressed SiC. Singhal states that the pores are caused by oxidation products at the SiC/SiO<sub>2</sub> interface. The desorption of CO<sub>(g)</sub> from the interface was thought to be the rate controlling step in the oxidation reaction. Singhal also found that impurities concentrate in the glass-cristobalite scale. These impurities (e.g., Al, Na, Fe, K) alter the viscosity of the scale and thus the oxidation rate of the SiC.

Other workers<sup>(46,57)</sup> have observed bubbling on SiC at lower temperatures than those reported by Schiroky. The bubbling in these studies was thought to occur from oxidation of carbon inclusions in the SiC.

Silicon nitride is another Si-based coating that can be used to protect CCC.<sup>(58-60)</sup> Si<sub>3</sub>N<sub>4</sub> usually undergoes parabolic oxidation indicating a reaction controlled by diffusion.<sup>(61)</sup> Silicon nitride can have different oxidation properties when compared with SiC since the SiO<sub>2</sub> that forms can be quite different. Similar to SiC, porosity is often found in the SiO<sub>2</sub> scales formed on Si<sub>3</sub>N<sub>4</sub>.<sup>(51,61)</sup> The porosity is thought to be caused by oxidation products. Silicon nitride reportedly oxidizes faster than SiC at T>1450°C.<sup>(58)</sup> The difference in oxidation rate may be related to impurities. Silicon nitride

also erodes faster than SiC and has a higher vapor pressure.<sup>(51,58)</sup> A major factor favoring the use of silicon nitride coatings on CCC is a smaller thermal expansion mismatch than SiC.

#### 2.4.2 Coatings Systems

Most of the coatings used to protect CCC are fabricated by chemical vapor deposition (CVD).<sup>(62)</sup> CVD coatings are made by passing a source gas and a reductant together over a heated substrate. The source gases for SiC are usually trichloromethylsilane (TMS) and H<sub>2</sub> at 1000-1400°C. The sources for Si<sub>3</sub>N<sub>4</sub> are tetrachlorosilane and ammonia at 1000-1400°C. The temperature of the deposition process can be lowered by using Plasma Assisted Chemical Vapor Deposition (PACVD). The plasma is generated by using radio frequency radiation. Lowering deposition temperatures may reduce cracking induced by cool down from the process temperature. Coatings of SiC can also be formed on carbon using gases that fix a silicon activity in the gas whereby the carbon is siliconized.

Adhesion to the substrate is a problem with all coatings.<sup>(62)</sup> The thermal expansion mismatch between a coating and the substrate is a critical parameter. A large mismatch leads to a coating that is not adherent. Graded coatings have

been developed with compositions ranging from the substrate to the protective coating phase. These coatings may have better adherence to the substrate.

The mechanical properties of a coating are also important. Ceramic coatings undergo little plastic deformation to relieve expansion stresses while metal coatings/substrates can deform plastically. The tensile behavior of coatings depends on the deposition microstructure.<sup>(62,63)</sup> The amount of the reductant affects the morphology of the CVD coating. Low supersaturations result in columnar grains with domed tops. High amounts of reductant cause a structure composed of fine equiaxed grains.

The strength of CVD SiC is reduced from that expected of the bulk. Das and Saigal<sup>(63)</sup> found that the tensile strength of CVD  $\beta$ -SiC can be as low as 15 k.s.i. This strength is much lower than 75 k.s.i. obtained in some bulk SiC materials.<sup>(64)</sup>

Coating systems chosen to protect CCC for long times depend on the intended service temperature. Roughly the service temperature intervals for coatings are low temperature ( $T < 1400^\circ\text{C}$ ), intermediate temperature ( $1400^\circ\text{C} < T < 1800^\circ\text{C}$ ), and high temperature ( $T > 1800^\circ\text{C}$ ). These three regimes will be discussed based on work by Strife and Sheehan.<sup>(58,60)</sup>

The low temperature regime ( $T < 1400^\circ\text{C}$ ) has received the most attention commercially. Most efforts deal with coating

the CCC with SiC, Sialon, or  $\text{Si}_3\text{N}_4$ . The SiC and  $\text{Si}_3\text{N}_4$  coating, however, have significant thermal expansion mismatches with CCC. The net result is that thermal cycling results in cracking of the coating. The cracking is a serious problem because oxygen can diffuse rapidly down the cracks and react with unprotected CCC. The oxidation of unprotected CCC is catastrophic at these temperatures and, therefore, the cracks must be sealed. The composite is sealed internally or externally. One external method uses tetraethylorthosilicate (TEOS) to deposit silica in cracks and fissures that are present in the coating.<sup>(65,66)</sup> The purpose of the glass is to fill the cracks that open during thermal cycling. This requires the glass to have a low enough viscosity to wet the coating-substrate system. Too low a viscosity, however, will result in the glass flowing off the surface by gravitational or convectional forces. One can see from this discussion that the glass chemistry is critical. Borate glasses can also be used to seal the coatings both internally and externally. Borate glasses have viscosities and wetting characteristics that make them attractive additions to the coating protection system. Two disadvantages of the borate glasses are moisture sensitivity and fluxing of silica scales. Moisture sensitivity refers to the swelling of the glass when water is absorbed into the glass network. Glass swelling may disrupt



the coating. Fluxing of the silica by reaction with the borate glasses causes a break down in the protective mechanism of the coating. The fluxing may be lowered by additions of  $\text{SiO}_2$  to the borate glasses. Borates can seal the coating internally by adding the glass formers to the CCC. When oxygen diffusing through cracks encounters the glass formers a borate glass forms. There is a volume expansion that causes the borates to fill cracks and pores.

The intermediate temperature range,  $1400 < T < 1700^\circ\text{C}$ , still requires that the coating be based on  $\text{SiO}_2$  growth. The growth rates of  $\text{Cr}_2\text{O}_3$  and  $\text{Al}_2\text{O}_3$  are too rapid at these temperatures to be considered. The coating system in the intermediate range is sensitive to reduction of oxides by carbon. Carbon reduction of oxides causes large pressures of CO to form. Large pressures of CO can cause the coating to crack or even blow it off. Unalloyed borate glasses are susceptible to carbon reduction at temperature around  $1500^\circ\text{C}$ . Borate glasses used in this range should, therefore, avoid contact with regions of high carbon activity like the CCC substrate. At temperatures above  $1700^\circ\text{C}$   $\text{SiO}_2$  is reduced by  $\text{SiC}$  and  $\text{Si}_3\text{N}_4$ . This temperature is the upper limit for the use of Si-based coatings as the primary oxygen barrier. Thermal cycling problems still exist in the intermediate range even though the coating and scale should exhibit more plasticity. Only

vitreous  $\text{SiO}_2$  has similar thermal expansion characteristics with the CCC at these temperatures. Unfortunately the  $\text{SiO}_2$  devitrifies rapidly at these high temperatures. No simple solution to the thermal cycling problem is currently available. The other problems of oxide scale fluxing and viscosity changes will also be aggravated in this temperature range.

The high temperature regime of  $T > 1800^\circ\text{C}$  will require a coating based on something different from  $\text{SiC}$  or  $\text{Si}_3\text{N}_4$ . Nonoxide ceramics like  $\text{HfB}_2$  oxidize in a parabolic fashion, but at rates much too high for practical use. Coatings with these phases would have to be very thick, thus detracting from the attractive properties of the CCC substrate.

Graphite composites have been made with  $\text{ZrC}$ ,  $\text{ZrN}$ , and  $\text{HfB}_2$  additions to achieve oxidation resistance.<sup>(67-69)</sup> Oxides have to be considered the primary candidates for oxygen barriers. Of the many oxides available only  $\text{HfO}_2$ ,  $\text{ThO}_2$ ,  $\text{ZrO}_2$ ,  $\text{Y}_2\text{O}_3$ , and  $\text{Al}_2\text{O}_3$  could be used at  $T > 1800^\circ\text{C}$ . Many of these oxides allow oxygen to diffuse through them too rapidly to be considered. These oxides would also have to be in contact with refractory carbides with  $a_c$  much less than 1.0. Contact with the CCC substrate would cause reduction of the oxide by carbon. Volatility, chemical compatibility, thermal expansion mismatch, and oxygen (and carbon) permeability are all issues

that would have to be solved to obtain a reliable coating.

One successful coating in the high temperature range has been discovered.<sup>(68)</sup> Iridium is essentially impervious to oxygen and does not react with graphite until the eutectic temperature of 2110°C. Iridium forms volatile oxides much like Pt. The Ir oxides cause a recession rate of 1 to 10 mil per hour in high velocity gas streams at 2000°C.

NASA has done mission simulation testing on some current state-of-the-art coatings.<sup>(70)</sup> These coatings were SiC-based with various intermediate layers. These workers found that 10 to 20 hour protection could be expected in environments where temperature and humidity were changed to simulate a service mission. Coating adhesion and delamination of CVD layers was the major problem in achieving oxidation resistance.

In summary, the approaches to protect CCC using coatings have usually involved the formation of SiO<sub>2</sub> reaction product barriers with sealants to attempt to overcome the problems arising from cracks in the coatings. The success of such approaches requires more detailed examination than has been performed to date.

### 3.0 EXPERIMENTAL

#### 3.1 Sample Procurement

The CCC used in this study were fabricated by HITCO (1600 West 135<sup>th</sup> St., Gardena, California). Table I shows the HITCO designation codes for the acquired materials.

Table I

Carbon-Carbon Composites  
Investigated in the Current Program

<u>Designation Code</u>	<u>Fiber Precursor</u>	<u>Matrix Precursor</u>	<u>Filler</u>	<u>Densification</u>
CC136E	PAN	Phenolic Resin	Boron+ Carbon	CVD Carbon
CC137E	PAN	Phenolic Resin	B <sub>4</sub> C+ Carbon	CVD Carbon
CC139E	PAN	Phenolic Resin	Carbon	CVD Carbon
CC139C	PAN	Phenolic Resin	Carbon	CVD Carbon+ Extra Heat Treatment

The composites tested were constructed with T300HS fibers manufactured by Fiberite. These fibers were made from a polyacrylonitrile (PAN) precursor and woven in a satin weave

plies before lay up. The fibers had a 0-90° orientation in the composite. The matrix was created using several pressure-impregnation-carbonization (PIC) cycles with phenolic resin. Final densification of the composites was accomplished with two C.V.D. treatments in a carbon bearing gas. A "C" designation instead of a "E" represents an extra heat treatment during densification.

The fabricated CCC were roughly 50 volume percent fiber and 41 v/o matrix with the remainder being porosity. Inhibited composites were created by the addition of B or B<sub>4</sub>C with the carbon filler during PIC cycles. Uninhibited composites received no additives in the filler. The manufacturer reports the density of the composites to be between 1.69 and 1.77 g/cc. The higher densities are associated with the inhibited composites.

Table II shows the designations of the coated CCC used in this work. All coatings used are SiC-based. Most of the coatings were processed by HITCO and Chromalloy.

Table II

## Coated Sample Designations

<u>Name</u>	<u>SiC Layer</u>	<u>Additional Treatment</u>	<u>Coating</u>
HP24	thick	None	
HP24/M185	thick	HITCO coats the SiC with a silicate-based glaze	
HP24/BXC/RT42	thin	Chromalloy puts down boron carbide intermediate layers and a CVD SiC top layer	
HP24/BXC/RT42/G	thin	Same as above but a glaze is on top of the CVD SiC	

All coated CCC had a layer of the CC137E substrate converted into SiC by a pack cementation process designated HP24. In the process, Si vapor reacts with the surface of the composite to form a SiC layer. The thickness of this layer depended upon which coating process was to follow. A thin SiC layer was used in the Chromalloy processes, while a thick SiC layer was used in the HITCO M185 process. The details of both coating processes are proprietary.

### 3.2 Isothermal Oxidation

At temperatures between 300-1450°C isothermal oxidation kinetics were characterized in terms of weight change

measurements using continuously recording Cahn RH-100 and 2000 microbalances. Above 800°C most of the experiments were performed in the apparatus shown schematically in Figure 3. At lower temperatures the experiments were performed in similar equipment, but used furnaces other than the molydisilicide. Two sample sizes were standardized for uncoated CCC tests. These were designated large and reduced. The large size was 25x10x4 mm with a bulk surface area of 7.8 cm<sup>2</sup>. The small or reduced size was 13x5x3 mm with a bulk surface area of 2.4 cm<sup>2</sup>. All coated samples were 26x20x4 mm in size with a bulk area of about 14 cm<sup>2</sup>. The coated samples were large, but the size limited potentially significant "edge" effects.

The gas flow rates used in the testing of uncoated CCC varied between 14 and 550 cc/min. These volume flow rates correspond to linear velocities between .03 and 1.16 cm/sec. The flow rates used in coated sample work were between 50 and 70 cc/min. The gas used in most isothermal oxidation tests was ultra high purity O<sub>2</sub>.

To examine the effects of water vapor on the oxidation of uninhibited and inhibited CCC, experiments were performed in which oxygen was passed through two consecutive water baths at a fixed temperature prior to passing over the specimen. The weight changes of specimens were measured using a Cahn

microbalance.

### 3.3 Cyclic Oxidation

Cyclic oxidation tests combine isothermal oxidation with controlled thermal cycles. The combination of high temperature oxidation conditions and thermal cycling has the effect of spalling or cracking oxides and coatings. The cracking and spalling also occurs between coating and substrate. The damage is mainly the result of differing thermal expansion coefficients. The cyclic oxidation tests were performed in air in an apparatus which automatically inserted and removed the specimens from the hot zone. One cycle consisted of 45 minutes at the test temperature and 15 minutes at room temperature. The kinetics for cyclic oxidation testing were obtained by measuring weight change versus the number of cycles.

### 3.4 Acoustic Emission

Acoustic emission tests combine isothermal and cyclic oxidation test characteristics to analyze the cracking and spalling behavior in a material system. Cracking and spalling of protective oxides and coatings may involve the release of elastic waves that can be transduced into electronic signals. The electronic signals can then be processed to get



information about the cracking and spalling process. Kinetics are usually presented in terms of arbitrary counts versus a known temperature profile.

A schematic diagram of the acoustic emission device used in this work is presented in Figure 3. An alumina wave guide transmits the elastic waves from the sample in the hot zone to the PZT transducer. The alumina wave guide attaches to the sample with Cermabond 569 alumina cement. The transduced electronic signal is sent to a preamplifier via low noise coaxial cable and then to a Dunegan Endevco distribution analyzer and a chart recorder. The arbitrary acoustic emission counts are taken during the insertion, isothermal hold, and withdrawal of the sample from the hot zone. The atmosphere used in these tests was static air. The only samples tested with the acoustic emission device were coated samples.

### 3.5 BET Surface Area Measurements

In this work a Quantasorb BET device was used to measure the surface area of uncoated CCC. The surfaces of the samples were cleaned by flowing He at 150°C for 1 day prior to surface area measurements. The samples (20x15x4 mm) were then placed in a quartz fixture connected to a flowing gas line in the BET unit. Adsorption ( $T=77K$ ) and desorption ( $T=298K$ ) of

10%, 20%, and 30% N<sub>2</sub> in He were then used to determine the adsorbed amounts of N<sub>2</sub> gas. The actual amount of gas was determined by measuring arbitrary counts from a wheatstone bridge against a calibration volume of pure N<sub>2</sub>. Each mixture was run through 3 adsorption-desorption cycles to ensure reproducible results.

### 3.6 Density Measurements

Bulk density measurements were made in a standard fashion by measuring the volume of a sample with calipers and dividing this value into the weight. He-measured densities were made with a Quantasorb pycnometer. The pycnometer measures the pressure, volume, and temperature of helium in a reference cell and then exposes the same gas to a cell with the sample. By measuring the pressure and temperature in the work cell the volume that the gas occupies can be measured. This volume is subtracted from the known volume of the work cell to obtain the sample volume and, hence, the density.

### 3.7 Metallography

Dense coated and uncoated CCC samples were cross sectioned and polished using standard metallographic procedures. The mounting compound used was fine Epomet with an alumina dispersion. The alumina dispersion limited the

rounding of the edges that occurred during polishing, especially in coated samples. X-ray diffraction (XRD) was performed on all samples prior to metallographic procedures in a G.E. diffractometer using Cu-K $\alpha$  radiation.

Specimen preparation for metallography involved rough polishing using SiC grinding paper and final polishing with 15, 6, and 1.0  $\mu$ m diamond paste with a diamond extender. Scratches were difficult to avoid in oxidized composites due to loose particulates. Optical metallography was done on a Leitz Epivert metallograph.

Coating of the sample for SEM observation was done in a Poloron sputter chamber. Early in the work, Pd was used to coat the samples. It was found that normal sputtering with Pd still caused large amounts of charging to occur in the SEM. Later in the work it was found that a Au target with hard magnets surrounding the work area resulted in a more satisfactory coating. The samples were coated for 30 seconds and cooled for 30 seconds. This cycle was repeated six times. High currents were necessary during the process to achieve good coatings.

The samples were examined on a JEOL 35-CF scanning electron microscope (SEM). The SEM was equipped with wavelength dispersive (WDS) and energy dispersive (EDS) spectrometers for elemental analysis of observed

microstructures. EDS work was done for elements whose  $Z > 11$ . The WDS analyses were capable of detecting elements of  $Z > 4$ .

Preparation of transmission electron microscopy (TEM) samples was difficult. Uncoated samples were cut into thin wafers with a low speed diamond saw. The samples were placed on a polishing jig with wax and polished to a thickness of 1-2 mils. Often the samples during polishing lost cohesion and broke apart. This prompted the use of thicker samples ( $t > 3$  mils) and a Gatan dimpler. The samples were then ion milled with a Gatan ion miller. Transmission electron microscopy was done on a JEOL 200CX or a JEOL 2000FX. Coated (TEM) samples followed a similar preparation procedure. The coated samples, however, when polished to  $t < 10$  mils showed signs of a continuous crack network in all coated layers. The coated samples when removed from the jig broke apart. It was found that the CCC substrate aided in keeping the coated layer together. Further polishing used thick samples with a thin layer of CCC remaining. These samples were then dimpled, ion milled, and analyzed on the TEM.

## 4.0 RESULTS AND DISCUSSION

### 4.1 Uncoated Carbon-Carbon Composites

#### 4.1.1 Initial Characterization

Micrographs of the uncoated CCC samples are seen in Figures 4, 5, 6 and 7. Some figures contain both SEM and optical images of the CCC. Included in Figures 4 and 6 are the surface morphologies of the composites. Common features of the composites include: 50-100  $\mu\text{m}$  cracks in the C.V.D. carbon layer at the surface; 5-50  $\mu\text{m}$  fissure cracks in the planar and traverse cross sections; 25  $\mu\text{m}$  pores located at regions where fiber directions intersect each other; and a finer network of porosity concentrated at the interstices of the fibers and matrix.

The cracks observed in the initial microstructures result from differences in the thermal expansion coefficients of the carbons. Thermal expansion mismatch leads to cracks by the rupturing of bonds at interfaces during the complex heat treatments involved in the composite fabrication. There are at least four types of carbons contained in these 2D composites. These forms of carbon will be subsequently discussed.

Figures 8 and 9 show that the fibers are composed of fine 100 Å microcrystals. The size of the crystals was estimated by XRD measurements using the Scherer formula.<sup>(71)</sup> The XRD size measures regions of high crystalline order. The microcrystals in the carbon

fibers show a preferred orientation aligning their (002) basal planes parallel to the fiber axis. The preferred orientation is demonstrated by the large diffracted intensity (spots) normal to the fiber axis in the selected area diffraction (SAD) pattern in Figures 8 and 9. A further indication of this preferred orientation is seen in Figure 10 which shows a (002) pole figure of a 0-90° 2D composite. A 0-90° weave of the fibers results in a strong "cross" pattern. The "cross pattern" would be predicted if basal planes were oriented circumferentially or radially with respect to the fiber axis. Note that radial and circumferential orientations maintain the basal planes of carbon parallel to the fiber axis. The strong alignment of basal planes parallel to the fiber axis results in a high degree of anisotropy. These fibers, therefore, expand only a small amount along their length (covalent bonds), but a relatively large amount in the radial direction (Van der Waals bonds).

Figure 11 shows a transmission electron micrograph of the matrix. Two types of carbon are distinguishable. One type of carbon looks like "rosettes". The other type is the featureless carbon surrounding the rosettes. The rosettes are composed of randomly oriented microcrystals which are about the same size as those crystals that compose the fibers. The rosettes have a structure similar to forms of carbon black. The SAD pattern of the rosettes shows no preferred orientation of the microcrystals. The

other carbon comprising the matrix appears to be highly disordered carbon, i.e., glassy carbon. These carbons have thermal expansion coefficients that are between the limits set by the anisotropy of the carbon fiber parallel and normal to the fiber axis.

The last type of carbon observed in the composites was the CVD carbon. The CVD carbon was deposited from methane gas at elevated temperatures to densify the composites. The CVD carbon was not isolated for TEM or X-ray pole figure studies. Optical micrographs of composite cross sections show a structure reminiscent of pyrolytic carbon as might be expected from the deposition conditions. The micrographs reveal columnar nodules growing out from the surface to a thickness of 20  $\mu\text{m}$ . The CVD carbon also fills pores in the composite up to a distance of 100  $\mu\text{m}$ . Pyrolytic carbon has a preferred orientation of crystals as a result of the growth process. This preferred orientation results in anisotropic behavior with respect to the thermal expansion of the carbon.

The four types of carbons comprising the CCC all have dissimilar coefficients of thermal expansion. Cracking, therefore, is expected during temperature changes experienced in the fabrication processes.

X-ray diffraction results for CC137E (inhibited CCC) are presented in Figure 12. The XRD pattern shown is typical of inhibited composites. Uninhibited composites do not exhibit peaks from the  $\text{B}_4\text{C}$  inhibitor but in all other respects are identical.

The (001) peak in the graphite is normally an absent reflection. The (001) occurs in the pattern because the carbon in the composite is defective and many atoms are missing between aligned basal planes. The spacing of the (002) basal planes in the composites are about 3.43 Å. Perfect graphite has a spacing of 3.35 Å. The carbon in the composites is not graphitic. The (002) peak is also very broad as a result of the microcrystallinity of the carbon. The (004) peak was used to calculate the microcrystalline size with the Scherrer equation. The lattice parameters for hexagonal carbon are  $a_0 = 2.41$  Å and  $c_0 = 6.80$  Å. The XRD pattern also indicates that  $L_c$ , the basal plane spacing is 3.41 Å. A hump in diffracted intensity centers on a d-spacing of 1.85 Å. The nearest neighbor distance of atoms in the basal plane of graphite is 1.68 Å. This hump is from the glassy or disordered carbon observed in the matrix.

The other peaks in Figure 12 correspond to  $B_4C$ . Boron carbide is hexagonal and the lattice parameters from the pattern indicate that  $a = 5.64$  Å and  $c_0 = 11.90$  Å. No peaks from pure boron (tetragonal) were observed. This meant that elemental boron additions in CC136E convert to  $B_4C$  during the heating cycles used in fabrication of the composite. Figure 6 shows a  $B_4C$  particle in CC136E. Accompanying this micrograph is a WDS boron map.

The distribution of inhibitor in the inhibited composites varied. In the composite inhibited with  $B_4C$  (CC137E) the particles



were finer and more evenly distributed. In the composite inhibited with elemental B (CC136E) the boron carbides were larger and more unevenly distributed. No other elements besides B or C were detected by WDS or EDS.

#### 4.1.2 Oxidation Kinetics of Uncoated CCC in Dry Oxygen

The results obtained from weight change versus time measurements during the oxidation of uninhibited and inhibited carbon-carbon composites in dry oxygen at temperatures over the interval between 800 and 1300°C are presented in Figures 13 to 18. In these Figures both types of composites lose weight during oxidation but the weight losses are usually less for the inhibited samples. The weight change curves for both types of composites exhibit initial regions where the rates are increasing with time. This stage at  $T > 800^{\circ}\text{C}$  occurred because a few minutes elapsed before the specimens reached the temperature of the furnace. A thermocouple was placed within a specimen and the time to uniformly heat this specimen to the furnace temperature was the same as the time over which the initial stage was observed. The initial stage at lower temperatures ( $T < 600^{\circ}\text{C}$ ) may be the result of inhibitors or oxidation of the CVD carbon layer in addition to transients in temperature. The oxidation kinetics for both types of composites exhibit a linear second stage. These rates are linear as a result of the oxidation of carbon to CO and CO<sub>2</sub>. Only the inhibited

composites exhibited a third stage over which the rates decreased with time. This region was caused by the oxidation of boron in the composite.

#### 4.1.2.1 Stage 2 Oxidation Behavior

In the linear second stage region ( $T > 700^{\circ}\text{C}$ ) the rate constants were affected by temperature, gas flow rate and specimen size. The effects of gas flow rate and specimen size became more pronounced as the temperature was increased. Typical results showing the effect of flow rates are presented in Figures 19 and 20. In Figure 19 the gas flow rate affected the linear rate constant to temperatures as low as  $700^{\circ}\text{C}$ . The data presented in Figure 20 are for temperatures between 800 and  $1300^{\circ}\text{C}$ . Higher rates are obtained for the higher flow rates. The oxidation rates are affected by gas flow rates, because the supply of oxygen to the surface cannot keep up with the rapid surface reactions. Depletion of oxygen at the surface causes a boundary layer to form. The thickness of the boundary layer is dependent on the gas flow rate. Consequently the oxidation rates are also affected by specimen size as shown in Figure 21, where the larger specimens oxidize at lower rates than smaller specimens. Large specimens deplete the oxygen supply at the leading edge. Oxygen depletion causes a larger boundary layer to form resulting in slower oxidation rates.

The change of the surface areas of specimens as a function of oxidation time was measured and typical results are presented in Figure 22. While the results from surface area measurements showed some scatter, it was apparent that the surface areas of specimens increased with the oxidation time. Density measurements, Figure 33, indicated that the inhibited samples may have more interconnecting porosity compared with uninhibited specimens. The linear oxidation rate constants for stage 2 could be lower than indicated in Figures 13 through 18 because of surface area increases. No attempts were made to correct these data for surface area changes, because the shape of these curves at high temperatures ( $T > 800^{\circ}\text{C}$ ) did not suggest any effect of the surface area change. At temperatures in the range between 300 and  $700^{\circ}\text{C}$  the oxidation rate is slow and surface area changes are small.

Figure 24 is a plot of the linear rate constants for stage 2 as a function of reciprocal temperature. At temperatures below about  $600^{\circ}\text{C}$  these constants obey an Arrhenius relationship with an activation energy of about 43 kcal/mole. In this temperature range, the rate constants are not affected by specimen size or gas flow rate. The rate controlling process must involve the adsorption, dissociation, and desorption of oxygen, CO, and  $\text{CO}_2$ . A large difference between rate constants obtained for uninhibited and inhibited CCC was not evident.

As is clear in Figure 24 the slope of the Arrhenius plot is greatly reduced at temperatures above about 800°C. Moreover, the magnitudes of the rate constants in this region are affected by specimen size and gas flow rate. The activation energy is about 0.5 kcal/mole which is consistent with diffusion in a gaseous boundary layer over the specimen as controlling the rate of oxidation. In this temperature range, the oxidation rate of uninhibited carbon-carbon was determined empirically as a function of flow rate and sample size. The following expression was obtained:

$$\text{Oxidation Rate (gm/cm}^2\text{-s)} = .001(F/A)^{0.68}$$

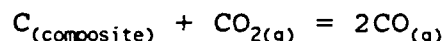
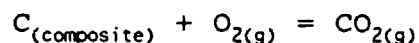
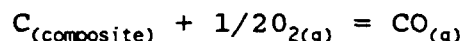
where F is the linear flow rate (cm/S) and A is the bulk specimen area (cm<sup>2</sup>).

At temperatures between about 600 and 800°C, Figure 24, the linear rate constants are influenced by flow rate and specimen size, but the activation energy is higher than that for gaseous diffusion. In this region the rate is determined by a coupling of the phase boundary chemical reactions and diffusion in the boundary layer.

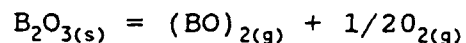
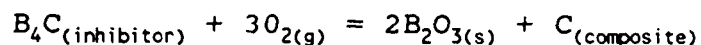
In Figures 13 through 18 it can be seen that the weight losses of the inhibited samples are usually less than those of the uninhibited samples. In Figure 24 it can be seen that at temperatures between about 600 and 800°C, the temperature regime where the oxidation rate is controlled by coupling of the phase

boundary and diffusion reactions, the inhibited specimens have lower rate constants than the uninhibited specimens. Furthermore even in the gas diffusion controlled regions the inhibited samples have the lower rates, Figure 24.

In the oxidation of an uninhibited CCC as shown in the Appendix three major chemical reactions occur. These are:



All three of these reactions lead to weight losses. For the inhibited composite several new reactions are possible. These are:



The first reaction results in specimen weight gains on the microbalance while the sublimation reactions of boron oxide result in weight losses. These reactions complicate the analysis of the oxidation kinetics. In the Appendix it is shown that the sublimation reactions for boron oxide are negligible at temperatures below about 900°C. To further examine the effects of boron on CCC oxidation, experiments were performed in which the exit gas was passed through a container of ascarite (NaOH). The ascarite absorbed CO<sub>2</sub> in the gas allowing the amount of CO<sub>2</sub> produced during oxidation to be determined. In Table III results are

presented for a temperature of 525°C.

TABLE III

Reaction Rate on a Carbon Basis at 525°C

Time: 24 hours  
Flow: 25 cc/min O<sub>2</sub>

Sample	Wt. Change (g)	%Wt. loss	Calc.CO <sub>2</sub> <sup>1</sup>	Corr.CO <sub>2</sub> <sup>2</sup>	Exp. <sub>3</sub> CO <sub>2</sub>	%Calc.	%Corr.
Inh.	-.101	8.3 <sup>4</sup>	.37g	.572g	.485g	131	85
Uninh.	-.156	14	.572g	-	.455g	80	-

Time: 62 hours  
Flow: 100 cc/min O<sub>2</sub>

Sample	Wt. Change (g)	%Wt. loss	Calc.CO <sub>2</sub> <sup>1</sup>	Corr.CO <sub>2</sub> <sup>2</sup>	Exp. CO <sub>2</sub>	%Calc.	%Corr.
Inh.	-.273	22.5 <sup>4</sup>	1.009g	1.475g	.784g	78	53
Uninh.	-.400	32	1.467g	-	.704g	48	-

1. Assumes CO<sub>2</sub>(g) is the only reaction product.
2. Assumes difference between weights is carbon converted to CO<sub>2</sub>.
3. Experimentally obtained CO<sub>2</sub> from Ascarite adsorption.
4. Value includes weight gain from boron oxide formation.

Table III shows that the inhibited samples give off more carbon (Exp. CO<sub>2</sub>) than the uninhibited sample. The inhibited samples were observed to give off more carbon (Exp. CO<sub>2</sub>) than the uninhibited sample, even though the former had smaller weight losses. Such results indicate that B<sub>4</sub>C is masking the weight loss via the formation of boron oxide upon the specimen surface. The experimentally measured CO<sub>2</sub>, however, was less than 100% of what

would be expected if all the carbon as indicated by weight losses had been converted to  $\text{CO}_2$ .

The experimentally measured  $\text{CO}_2$  was less than 100% of what is calculated for the observed weight loss. This indicates that the ascarite did not absorb all the carbon that was reacted. This would occur if the carbon was in the form of  $\text{CO}_{(g)}$ . Another reason for low carbon pick up is streaming of the gas through the adsorption chamber. This is supported by the smaller observed amount of carbon absorbed per unit time in ascarite with a faster flow of oxidant in Table III.

Inhibitors have been known to alter  $\text{CO}/\text{CO}_2$  ratios.<sup>(4,31)</sup> Gas chromatography was done in conjunction with TGA studies to determine if this was a factor in CCC oxidation. Results obtained from gas analyses performed at  $525^\circ\text{C}$  are presented in Table IV.

TABLE IV

Uninhibited CCC (CC139E)			Inhibited CCC (CC137E)		
Gas Analysis at 525°C					
%w <sub>o</sub> <sup>*</sup>	CO/CO <sub>2</sub> <sup>**</sup>	μgC <sup>***</sup>	%W <sub>o</sub>	CO/CO <sub>2</sub>	μg C
99.5	.588	.30	99.8	.585	.37
98.6	.641	.81	99.7	.599	.48
98.3	.641	.80	93.0	.455	.59

\*

$\%W_o$  is percent initial weight.

\*\*

$\text{CO}/\text{CO}_2$  is the ratio of the gas species in the gas samples.

\*\*\*

$\mu\text{gC}$  is the weight of carbon in the gas samples.

These results indicate that similar CO/CO<sub>2</sub> ratios and carbon amounts are given off by the two types of CCC which suggests that the absorption experiment is a reliable measure of the amount of carbon reacted.

The data in Tables III and IV are incomplete because the gas analyses for inhibited and uninhibited samples were performed at various burnoffs and not at the same times. Another ascarite experiment was performed that measured the weight changes of the ascarite at the same times. In addition, a catalysis chamber was inserted in the flow line between the reaction chamber and ascarite chamber. The catalysis chamber was composed of an alumina tube packed with 1.5 ft. of platinized alumina honeycomb. The chamber was in a furnace at 425°C. Gas chromatography of the effluent gases from the catalysis chamber showed 100% CO<sub>2</sub>. The catalysis chamber oxidized all the CO<sub>(g)</sub> into CO<sub>2(g)</sub>, therefore, the ascarite reacted with all of the carbon bearing gas from the reaction chamber. The results of this experiment are summarized in Table V.

TABLE V

Reaction Rate on C Basis at 525°C in 25 cc/min O<sub>2</sub>

Time (hrs.)	Inhibited CCI37E	Uninhibited CCI39E	Difference(%)
	Wt. Gain Ascarite (g)	Wt. Gain Ascarite (g)	
3.75	.1160	.1445	19.7
7.5	.1536	.1707	10
27	.6066	.6122	.91



The times taken correspond to a 2, 4 and 8% weight loss for the inhibited CCC sample. The uninhibited sample had larger amounts of  $\text{CO}_2$  early in the experiment, but the difference at 27 hours is negligible. The difference in weight gain at early times may be even smaller, because the CC139E ( $7.36 \text{ cm}^2$ ) sample had a larger bulk surface area than the CC137E sample ( $7.18 \text{ cm}^2$ ). The difference in sample size means more surface can react with oxygen for the CC139E sample. Variations in pore structure and density can also cause disparities at early times.

The data in Tables III - V indicate that inhibitor may affect the oxidation reaction at short reaction times. The effect of the inhibitor is not as great as mass change data would indicate and disappears at higher burnoffs. The effect reappears at longer times when  $\text{B}_2\text{O}_3$  coats the surface of the remaining CCC. Weight losses of 2-8% cause a severe reduction in the mechanical properties of the CCC, perhaps precluding their use. The  $\text{B}_4\text{C}$  inhibitor at these low weight losses does not significantly alter the oxidation kinetics on a carbon basis. The data here suggests that a more effective scheme than  $\text{B}_4\text{C}$  inhibitors should be developed for the intrinsic oxidation protection of CCC.

Oxidation of  $\text{B}_4\text{C}$  is necessary to obtain an inhibition effect if present. Mencuri and Litz<sup>(72)</sup> have studied the oxidation of powdered  $\text{B}_4\text{C}$  in air and in water mixtures. They found that

oxidation of  $B_4C$  in air is detectable at  $T > 450^\circ C$ . Boron inhibition effects can, therefore, be expected at  $T > 450^\circ C$ .

#### 4.1.2.2 Stage 3 Oxidation Behavior

Only the inhibited samples exhibited stage 3 behavior. This is clear in Figures 13 through 18 where the oxidation kinetics for uninhibited and inhibited carbon-carbon are compared. As shown in Figures 25 through 27, the oxidation rates for stage 3 can be approximated by a linear rate law. The linear rate constants for stages 2 and 3 are compared in Figure 28 as a function of reciprocal temperature. The stage 3 rate constants are substantially less than those of stage 2.

The transition to stage 3 for the inhibited samples occurs at a weight loss of about 65%. The rapid removal of carbon from the composite by oxidation increases the relative concentration of  $B_4C$ . The inhibitor at the same time is oxidizing into molten  $B_2O_3$  at a slower rate than the carbon. At weight losses of 50 - 70% the enrichment or wetting of boron oxide is enough to coat the remaining composite, Figure 29. The remaining composite is mostly fibers since the matrix is oxidized at a higher rate. The boron oxide that coats the CCC, wets the fiber which maintains the original shape of the samples. The uninhibited composites did not show this shape retention, Figure 30. The minimum burn off to reach stage 3 is related to accumulation of boron oxide, the time

dependent wetting characteristics of boron oxide on carbon, and the oxidation of matrix carbon. The matrix carbon oxidizes faster than the fibers because of a larger reactive surface area. The reactive surface area refers to the edge carbon atoms and the microporosity found in the matrix carbon.

Once coated, the CCC oxidizes at a dramatically reduced rate. One might argue that the reduced rate results from the smaller amount of carbon remaining. This argument is not true since uninhibited composites show linear oxidation rates until burn offs of greater than 90%. The large drop in oxidation rates is caused by a change in nature of the rate controlling step. The flat curves show diffusion through a layer is still controlling the reaction, i.e., the diffusion of reactants through the molten boron oxide controls the reaction. The diffusing species which controls this reaction have not been identified. Bubbles were present in some of the boron oxide layers at large burnoffs indicating gaseous reaction products and some oxygen penetration through the oxide layer. The boron oxide layer also had holes in it when cooled to room temperature. The holes may be the result of gas evolution or incomplete wetting of the CCC surface.

These results indicate that boron oxide coatings could protect CCC composites for long times (Luthra 2000 hr. criterion)<sup>1</sup> up to a temperature of 750°C. It is important to note, however, that the reduced reaction rates of stage 3 are achieved too late in the

oxidation process. The loss of 65% of the initial mass of the composite means that a porous skeleton of the CCC, mostly fibers, is all that remains, Figure 30. The porous CCC would have degraded mechanical properties and could not be used safely in load bearing applications.

#### 4.1.2.3 Microstructures of Oxidized Carbon-Carbon Composites

The inhibited and uninhibited composites showed different degradation morphologies. Uninhibited CCC oxidized in a manner that individual fibers were easily discernible. The fibers were loose and easily scraped from the surface. Inhibited CCC oxidation morphologies displayed few individual fibers. Instead smooth fiber bundles were covered with boron oxide.

Both types of CCC oxidized for a short time exhibit a pitted morphology, Figures 31 and 32. The pits might be caused by porosity, spalling, catalytic impurities, or oriented microcrystals. Porosity would result in these pits if oxidation uncovered preexisting voids in the carbon. Spalling along cracks in the carbon might cause small chunks to fall out and form the pits. Catalysis may cause a higher reaction rate to occur in areas where the impurities reside. Finally the orientation of carbon crystals may be such that the surface reaction is faster on certain exposed crystallographic planes. This faster reaction would result in the etching of these crystals and the "pitted" morphology.

Of these possible causes the catalytic processes are the most likely. Impurity levels in CCC are larger than in many grades of commercial carbon<sup>(3,73)</sup> where catalysis is known to occur. The impurities are leftover from the precursor in CCC fabrication. Thus catalysis is the rule rather than the exception.

The morphologies of the uninhibited composites show that the matrix carbon is oxidized before the fibers, Figures 33 and 34. The preferential attack of the matrix phase has also been documented by Yasuda et. al.<sup>(74)</sup> In the present investigation the pole figure shown in Figure 35 was constructed for CC139E after 2 days of oxidation in air at 625°C. This exposure resulted in a 96% weight loss. The pole figure shows the persistence of the "cross" pattern generated by the 0 - 90° weave of fibers which documents that the fibers are the last carbon constituent remaining.

Inhibited CCC have similar morphologies to uninhibited composites at short times. During oxidation the B or B<sub>4</sub>C inhibitor changes the oxidation morphology. The most prominent change is the coating of large bundles of fibers and matrix. The first stage involves the oxidation of inhibitors into molten boron oxide. Figure 36 shows the coating of fibers and matrix into bundles. Note that individual fibers are about 10 μm in diameter. The bundles are about 200-500 μm. Large weight losses result in thicker boron oxide coatings on the fibers. In Figure 37 bundles of fibers coated with B<sub>2</sub>O<sub>3</sub> are evident along with a thin layer of

this oxide that has spalled upon cooling. At times, as indicated in Figure 38, pores were evident in the  $B_2O_3$  which may arise because of CO evolution. Finally it is important to note that, as shown in Figure 30, the  $B_2O_3$  coated the fibers and, therefore, helped to retain the shape of the inhibited samples. The fact that the inhibited samples retain their shape implies that the boron oxide coats the fibers more than the matrix, i.e., the inhibitors protect the fibers to a large extent. This greater dimensional stability with oxidation is a benefit of the inhibitors. The apparent and He-measured densities for inhibited CCC vary by a larger degree than the uninhibited composites. This means that the inhibited composite is forming significant open porosity as it oxidizes.

#### 4.1.3 Oxidation Kinetics in Oxygen-Water Vapor

Weight change versus time measurements obtained for the oxidation of inhibited carbon-carbon composites in dry oxygen and in oxygen containing water vapor are compared in Figures 39 through 44 for temperatures between 400 and 900°C. Typical surface morphologies that were observed upon specimens after exposure are presented in Figures 45 through 47. At the lower temperatures, such as 600°C, there was not a significant difference in surface morphologies between oxidation in wet and dry oxygen, Figure 45. At higher temperatures much more  $B_2O_3$  was evident upon the specimens oxidized in dry oxygen than in wet oxygen. In some experiments in

wet oxygen, it appeared that all the  $B_2O_3$  had been removed, Figure 46, while in others some  $B_2O_3$  remained, Figure 47.

Kinetic data for the oxidation of uninhibited carbon-carbon in dry and wet oxygen are presented in Figures 48 through 51. It can be seen that water vapor has a negligible effect on the oxidation of uninhibited carbon-carbon at temperatures above about  $700^\circ C$ . At a temperature of  $500^\circ C$  water vapor was observed to accelerate the oxidation of the uninhibited composites, Figure 48.

Water vapor affects the oxidation of the uninhibited carbon-carbon at temperatures where a phase boundary reaction involving adsorption, dissociation, and desorption of gases is controlling the reaction rate. It, therefore, appears that the water vapor may permit these processes to occur at faster rates than oxygen.

The morphological data and the oxidation kinetics for inhibited carbon-carbon show that the water vapor removes the  $B_2O_3$  from the surfaces of specimens during oxidation. As shown in the Appendix, water vapor reacts with  $B_2O_3$  to form the volatile species  $H_3BO_3$  and  $HBO_2$ . At temperatures between  $400$  and  $600^\circ C$  this could contribute to the increased weight losses of the inhibited specimens, Figures 39, 40 and 41. However, the major cause of this increased oxidation is believed to be the increased oxidation of carbon caused by water vapor.

At temperatures above about  $700^\circ C$ , stage 3 of the oxidation kinetics is apparent for specimens oxidized in dry oxygen but this

stage is not clearly evident for specimens oxidized in water vapor, Figures 42-44. Stage 3 does not appear for inhibited samples oxidized in water vapor because of removal of  $B_2O_3$ . Above 700°C the stage 2 linear rate constants are slightly smaller for oxidation in water vapor than in dry oxygen, Figures 42-44. At temperatures above about 700°C diffusion in a boundary layer adjacent to the surfaces of the specimens becomes increasingly important. The pressure of water vapor may cause diffusion in this boundary layer to be decreased, however, no such effect was observed for oxidation of uninhibited specimens in wet oxygen. It is therefore possible, that the smaller rate constants for stage 2 in water vapor may be caused by increased oxidation of  $B_4C$  in the inhibited specimens as reported by Litz and Mencuri.<sup>(72)</sup>

The results obtained at different water vapor pressures show that  $B_2O_3$  is removed faster as the water vapor pressure is increased, Figures 42 and 43. Such effects are consistent with higher pressures of the volatile species as the water vapor pressure is increased.

Experiments were also performed in which inhibited specimens were exposed to water vapor before oxidation in dry oxygen and in moist oxygen. Two different preexposure conditions were used. In one case water condensed upon the surface of the specimens. In the other case no condensation occurred. None of these preexposures to water vapor affected the oxidation of inhibited carbon-carbon



in dry oxygen or in wet oxygen.

Isothermal oxidation experiments were also performed in still laboratory air on both uninhibited and inhibited specimens at temperatures between 400° and 1200°C. The oxidation kinetics did not exhibit a stage 3 region for inhibited samples even at the higher temperatures, Figure 52 and 53. Such results may have been caused by water vapor in the laboratory air. In these experiments the weight change measurements were performed in a discontinuous manner by removing the specimens from the furnace rather than using a continuous recording microbalance. The oxidation kinetics are not linear but increased slightly with time. Some cracking of the specimens may have occurred which could cause such oxidation kinetics. The linear rate constants obtained from these curves were much lower than in flowing oxygen since the gas over the specimens became depleted of oxygen to a larger extent than in the flowing oxygen. It is important to emphasize that while oxidation was very slow at 400°C, Figure 52, some attack did occur and, therefore, for very long exposure times some adverse effects of oxidation on carbon-carbon composites could occur.

#### 4.2 COATED CARBON-CARBON COMPOSITES

##### 4.2.1 Initial Characterization

###### 4.2.1.1 HP24

All the coatings used in this work had a SiC conversion layer of CCC substrate. Figures 54 and 55 show the HP24 light and moderate conversion coatings. The only difference between the coatings is the coating thickness. The light coating is about 150  $\mu\text{m}$  thick, while the moderate coating is 300  $\mu\text{m}$  thick. The coating thickness, however, is not uniform around the surface of the sample and contains cracks. The phases Si,  $\text{B}_4\text{C}$ , and  $\beta\text{-SiC}$  appeared in all HP24 conversion coatings. These observations will be discussed.

The phases that appear in the conversion coating were a direct result of the pack cementation process. In the process Si vapor was passed through a CC137E substrate to convert carbon into SiC. The Si reacted with the carbon fibers and matrix to form SiC. The SiC that formed was mainly the  $\beta$  (cubic) polymorph with a lattice parameter of 4.37 Å. Thicker conversion coatings such as the HP24 moderate show x-ray diffraction peaks from hexagonal polymorphs of  $\alpha\text{-SiC}$ . A TEM micrograph of a  $\beta\text{-SiC}$  grain presented in Figure 56 shows that the grains range from 0.1 to 0.5  $\mu\text{m}$  in diameter. Fine  $\text{B}_4\text{C}$  (dark) particles are found to outline the converted fibers in SEM (not visible in optical micrographs) micrographs. The  $\text{B}_4\text{C}$  outlines the fibers because the inhibitor does not interact significantly with the Si vapor. Often the boron carbide is seen to follow the outline of the fibers from the CCC substrate into the HP24 coating. The hexagonal  $\text{B}_4\text{C}$  grains vary from 0.1 to 1.0  $\mu\text{m}$  in

diameter. The interaction of the Si with open porosity results in the deposition of free Si. The free Si appears white in optical micrographs but is very hard to detect in SEM micrographs since the contrast is similar to that from SiC. The Si has a coarse microstructure which depends on the prior porosity and often exhibits the size and shape of carbon fibers and extends at various angles from the substrate to the surface of the coating. The Si appears to have been oxidized to a small extent during coating fabrication. The Si also fills some cracks and blocky pores assuming these shapes. The Si has a diamond cubic structure with a lattice parameter of 5.45 Å.

Cracks are observed in the planar-surface and transverse-cross sections of the HP24 coatings. A planar-surface, shown in Figure 54, shows that cracks are spaced regularly from 200 to 600  $\mu\text{m}$  on the surface. In addition the surface has 10-20  $\mu\text{m}$  cavities which are aligned in a parallel manner. The cross section in the same figure shows that the large surface cracks extend from the surface to the CCC substrate. The cracks are roughly 0.9 mm apart.

The cracks present in the initial microstructure result from the thermal expansion mismatch between the substrate and coating phases. Figure 57<sup>(60)</sup> shows a plot of the thermal expansion coefficients of several ceramic phases versus temperature. Note that a mismatch of greater than 0.5% occurs between CCC fibers and SiC at temperatures greater than 1000°C. The temperature used in

the pack process is not known, but is probably higher than 1000°C. A mismatch of 0.5% would produce a stress on the order of 35000 p.s.i. on the sample configurations used in this work. This stress is calculated from a formula based on thermal expansion coefficients, thickness of the coating and substrate, and the elastic moduli of the constituent phases.<sup>(56)</sup> The modulus of rupture of bulk SiC can range from 25 to 75 k.s.i. and, therefore, cracking is likely to occur.

#### 4.2.1.2 HP24/M185

The M185 coating produced by HITCO is directed at adding a glaze to the HP24 coating layer to seal the cracks. Figure 58 shows the surface and a transverse cross section of this coating. The M185 is 200  $\mu\text{m}$  thick and is composed of vitreous silica and a dispersion of particles. The additives are present presumably to alter the viscosity of the silica in critical temperature ranges where cracking occurs. Cracks are seen on the surface and through the cross section.

The major phase of the M185 coating is vitreous silica. A TEM micrograph with an electron diffraction pattern is shown in Figure 59. The broad rings of the diffraction pattern correspond to the Si-O bonding distance in silica.<sup>(75)</sup> The presence of more than one ring means that the silica is not amorphous and shows some short range order. EDS analysis of the silica indicated the presence of

Al and K. There are at least four types of particles in the silica detected by EDS and XRD. The large grey particles were pure Si which ranged from 10 to 30  $\mu\text{m}$  in diameter. The darker particles were associated with Al, probably  $\text{Al}_2\text{O}_3$ . XRD confirmed the presence of  $\text{B}_4\text{Si}$  in the M185 layer. The other type of particle seen in the coating was rich in V and Ti.

Cracking was prevalent in the M185 sample. The cracks on the surface are about 0.5 to 1.0 mm apart and often had a star-like morphology. The star burst morphology was linked with the presence of Al and possibly occurred at intersections between the surface and the Al-rich particles. Cracking in the transverse cross section is seen to extend from the coating/gas interface to the substrate. These cracks are about 400  $\mu\text{m}$  apart. Figure 58 shows that some of the cracks in the M185 extend through the HP24. This observation and the similar crack spacing and distribution of M185 and HP24 indicate that the existing cracks in the HP 24 have propagated into the M185.

#### 4.2.1.3 HP24/BXC/RT42/Glaze and /No Glaze

The other complex coating used in this study was fabricated by Chromalloy and is designated HP24/BXC/RT42A/Glaze. This coating is shown with and without the glaze in Figure 60. The coating is 350  $\mu\text{m}$  thick, and the glaze only about 15  $\mu\text{m}$  thick. Some regions are noticeably thicker than others so the coating is nonuniform.

The coating consists of HP24 light conversion coating, several  $B_4C$  intermediate layers, 6-8 C.V.D. SiC layers, free Si and a vitreous glaze. Cracking is also found in this coating.

The three dark intermediate layers comprising the BXC designation are 30  $\mu m$  thick,  $B_4C$  layers. These layers have morphologies expected from a C.V.D. process. There are large cracks and microcracks (pores) seen in these layers. The large cracks either extend through the entire coating section or are confined to the  $B_4C$ . The confined cracks may mean that the  $B_4C$  is accommodating stresses that develop during processing. This can also be an effect of the cracks running along the interfaces. The smaller microcracks are seen more clearly in Figure 61 which shows a high magnification micrograph of etched  $B_4C$  layers. The cracks or pores are about 1  $\mu m$  in diameter and are elongated toward the surface. There are also thin, 3  $\mu m$  SiC layers between the boron carbide layers.

On top of the  $B_4C$  intermediate layers are C.V.D. SiC layers. A high magnification micrograph of the C.V.D. layers is seen in Figure 62. The C.V.D. SiC is cubic with a lattice parameter of 4.37 Å. The deposition conditions are such that Si is in excess since diamond cubic Si is detected in these layers with XRD. The free Si is also seen at the interfaces between successive SiC layers. The individual  $\beta$ -SiC layers are about 30  $\mu m$  thick. Six to seven of these SiC layers (10  $\mu m$  total thickness) are deposited

and form the RT42A part of the coating designation. The layers exhibit a wavy morphology and result in a nonuniform coating thickness. The surface of the coated sample exhibits this wavy morphology in the form of SiC hemispherical caps. Cracks in the RT42A layer are either large and extend through the entire coating thickness or are microcracks confined to the  $\beta$ -SiC layer. The abundant microcracks are about 0.5  $\mu\text{m}$  wide and are present in each RT42A layer. The microcracks propagate across the interface between individual C.V.D. layers. These microcracks image darker than expected in SEM micrographs possibly as a result of silica formed in the microcracks.

The glaze on the Chromalloy coating is about 15  $\mu\text{m}$  thick and based on vitreous silica. Besides the silica, K and Al are detected by EDS in the glaze. The purpose of the glaze is to seal cracks that form during coating deposition and service.

#### 4.2.2 Oxidation Kinetics of Coated Carbon-Carbon Composites

##### 4.2.2.1 Isothermal Oxidation

Isothermal oxidation tests were performed on the coated samples at 1100, 1200, 1300, and 1400°C. The results of these experiments are shown in Figures 63 through 66. Generally the weight change verses time curves showed two types of behavior. One type is slow weight change, usually weight gain, over a long period of time. The other behavior is a dramatic weight loss when the

coating fails. All coated samples showed enhanced life over uncoated CCC. The oxidation kinetics exhibited by the samples do not conform to a parabolic rate law. Instead many processes are occurring, causing the irregular oxidation curves seen in some of the figures. The results of these tests will now be discussed in terms of the individual coatings.

#### HP24

The HP24 sample loses weight rapidly from the start of the oxidation test at all temperatures except 1200°C. The high weight loss means that the SiC conversion layer does not form a continuous protective SiO<sub>2</sub> scale. Instead it is necessary to postulate that a defect in the coating bypasses the protection provided by SiO<sub>2</sub>. A micrograph shown in Figure 67 shows such a defect. In the micrograph a circular hole appears on the surface of the HP24. The glassy phase around the hole is boron oxide. The holes form at cracks in the coating which extend through the coating into the CCC substrate. These holes/cracks provide a rapid diffusion path for oxidants that gasify the CCC. The rate of gasification (weight loss) is not as great as for uncoated CCC for two reasons. First the oxidants react with a smaller surface area, i.e., the entire sample is not exposed. Second the transport of the oxidant to the CCC composite is limited by diffusion in the crack. The rate of diffusion is determined by the crack size. Figure 68 shows that B<sub>2</sub>O<sub>3</sub> and SiO<sub>2</sub> exist in the cracks that extend from the substrate to



the surface. Evidence of bubbling in these cracks can be seen from the spherical morphology of the oxide in the cracks. The bubbling results from CO evolution that occurs in the substrate.

Thermal stresses are the cause of the crack/hole defect. The rapid loss of weight at the beginning of testing supports this observation. The thermal stresses either open preexisting cracks or create new cracks. At 1100°C the thermal stresses are greater than the 35 k.s.i. calculated in section 4.2.1.1 for 1000°C. The strength of C.V.D.  $\beta$ -SiC on graphite has been found to depend on deposition conditions but is around 12-20 k.s.i.<sup>76</sup> These large stresses are more than enough to rupture the SiC coating.

Further complications arise in the  $B_4C$  stringers that outline the converted fibers in the coating. These particles might be continuously linked from the substrate to the surface and could be preferentially oxidized into  $B_2O_{3(l)}$  and  $CO_{(g)}$ . This would lead to bubbling in the coating and on the surface of the composite. Evidence of this type of bubbling is seen in Figure 68 for the sample tested at 1200°C. This type of morphology was observed at all temperatures. The liquid boron oxide can react with silica to form lower melting point oxides. The phase diagram presented in Figure 69 shows that liquid solutions of  $B_2O_3$  and  $SiO_2$  can be formed at temperatures above 430°C. Any liquid is less protective than solid silica because of rapid transport of oxidants and products. The observation of  $B_4C$  particles extending from the CCC to the

surface is, therefore, deleterious. This type of failure, however, would occur less rapidly than the ones caused by thermal stresses.

Any boron oxide that forms in contact with the silica may alter the protective properties of the scale. The boron oxide can do this by changing the defect structure of the glass or crystalline silica. A change in the structure can result in rapid diffusion of oxygen through the scale. Boron oxide can also lower the viscosity of the silica scales.

The appearance of free Si extending from the surface to the CCC substrate is another deleterious morphology and may be a greater problem than the  $B_4C$  particle stringers. Optical micrographs in Figure 70 show that the preferential oxidation of Si can penetrate deeply into the coating. The nonprotective silica that results is frequently "pulled out" during final polishing leaving the voids observed in the figure. The penetration of this nonprotective silica can be up to 200  $\mu m$  in less than 4 hours. These deep penetrations leave little useful coating thickness on the CCC. If the unprotective silica reached the substrate rapid weight losses would ensue from  $CO_{(g)}$  production from high carbon activity phases. This type of coating failure was not observed in these tests, but could occur at longer exposures.

The results presented in Figure 64 show that the HP24 conversion coating can be an effective barrier to CCC isothermal oxidation. The sample tested at 1200°C isothermally oxidized for

115 hours with only a small weight change. The difference in this case was that thermal stresses did not cause failure early in the test. Apparently the cracks in this sample sealed or were too small to cause the rapid degradation processes described earlier. The sealing of cracks occurs if SiC expands with the rise in test temperature closing the cracks. The cracks would also seal if oxides formed in a continuous manner that stopped rapid degradation processes. The silicon oxides that formed on the HP24 were  $\alpha$ -cristobalite at  $T > 1200^{\circ}\text{C}$ , but remained vitreous at lower temperatures.

The conversion layer often showed the presence of fibers in the coating, Figure 71. The appearance of fibers in the coating may be caused by two related factors. One appears to be that the more porous matrix is converted to SiC more rapidly than the fibers. The second is that the denser fibers may not be completely converted to SiC, especially at their center. The incomplete conversion is expected at the center of the sample because slow solid state diffusion reactions control the conversion process. The result of this morphology is that carbon pegs extend into the coating. The carbon pegs are regions of high C activity that can react with oxygen to form large pressures of  $\text{CO}_{(g)}$ . These unreacted fibers must be viewed as deleterious because they decrease the effective thickness of the conversion coating.

The fabrication of the HP24 coating is very important in determining the oxidation behavior that can be expected in service. The observations of coating failures and successes at these temperatures show that irregularities exist during fabrication, causing a scatter in oxidation behavior. The irregularities involve three microstructural variations: cracks, high carbon activity phases in the coating, and deleterious phases in the coating.

#### HP24/M185

The M185 samples were tested only at 1100°C and 1300°C, because of the limited number of samples available. Two samples were tested at 1100°C to see how reproducible the oxidation kinetics were at this temperature. Figure 63 and 65 show the oxidation kinetics. The M185 oxidized in O<sub>2</sub> showed only slight weight losses and in general was greatly improved over the HP24 sample. The weight losses occurred in a parabolic fashion, i.e., the sample lost weight at a decreasing rate throughout the test. The improved oxidation resistance must be attributed to the M185 glaze. The vitreous silica in the glaze seals cracks caused by thermal stresses during the heating of the samples.

The M185 samples initially exhibited small weight losses at the onset of testing. These weight losses are caused initially by carbon oxidation. The carbon is present as SiC, B<sub>4</sub>C, and the CCC substrate. Metallography did not show conclusively which

component was being oxidized, but indicated that the oxidation kinetics were misleading. Figure 72 shows the surface of the M185 after oxidation at 1100°C. The upper micrograph shows a large circular mound on the surface of the sample. The cause of the mound formation is not clear. Thermal stresses can be ruled out since failure did not occur rapidly at the start of the oxidation test. The thermal stresses may, however, initiate the process causing the mound to form. In this case it is more likely that oxygen was able to reach areas of high carbon activity in the vicinity of the mounds via cracks. The carbon then oxidized to form large pressures of  $\text{CO}_{(g)}$ , which either escaped by blowing the viscous coating off or provided easy diffusion paths for oxygen. The underlying composite can be seen in the center of the mound. The composite has been oxidized to the point that  $\text{B}_2\text{O}_3$  is coating the  $\text{CC}$ .

A micrograph in Figure 73 shows a cross section from a sample tested at 1100°C that is free of mounds. The cross section shows no cracks from the substrate to the surface although some of these cracks existed. The conversion layer again shows some preferential oxidation of the free Si even with the M185 treatment.

The Si and  $\beta_4\text{Si}$  particles in the M185 show signs of oxidation and transformation into a different phase on their periphery, Figure 74. The  $\text{SiO}_2$  is evidence that oxygen penetrates the M185 during oxidation testing. The penetration may be by diffusion in

microcracks or by diffusion in the silica-based glaze.

Figure 75 shows a cross section near a mound in the M185 (1100°C) which shows oxide surrounding a crack extending from the CCC to the surface. The spherical morphology of some of the oxide indicates that gaseous CO is being evolved from the CCC through a viscous oxide. Pure silica does not deform so easily so the presence of liquid  $B_2O_3$  in the mound is likely.

The M185 sample tested at 1300°C showed little weight change in the 50 hours of testing. No bubbling was seen on the surface although the star bursts associated with Al in as-received structures has oxidized. Large cracks were frequently observed on the surface. The oxidation degradation of M185 occurs by oxygen transport through the glaze to the HP24 conversion coating.

The particles in the M185 layer are severely degraded into oxides indicating that oxygen diffuses rapidly in the glaze. Figure 76 shows optical micrographs of the attacked particles. The outer edge of the particles has transformed to a new phase. The contrast of this phase is similar to the  $\beta$ -SiC in the HP24 layer. The top figure also shows unconverted fibers in the HP24 layer. The centers of the particles have holes in them from pullout of silica that has formed during exposure. Figure 76 also shows the attack of free Si in the HP24 layer. The free Si in the HP24 also shows some signs of a new phase forming in advance of silica formation.

The M185 layer is composed mostly of vitreous silica. XRD after exposure at 1100 and 1300°C shows signs of formation of crystalline tridymite ( $d=4.111 \text{ \AA}$ ). The XRD was done after long times at temperate and other polymorphs of silica may have preceded the tridymite.

The M185 is a large improvement over the conversion coating. However, cracking and high oxygen permeability of the M185 layer detract from good oxidation resistance. The coating also contains the HP24 layer and, therefore, has the microstructural weaknesses associated with that layer.

#### HP24/BXC/RT42 (No Glaze)

Isothermal testing of the Chromalloy coating without a glaze revealed surprisingly slow oxidation rates. The No Glaze sample consistently showed little weight change at temperatures between 1000-1400°C. The No Glaze sample did not show signs of rapid weight loss from the oxidation of carbon and maintained thin films of silica on the surface. In addition, the No Glaze samples were the only coatings that oxidized with parabolic kinetics. The parabolic rate constants at 1300 and 1400°C were  $7.5 \times 10^{-15}$  and  $4.0 \times 10^{-13} \text{ g}^2\text{cm}^{-4}\text{sec}^{-1}$ , respectively. These rate constants should be considered approximate since bubbling indicated that a small weight loss was coincident with the recorded weight gains.

Figure 77 shows the surface of the No Glaze sample after testing at 1100°C. At early times this silica coating was vitreous

and progressed to cristobalite and tridymite formation. The silica appears crazed from the cool down of the specimen. The crazing of the silica indicates incompatible thermal expansion between the C.V.D. SiC and the scale during temperature changes.

Figure 78 shows the surface of the No Glaze sample after isothermal oxidation at 1300°C. Cracks and bubble formation is noticeable, but no large mounds or hole defects are observed. It appears that crack and bubble formation are general morphological characteristics of CCC coating oxidation.

The No Glaze sample performed better than the other coatings. Microcracking of the C.V.D. SiC outer layers is a problem with this coating even though thermal shocking did not occur. The No Glaze sample when exposed to high temperature environments produced a thin silica layer on the surface that controlled the oxidation process. Bubbles indicate that CO evolution is occurring but not in a manner that renders the silica nonprotective. The success of the No Glaze sample indicates that an outer glaze is not necessary for good oxidation resistance.

#### HP24/BXC/RT42/Glaze

The Chromalloy sample with the glaze is the most complex coating studied in this work. The glaze samples were prone to thermal shock failures at  $T > 1100^{\circ}\text{C}$  and did not perform as well as the No Glaze samples.



Rapid weight gains were exhibited at early time in the oxidation tests (Figs. 63 to 66). The rapid weight gains were the result of oxidation of the cracks and microcracks. The cracks as discussed above are caused by thermal expansion mismatch. The cracks that oxidize are newly formed cracks since some oxide was observed to be in cracks in the as-processed microstructures. The vitreous glaze was intended to seal the cracks but was not effective.

The glaze may not be effective, because the layer may change the stress state of the coating in such a manner as to create cracks. Vitreous silica (see Fig. 57) has a thermal expansion coefficient near that of CCC, but less than SiC. The silica layer is on top of the C.V.D. SiC layers and thus restrains them from expanding or contracting, causing additional stresses. The glaze may also accelerate corrosion of the SiC by reacting with oxidation products. The glaze contains K which can form salts known to increase the degradation rates of SiC.<sup>(53,54)</sup> In addition elements like Al and K strongly segregate to the silica scales that form on sintered silicon carbide.<sup>(52)</sup> Elements such as Al and K can alter the glass network of the silica and enhance devitrification.

After the initial weight gain, most of the glazed samples lost weight at a high rate. The oxidation was the result of large cracks which formed along the edges of the samples. The cracks were large enough to view with the unaided eye and oxides could not

seal these cracks off. Perhaps rapid evolution of reaction products such as  $\text{CO}_{(g)}$  prevented crack sealing. In any case the cracks exposed the CCC substrate to rapid oxidation. The cause of the cracks was thermal shock during heating.

To show that sample heating caused the cracking an additional experiment was performed. Figure 79 shows the results of an isothermal test in which the sample was heated at  $100^\circ\text{C}$  increments every 20 hours from  $1000^\circ\text{C}$  to  $1400^\circ\text{C}$ . No rapid weight losses were evident, although losses occurred at a slow rate at  $T > 1200^\circ\text{C}$ . Figure 66 shows that the glaze samples when heated directly to  $1400^\circ\text{C}$  failed rapidly. The difference between the tests is that stresses were relieved more in the slow heating test. A cross section of the incrementally heated sample in Figure 80 shows that oxygen has penetrated to within  $30\text{ }\mu\text{m}$  of the boron carbide layers. If oxygen should reach these  $\text{B}_4\text{C}$  layers catastrophic oxidation would occur at  $T > 1000^\circ\text{C}$ . The cross section also shows that the Si phase which is present in the RT42 layer is preferentially oxidized. The free Si is also seen on the No Glaze sample, but attack of this phase was not evident.

The glaze samples also exhibited failures of the mound/hole type during oxidation testing. The defect was usually observed near the edges of the sample. Figure 81 shows the surface of a glaze sample and the mound that formed. The mound has the characteristic glassy appearance around the periphery found for the

HP24 and HP24/M185 samples. Other areas on the surface revealed that bubbling had occurred at the test temperature.

Bubbling, which was caused by evolution of gaseous products, was a surface morphological feature seen on all samples to various degrees in every oxidation test. The bubbles are thus characteristic of coating oxidation. Schiroky<sup>(55)</sup> oxidized high purity C.V.D. SiC and did not see bubbling until test temperatures reached 1600°C. Schiroky indicated that CO was the major gas species instead of SiO. There are other cases where bubbling of SiC occurs at lower temperatures (1300°C).<sup>(57)</sup> In these cases carbon inclusions were thought to be the cause of the bubbling. In any case, the bubbles represent the loss of CO<sub>(g)</sub> from the coating or CCC. Thermodynamic calculations show that very high pressures of CO can develop during the oxidation of SiC when the activity of C is high. The reason for the CO evolution, therefore, are regions of high C activity in the coating and substrate. The CO pressures generated are great enough to rupture the coatings. High C concentrations must be viewed as deleterious in the coating, but unavoidable in the substrate. Better oxidation performance can be expected from SiC-based coatings with no regions of high C activity. This problem becomes greater as the temperature is increased.

The observation of bubbling at short exposure times on samples coated with a glaze indicates that the glazes do not effectively

stop all oxygen diffusion into the coatings. Bubbling also indicates that the glazes have some solubility for oxygen. Crack sealing to some extent is done by oxygen that diffuses through the glaze and reacts with SiC to form silica along microcracks. Perhaps other glazes with lower oxygen solubility would be more effective oxygen barriers.

The Glaze sample has poor thermal shock resistance that resulted in poor oxidation resistance. The sample is only different from the No Glaze sample by the addition of a 15  $\mu\text{m}$  glaze. The glaze introduces A and K which can be detrimental to oxidation resistance. The glaze causes a new stress state in the coating that is not beneficial. The thermal shocking of the glaze coating causes severe cracking. Only once was the severe cracking sealed by oxides that form in the coating.

#### 4.2.2.2 Cyclic Oxidation

Cyclic oxidation of all of the coatings systems was performed at 900 and 1125°C. Typical results are presented in Figures 82, 83 and 84. All the coatings were degraded in these tests. Details observed at each of these temperatures are presented in the following.

##### Results Obtained at 1125°C

Isothermal oxidation results at 1100°C showed that all coated samples except for HP24 developed continuous silica scales for

extended times ( $t = 165$  hrs.). The cyclic oxidation kinetics, Figure 83, show that continuous silica scales can be reformed and/or maintained for extended times ( $t = 200$  hrs.) on the coatings even when thermal cycling occurs. Failure of the coatings does occur and rapid oxidation of the substrates follows.

The degradation morphologies of the coated samples were similar. All coatings showed bubble formation especially near or on surface cracks. The coatings also failed in a fashion that was observed previously in isothermal tests, namely through formation of a volcano-shaped mound on the surface. The frequency and large amounts of bubbling in this test show that cracking allows oxygen to reach areas of high carbon activity.

The M185 sample went through 450 cycles before catastrophic oxidation occurred. The M185 glaze seems to be relatively effective in sealing the cracks that form in the HP24 layer. Crack sealing was evident upon visual examination of exposed specimens.

The oxidation kinetics of the M185 before failure show large weight gains of almost  $2 \text{ mg/cm}^2$ . This weight gain is much larger than the weight gains exhibited by the M185 in isothermal tests. The larger weight gain is a result of more rapid ingress of oxygen to phases in regions that have not been oxidized. The unoxidized phases are SiC in the HP24 and the particles in the M185 glaze. The weight gain may also represent dissolved oxygen in the vitreous silica. The greater penetration of oxygen and weight gain of the

sample in cyclic oxidation is the result of cracking in the HP24 and M185 layers.

The glaze and no glaze samples were tested in air and oxygen. Oxygen was the more hostile environment. In oxygen, the no glaze sample performed much better than the glaze sample. The glaze sample suffered catastrophic weight loss after only 50 thermal cycles in  $O_2$ . The no glaze sample showed a weight gain of 2.5 mg/cm<sup>2</sup> after 121 cycles. Visually the no glaze sample had a clear silica layer with only a little bubbling. The glaze sample failed on a corner. A micrograph of the failure site is presented in Figure 85. The corner represents a region of the sample where complex thermal stresses occur between the coating and substrate. Edges and corners were the failure sites observed on the glaze samples in isothermal testing. The same types of failure sites may be aggravated by the repeated tensile stresses the coating experiences upon heating to test temperature. A low magnification cross section of the glaze sample after catastrophic attack in  $O_2$  is presented in Figure 86. The micrograph shows that the CCC is rapidly consumed, while the coating is left intact. The CCC once penetrated by  $O_2$  is attacked preferentially near the coating-substrate interface. Figure 86 shows profuse bubbling in the outer 75  $\mu$ m of the coating. A viscous oxide network is also seen in the intermediate  $B_4C$  layers. The oxide network means that oxygen has penetrated to the  $B_4C$ . The  $B_2O_3$  that forms fills microcracks in the

intermediate areas forming the oxide network. The glaze and no glaze samples which both failed after 225 cycles in air, had similar microstructures.

The HP24 sample lost weight at unacceptable rates during the first thermal cycles. Cracks on the edges of the sample were the visible failure sites. The behavior of the HP24 sample was expected, because the isothermal oxidation results also showed rapid weight loss at early times, Figure 63. The thermal cycling resistance of the simple conversion coating is not good compared with the complex systems. The morphology of the oxidized HP24 was not significantly different from the morphologies observed in isothermal testing.

#### Results Obtained at 900°C

Cyclic oxidation kinetics at 900°C in static air are shown in Figure 82. The best resistance to cyclic oxidation at 900°C was exhibited by the no glaze sample. The no glaze sample underwent 1600 cycles before unacceptable weight loss occurred. The other complex coatings, glaze and M185, withstood about 500 cycles before rapid weight loss developed. The HP24 again displayed rapid oxidation weight loss at the beginning of the test.

All the complex coatings had weight gains of near 2 mg/cm<sup>2</sup> during the cyclic oxidation test. Isothermal oxidation rates of these coatings at 900°C are very small. The difference in the weight changes observed is evidence of cracking in the coating.

The cracks that form allow oxidation. Oxygen is supplied by diffusion down cracks or through glazes if present. Oxygen diffusion through an external silica boundary is not great enough to cause the observed weight gain. The ingress of oxygen at 900°C is therefore not stopped for long times by the external glazes in the M185 and glaze samples. The glazes at these temperatures bring on premature failure of the coating when compared with the no glaze sample. The reason for this failure is not clear but is likely related to the viscosity and wetting characteristics of the glaze at 900°C.

The M185 sample exhibited the best resistance to cyclic oxidation at 1125°C, but performed poorly at 900°C. The M185 coating buckled and failed with an ablated region near the center of the coating after about 500 cycles. Figure 87 shows these features. The underlying CCC can be seen to be very porous with  $B_2O_3$  platelets on the surface. Boron was detected on the edges of the ablated region. The buckling is a result of the loss of adhesion of the coating with the substrate in the central portion of the sample. A loss of adherence allows the coating to expand freely without the restraint of the underlying substrate. Cracking in the middle region caused the coating to spall.

The no glaze sample showed the best resistance to cyclic oxidation at 900°C. The no glaze sample withstood 1500 cycles, while the glazed sample lasted 600 cycles. The weight change vs.



time curve for the no glaze sample shows three types of behavior. The first is a steady gain in weight from oxidation of phases that are cracked during thermal cycling. The second type of behavior is a slow loss of weight resulting from spallation of  $\text{SiO}_2$ . The final rapid weight loss is a result of oxidation of the CCC substrate.

The HP24 sample lost weight at a rapid rate from the beginning of the test. The observed microstructure showed little difference from that of HP24 in the  $1125^\circ\text{C}$  cyclic test. The same reasons given for the poor performance of the simple coating at  $1125^\circ\text{C}$  apply at  $900^\circ\text{C}$ .

The glaze sample showed a different behavior. Initially a rapid weight gain was observed similar to the weight gains seen in other oxidation tests. The rapid weight gain was followed by a period of little weight change. After the period of little weight change, rapid oxidation of the CCC ensued. Micrographs presented in Figure 88 show the glaze sample after testing. The glaze sample differs from the no glaze sample only by a  $15\text{ }\mu\text{m}$  glaze. A comparison of the kinetics of the two samples indicates that the glaze treatment causes both the rapid weight gain and the premature failure. The glaze may do this by either providing stress raisers that cause more cracking or altering oxides that form in the coating. An interesting observation is that after any of the complex coatings gain about  $1.75\text{ mg/cm}^2$ , failure follows in a

relatively short period of testing. The weight gain is a measure of cracking. This weight gain might indicate a threshold of damage that the coating can tolerate.

The kinetics of the cyclic oxidation tests show the need for an improved inhibition system for coated CCC. Generally the substrates in coated systems<sup>(78)</sup> have some intrinsic resistance to oxidation. The results for coated CCC show that once the coating fails little protection from oxidation attack can be expected. No protection is expected because CCC has little intrinsic resistance and the current inhibition is not advanced enough to establish acceptable oxidation rates after the coating has failed.

#### Summary of Cyclic Oxidation Results

Cracking of the ceramic coating is the major factor determining the life of coated CCC in cyclic oxidation tests. Cracking of the coating is caused by the thermal expansion mismatch of the SiC and other ceramic phases with the CCC substrate. SiC has a low thermal expansion coefficient when compared with metals, but 2D CCC has an even lower coefficient. An added aggravation to this problem is the poor mechanical properties of C.V.D. SiC compared with bulk SiC, especially the response of the C.V.D. SiC to tensile stresses. The thermal expansion mismatch between CCC and SiC increases with temperature. This temperature dependence should favor poor cyclic oxidation resistance at higher temperatures. The temperatures used for cyclic oxidation in this

work are not high enough to allow significant plasticity in the SiC. At temperatures above 1400°C some creep of the SiC can be expected to allow better compatibility with the CCC.

None of the coatings used in the present investigation are based on  $\text{Si}_3\text{N}_4$ . Silicon nitride has a lower thermal expansion mismatch with CCC. The better thermal compatibility might provide better cyclic oxidation resistance than SiC-based coatings.

Vitreous glazes have viscosities that decrease with increasing temperature. The viscosity of the glazes is magnitudes smaller than that of silica. The low viscosity at high temperatures should allow the glaze to seal cracks in the coating. A higher flow rate of oxidant than that used in these tests might be able to blow the glaze off the sample. The coatings with glazes in these tests should show better cyclic oxidation resistance at higher temperature.

#### 4.2.2.3 Acoustic Emission

Figures 89 and 90 show the results of the acoustic emission testing. Figure 89 shows the results occurring during cool down after isothermal oxidation in air for 72 hours at 800°C. Figure 90 shows similar kinetics at 1100°C.

A comparison of these figures shows little difference in the counts/cm<sup>2</sup> between the two samples. The small difference indicates that the amount of damage, i.e., elastic waves measured, are

similar. The counts generated by the sample are thought to emanate from the coating and not the oxide that forms. The acoustic emission results indicate that the complex coating does little to halt the production and propagation of cracks in the coating.

The kinetics of the acoustic emission test show the extreme sensitivity of the glaze and HP24 sample to temperature change. A change of only 100°C at either test temperature caused the production of many acoustic emission counts. The acoustic emission test results are consistent with the poor cyclic oxidation resistance of the two samples observed at 900 and 1125°C.

The morphologies of the samples after acoustic emission testing are similar to the morphologies described for isothermal testing. Little oxidation degradation was observed on the samples after testing at 800°C.

#### 4.2.2.4 Recommendations Concerning Coating Performance

##### HP24

The HP24 conversion coating is the basis on which all of the other coatings are fabricated. The HP24 coating suffers from three microstructural deficiencies: free Si, unconverted fibers, and B<sub>4</sub>C stringers. These failings are shortcomings of all the coatings studied.

The free Si in all the coatings is preferentially oxidized. The oxidation reduces useful coating thickness, especially when the

free Si extends directly to the CCC. The Si, however, is necessary to establish low C activities in the CVD SiC. High activities of carbon result in  $\text{CO}_{(g)}$  pressures that can disrupt the protective properties of the coating. Large amounts of free Si might be avoided if porosity in the outer layers of the composite is diminished. Densification of the outer layers of the composite is partially accomplished by the final CVD carbon treatments. Cracking in this carbon layer still allows Si to enter more porous regions of the composite.

Unconverted fibers provide regions of high carbon activity in the conversion layer. The fibers decrease the useful thickness of the coating. The thickness of the coating is reduced because the fibers oxidize at the rate of carbon and provide no solid barrier to further oxidation. A thick layer of homogeneous carbon that converts to SiC in a uniform manner will avoid this situation.

The boron carbide stringers are present to provide an inhibitor for the CCC. The present investigation has shown that boron carbide inhibitors are not effective in slowing oxidation reactions between CCC and oxygen. The  $\text{B}_4\text{C}$  in the coating provides several features which detract from the oxidation resistance at high temperatures. These include rapid oxidation of continuous stringers and fluxing reactions between  $\text{B}_2\text{O}_3$  and  $\text{SiO}_2$ , which may cause the active oxidation of Si-based phases. The simplest way to avoid these effects is by elimination of B-based inhibitors.

### M185

The M185 coating is a complex coating with oxidation resistance comparable to that of the glaze and no glaze samples. The oxidation resistance of M185 is obtained with a less intensive and expensive processing treatment.

The M185 layer seals through-thickness cracks better than the other coatings studied in this work. The capacity to seal cracks was better at  $T > 1000^{\circ}\text{C}$  since dramatic failure was observed during the  $900^{\circ}\text{C}$  cyclic test. The ability of the coating to seal cracks at high temperature is a result of the presence of the M185 layer, since effective crack sealing was not seen in the HP24 coating by itself.

The M185 layer, however, allows oxygen penetration into the coating system. The oxygen penetration is observed as attack of Si-based particles in the M185 layer and preferential oxidation of free Si in the HP24 layer. A finer dispersion of these Si-based particles in the M185 layer might result in oxygen reacting in the M185 layer rather than the HP24 conversion coating. The fine dispersion also has a greater chance of being near cracks that form in the coating which might reduce oxygen transport. Smaller particles would provide more surface area to react with diffusing species in the coating.

Better protective properties of the M185 layer might result if other oxides are used in the coating. Ge is an element that is

used to prevent pesting of  $\text{MoSi}_2$  at  $T < 900^\circ\text{C}$ .  $\text{GeO}_2$  lowers the viscosity of  $\text{SiO}_2$  without altering the oxidation properties of the oxide. Perhaps Ge has application in this situation.

#### No Glaze and Glaze

The no glaze sample had better oxidation resistance than the glaze sample. The no glaze sample was procured so that the effect of the thin glaze could be tested. The thin glaze was found to be detrimental to the oxidation resistance of the coating. Industrial users of this type of coating are probably not aware that the no glaze sample has better oxidation resistance than the glaze sample. One way to make the Chromalloy coating better is to eliminate the glaze layer.

Microcracking of the CVD  $\text{SiC}$  layers was prevalent in these coating samples. The microcracks extend through all of the  $\text{SiC}$  layers with the more frequent and intensive cracking occurring at the outermost areas. The microcracking might be unavoidable considering the thermal expansion mismatch of the components involved in this system. Plasma Assisted C.V.D. processes can reduce the processing temperatures of the coating and might relieve some of the microcracking. Most microcracks observed in the coating have some  $\text{SiO}_2$  forming in them. Formation of  $\text{SiO}_2$  in these cracks depletes the coating of Si, the element needed to create the oxygen barrier. The silica in the microcracks may also help propagate cracks in the coating during thermal cycling.

The geometric layout of the CVD layers in these coating systems may also affect oxidation resistance. The position and thickness of various layers might be altered to improve performance. Three  $B_4C$  layers, comprising 30% of the coating thickness, might be too much. The  $B_4C$  has poorer thermal shock resistance than SiC or  $Si_3N_4^{(64)}$ , and introduces B that may be detrimental to oxidation resistance. Because the  $B_4C$  layer is intended to seal cracks from oxygen penetration, one layer is probably as effective in this capacity as three. The  $B_4C$  layer might also be more effective if it was located closer to the coating gas interface. This might result in less oxidation of the microcracks in the CVD SiC layers. The SiC layers might be varied in a similar fashion. Thicker layers might result in differing degrees of oxidation resistance and may improve performance.

The free Si phase in these coatings is deleterious to coating performance. The Si phase is attacked preferentially by oxygen at long exposure times. The Si phase is often located at the base of the spherical nodules and at interfaces in the CVD SiC layers of the initial microstructure. The elimination of these nodules and interfaces in the CVD process may be difficult but might lead to better oxidation resistance. A larger SiC layer thickness would eliminate some of the interfaces seen in the coating. The absence of the nodules and interfaces might result in a more uniform coating thickness and structure.



## 5.0 CONCLUSIONS

1. Kinetic measurements indicate that current uncoated CCC can be used for long times at temperatures below about 400°C (t>2000 hr. with 12.5 mil recession)<sup>(1)</sup> without coatings; however, under such conditions the composites do react with oxygen at very slow rates.
2. Inhibited and uninhibited CCC have different weight loss vs. time curves in isothermal oxidation tests. The inhibited composite shows three distinct stages of oxidation behavior, while the uninhibited CCC show two. Both types of CCC have regions associated with transients in temperature (stage 1) and oxidation of carbon (stage 2). Only the inhibited CCC has a region associated with the coverage of the CCC with B<sub>2</sub>O<sub>3</sub> (stage 3).
3. A plot of the log of the oxidation rate, stage 2, vs. reciprocal of temperature (400-1300°C) reveals two distinct regions of behavior. At low T (T<700°C) the oxidation is controlled by a surface reaction. At high T (T>900°C) the oxidation rate is controlled by diffusion through a gas boundary layer. At intermediate temperatures mixed control exists. In the diffusion controlled regime higher oxidation

rates are controlled by experimental variables, i.e., oxidation rate increases with increasing flow rate and decreasing sample size.

4. The oxidation rates in stage 3 are about two orders of magnitude lower than stage 2 rates. Stage 3 rates indicate the rates associated with oxidizing  $B_2O_3$ -coated CCC. The observed oxidation rates indicate that long term use<sup>(1)</sup> of  $B_2O_3$  coatings would be limited to 750°C. Inhibited CCC should be distinguished from coated CCC, since inhibited composites exhibit stage 2 behavior.
5. B-based particle inhibition of CCC is ineffective because carbon is oxidized from the composite at comparable rates (during stage 2) regardless of the presence of the inhibitor. A significant lowering of the oxidation rate with inhibitors occurs after a 65% weight loss. This weight loss is beyond the limit where mechanical properties could be maintained.
6. Water vapor was found to accelerate the oxidation of both uninhibited and inhibited CCC at temperatures where the rate was controlled by chemical reaction ( $T < 700^\circ\text{C}$ ). Water vapor also led to the removal of substantial amounts of inhibitor at high temperatures by formation of volatile, boron oxide

species.

7. SiC-based coatings on CCC have poor oxidation resistance compared with currently used coated superalloys under these test conditions.<sup>(78)</sup> The coatings used on CCC in this study, listed from most to least protective, are: 1) Chromalloy coating with no glaze; 2) the HITCO M185 coating; 3) the Chromalloy coating with a glaze ;and 4) the HP24 conversion layer coating.
8. The mechanical properties of the coatings limited their oxidation resistance at high temperature. Thermal shock resistance and cracking generally resulted in failures before oxidation degradation became severe. Oxidation, however, aggravates cracking of the coatings.
9. The simple conversion coating of HP24 had three microstructures that detracted from oxidation resistance. The structures were free Si, B<sub>4</sub>C stringers, and unconverted carbon fibers.
10. Free Si found in the M185 and Chromalloy coatings was preferentially oxidized. This preferential oxidation limits the useful thickness of the coating. The Si in the coatings

oxidized at a faster rate than the SiC.

## 6.0 REFERENCES

1. K. L. Luthra, "Oxidation of Carbon/Carbon Composites - A Theoretical Analysis", General Electric Corporate Research and Development Report No. 866rd096, May, 1987, Schenectady, New York.
2. D. W. McKee, "Chemistry and Physics of Carbons", Vol. 16; P. L. Walker, Jr. and P. A. Thrower eds., Marcel Dekker, New York, 1981.
3. McKee, D. W., "Borate Treatment of Fibers and C/C Composites for Improved Oxidation Resistance", Carbon, Vol. 24, 1986, pp. 737-741.
4. Erhbürger P. et. al., "Inhibition of the Oxidation of C-C Composite by Boron Oxide", Carbon, Vol. 24, 1986, pp. 495-499.
5. R. Keiser, "Oxidation Protection for High Strength Carbon-Carbon Composites", Report AFWAL-TR-82-4060, Prepared by Garrett Turbine Engine Co., Phoenix, Arizona for WPAFB Materials Laboratory, WPAFB, Ohio, June, 1982.
6. Gulbransen, E. and Andrew, K., "Reactions of Artificial Graphite: I. Kinetics of Oxidation 425-575°C; II. Surface Oxide Formation; III. Mechanism of Oxidation; IV. Reaction CO<sub>2</sub> With Pure Artificial", Industrial and Engineering Chemistry, Vol. 44, 1952, pp. 1034-1048.

7. Gregg and Tyson, "The Kinetics of Oxidation of Carbon and Graphite by Oxygen at 500-600°C", Carbon, Vol. 13, 1965, pp. 39-42.
8. McKee, D. W., "Effects of Adsorbed Phosphorus Oxychloride on the Oxidation Behavior of Graphite", Carbon, Vol. 10, 1972, pp. 491-497.
9. Gulbransen, E. et al., "Oxidation of Graphite at Temperatures From 600-1500°C at Pressures From 2 to 76 Torr O<sub>2</sub>", Journ. Electro. Chem. Soc., Vol. 110, 1963, pp. 476-483.
10. Blyholder, G. and Eyring, H., "Kinetics of Oxidation of Graphite", Journal of Phy. Chem., Vol. 61, 1957, p.682.
11. Blyholder, G. and Eyring, H., "Kinetics of Graphite Oxidation II", Journ. of Phy. Chem., Vol. 63, 1959, p.1004.
12. Gulbransen, E. et al., "Oxidation of Pyrolytic Carbon at 1000-1500°C in Oxygen Pressures of 2-38 Torr", Journ. Electro. Chem. Soc., Vol. 111, 1964, pp. 626-627.
13. Goto, T. et. al., "A Review on the Oxidation Kinetics of Carbon Fibre/Carbon Matrix Composites at High Temperature", Trans. ISIJ, Vol. 26, 1986, pp. 597-603.
14. Serpinet, J., Thesis, University of Nancy, 1956.
15. Chang, H. W. and Rhee, S. K., "Oxidation of Carbon Derived from Phenolic Resin," Carbon, Vol. 17, 1978, pp. 17-20.
16. Gulbransen, E. et al., "Oxidation of Graphite, Mo, and W at 1000-1600°C", Progress in Astronautics and Aeronautics, 1964,

pp. 227-250.

17. Wicke, E., Proceedings of the Fifth Symposium on Combustion, Rhienhold, New York, 1955, p. 245.
18. Walker and Reinoso, "Reaction of Glassy Carbon with Oxygen", Carbon, Vol. 13, 1975, pp. 7-10.
19. McKee, D. W., "Catalyzed Gasification Reactions of Carbon", Chemistry and Physics of Carbon, Vol. 15, Thrower and Walker ed., pp. 1-117.
20. McKee, D. W., et al., "The Effects of Boron Additives on the Oxidation Behavior of Carbons", Carbon, Vol. 22, 1984, pp. 507-511.
21. Yasuda et. al., "Oxidation Behavior of Carbon Glassy Fiber/Glassy Carbon Composites", Trans. JCSM Vol. 6, 1980, pp. 14-23.
22. Fishbach, D. B. and Uptegrove, D. R., "Oxidation Behavior of Some C/C Composites", Abstracts 13<sup>th</sup> Biennial Conference on Carbon, 1977, pp. 130-131.
23. Walker et al., "Effect of Oxidation at 873K on the Mechanical Properties of a C/C Composite", Carbon, Vol. 23, 1985, pp. 9-13.
24. Chang, H. W. and Rusnak, R. M., "Oxidation Behavior of C/C Composites", Carbon, Vol. 17, 1979, pp. 407-410.
25. Chang, H. W. and Rusnak, R. M., "Oxidation Mechanisms of C/C Composites", Abstracts 13<sup>th</sup> Biennial Conference on Carbon,

1977, pp. 449-450.

26. Peng, T. C., "Oxidation Erosion of Fiber-Matrix C Composite", Abstracts 13<sup>th</sup> Biennial Conference on Carbon, 1977, pp. 41-42.
27. Thrower and Marx, "The Oxidation of Graphite Under Compressive Stress", Abstracts 13<sup>th</sup> Biennial Conference on Carbon, 1977.
28. Dahl, R. E., USAEC Report HW-63902, 1960.
29. Day R. et. al., SCI Conf. Industrial Carbon and Graphite, London, 1957.
30. Arthur, J. R., Trans. Faraday Soc., Vol. 47, 1951, pp. 164.
31. Woodley, R. E., "The Oxidation of Boronated Graphite", Carbon, Vol. 6, 1968, pp. 617-626.
32. Asher, R. C. and Kirstein, T. B. A., "The Inhibiting Effects of Cl or CCl<sub>4</sub> on Graphite Oxidation", Journ. of Nuc. Matl's., Vol. 25, 1968, pp. 344-346.
33. Magne et. al., "Etude cinetque de l'oxydation du graphite inhibee par les phosphates", Bull. Soc. Chim. France, 1971, pp. 2005-2010.
34. Woodley, R. E., "The Reaction of Boronated Graphite with Water Vapor", Carbon, Vol. 7, 1969, pp. 609.
35. Arthur, J. R. and Bangham, D. H., "The Mechanism of Energy Release in the Combustion of Solid Carbonaceous Fuels", J. Chem. Phys., Vol. 47, 1950, pp. 559-562.
36. Walker, P. L. Jr. and Alldarice, D. J., "The Effect of Substitutional B on Kinetics of the C-O Reaction", Carbon,



Vol. 8, 1970, pp. 375-385.

37. Thomas, J. M., "Microscopic Studies of Graphite Oxidation", Chemistry and Physics of Carbon, Thrower and Walker ed., Vol. 1, 1965, p. 249.
38. McKee, D. W., "The Inhibition of Graphite Oxidation by Phosphorus Additives", Carbon, Vol. 22, 1984, pp. 285-290.
39. McKee, D. W., "Oxidation Behavior and Protection of C/C Composites, Carbon, Vol. 25, 1987, pp. 551-557.
40. Wallouch, R. W. and Hientz, E. A., "The Oxidation of Graphite Zone II Omission", Carbon, Vol. 12, 1974, pp. 243-249.
41. Hannache, H. et. al., "Composite Materials Made from a Porous 2D C/C Composite Preform Densified with BN by CVD", Journal Mat. Sci., Vol. 19, 1986, pp. 202-212.
42. Christin, et. al., in 7<sup>th</sup> International Conference on Chemical Vapor Deposition, edited by Blocher et. al., The Electrochemical Society Pennington, New Jersey, 1981, pp. 782-789.
43. Rossignol, J. Y. et. al., ICCM-4, Tokyo October 1982, Vol.2, edited by Hayashi et. al., JCSM Tokyo 1982, pp. 1227-1239.
44. Pettit and Goward, "High Temperature Corrosion and Use of Coatings for Protection", Proceedings at USA-China Bilateral Conference, Metallurgical Soc. of AIME, 1981, pp. 603-619.
45. Gulbransen, E. et al., "The Oxidation of SiC at 1150-1400°C at  $9 \times 10^{-3}$  -  $5 \times 10^{-1}$  Torr O<sub>2</sub> Pressure", Journ. Electro. Chem. Soc.,

Vol. 113, 1966, pp. 1311 -1314.

46. Costello, J.A. and Tressler, R.E., "Oxidation Kinetics of Hot-Pressed  $\alpha$ SiC", Journal of the American Ceramic Society, Vol. 64, 1981, pp. 327-331.
47. Tressler, R. E. et. al., "Fundamental Studies of Corrosion of Nonoxide Structural Ceramics", Final Report to G.R.I contract #GRI-5084-260-1083, 1988.
48. Cutler, I. B. et. al., "Oxidation of Silicon Carbide", Journ. American Ceramic Society, Vol. 12, 1959, pp. 613-616.
49. Pultz, W. W., "Temperature and Oxygen Pressure Dependence of Silicon Carbide Oxidation", J. Phys. Chem., Vol. 71, 1967, pp. 4556-4558.
50. Warburton, J. B. and Antill, J. E., "Active to Passive Transition in the Oxidation of SiC", Corr. Sci., Vol. 11, 1971, pp. 337-342.
51. Singhal, S. C., "Thermodynamics and Kinetics of Oxidation of Hot-Pressed Silicon Nitride", Journal Mat. Sci., Vol. 11, 1976, pp. 500-509.
52. Singhal, S.C., "Oxidation Kinetics of Hot-Pressed  $\alpha$ SiC", Journal of Material Science, Vol. 11, 1976, pp. 1246-1253.
53. Smialek, J. L. et. al., "Burner Rig Corrosion of SiC at 1000°C", Adv. Cer. Matl., Vol. 1, 1986, pp. 154-161.
54. Blachere, J. R. and Pettit, F. S., High Temperature Corrosion of Ceramics, Moyer Data Corp., Park Ridge New Jersey, 1989.

55. Schiroky, G. , "Oxidation Behavior of Chemically Vapor Deposited SiC", Adv. Cer. Matls., Vol. 2, 1987, pp 137-141.
56. Meier, G. H. and Birks, N., Introduction to High Temperature Oxidation of Metals, Edward Arnold, London, 1983.
57. Heuer, A. H. et. al., "Bubble Formation in Oxide Scales of SiC", Journal American Ceramic Society, Vol. 67, 1984, pp. 17-18.
58. Sheehan et. al., "High-Temperature Ceramic and Carbon Composites For Use In Oxidizing Environments", Presented to National Materials Advisory Board, 1987.
59. Sheehan, J. E., "Oxidation Resistant C/C Composites", from Metal-C/Graphite-Ceramic Matrix Composites, ASM publication, pp. 920-921.
60. Strife, J. R. and Sheehan, J. E., "Ceramic Coatings for CC Composites", Ceram. Bull., Vol. 67, 1988, pp.369-374.
61. Hirai et. al., "Oxidation of CVD Si<sub>3</sub>N<sub>4</sub> at 1550° to 1650°C", J. Am. Cer. Soc., Vol. 63, 1980, pp. 419-423.
62. Stinton et. al., "Advanced Ceramics by Chemical Vapor Deposition Techniques", Ceramic Bulletin, Vol. 67, 1988, pp. 350-355.
63. Das, N. and Saigal, A., "Effect of Deposition Parameters on the Strength of CVD  $\beta$ SiC", Adv. Cer. Matl., Vol. 3, 1988, pp. 580-583.

64. Engineering Property Data on Selected Ceramics Vol. 2, Metals and Ceramics Information Center, Batelle, Columbus Ohio, August 1979.
65. Becker, P. R., "Leading Edge Structural Material System of the Space Shuttle", Ceramic Bulletin, Vol. 60, 1981, pp. 1210-1214.
66. Clark et. al., "Coating Porous Substrates by the Sol-Gel Process", Adv. Cer. Matl., Vol. 3, 1988, pp. 253.
67. Zeitsch, K. J., "Oxidation Resistant Graphite-Base Composites", Modern Ceramics, Hove and Wiley ed., Wiley, 1967, pp.314-325.
68. Simmons, W. C., "High Temperature Oxidation Resistant Coatings For Graphite", Report AFML-TR-65-29.
69. Goldstein, E. M. et. al., "The Improvement of Oxidation Resistance of Graphite by Composite Technique, Carbon, Vol. 4, 1966, pp. 273-279.
70. Ohlhorst, C. W. et. al., "Performance Evaluation of Ox. Resistant CC Composites", 5th Natl Aero Space Plane Symposium Reno Nevada, October 1988.
71. Cullity, B. D., Elements of X-Ray Diffraction, Addison Wesley, London, 1978.
72. Litz, L. M., and Mencuri, R. A., "Oxidation of Boron Carbide by Air, Water, and Air-Water Mixtures at Elevated

- Temperatures", Journal EChem., Vol. 110, 1963, pp. 921-925.
73. McMahon, P. E., "Oxidative Resistance of Carbon Fibers and Their Composites", Advanced Composite Materials-Environmental Effects, ASTM STP 658, Vol. 1, 1978, pp.254-266.
  74. Yasuda et al., "Oxidation Behavior of Carbon Glassy Fiber/Glassy Carbon Composites", Trans. JCSM, Vol. 6, 1980, pp. 14-23.
  75. Warren, B. E., X-Ray Diffraction, Reading Mass., Addison-Wesley, 1969.
  76. Das, N. and Saigal, A., "Effect of Deposition Parameters on the Strength of CVD  $\beta$ -SiC", Adv. Cer. Matl., Vol. 3, 1988, pp. 580-583.
  77. Rockett, T. J., and Foster, W. R., "Phase Relations in the System Boron Oxide-Silica", Journal Am. Cer. Soc., Vol. 50, 1965, pp. 78.
  78. Schaeffer, J., "The Effect of Pt on the Behavior of Diffusion Aluminate Coatings", M.S. Thesis, University of Pittsburgh, 1987.

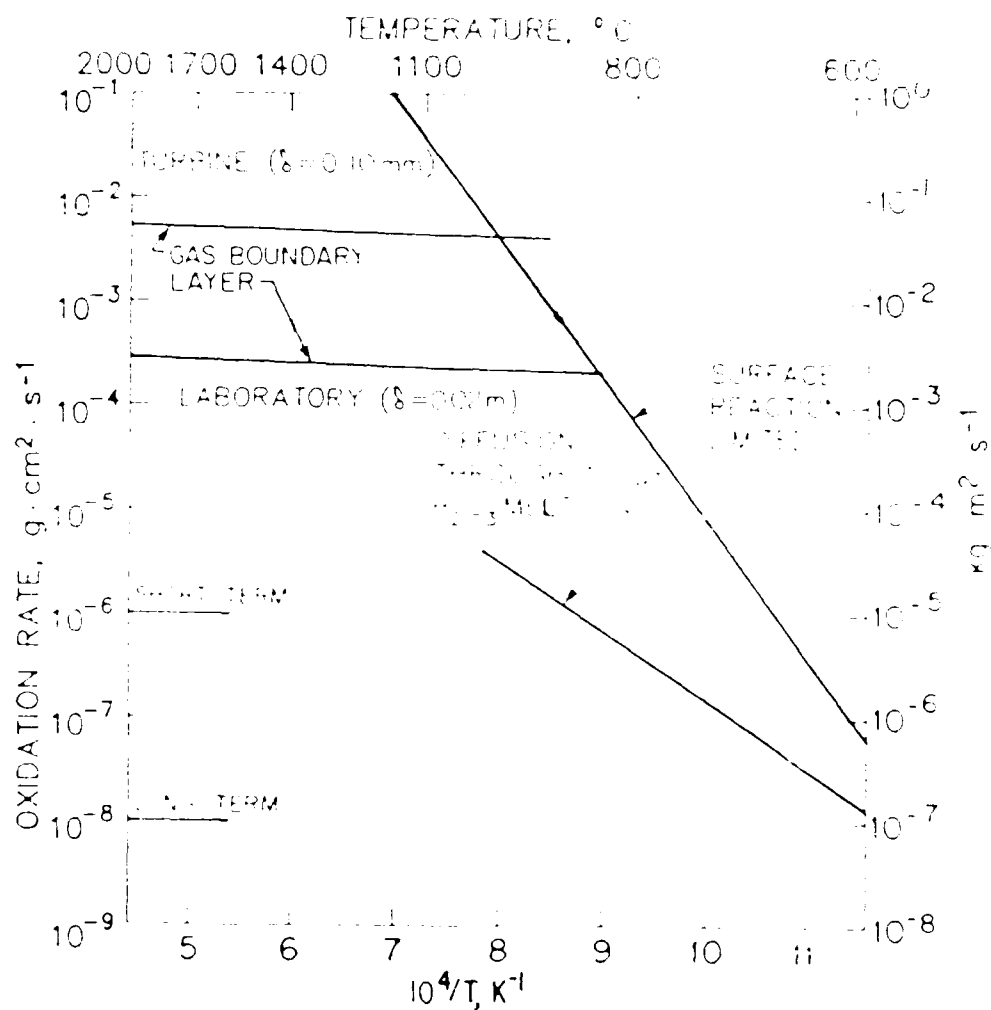


Figure 1. Plot of virtual maximum rates for various rate controlling steps. Short and long term goals are indicated.

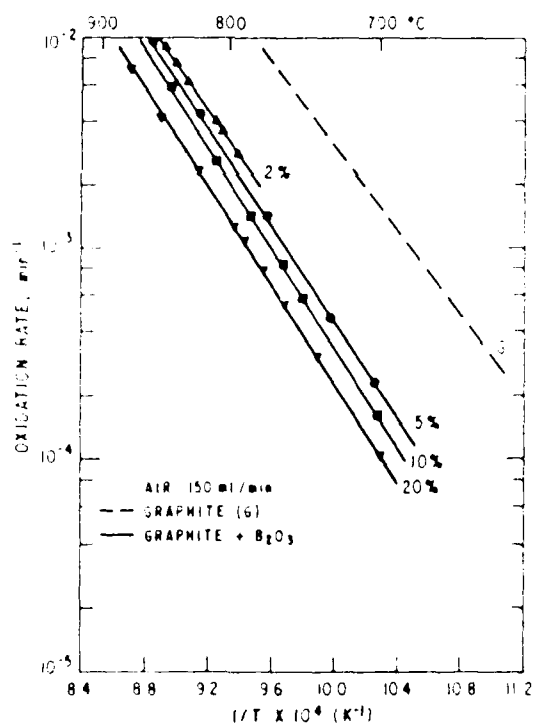
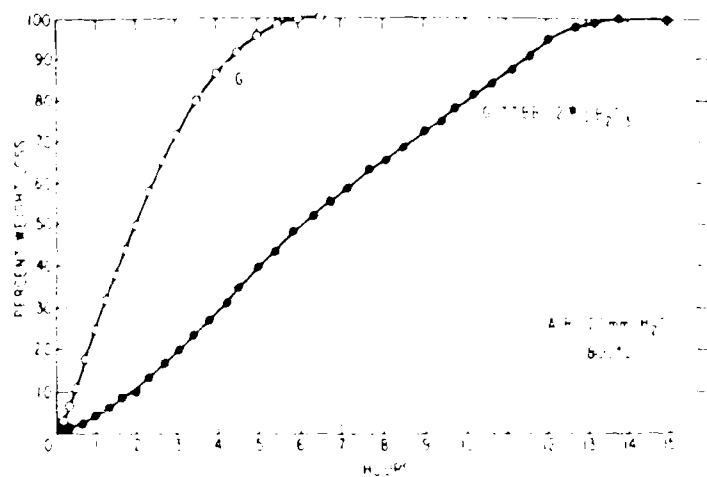


Figure 2. Oxidation kinetics show that B additions to carbon can reduce the oxidation rate.

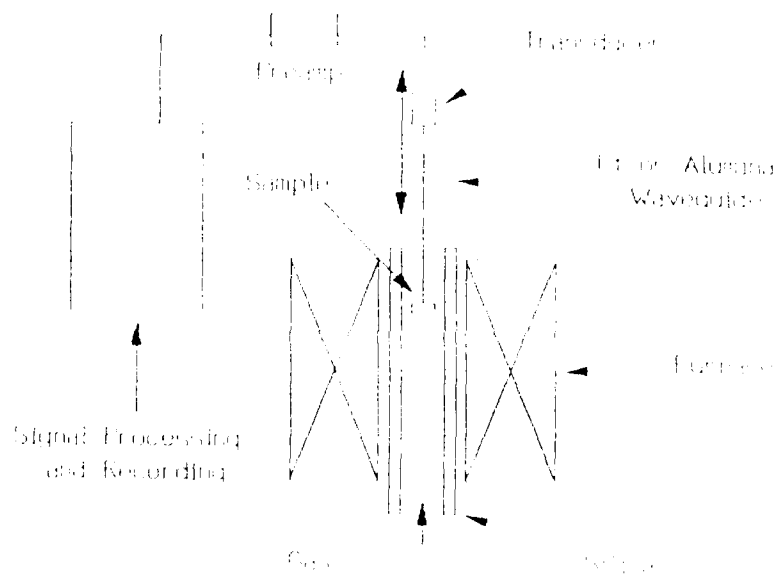
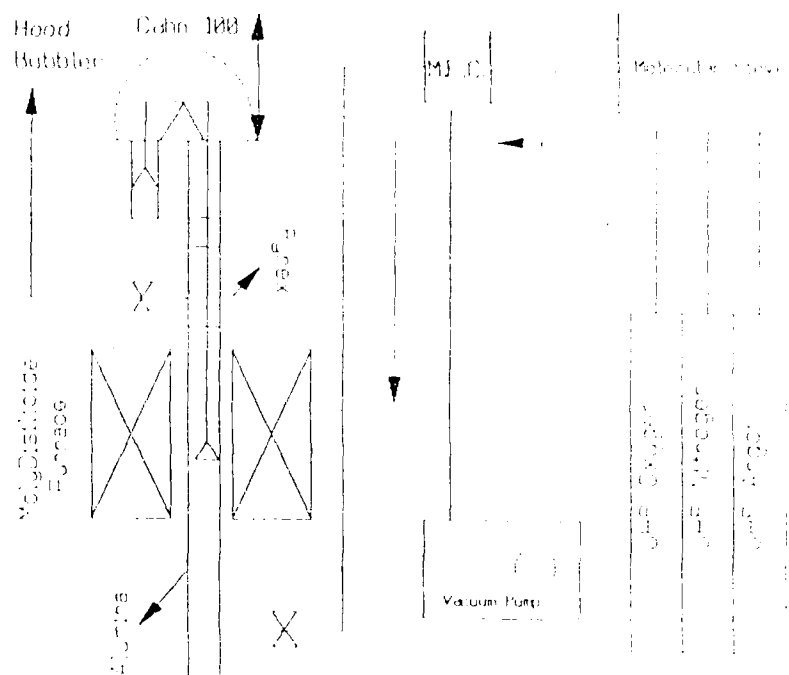


Figure 3. Schematic of the isothermal oxidation apparatus (top) and the acoustic emission apparatus (bottom).



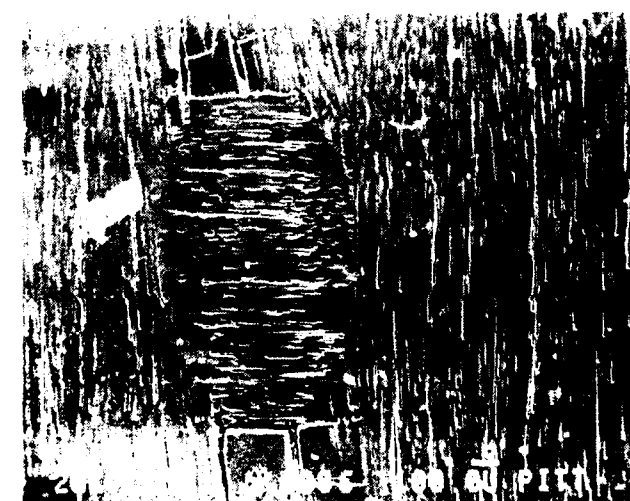
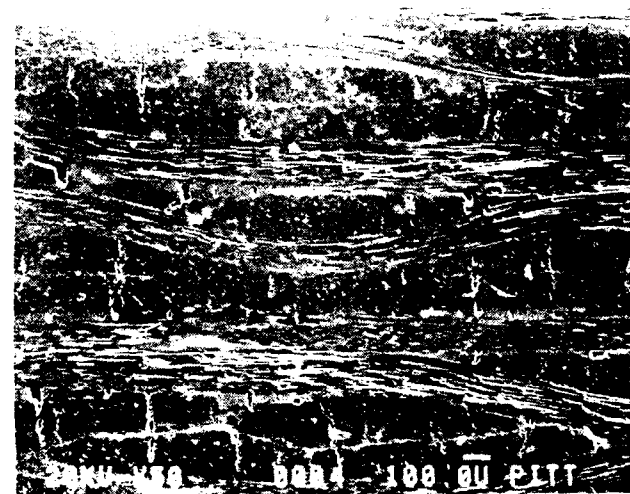


Figure 4. Initial microstructure of uninhibited carbon-carbon composite (HITCO CC139E). The top shows the surface, the middle shows a transverse cross section, and the bottom shows a planar cross section.

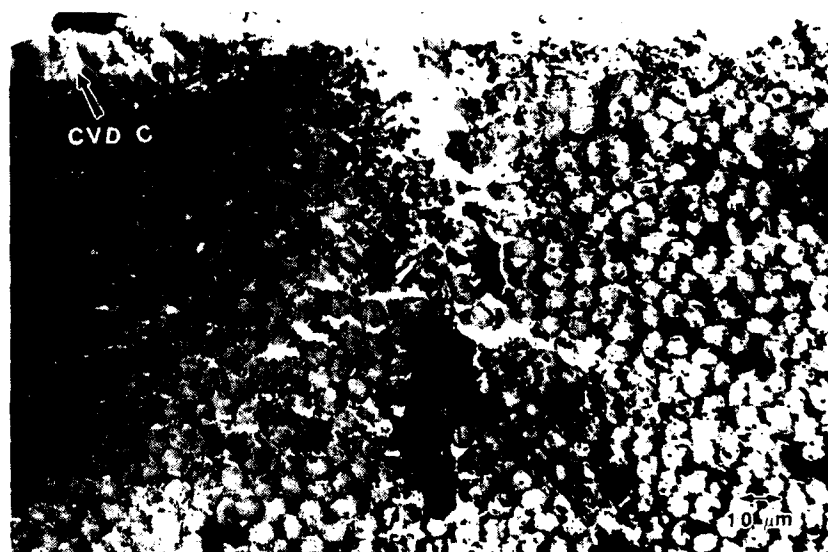


Figure 5. Optical micrographs showing the cross section of an inhibited carbon-carbon composite (HITCO CC136E). Top shows CVD carbon layer, while bottom shows a B<sub>4</sub>C particle.

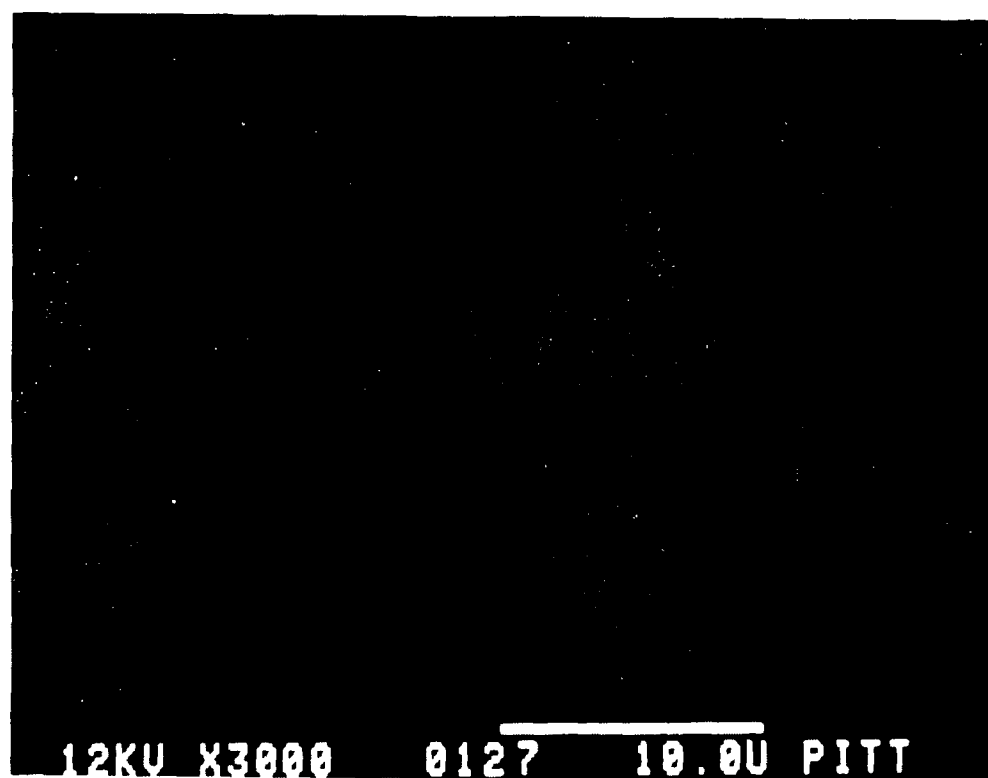
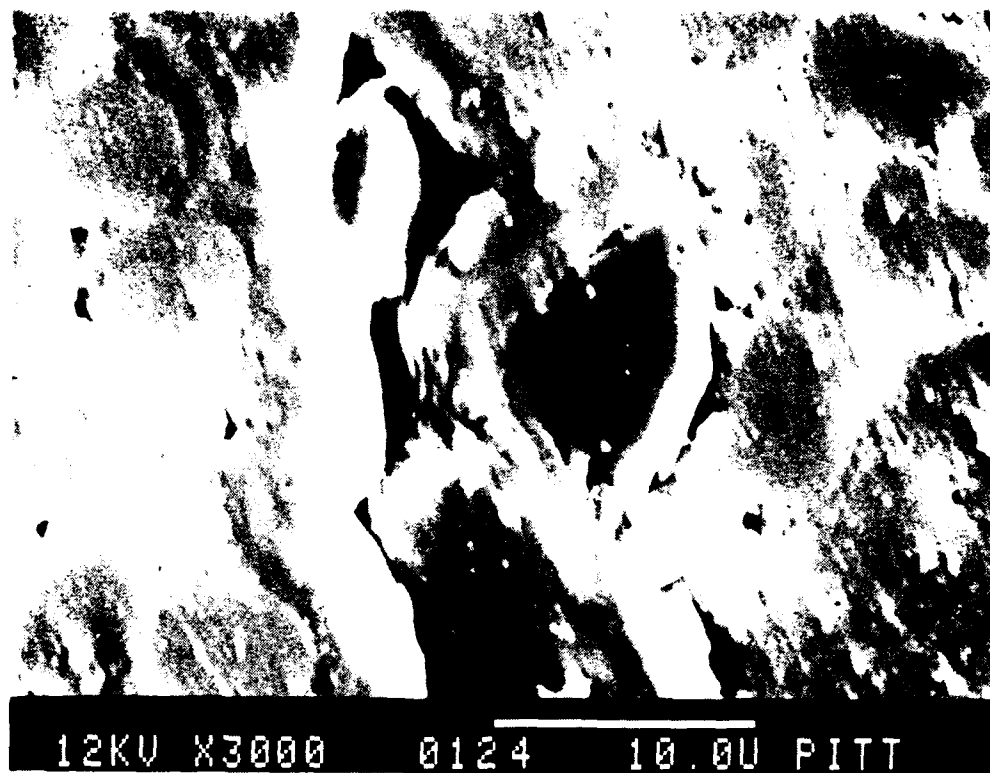


Figure 6. SEM micrograph of  $B_4C$  particle in CC136E. SEM contrast is low compared to optical contrast seen in Figure 5.

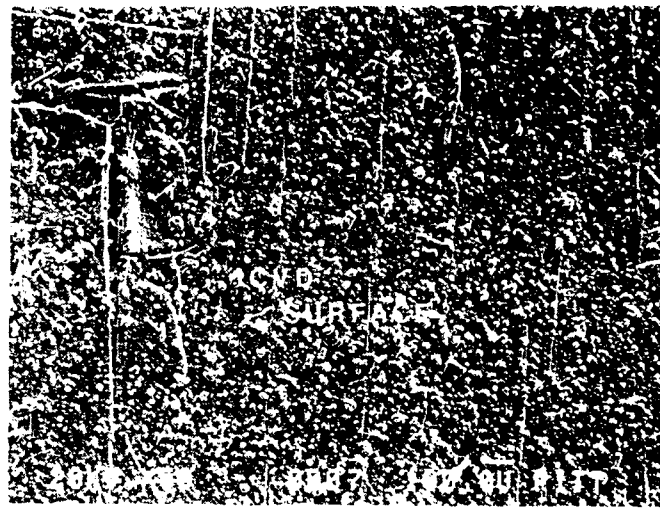


Figure 7. Initial microstructure of inhibited CC137E. Top shows surface, middle shows transverse cross section and bottom shows a planar cross section.



Figure 8. Bright field TEM image of a fiber and matrix in CC137E. SAD shows preferential orientation of (002) basal planes.

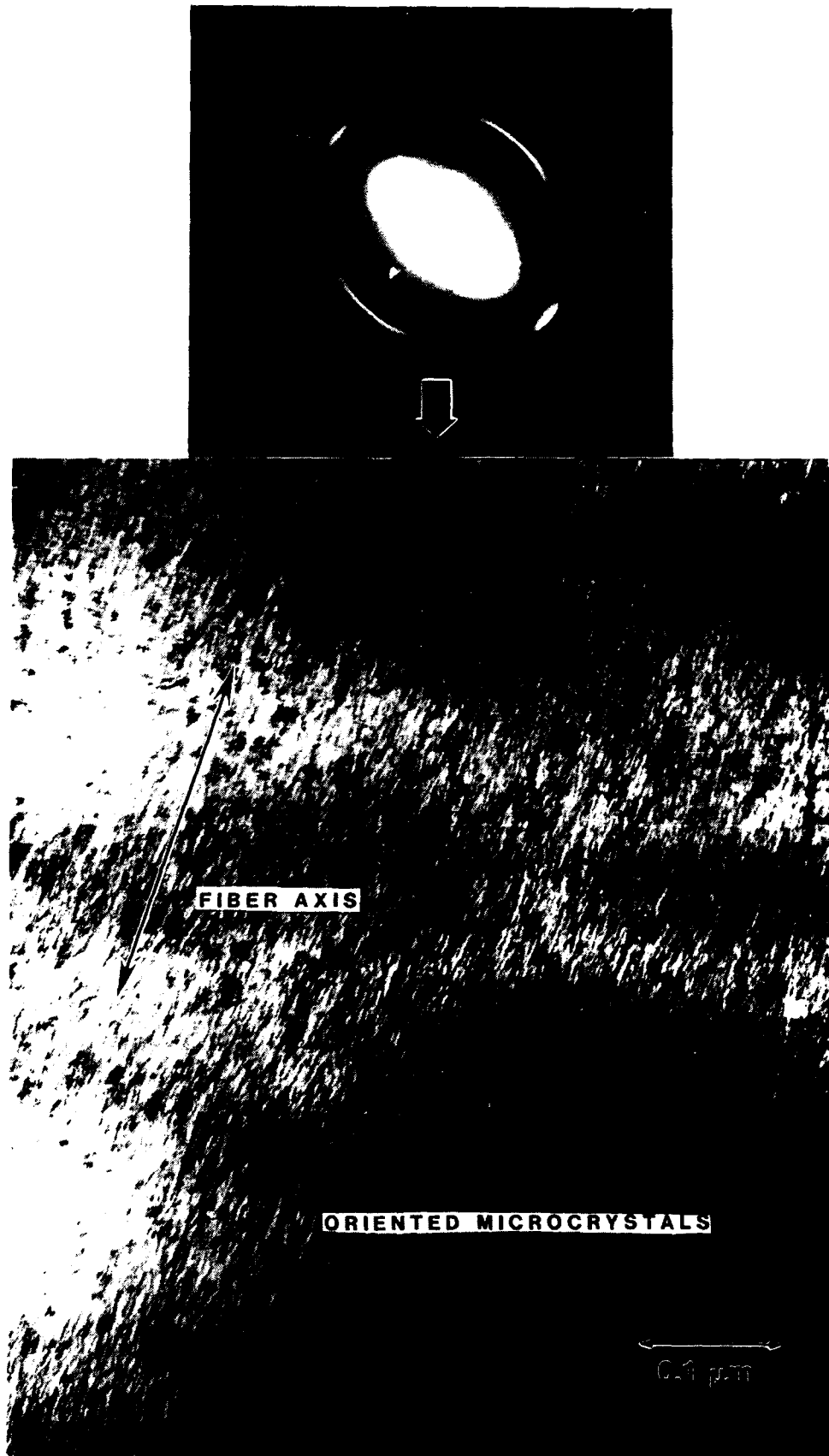


Figure 9. Bright field TEM micrograph of a fiber. Basal planes in the carbon fibers are oriented parallel to the fiber axis.

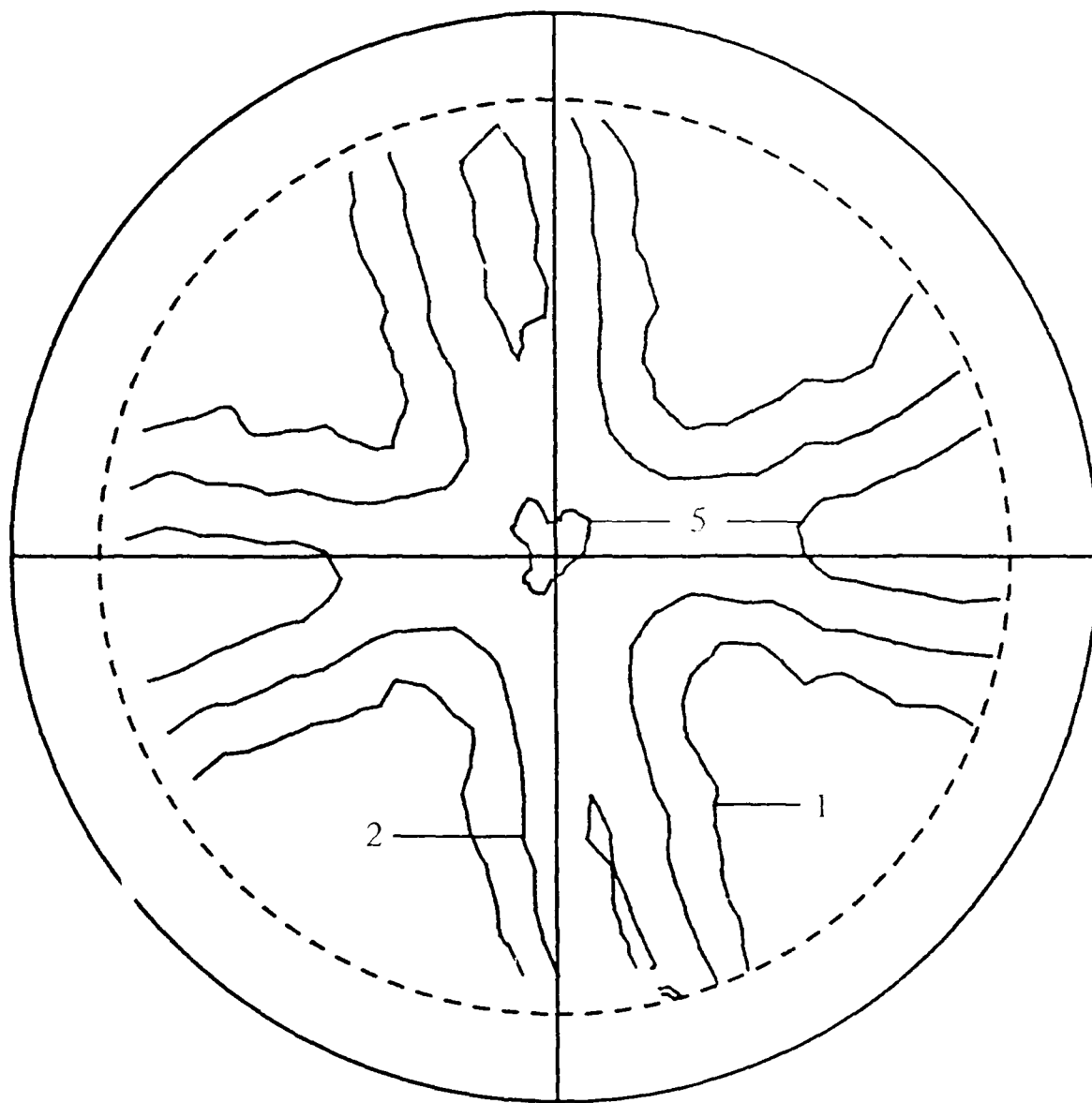


Figure 10. X-ray pole figure of (002) basal planes in as-received CC139E. The pole figure shows a "cross" pattern as a result of the 0-90° orientation of fibers. The numbers on the contours indicate the intensity of the sample compared to a random sample.



Figure 11. Bright field TEM micrograph shows the matrix carbon in as-received CC137E. The matrix is composed of microcrystalline rosettes and amorphous or glassy carbon.



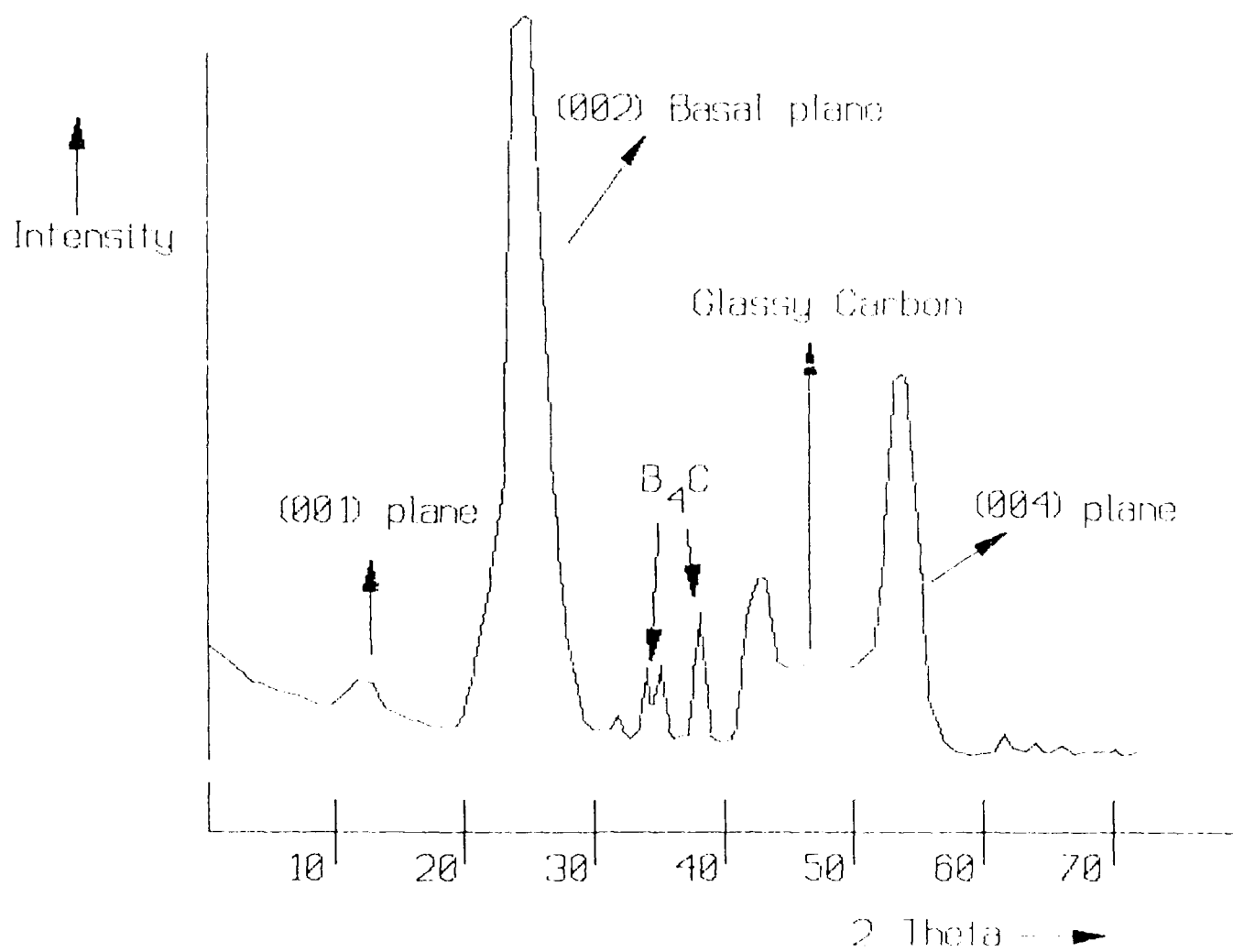


Figure 12. Schematic of an XRD pattern from as-received CC137E sample. The (001) plane for a graphite structure indicates a carbon with missing atoms.

# CARBON CARBON OXIDATION at 100 cc/min O<sub>2</sub> and 800°C

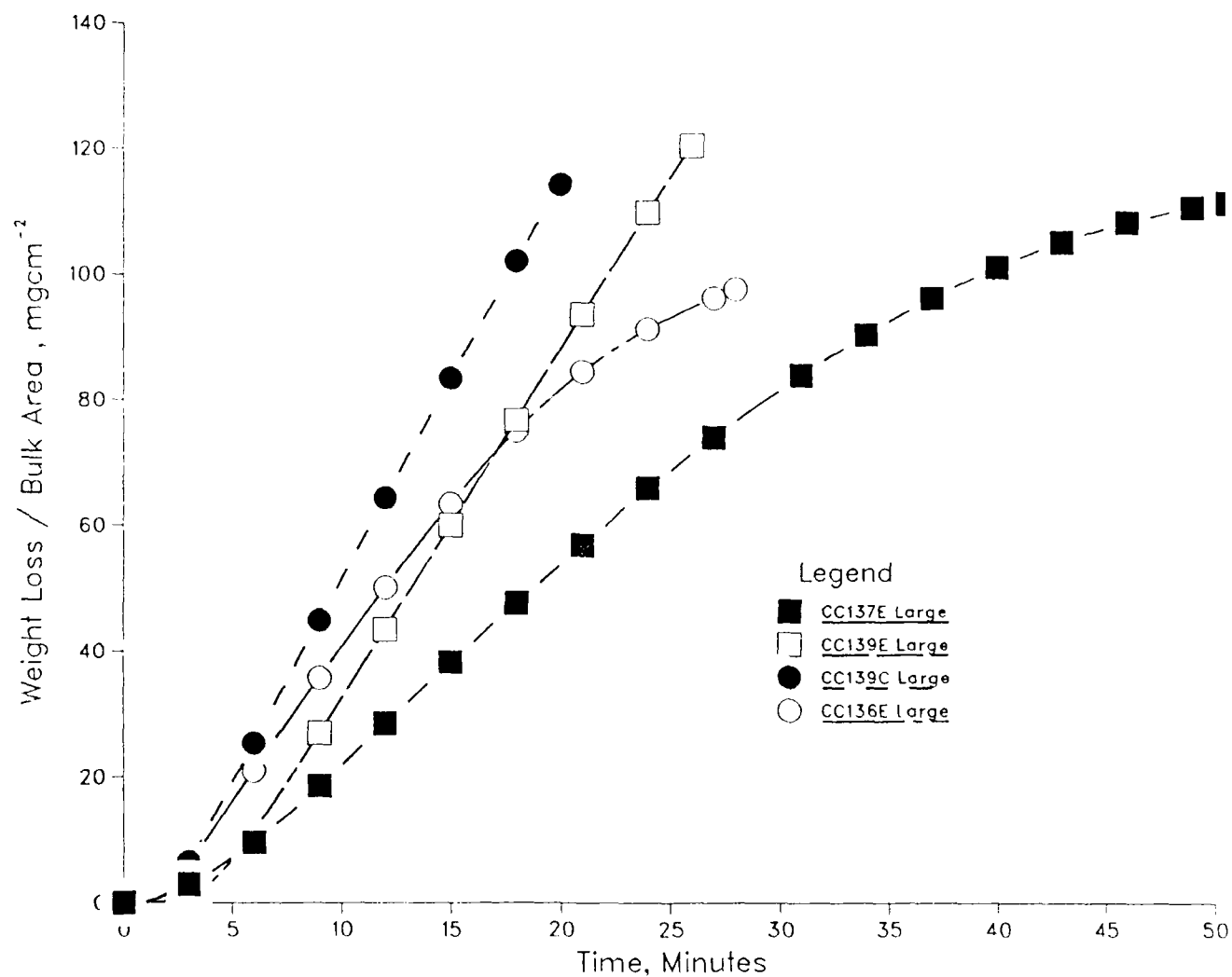


Figure 13. Isothermal oxidation kinetics for uncoated CCC at 800°C in O<sub>2</sub> flowing at 100 cc/min.

# CARBON CARBON OXIDATION at 100 cc/min O<sub>2</sub> and 900°C

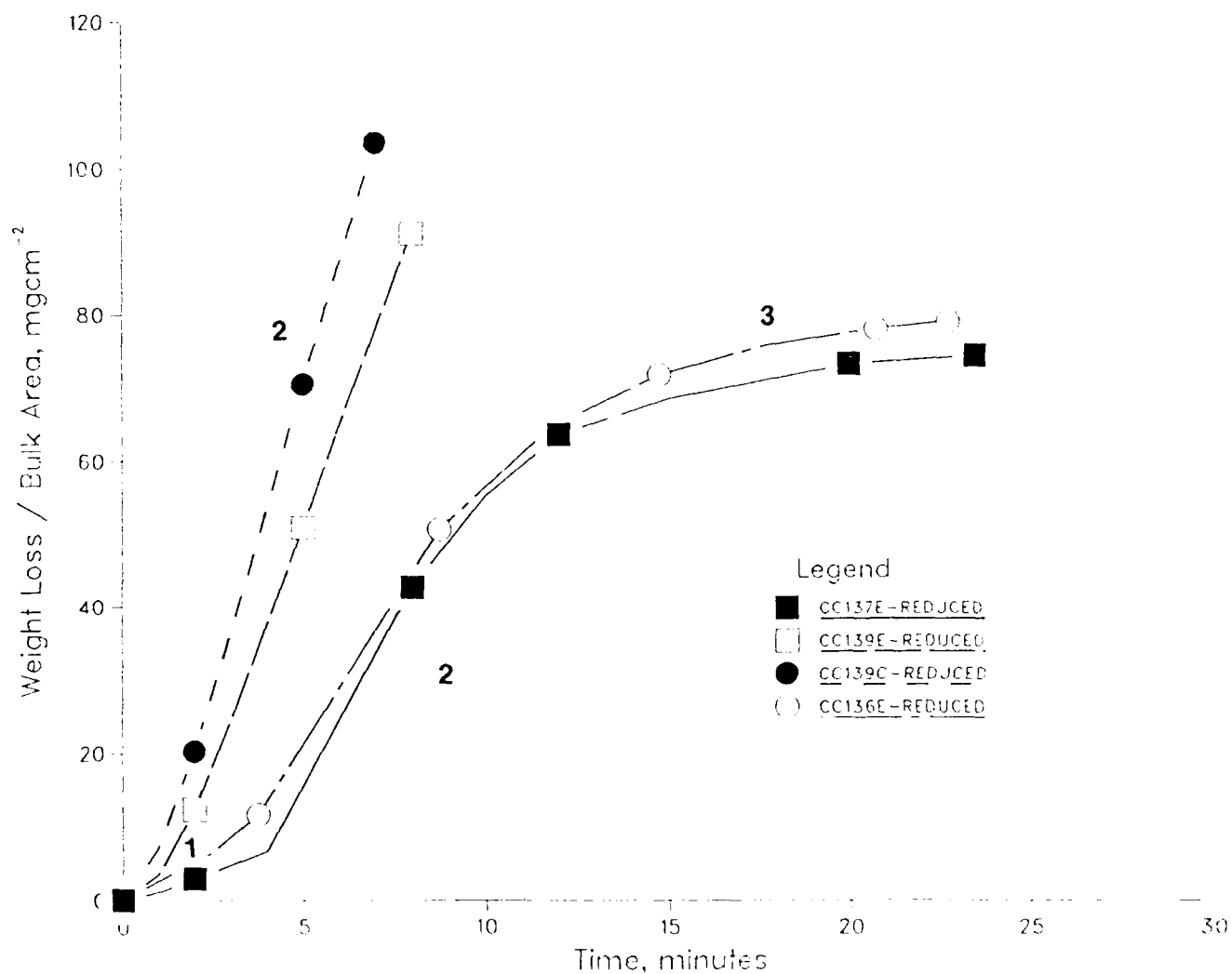


Figure 14. Isothermal oxidation kinetics for uncoated CCC at 900°C in O<sub>2</sub> flowing at 100 cc/min.

# CARBON CARBON OXIDATION at 100 cc/min O<sub>2</sub> and 1000°C

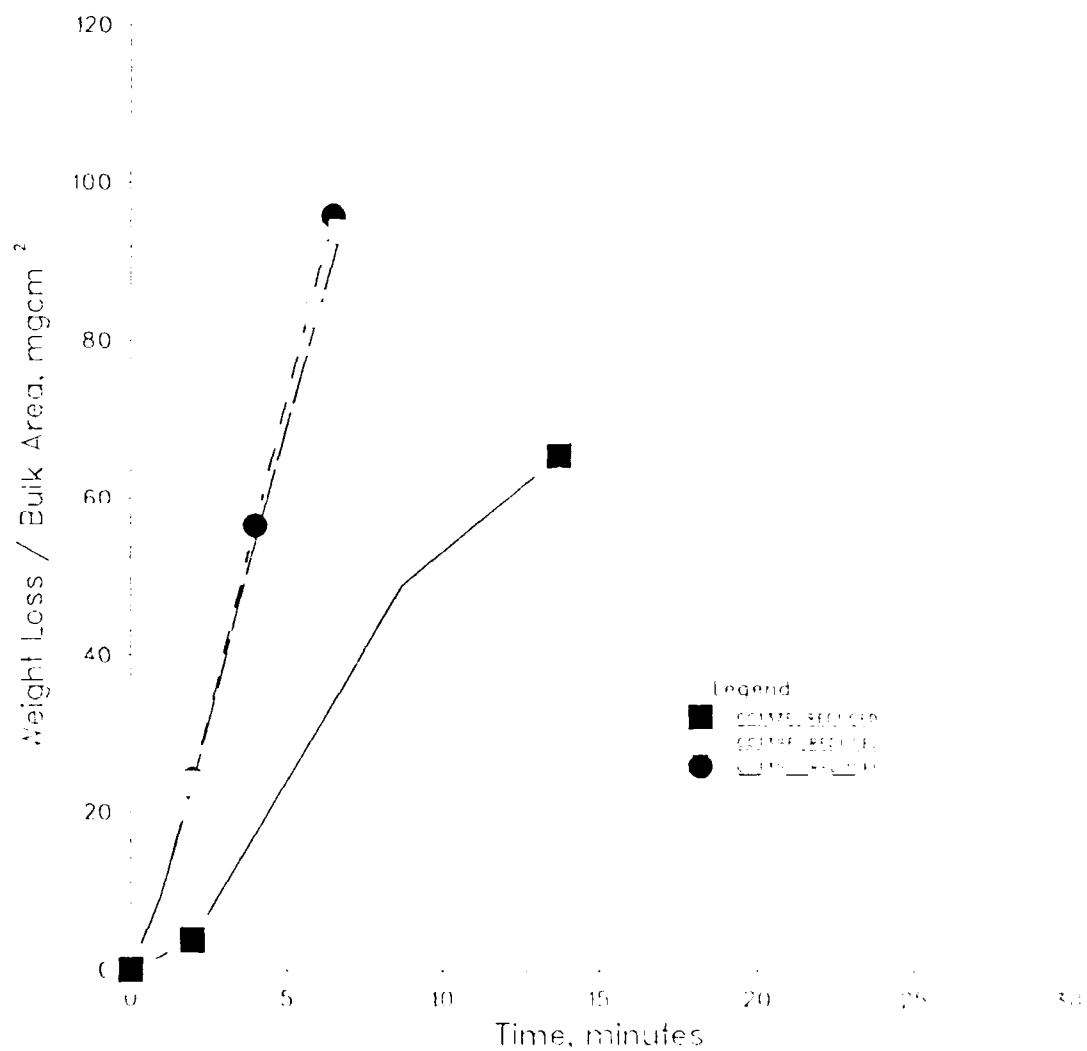


Figure 15. Isothermal oxidation kinetics for uncoated CCC at 1000°C in O<sub>2</sub> flowing at 100 cc/min.

# CARBON CARBON OXIDATION at 100 cc/min O<sub>2</sub> and 1100°C

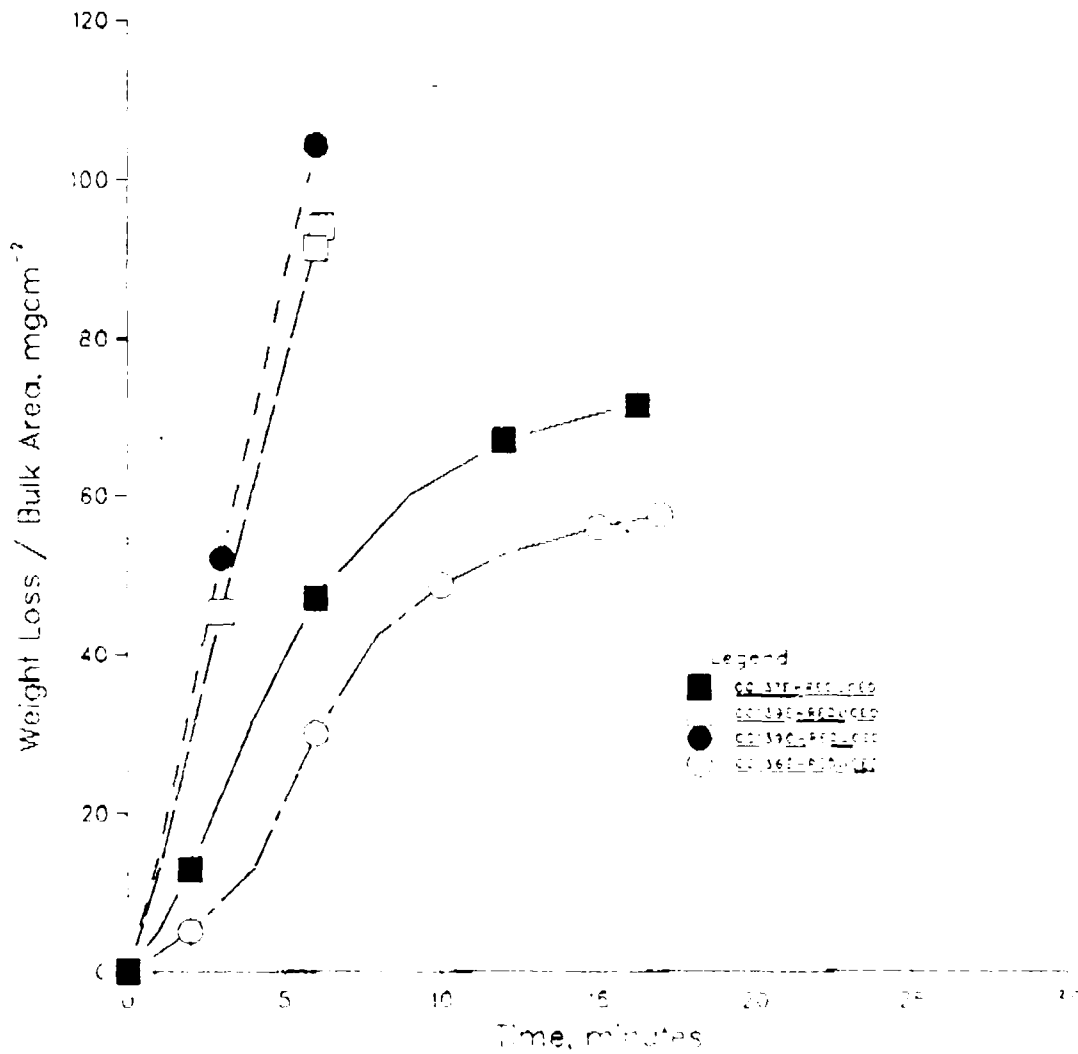


Figure 16. Isothermal oxidation kinetics for uncoated CCC at 1100°C in O<sub>2</sub> flowing at 100 cc/min.

# CARBON CARBON OXIDATION at 100 cc/min O<sub>2</sub> and 1200°C

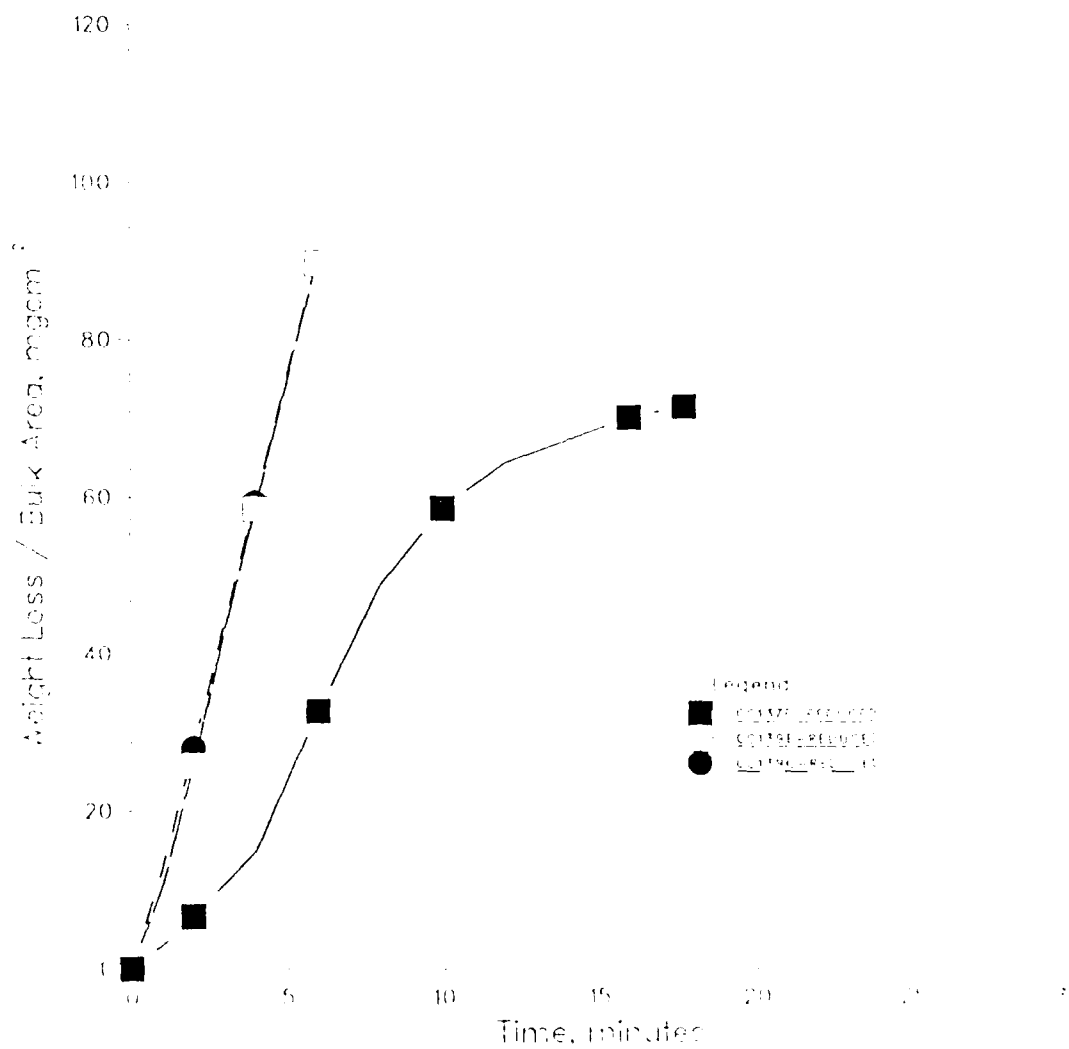


Figure 17. Isothermal oxidation kinetics for uncoated CCC at 1200°C in O<sub>2</sub> flowing at 100 cc/min.

# CARBON CARBON OXIDATION AT 100 cc/min O<sub>2</sub> and 1300°C

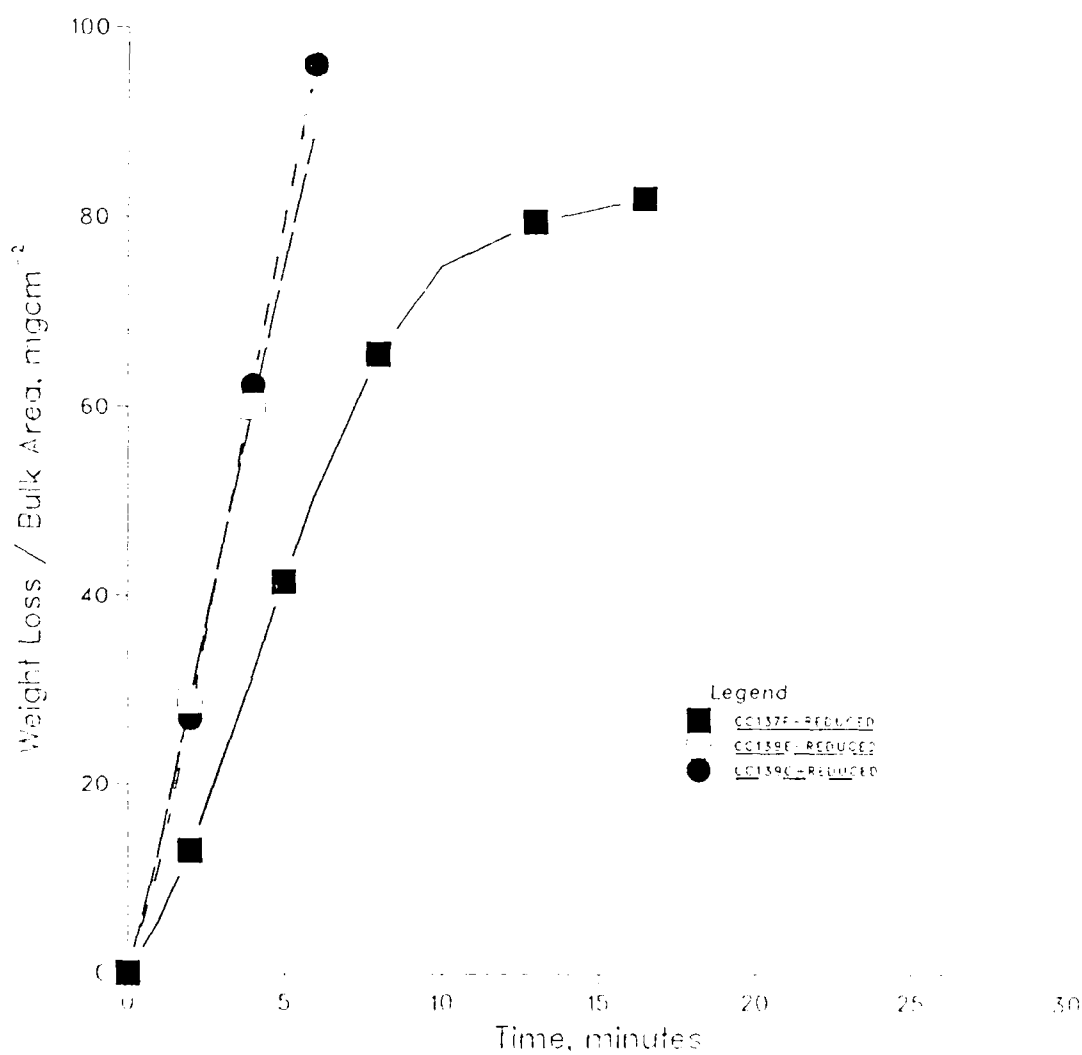


Figure 18. Isothermal oxidation kinetics for uncoated CCC at 1300°C in O<sub>2</sub> flowing at 100 cc/min.

# CC 139E OXIDATION AT 700°C

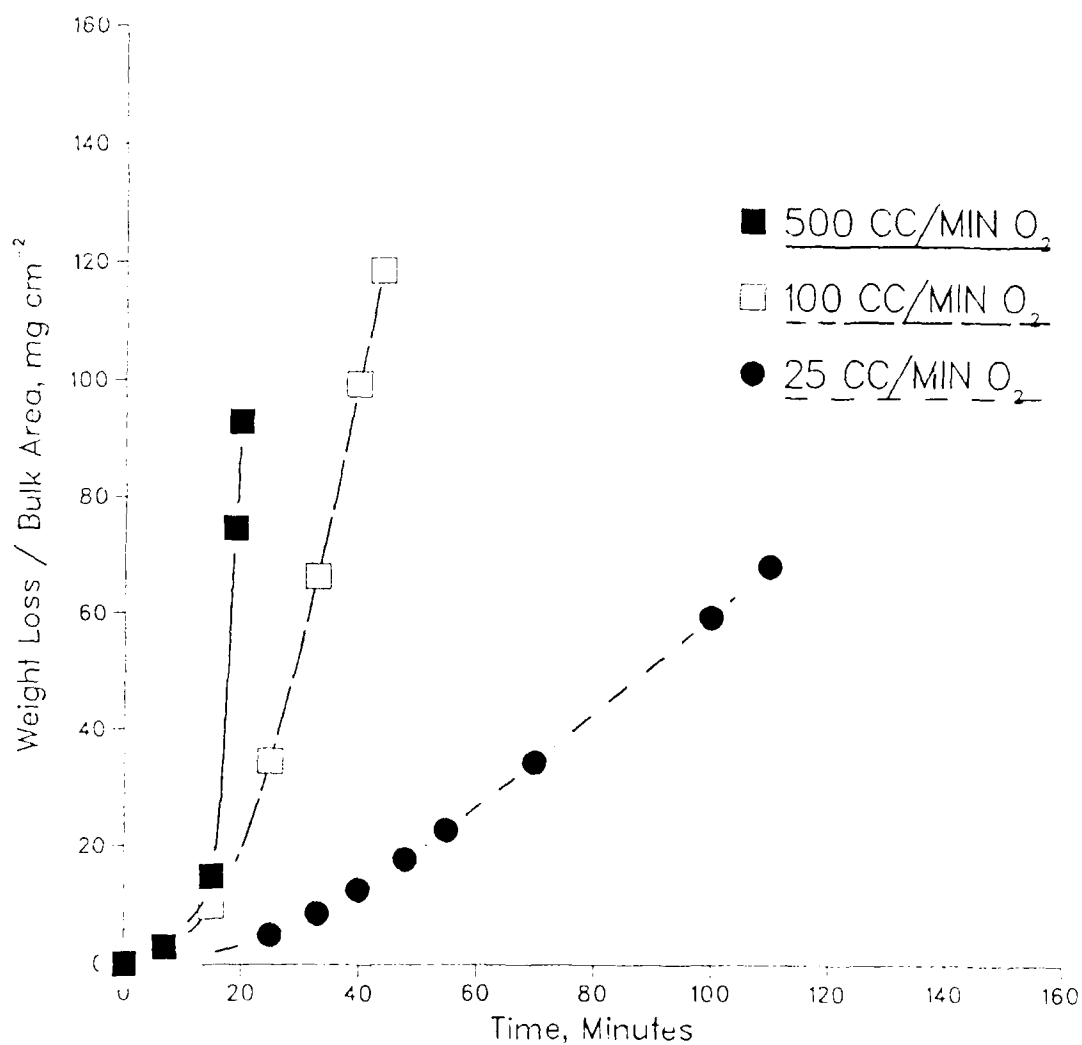


Figure 19. Isothermal oxidation kinetics for uncoated CCC at 700°C shows a dependence of oxidation rate on flow rate. At 700°C the oxidation reaction is still under mixed control.



# CARBON CARBON OXIDATION AT 100 AND 550 CC/MIN

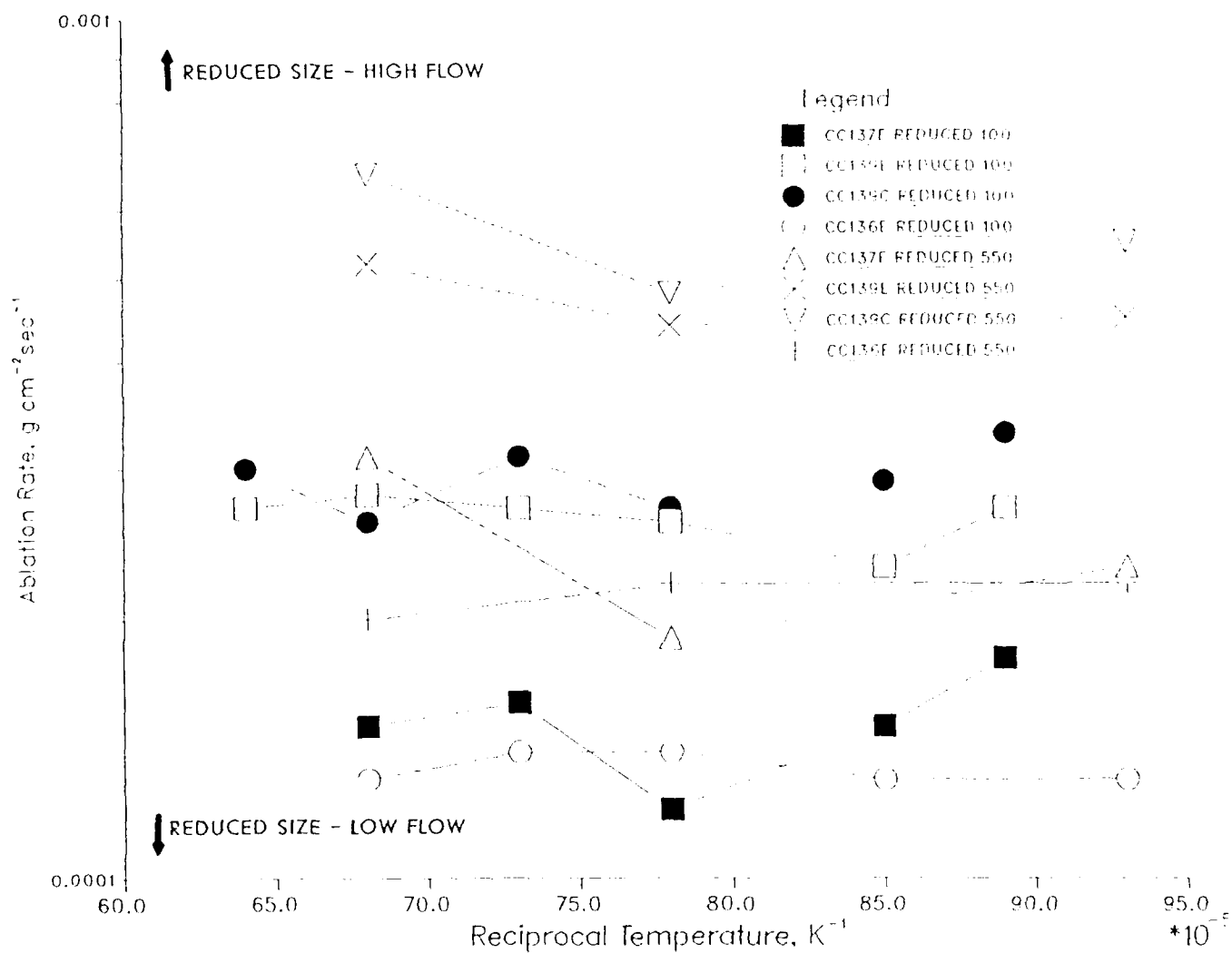


Figure 20. Log oxidation rate (weight loss) vs.  $1/T$  ( $\text{K}^{-1}$ ) for uncoated CCC showing the effect of flow rate in the diffusion controlled regime.

# CARBON CARBON OXIDATION at 550 cc/min

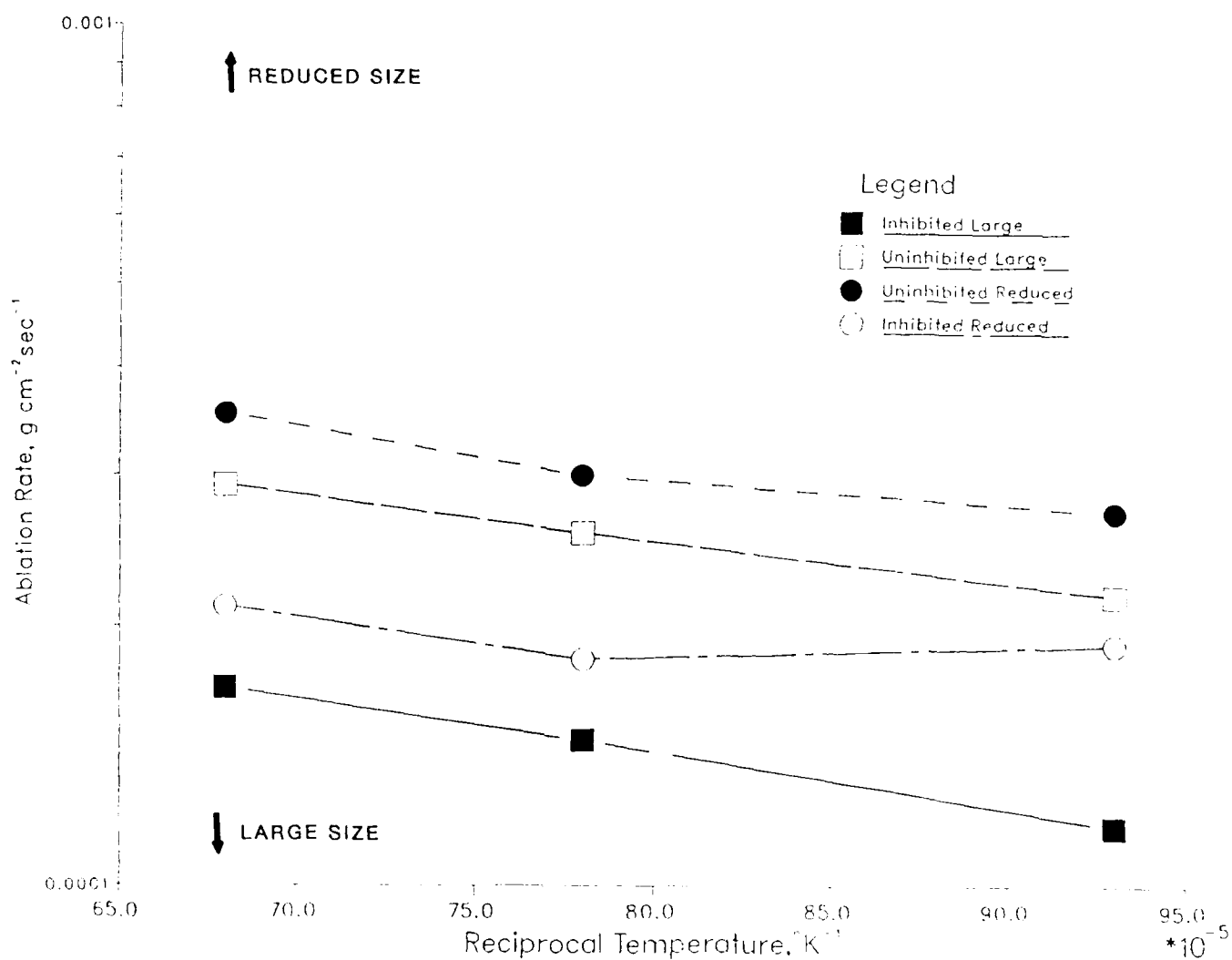


Figure 21. Log oxidation rate (weight loss) vs.  $1/T$  ( $K^{-1}$ ) for uncoated CCC showing the effect of sample size in the diffusion controlled regime.

## BET Measurements of Surface Area on CCC

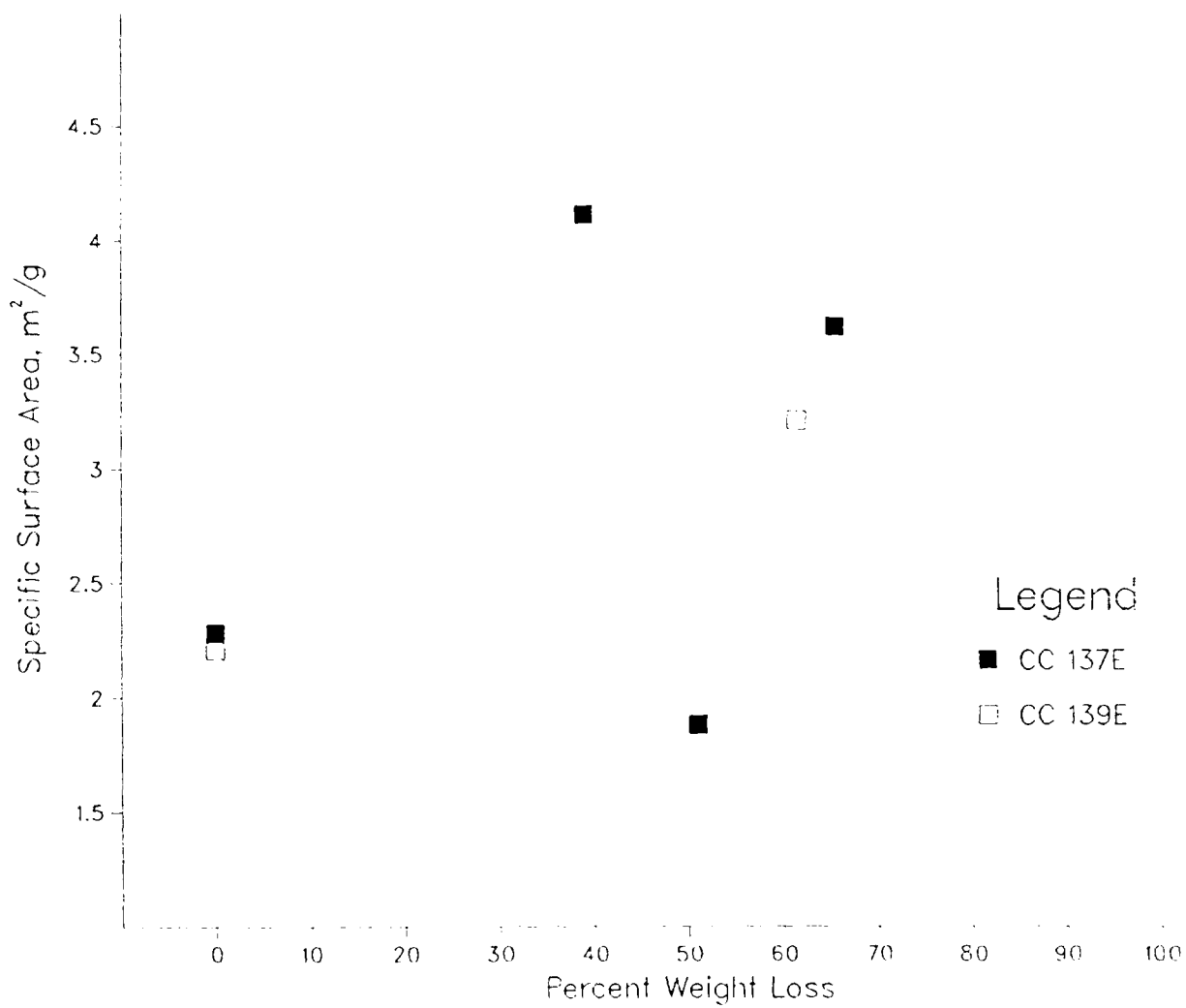


Figure 22. BET measurements of specific surface area for uncoated CCC vs. oxidative weight loss.

# DENSITY CHANGES DURING CARBON CARBON OXIDATION

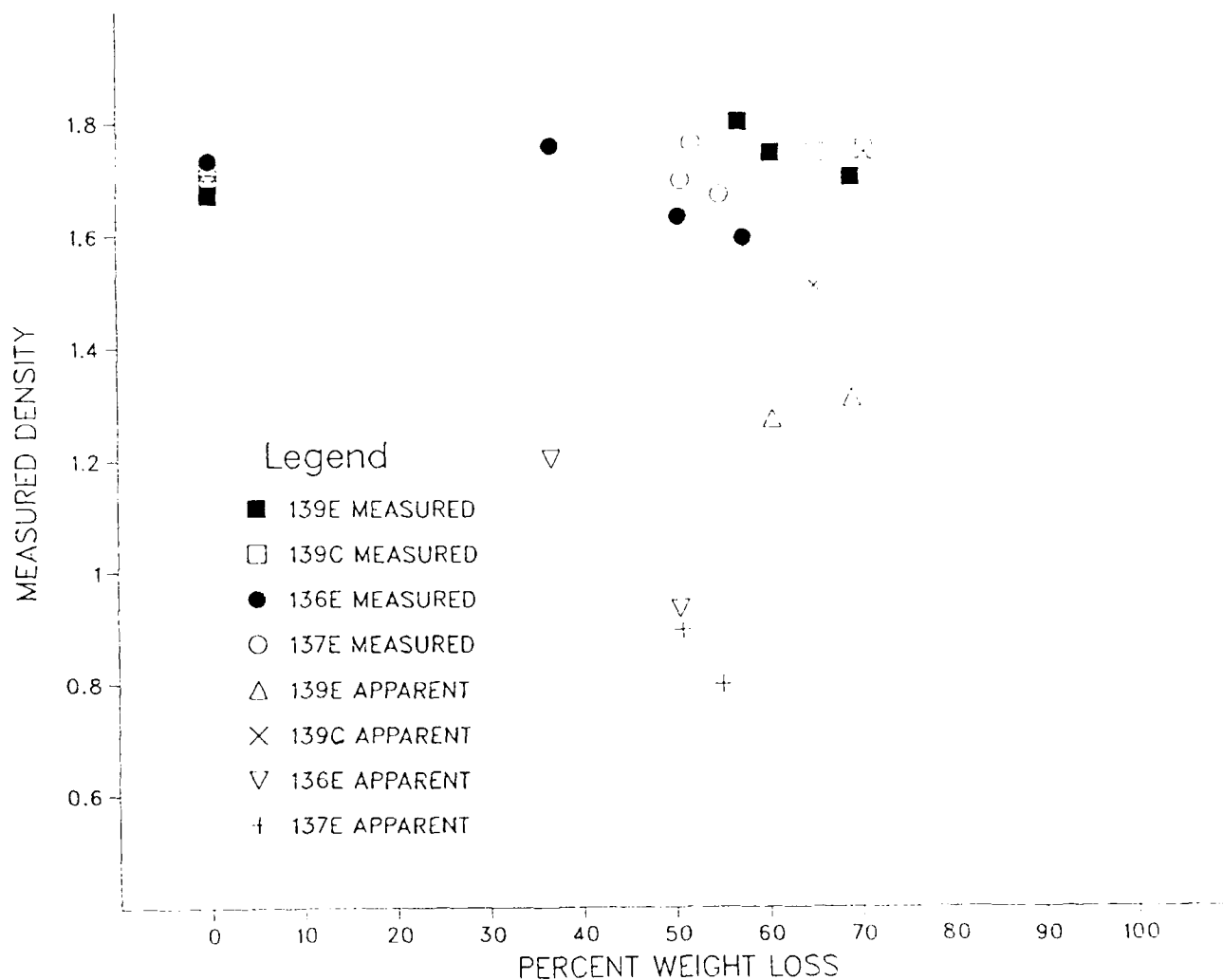


Figure 23. Density measurements of uncoated CCC before and after oxidative weight loss. Apparent density is measured by weighing the sample and dividing by instantaneous bulk volume. Measured density finds the open volume with a He pycnometer. Inhibited composites oxidize with more open porosity.

# CARBON CARBON OXIDATION AT 100 CC/MIN

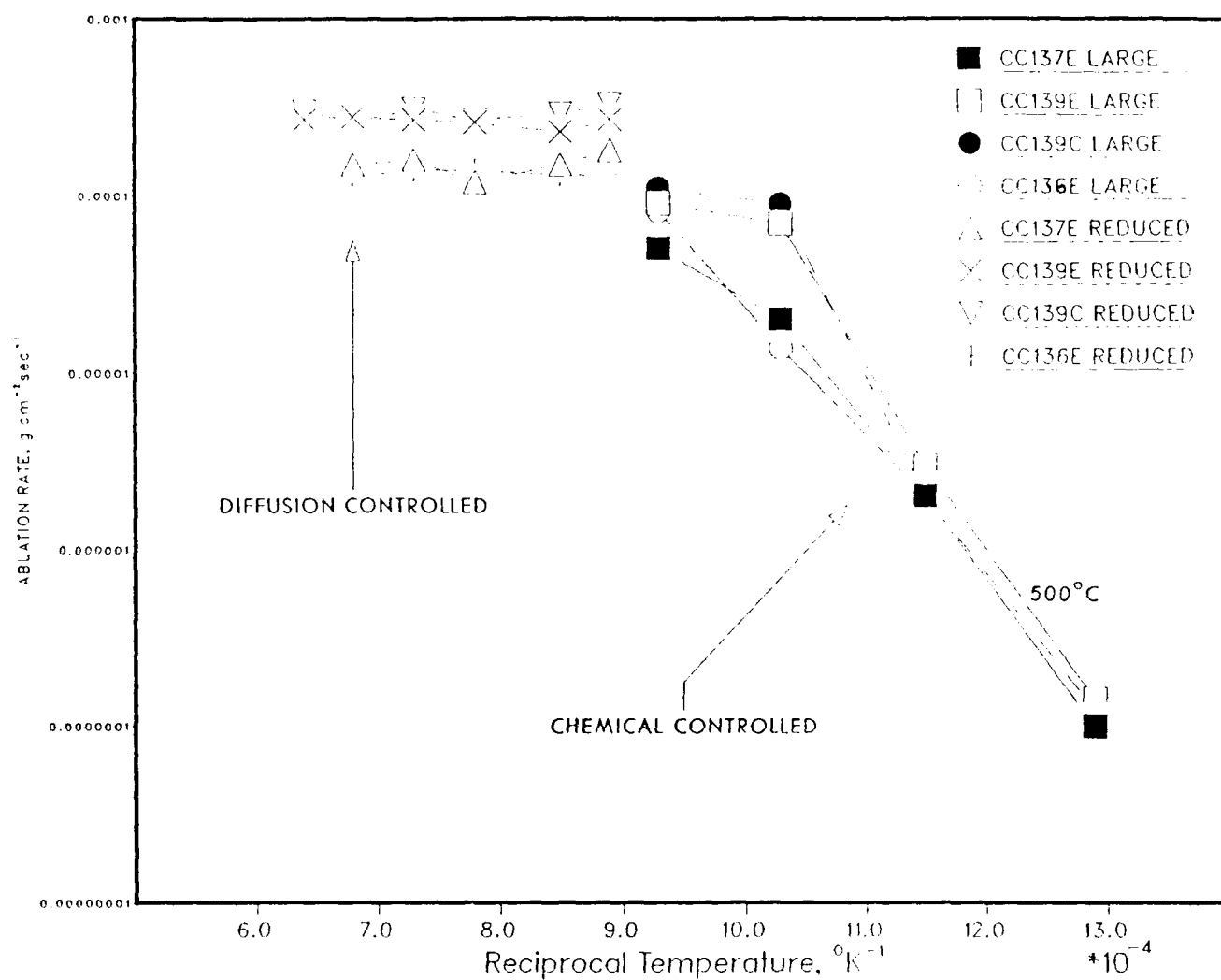


Figure 24. Log oxidation rate (weight loss) vs.  $1/T$  ( $K^{-1}$ ) for samples oxidized in  $O_2$  at 100 cc/min at various temperatures. Diffusion control dominates at high temperatures and surface control dominates at lower temperatures.

# CARBON CARBON OXIDATION at 550 cc/min O<sub>2</sub> and 900°C

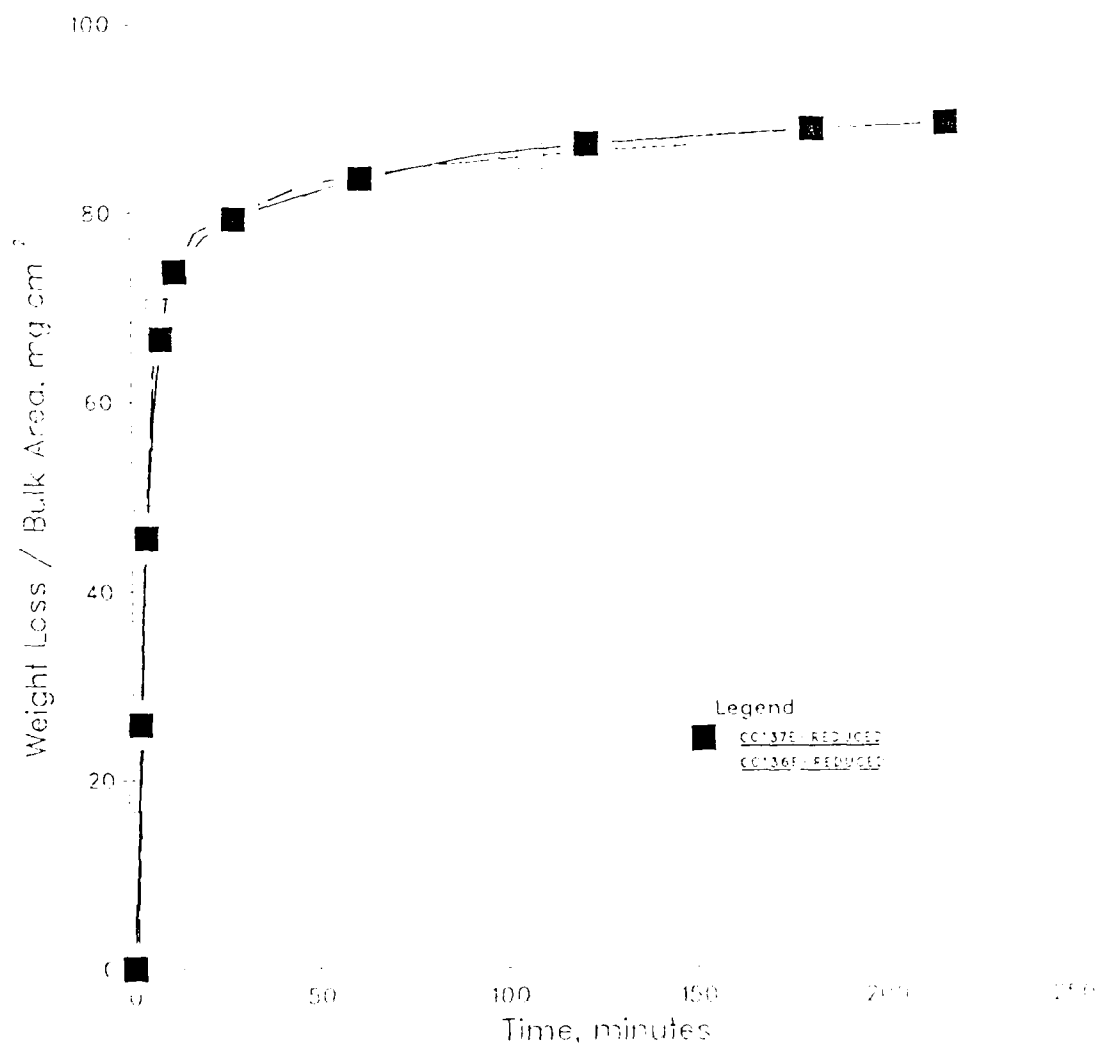


Figure 25. Isothermal oxidation kinetics for inhibited CCC at 900°C in O<sub>2</sub> flowing at 550 cc/min.

# CARBON CARBON OXIDATION at 550 cc/min O<sub>2</sub> and 1100°C

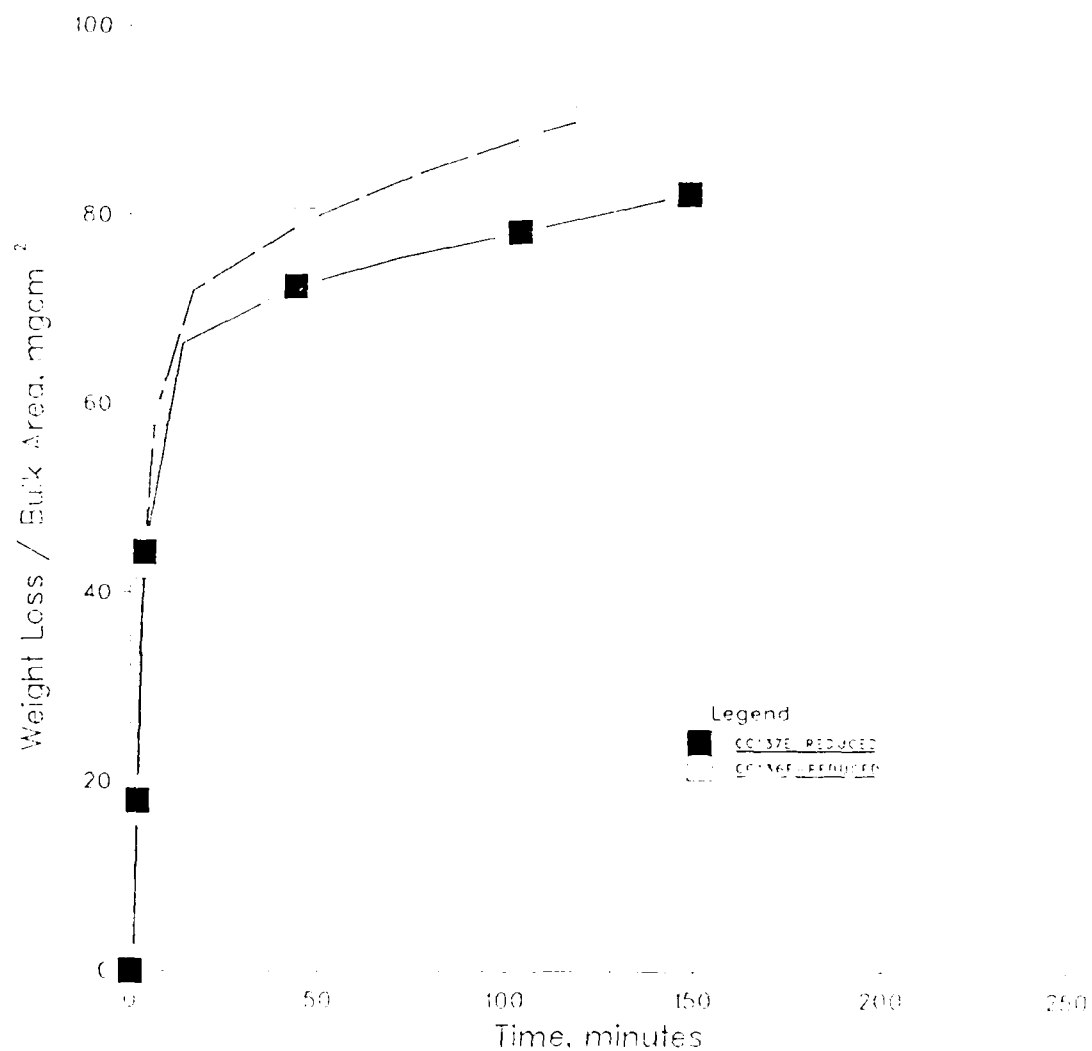


Figure 26. Isothermal oxidation kinetics for inhibited CCC at 1100°C in O<sub>2</sub> flowing at 550 cc/min.

# CARBON CARBON OXIDATION AT 550 cc/min O<sub>2</sub> and 1300°C

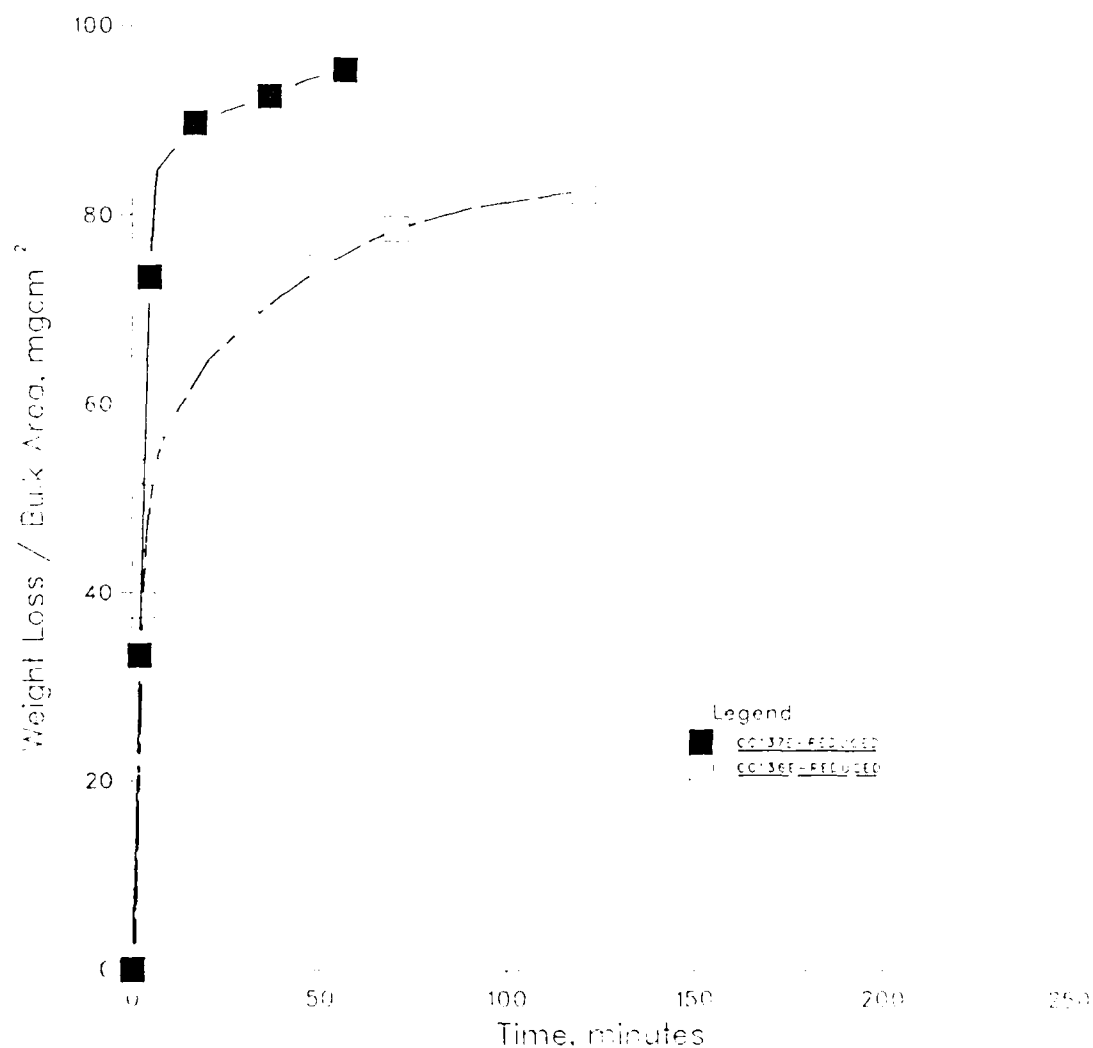


Figure 27. Isothermal oxidation kinetics for inhibited CCC at 1300°C in O<sub>2</sub> flowing at 550 cc/min.



# INHIBITED CARBON CARBON OXIDATION at 550 cc/min

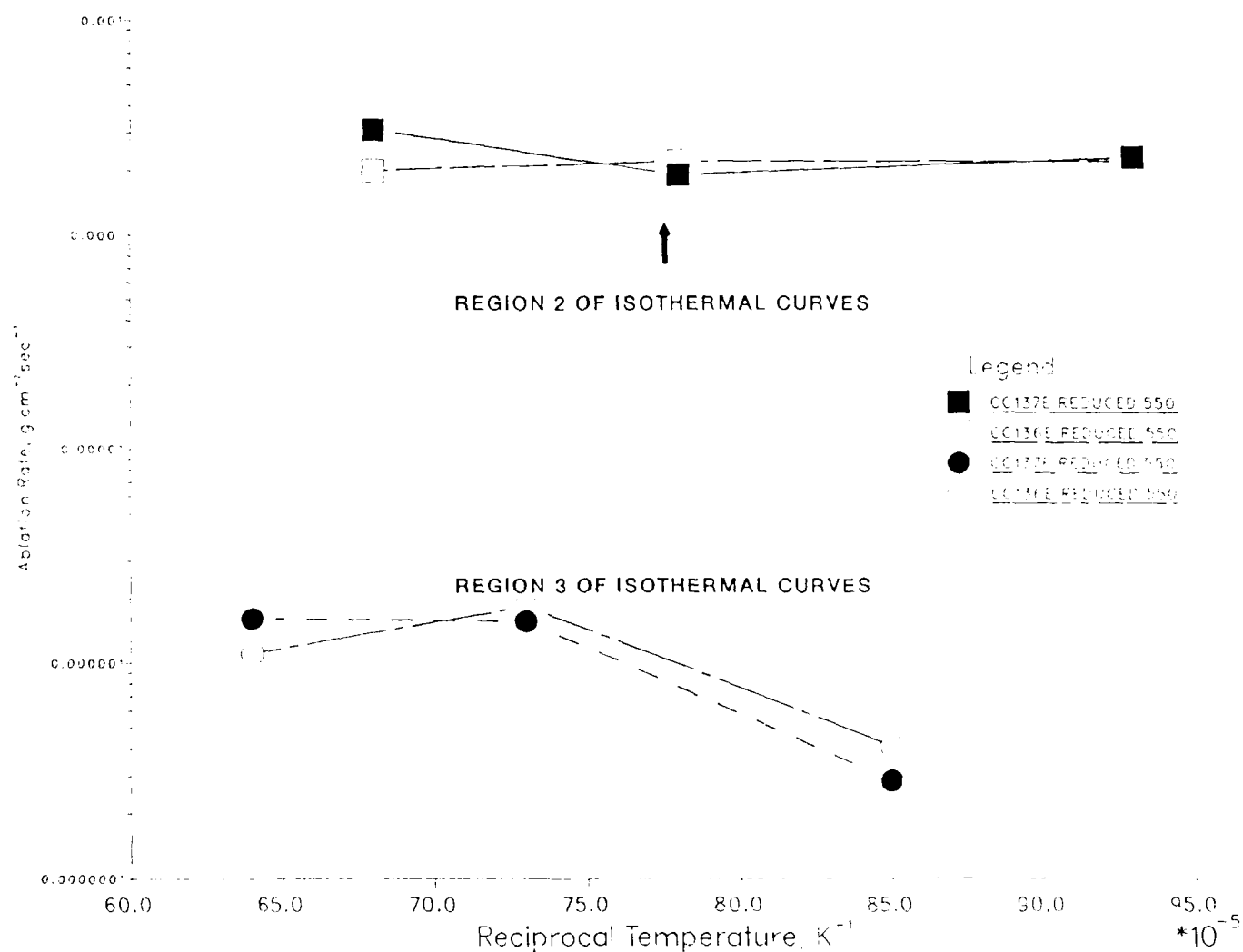


Figure 28. Log oxidative rate (weight loss) for stage 3 vs.  $1/T$  ( $K^{-1}$ ) for samples oxidized in  $O_2$  flowing at 100 cc/min. Oxidation rates for stage 2 are plotted for comparison.

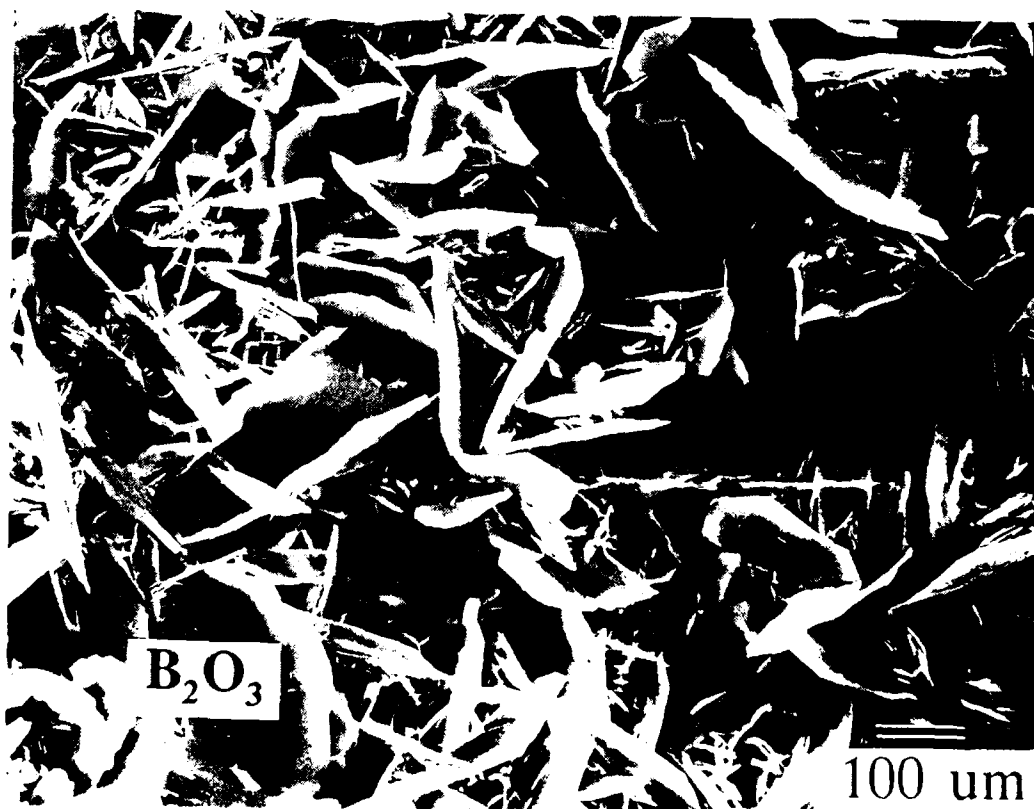


Figure 29. Micrographs show the coating of an inhibited sample by  $B_2O_3$  after large oxidative weight loss.  $B_2O_3$  plates cover the surface of the remaining CCC (bottom).

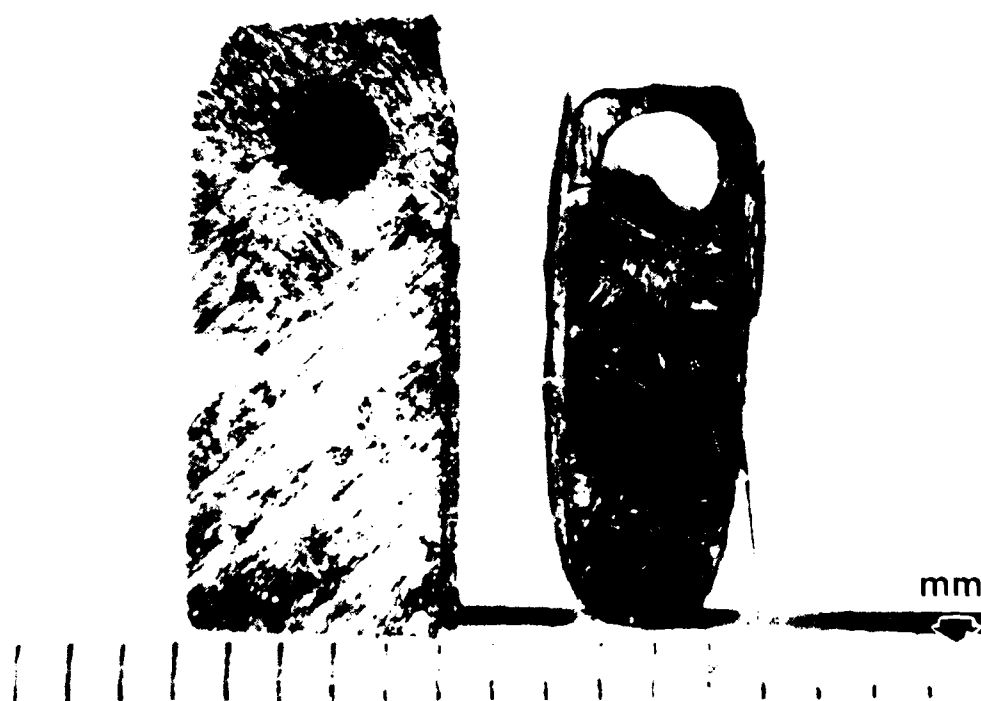
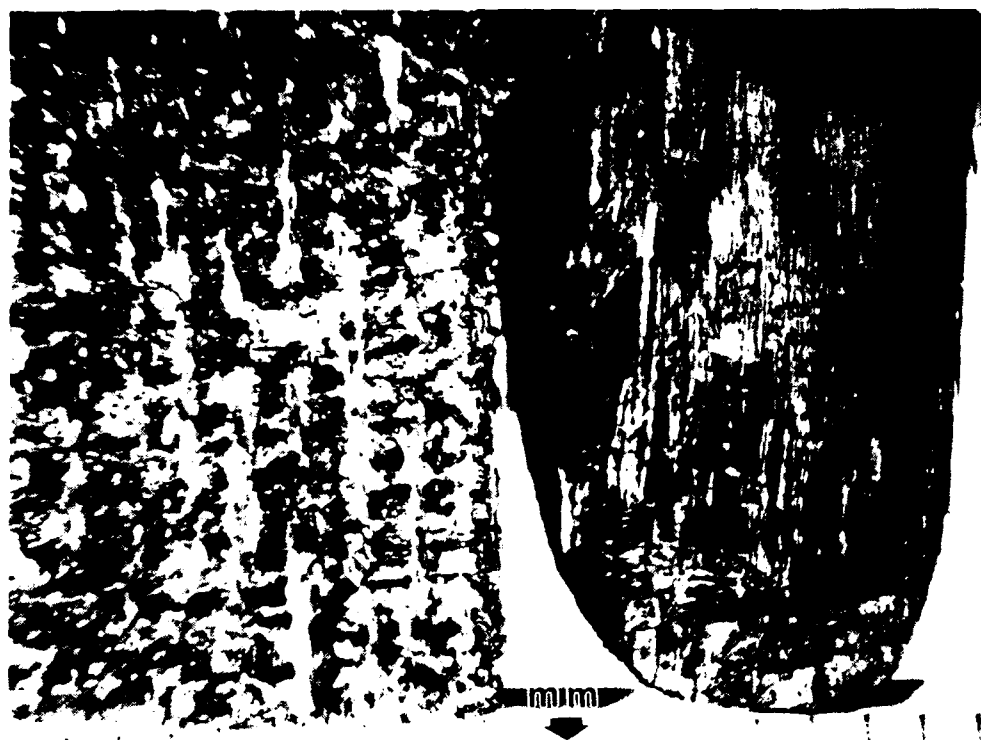


Figure 30. Optical comparison of CC137E (left) and CC139E (right) after isothermal oxidation at 1200°C. The inhibited CCC retains the initial rectangular shape, while the uninhibited CCC shows attack at the leading edge.

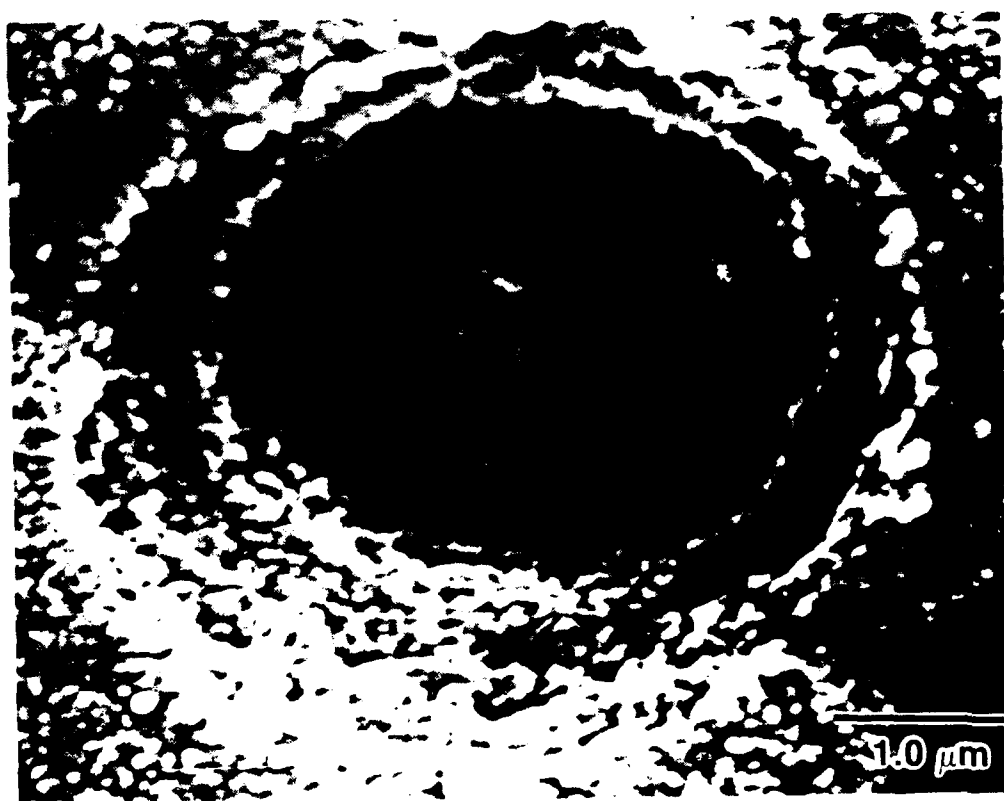
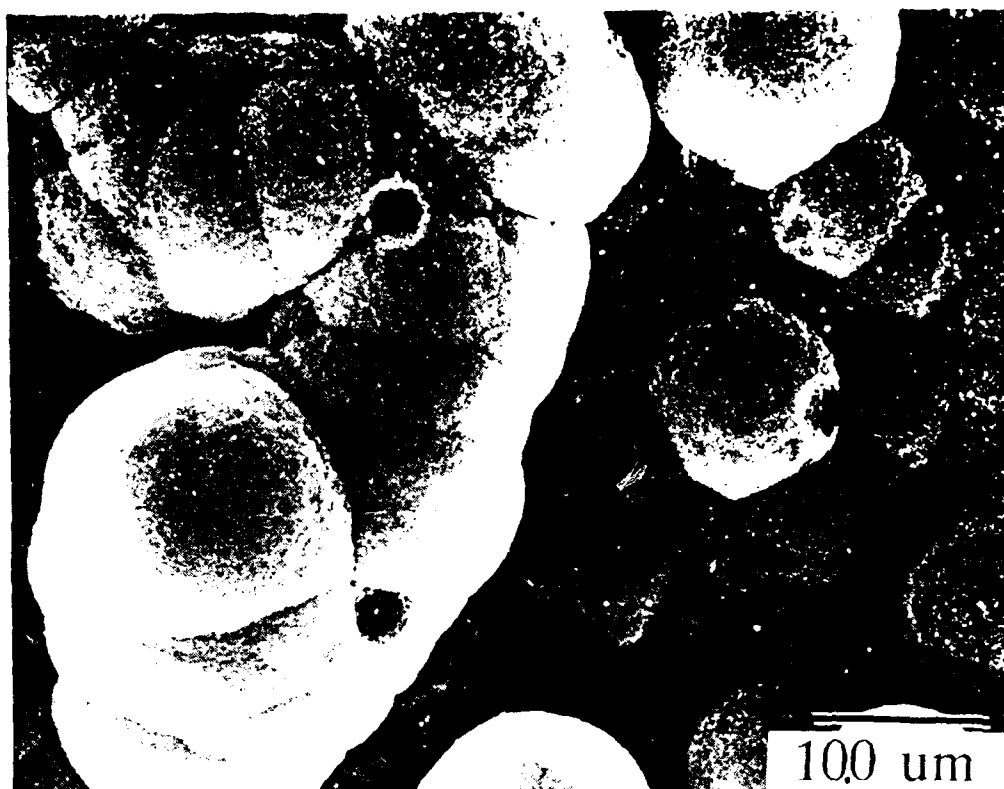


Figure 31. Micrographs show the beginning of the pits on CC137F after a 7% weight loss at 525°C. The bottom shows a particle at the bottom of one of the pits.

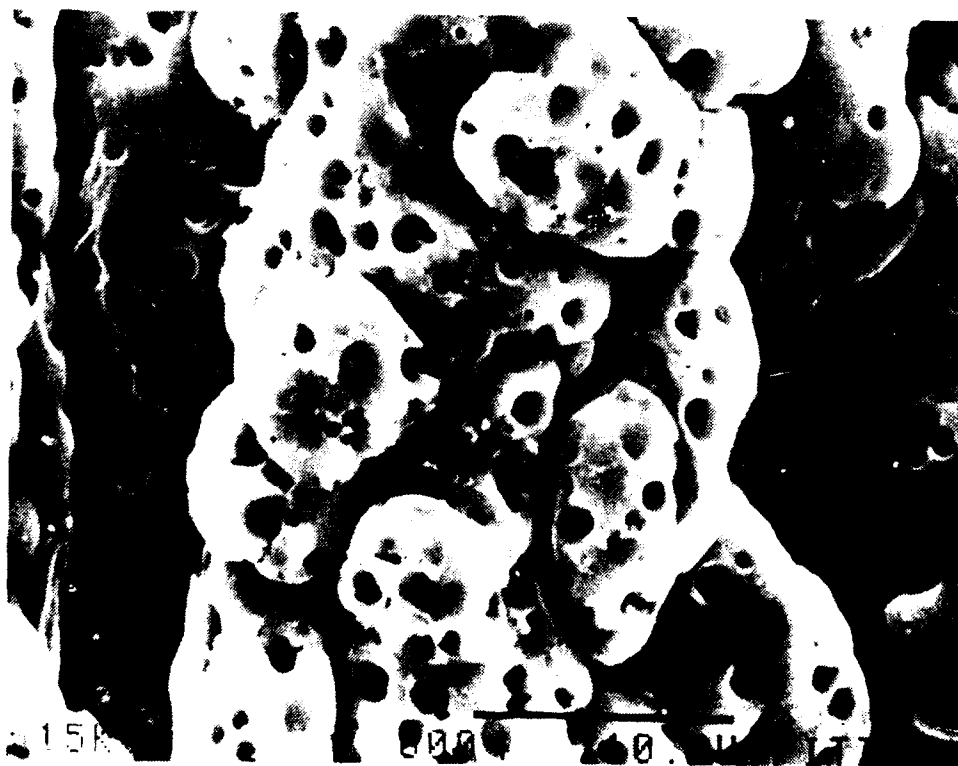


Figure 32. Mature pitted morphology on CC139E after isothermal oxidation at 600°C in O<sub>2</sub> flowing at 100 cc/min.

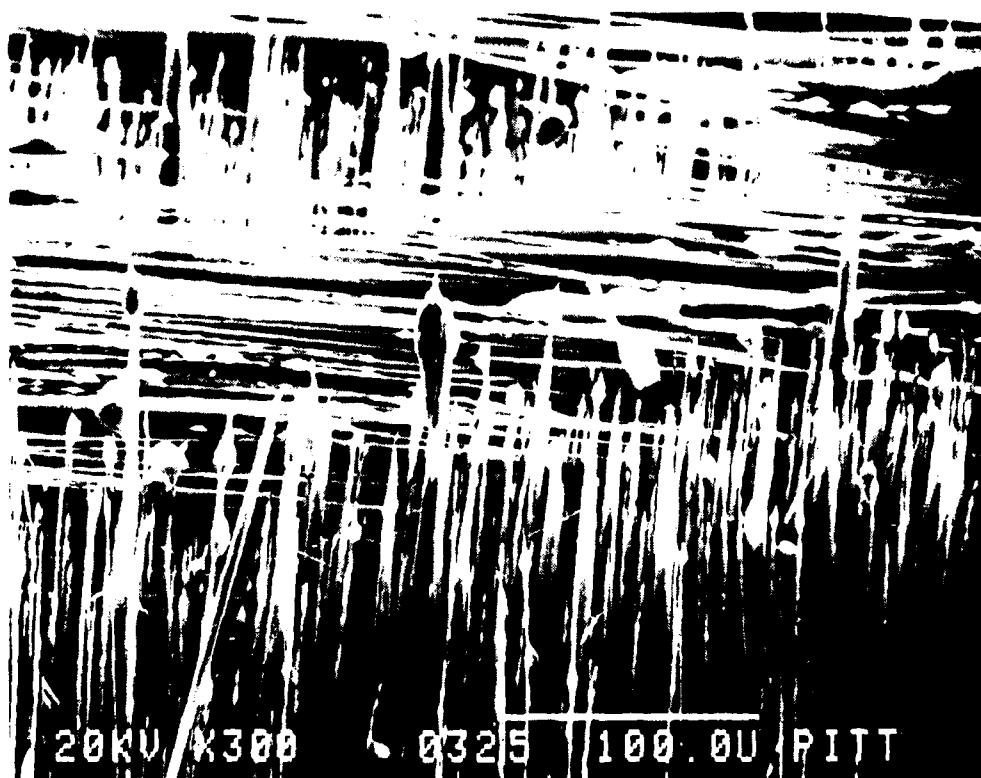
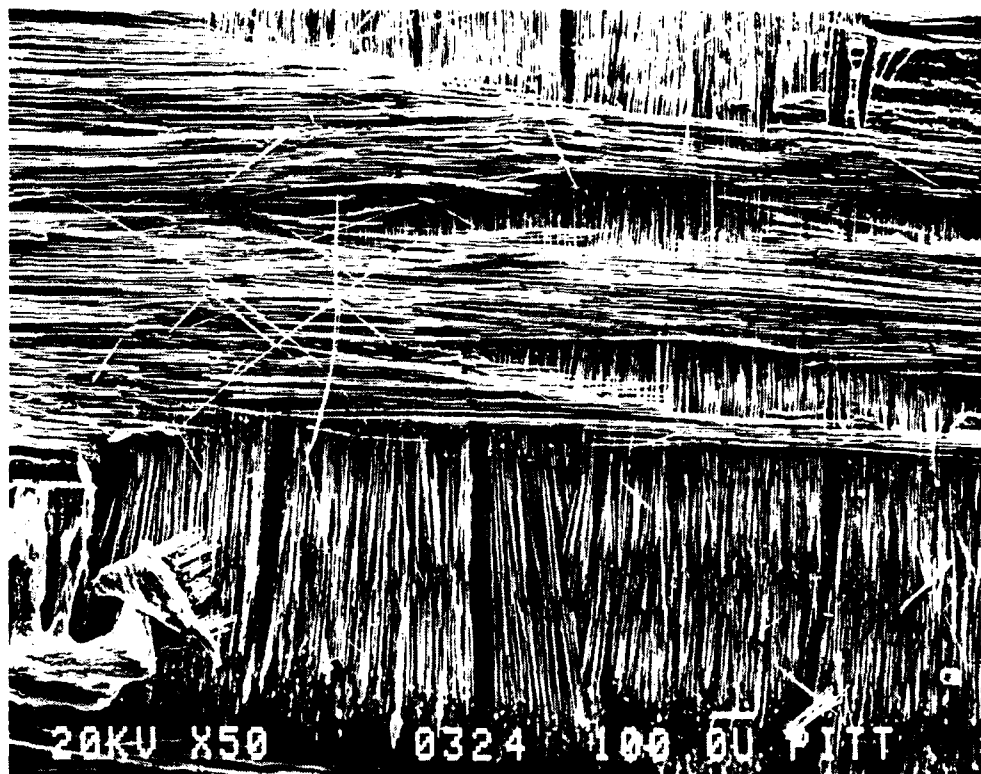


Figure 33. Thatched hut structure of CCl<sub>3</sub>9E after isothermal oxidation at 1100°C in O<sub>2</sub> flowing at 100 cc/min. Individual fibers are discernible.



Figure 34. Micrographs of CC139E after oxidation at 950°C in O<sub>2</sub> flowing at 14 cc/min.

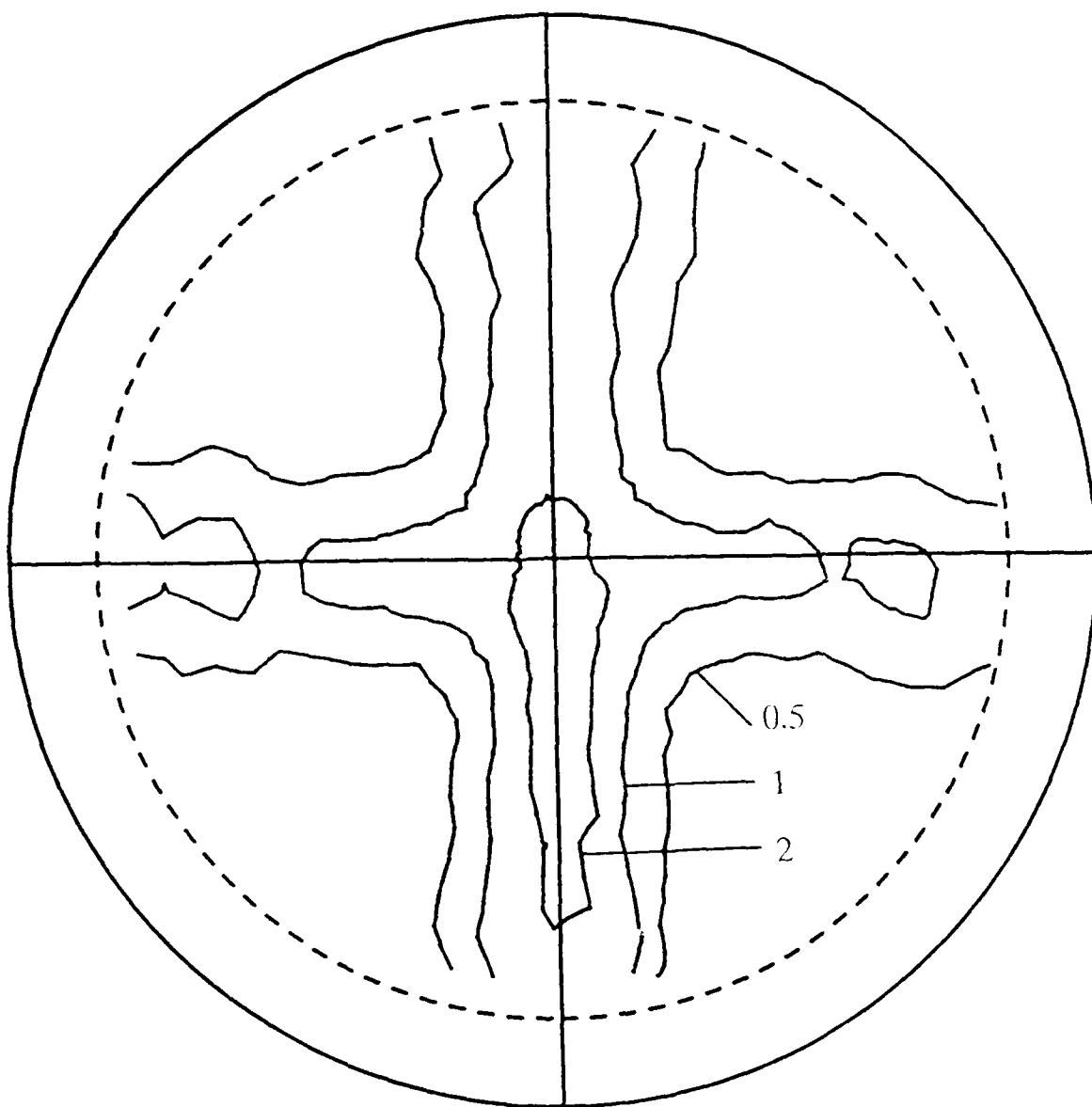


Figure 35. X-ray pole figure of (002) basal planes after oxidation in air for 2 days at 625°C. The pole figure still shows a "cross" pattern as a result of the fibers (see figure 10). The numbers on the contours indicate the intensity of the sample compared to a random sample.



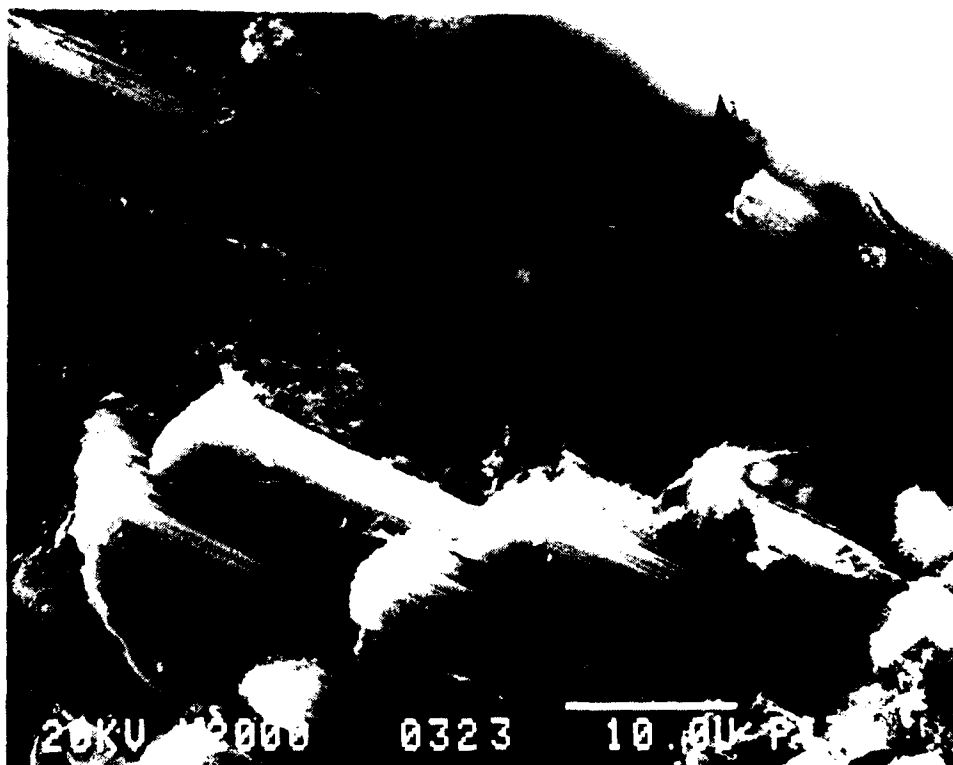
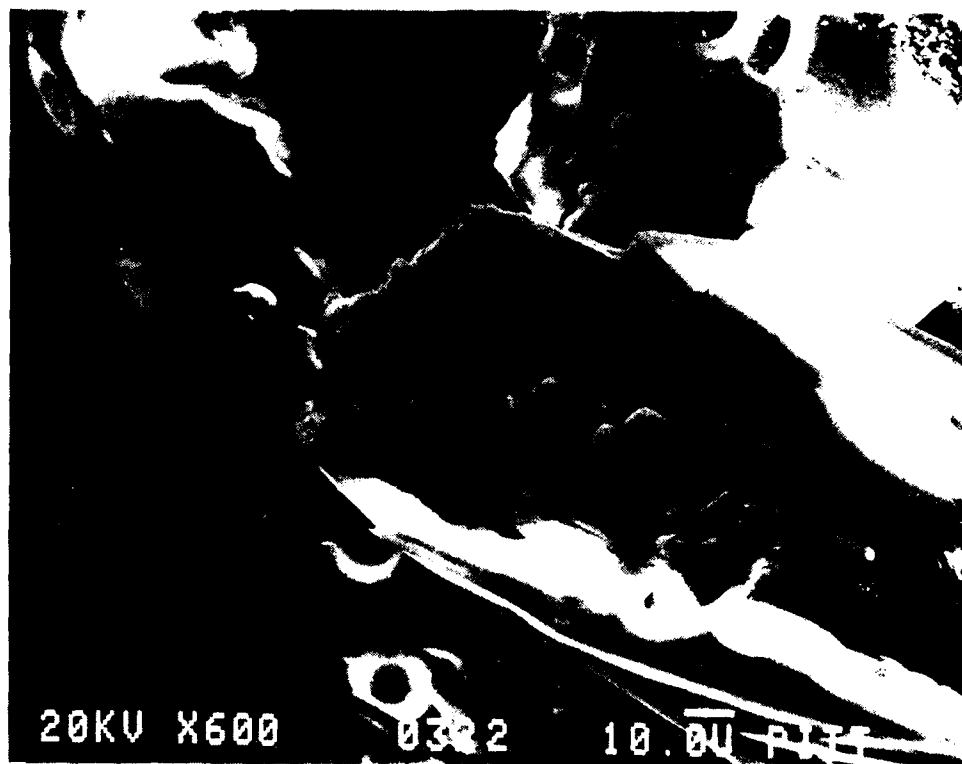


Figure 36. Boron oxide coats a bundle of fibers in CC137E after oxidation at 1100°C in O<sub>2</sub>. The top shows a cross section of a fiber bundle. The bottom shows the fiber and matrix coated by the B<sub>2</sub>O<sub>3</sub>.



Figure 37. Boron oxide coats fiber regions of CC136E after isothermal oxidation at 1100°C in O<sub>2</sub> flowing at 100 cc/min. The bottom shows cracking of the B<sub>2</sub>O<sub>3</sub> after cool down to room temperature.

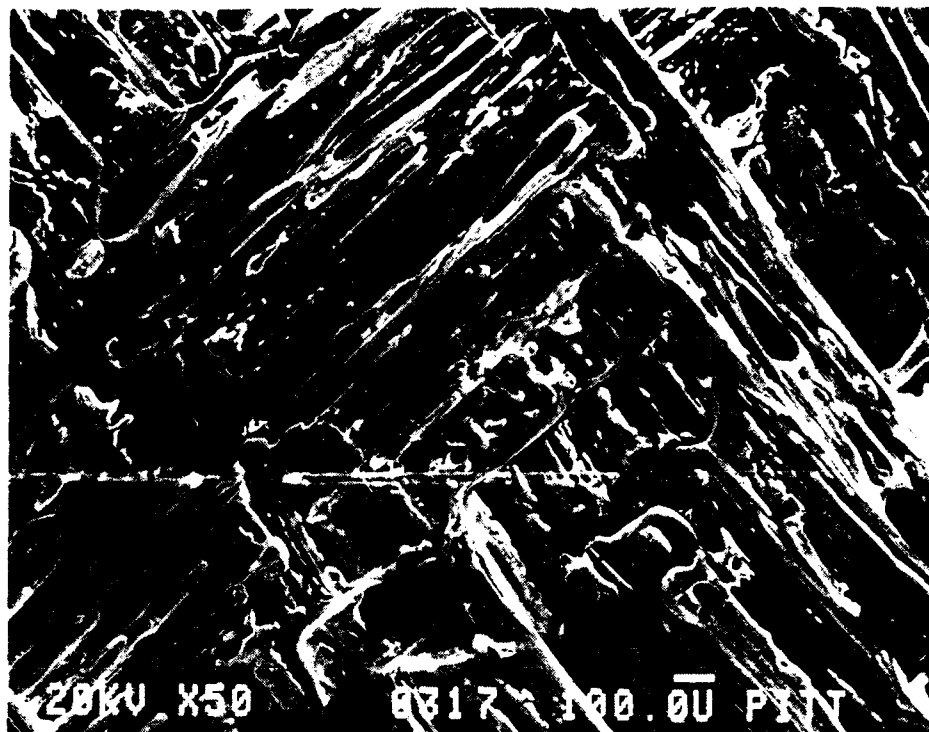


Figure 38. Micrographs of CC137E after isothermal oxidation at 1100°C in O<sub>2</sub> at 100 cc/min. The top shows boron oxide coating the CCC, while the bottom shows a B<sub>2</sub>O<sub>3</sub> globule.

# CC 137E OXIDATION AT 400°C AND 100 CC/MIN GAS FLOW

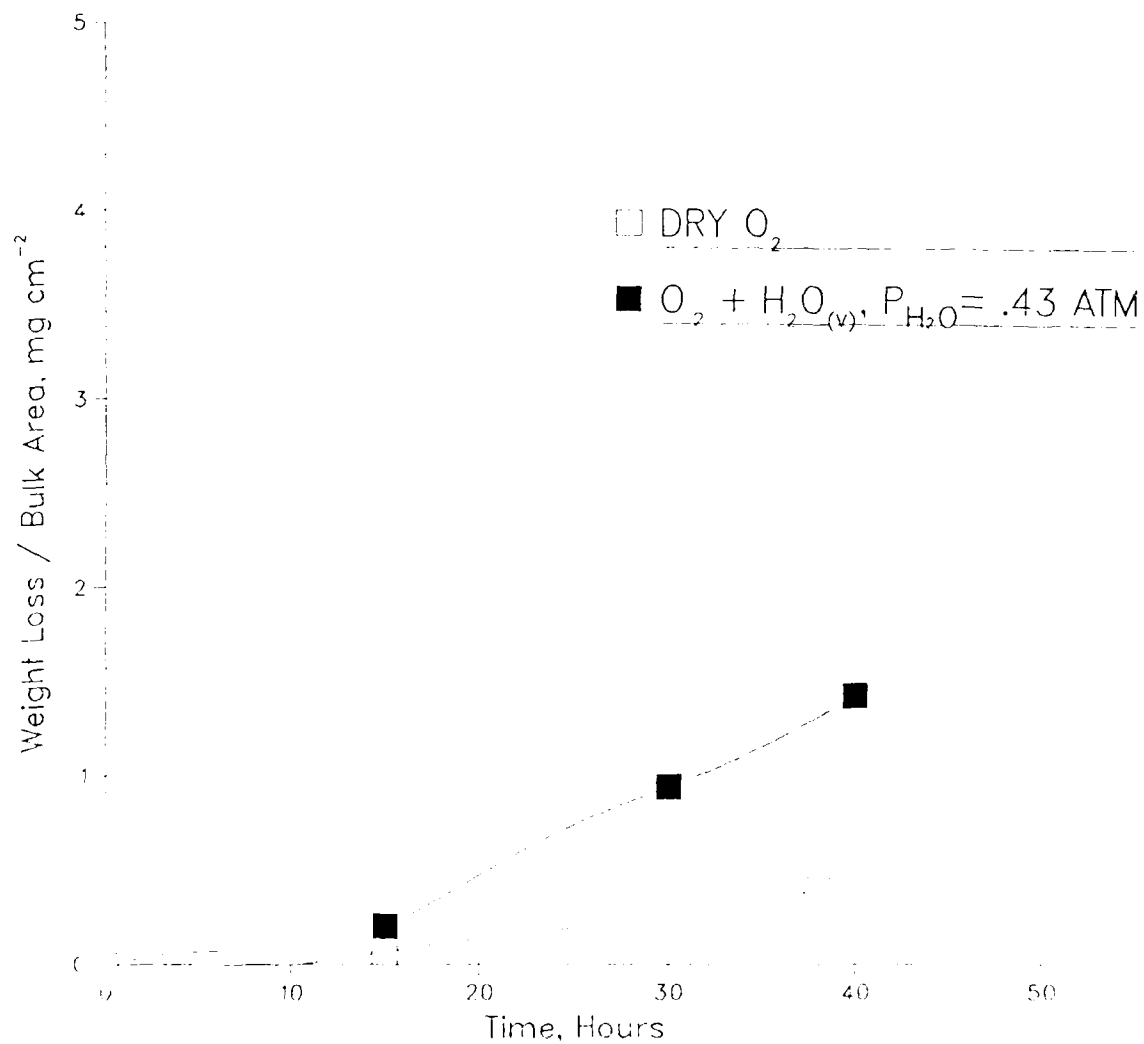


Figure 39. Oxidation kinetics for inhibited CCC at 400°C in flowing oxygen and oxygen-water vapor atmospheres.

# CC 137E OXIDATION AT 500°C AND 100 CC/MIN GAS FLOW

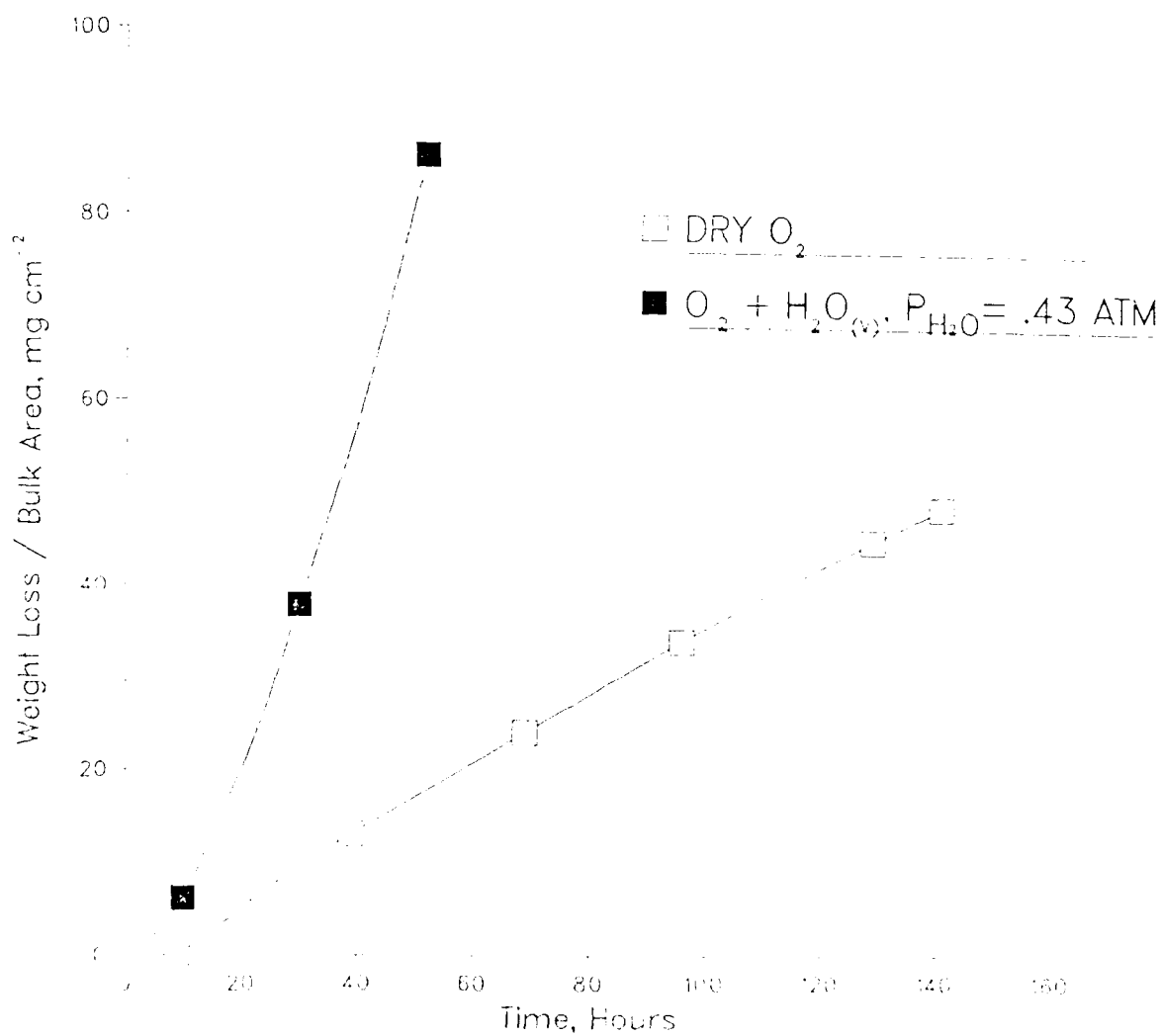


Figure 40. Oxidation kinetics for inhibited CCC at 500°C in flowing oxygen and oxygen-water vapor atmospheres.

# CC 137E OXIDATION AT 600°C AND 100 CC/MIN GAS FLOW

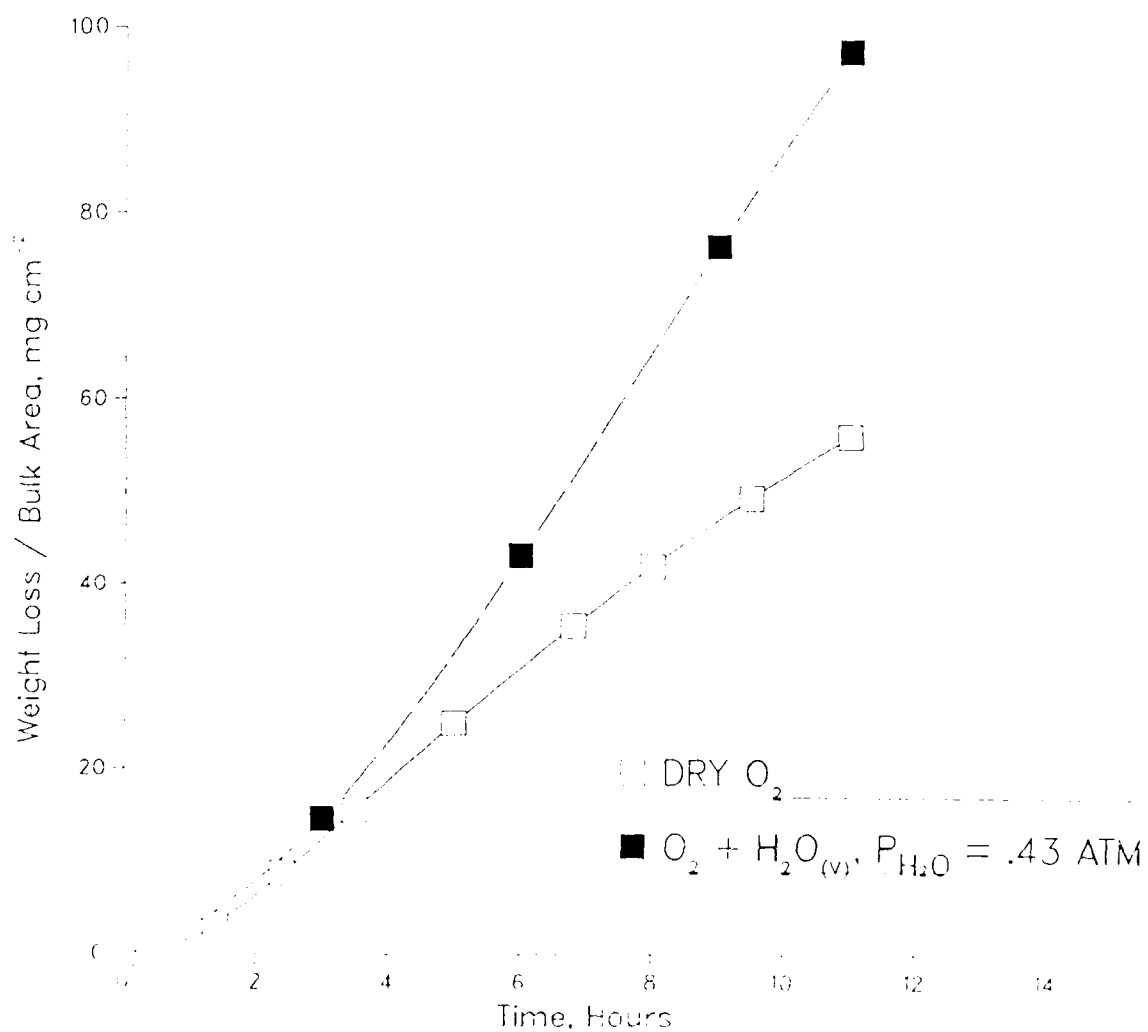


Figure 41. Oxidation kinetics for inhibited CCC at 600°C in flowing oxygen and oxygen-water vapor atmospheres.

# CC 137E OXIDATION AT 700°C AND 100 CC/MIN GAS FLOW

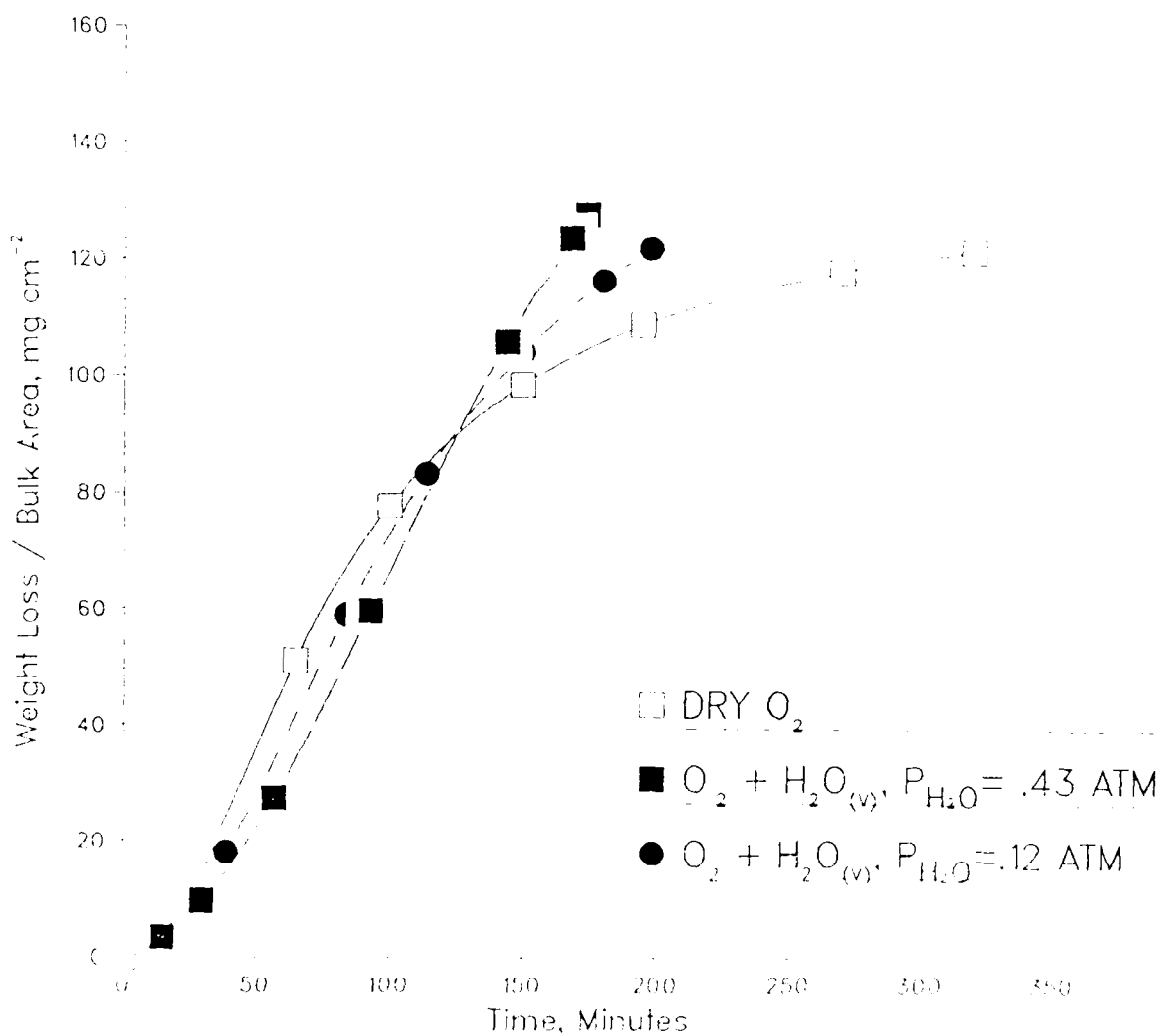


Figure 42. Oxidation kinetics for inhibited CCC at 700°C in flowing oxygen and oxygen-water vapor atmospheres.

# CC 137E OXIDATION AT 800°C AND 100 CC/MIN GAS FLOW

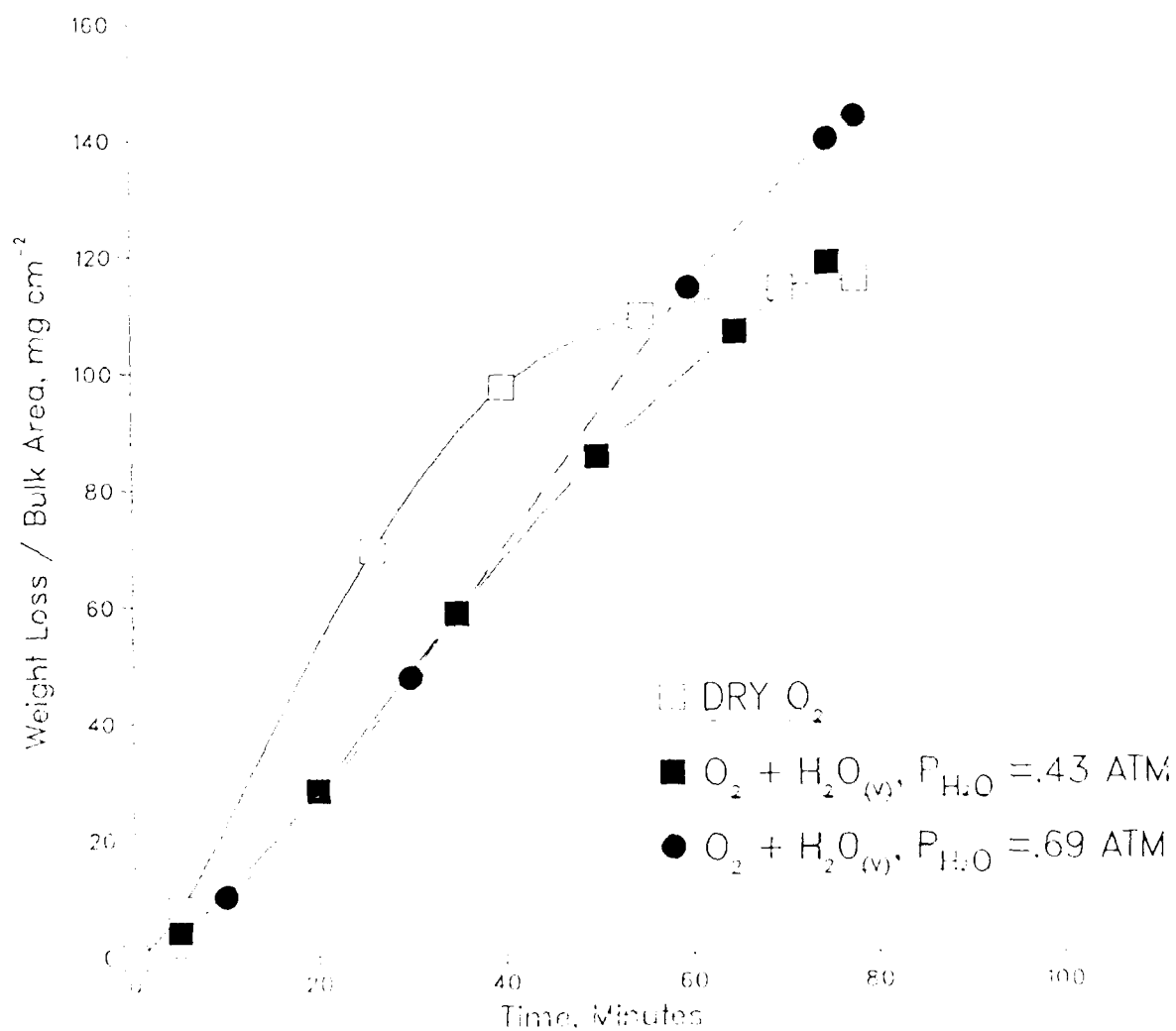


Figure 43. Oxidation kinetics for inhibited CCC at 800°C in flowing oxygen and oxygen-water vapor atmospheres.



# CC 137E OXIDATION AT 900°C AND 100 CC/MIN GAS FLOW

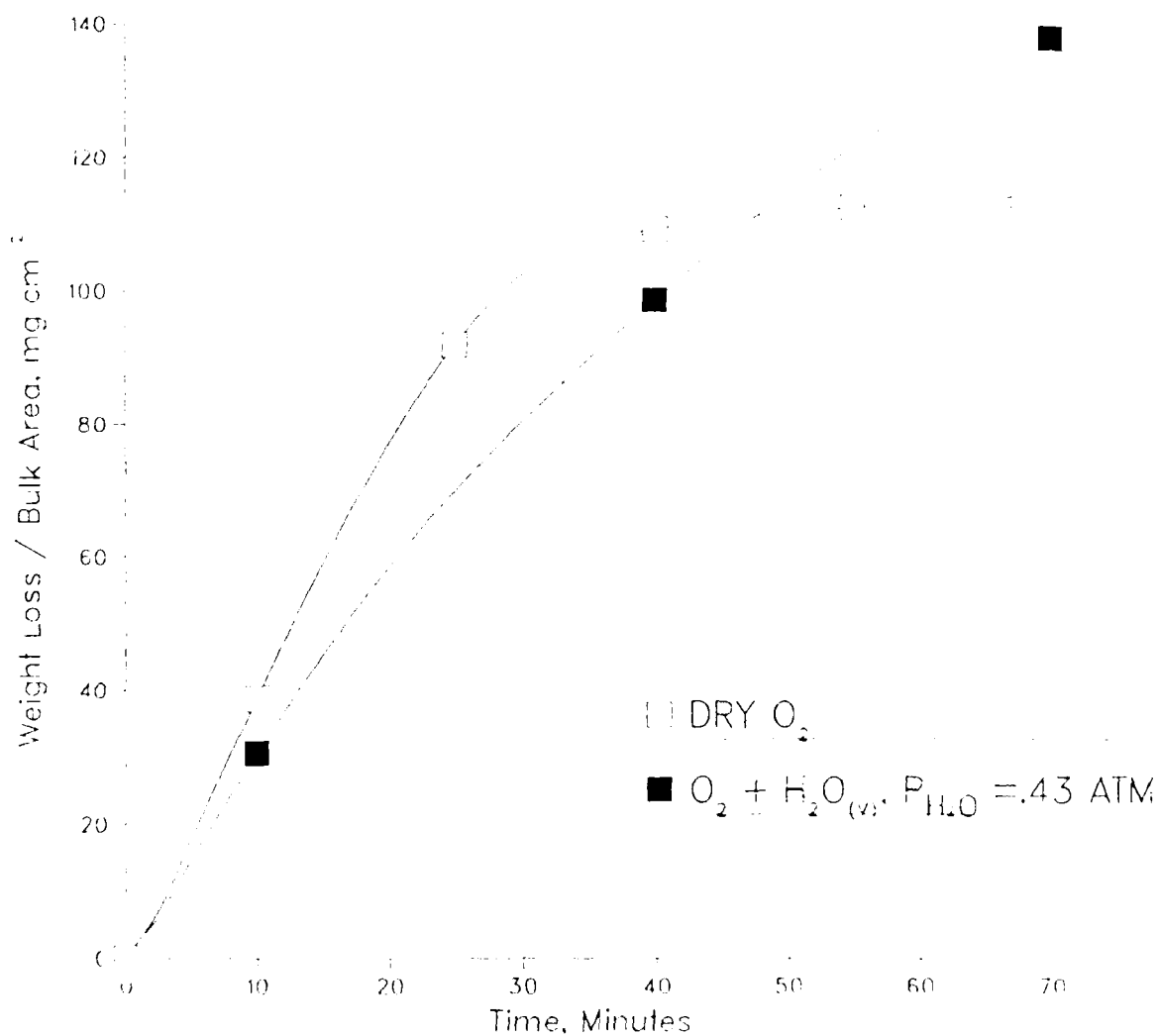


Figure 44. Oxidation kinetics for inhibited CCC at 900°C in flowing oxygen and oxygen-water vapor atmospheres.

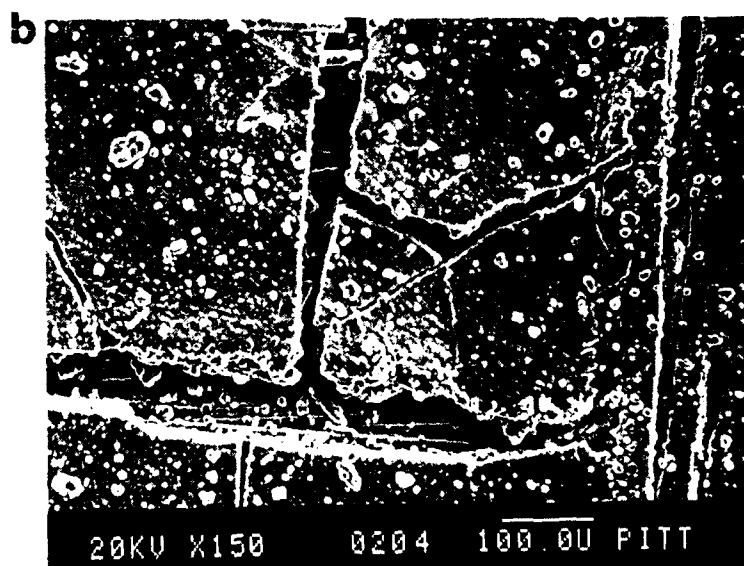
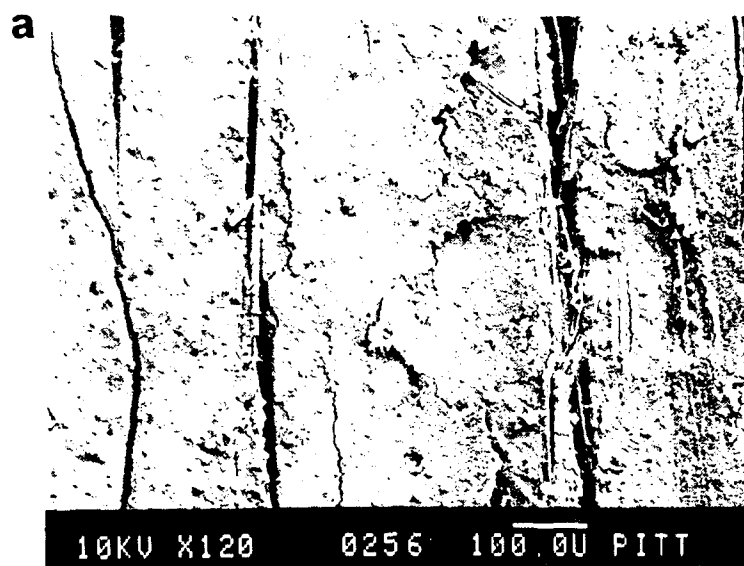
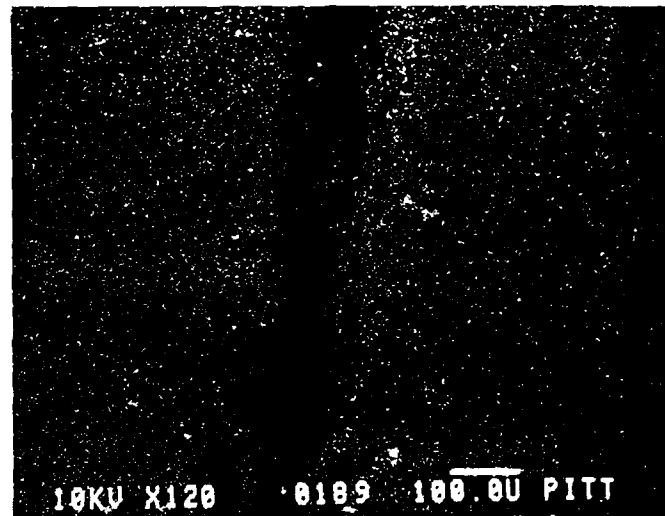
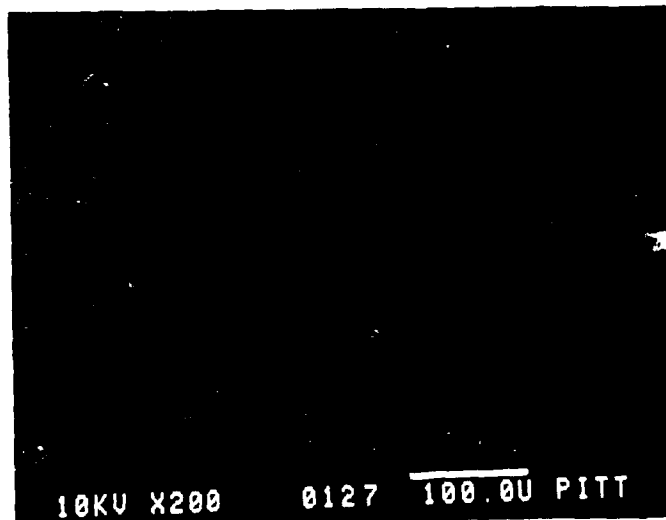
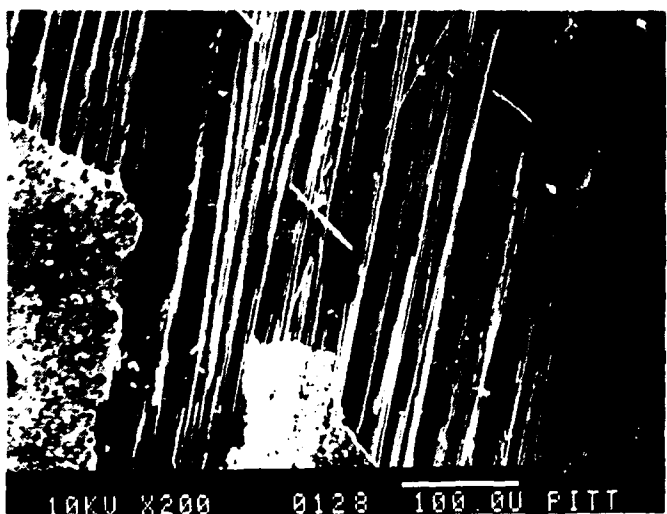


Figure 45. Surface morphologies of inhibited CCC after 12 hours of oxidation at 600°C in a) dry oxygen and b) oxygen-water vapor. Minor pitting is seen in the top micrograph.

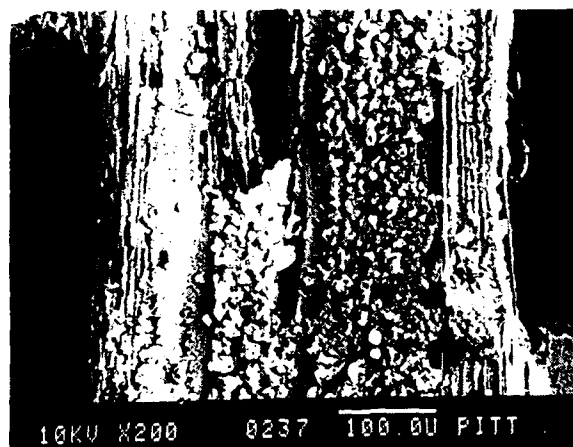


a

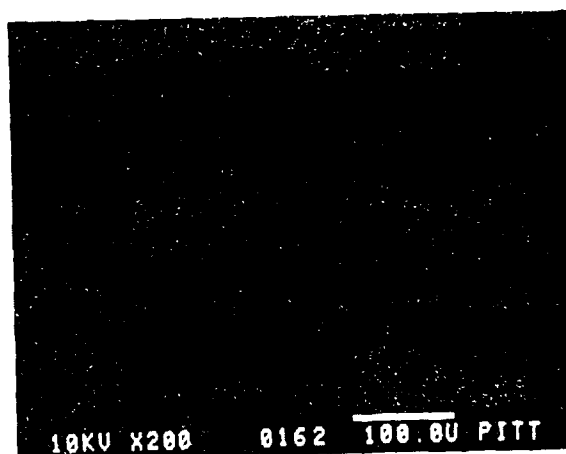


b

Figure 46. Surface morphologies and accompanying WDS boron maps of inhibited CCC after exposure at 700°C to a) dry oxygen (6 hours) and b) oxygen-water vapor (3 hours). Large scale boron oxide loss is observed after longer exposures to oxygen-water vapor at  $T > 700^{\circ}\text{C}$ .



a



b

Figure 47. Surface morphologies and accompanying WDS boron maps of inhibited CCC after exposure at 900°C to a) dry oxygen (68 min.) and b) oxygen-water vapor (68 min.). Shorter exposures to oxygen-water atmospheres result in larger amounts of boron oxide being retained on the surface.

# CC139E OXIDATION AT 500°C AND 100 CC/MIN GAS FLOW

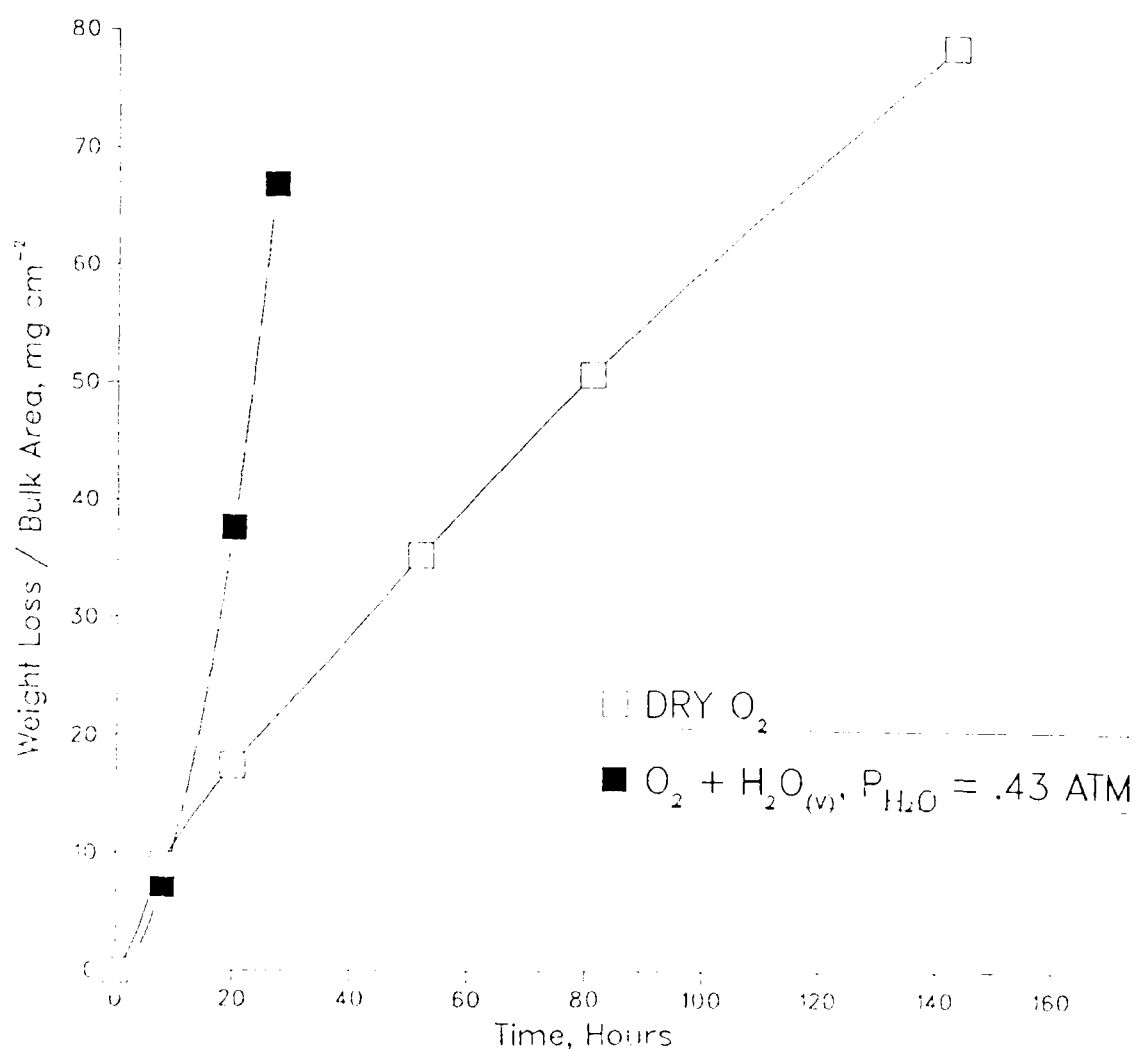


Figure 48. Oxidation kinetics for uninhibited CCC at 500°C in flowing oxygen and oxygen-water vapor atmospheres.

# CC 139E OXIDATION AT 700°C AND 100 CC/MIN GAS FLOW

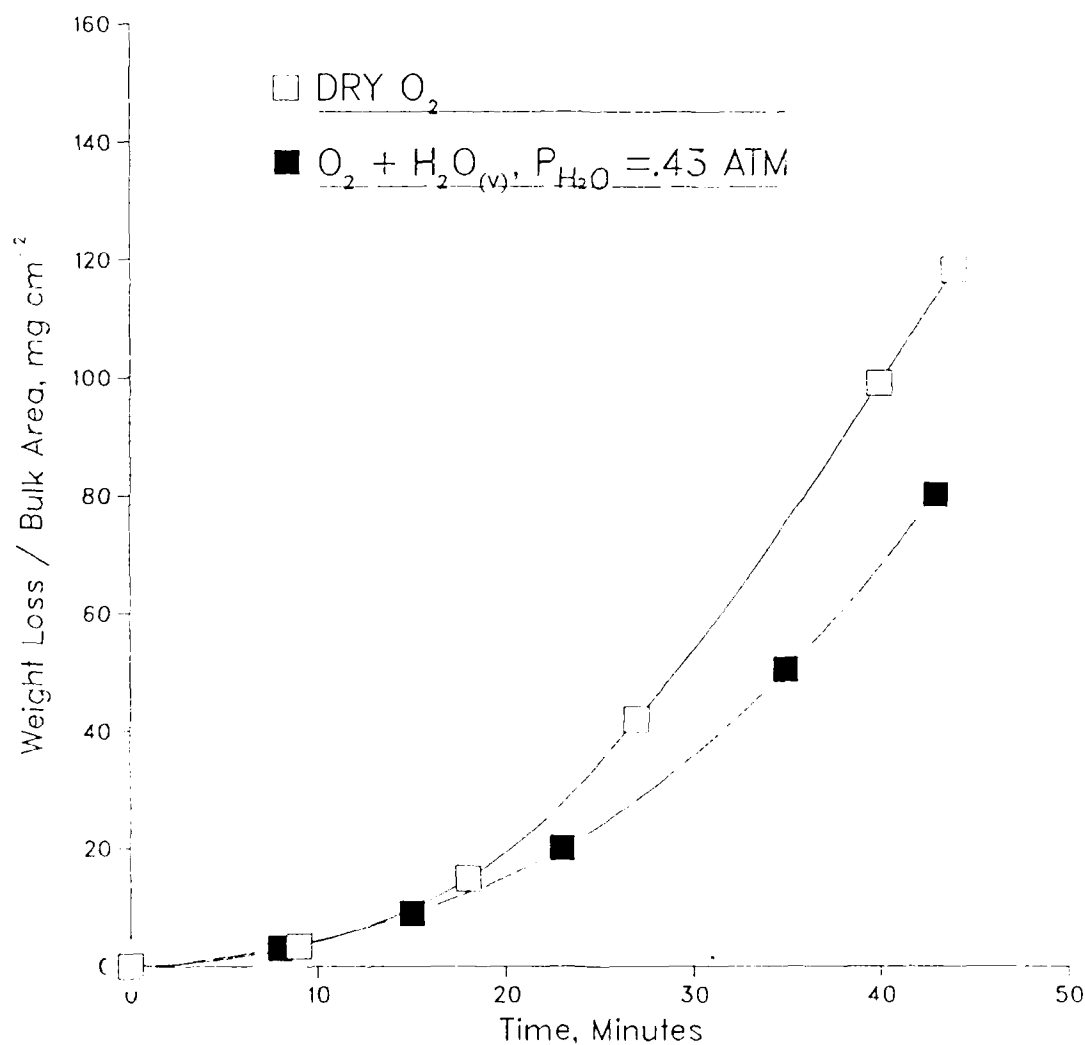


Figure 49. Oxidation kinetics for uninhibited CCC at 700°C in flowing oxygen and oxygen-water vapor atmospheres.

# CC 139E OXIDATION AT 800° AND 100 CC/MIN GAS FLOW

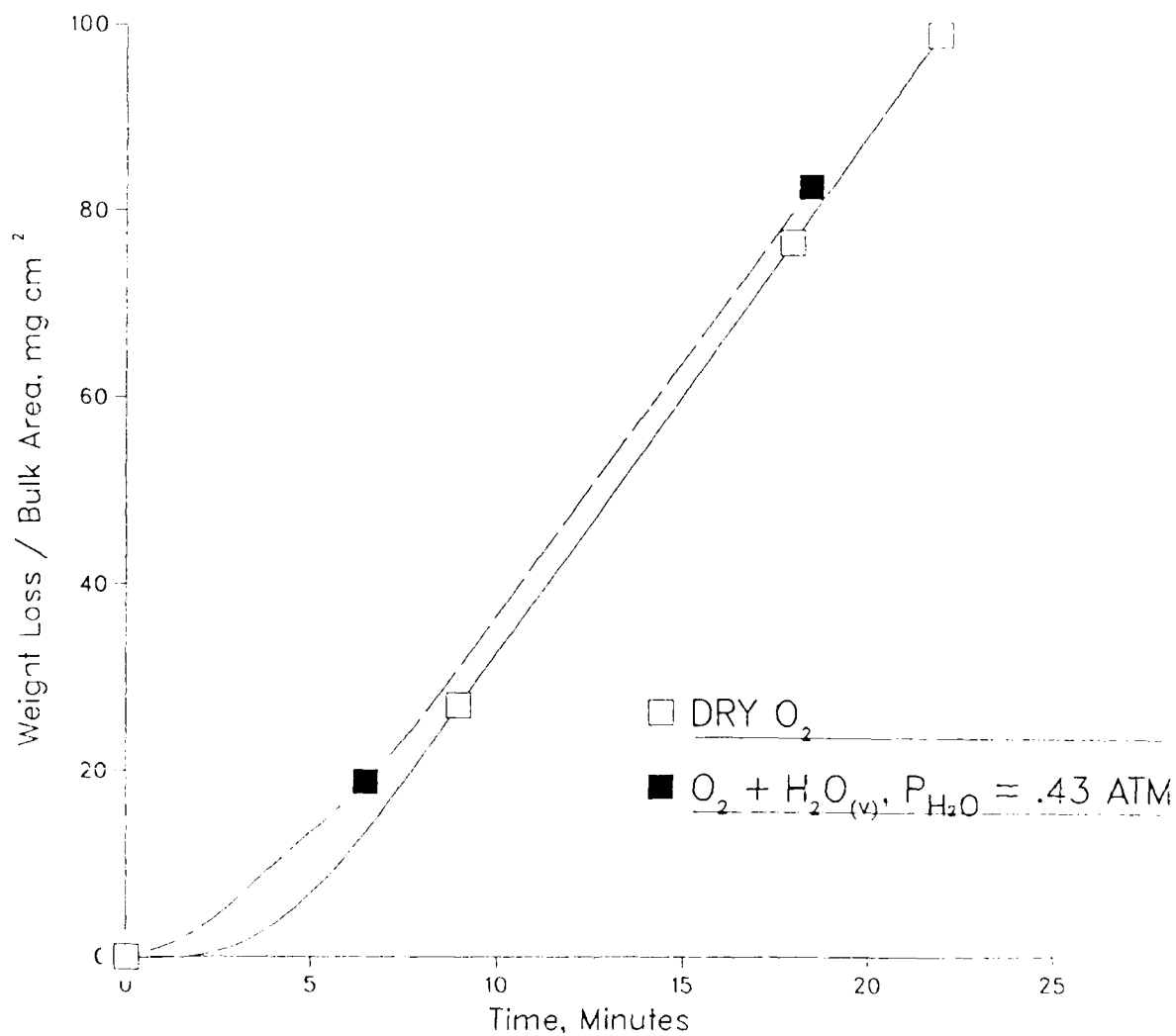


Figure 50. Oxidation kinetics for uninhibited CCC at 800°C in flowing oxygen and oxygen-water vapor atmospheres.

# CC 139E OXIDATION AT 900°C AND 100 CC/MIN GAS FLOW

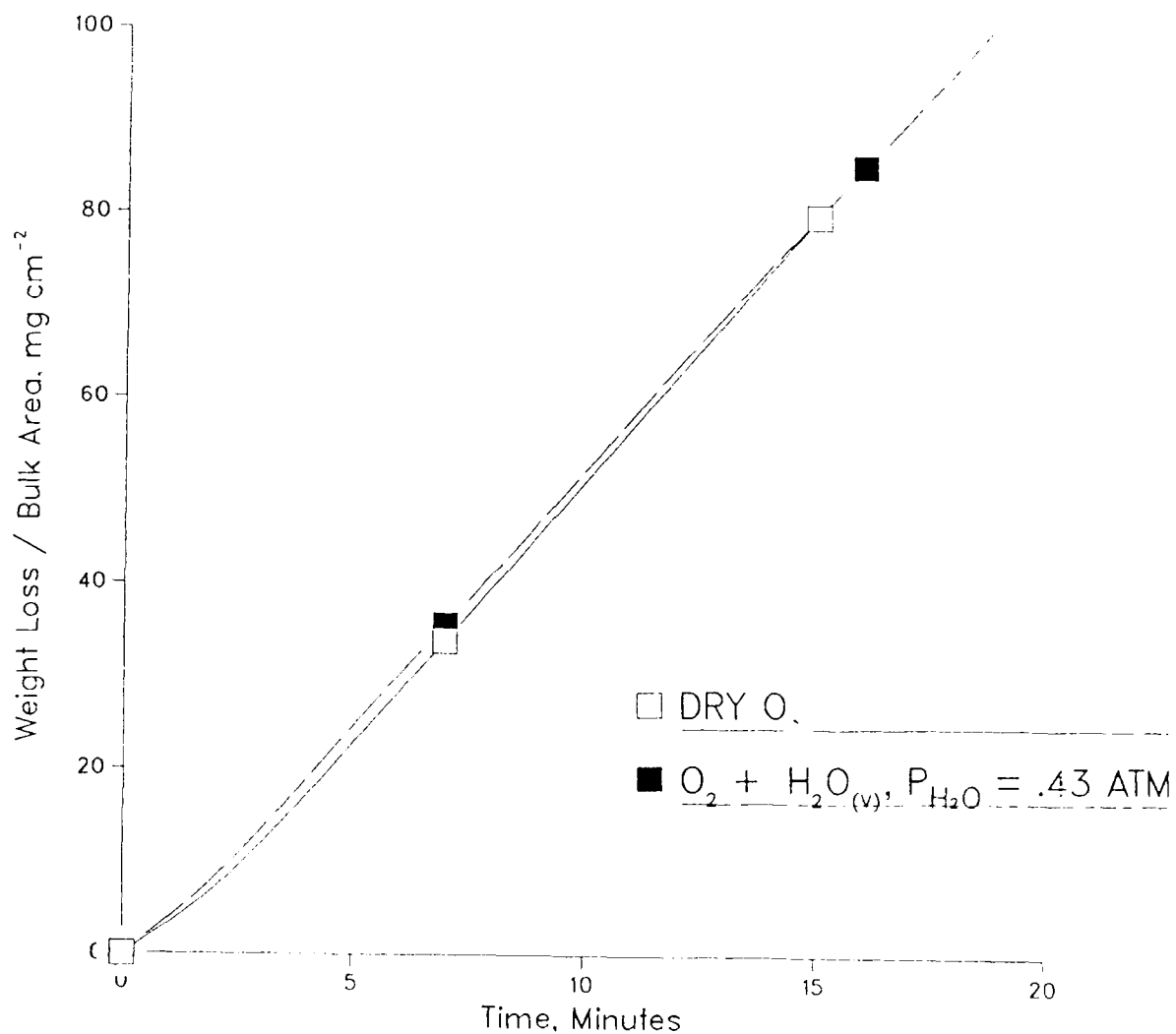


Figure 51. Oxidation kinetics for uninhibited CCC at 900°C in flowing oxygen and oxygen-water vapor atmospheres.



## Uncoated Carbon Carbon Oxidation in Still Air

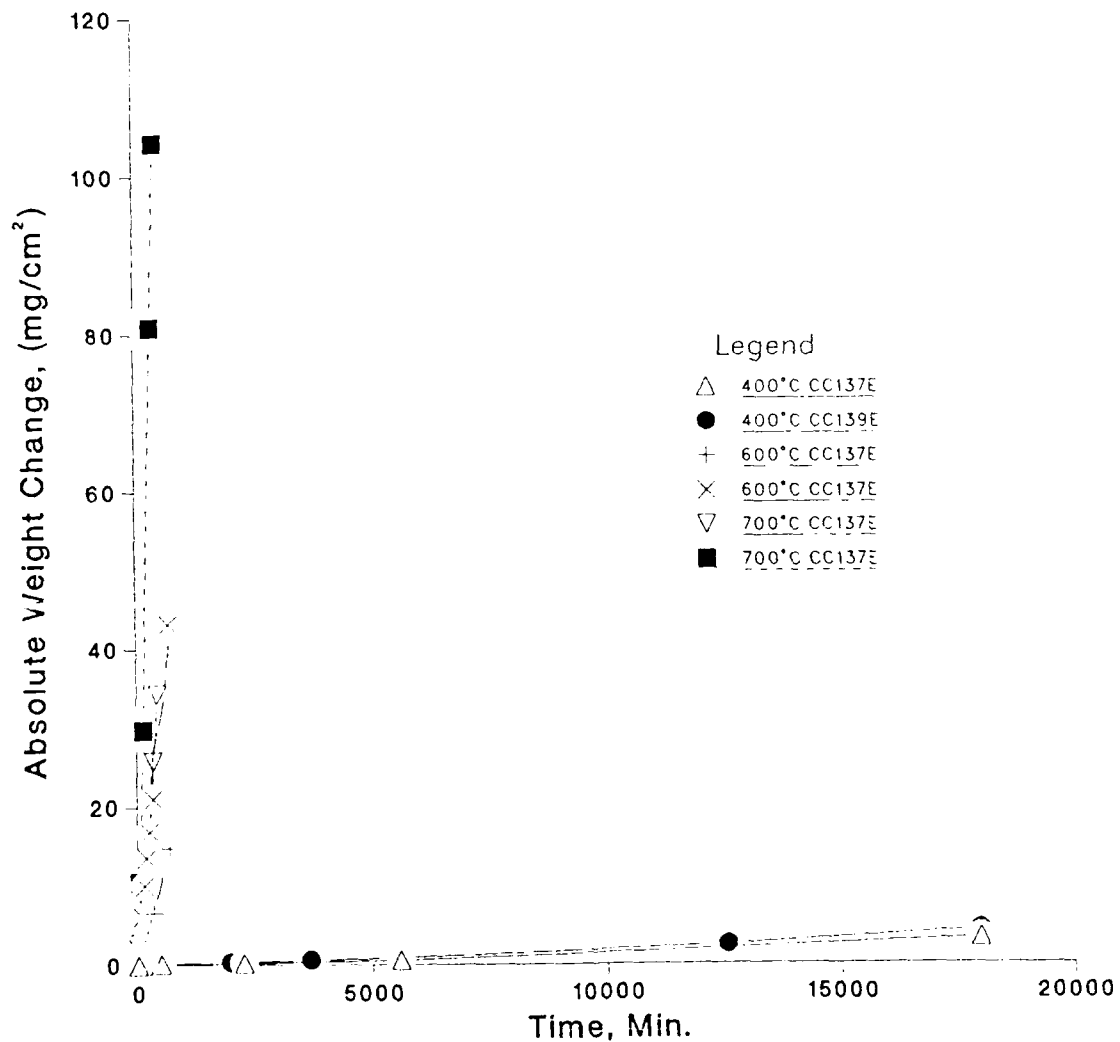


Figure 52. Isothermal oxidation kinetics (weight loss) for inhibited CC137E and uninhibited CC139E at low temperatures in still air.

## Isothermal Oxidation in Still Air

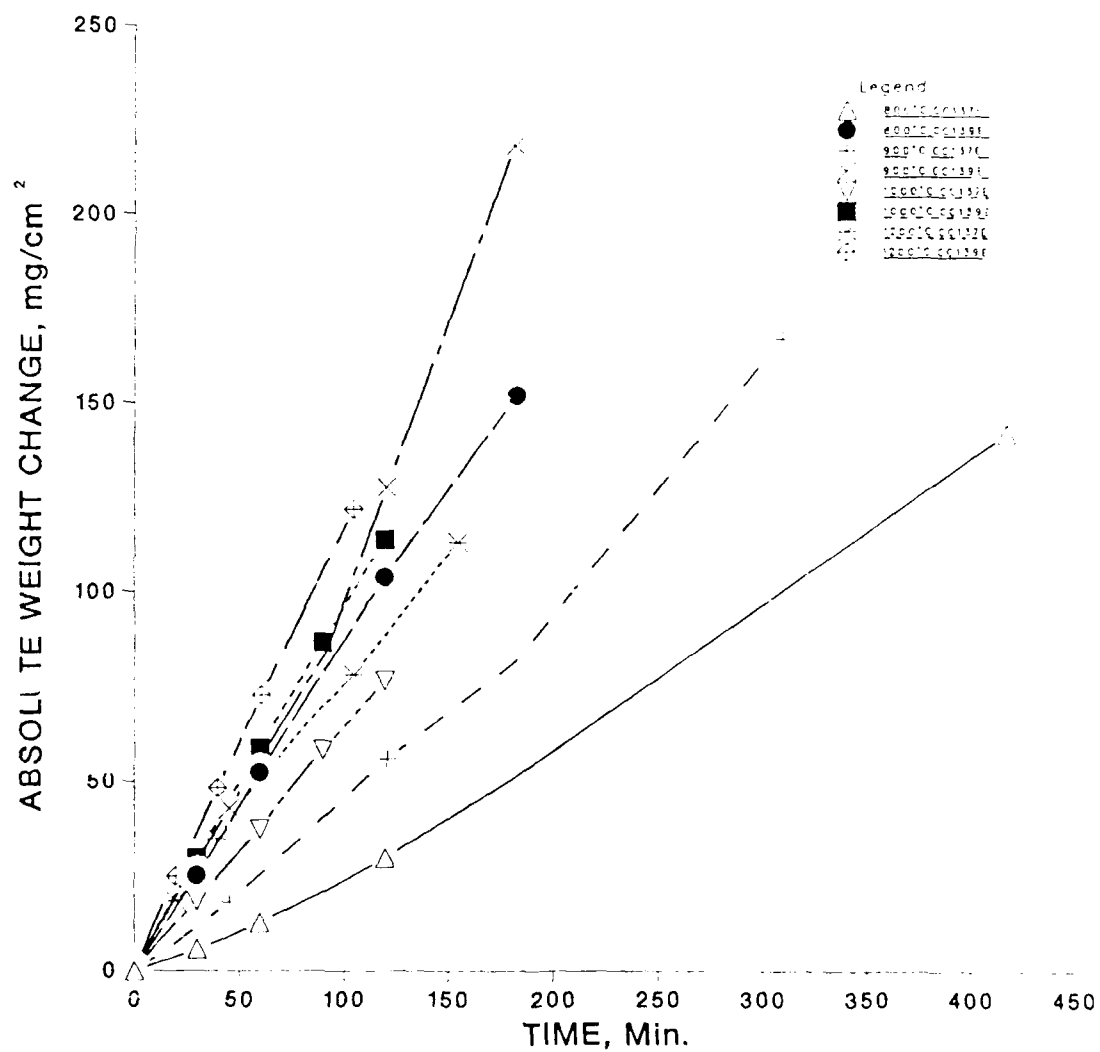


Figure 53. Isothermal oxidation kinetics (weight loss) for inhibited CC137E and uninhibited CC139E in still air at high temperatures.

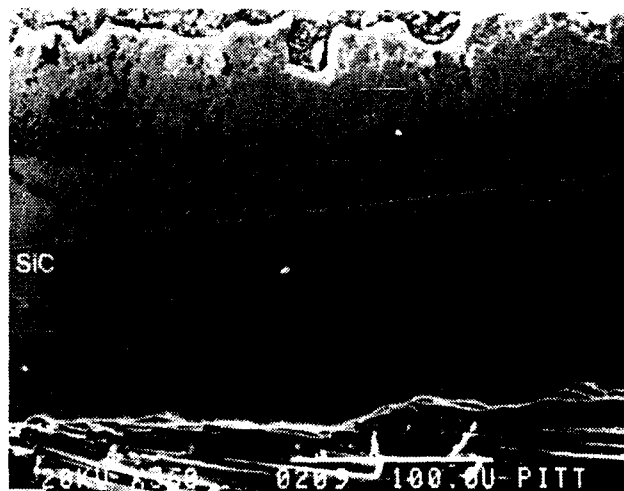
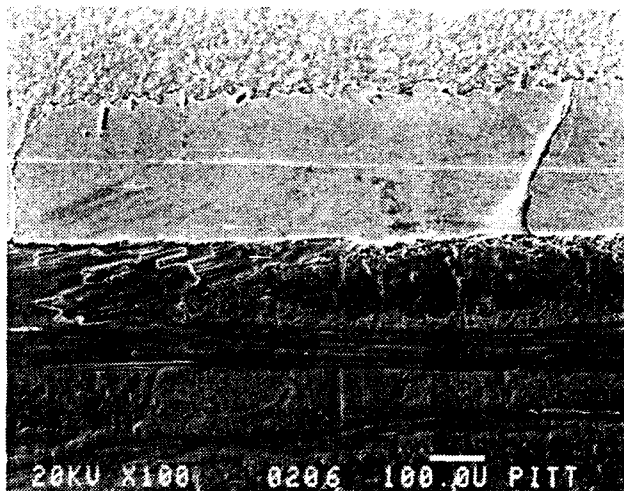
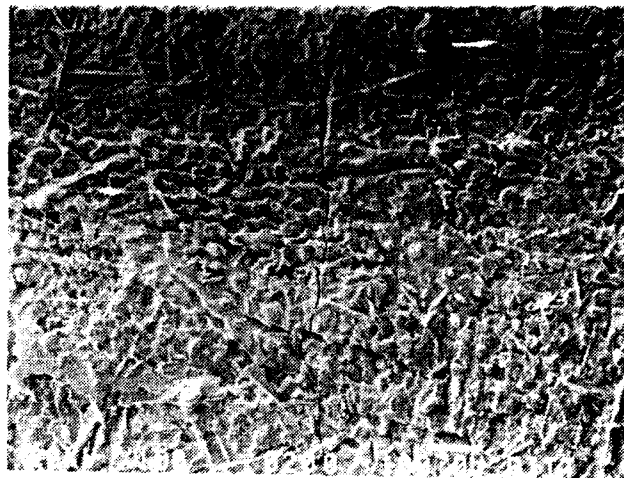


Figure 54. Initial structure of the thick HP24 coating on CC137E. The top shows the surface while the bottom shows cross sections.  $B_4C$  is seen in the  $\beta$ -SiC in the bottom micrograph.

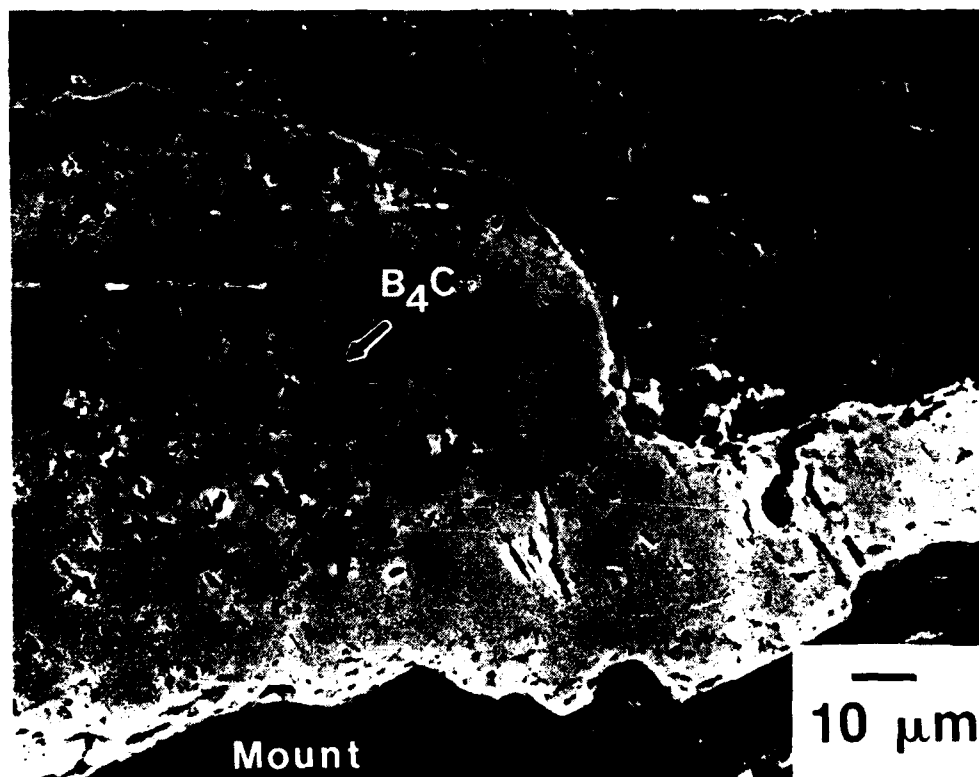
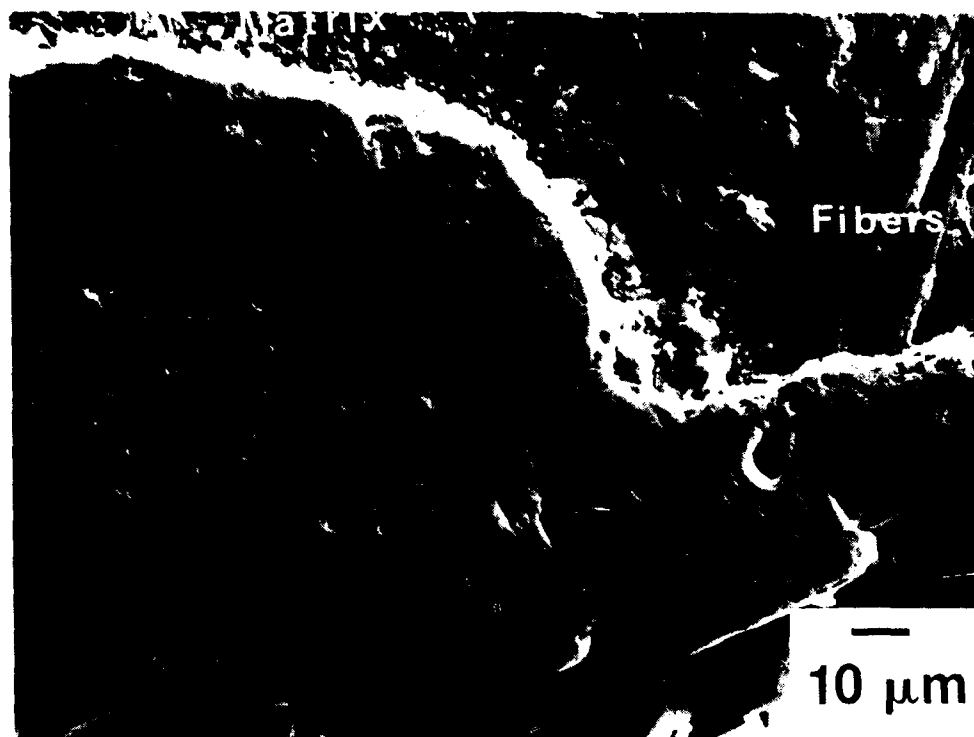


Figure 55. Microstructure (as-received) of thin HP24 coating on CC137E used for Chromalloy processes. The top is a SEI and the bottom is BEI. The thickness of the coating is less than that in Figure 54. A thicker coating with more B<sub>4</sub>C develops over the matrix.



Figure 56. TEM micrograph of  $\beta$ -SiC grains in the as-received HP24 coating.

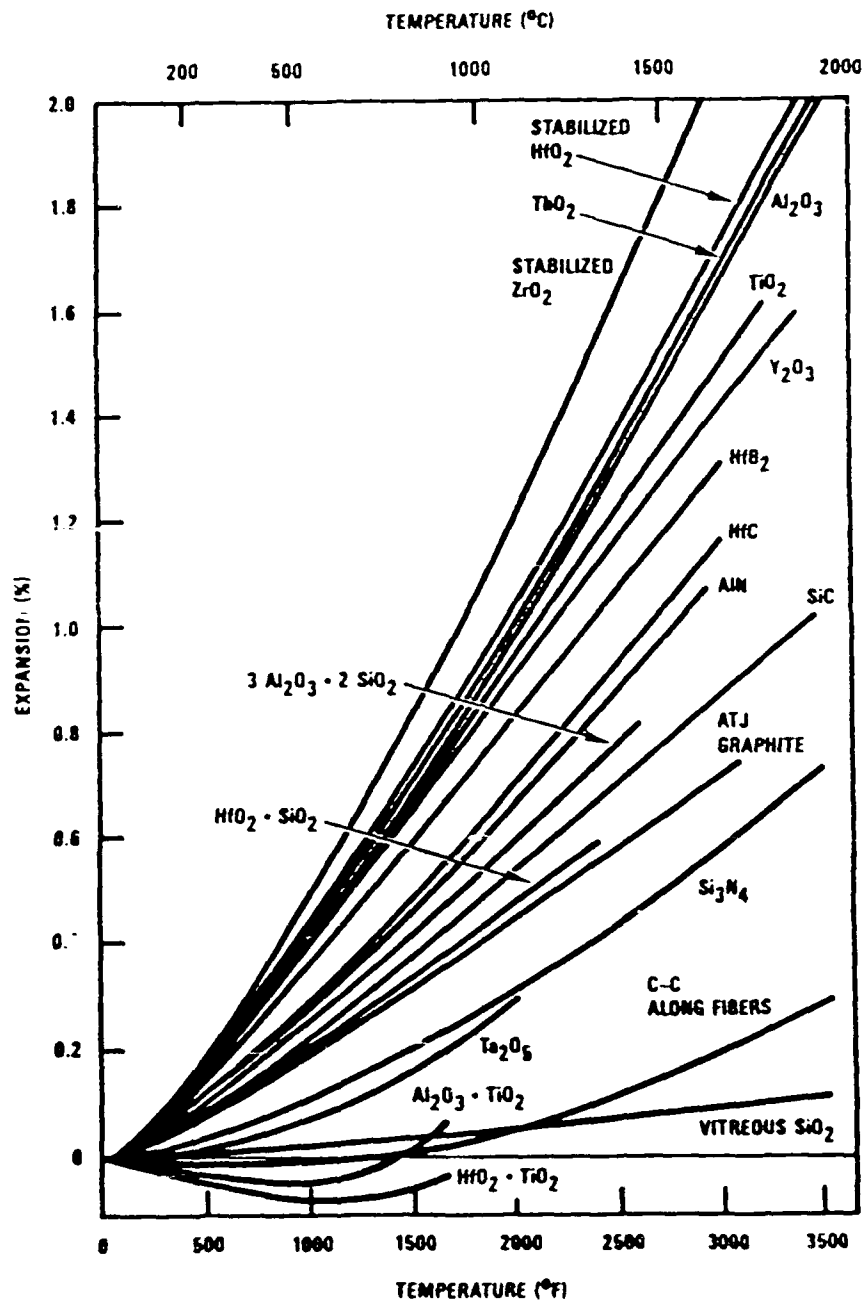


Figure 57. The thermal expansion behavior of ceramic materials as a function of temperature.

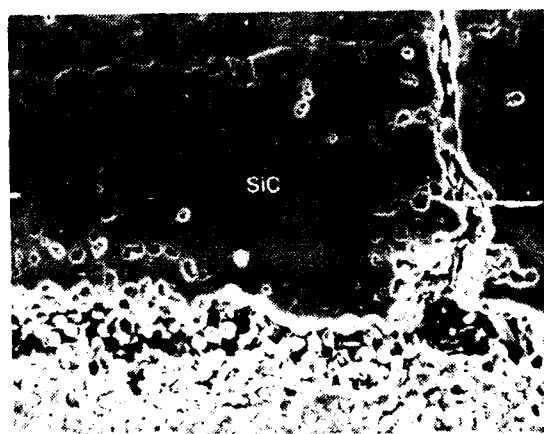
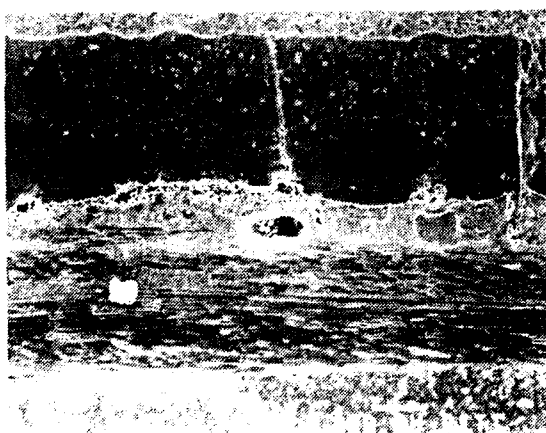
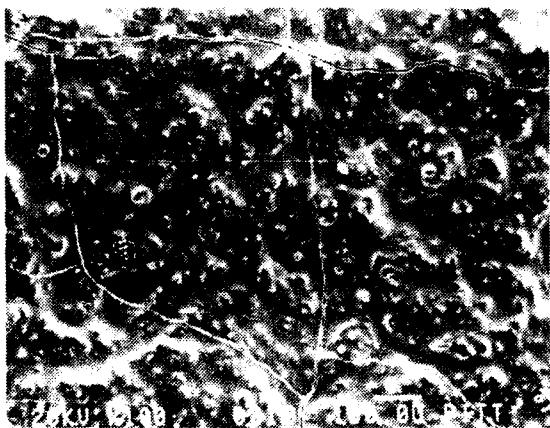


Figure 58. Micrographs showing the surface and cross section of the as-received M185.

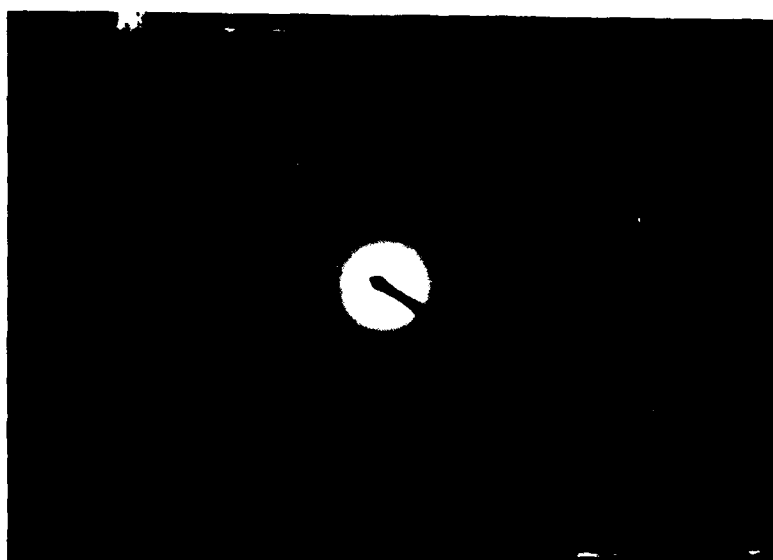


Figure 59. TEM micrograph and diffraction pattern of the silica glaze in the M185 coating.



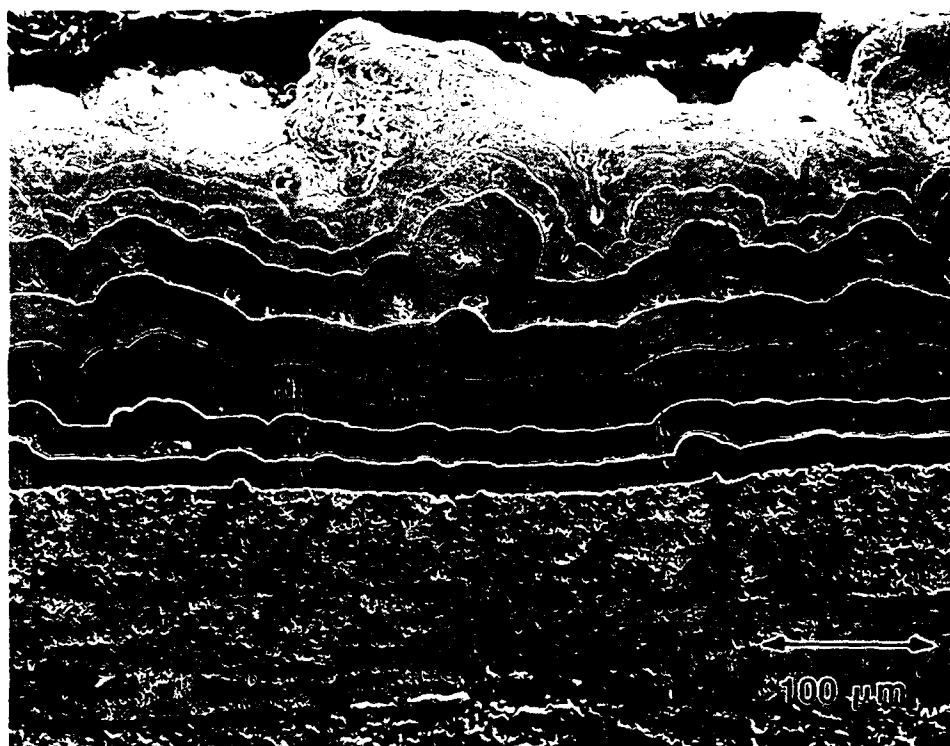


Figure 60. Etched cross sections of the Chromalloy Glaze (top) and Chromalloy No Glaze (bottom) coatings.



Figure 61. SEM micrograph of the BXC ( $B_4C$ ) intermediate layers in the Chromalloy coating.



Figure 62. SEM micrographs of the RT42A (CVD SiC) layers on the Chromalloy coating.

# COATED CARBON CARBON OXIDATION at 30 cc/min O<sub>2</sub> and 1100°C

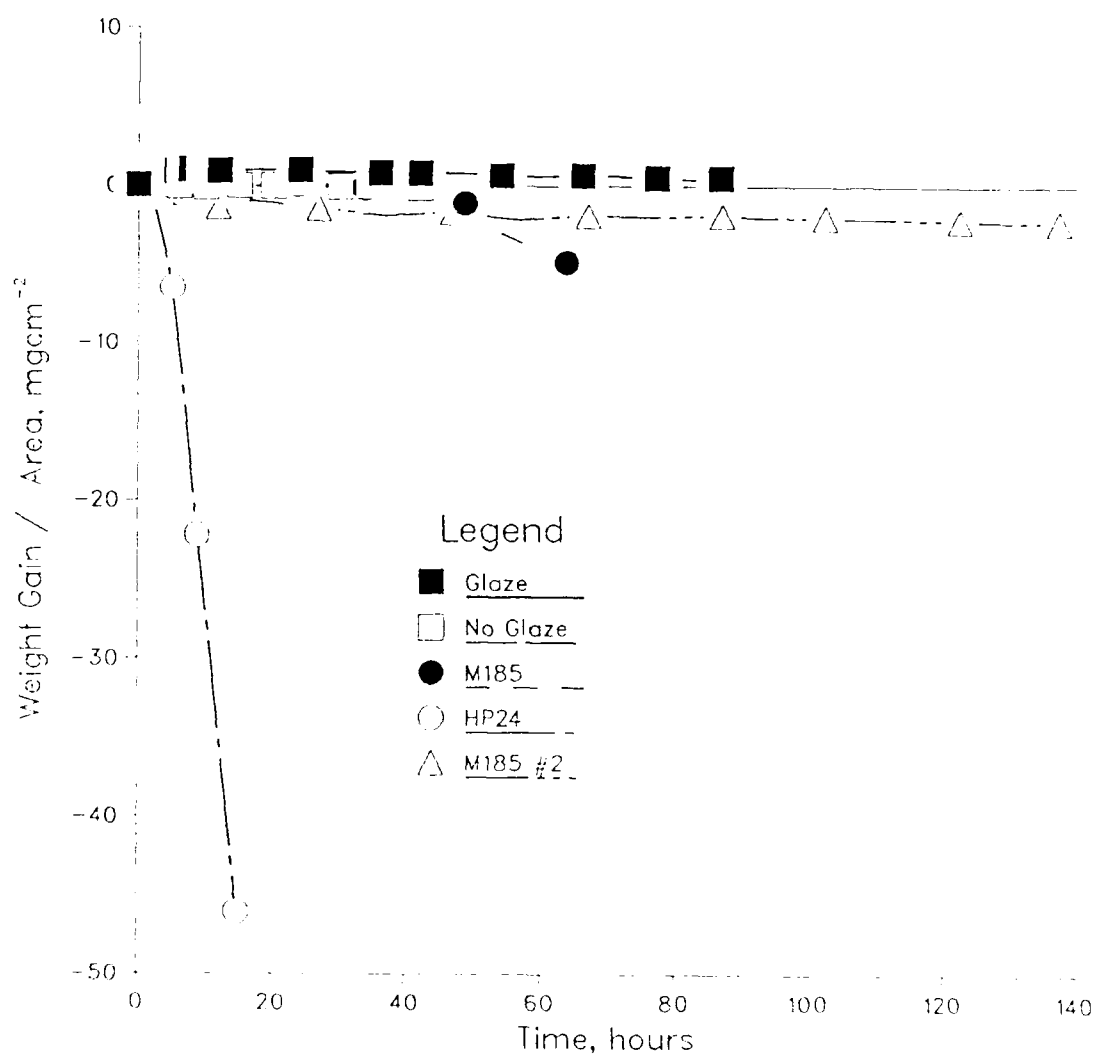


Figure 63. Isothermal oxidation kinetics for the coated systems in flowing oxygen at 1100 C.

COATED CARBON CARBON ISOTHERMAL OXIDATION at 1200°C in 50 cc/min O<sub>2</sub>

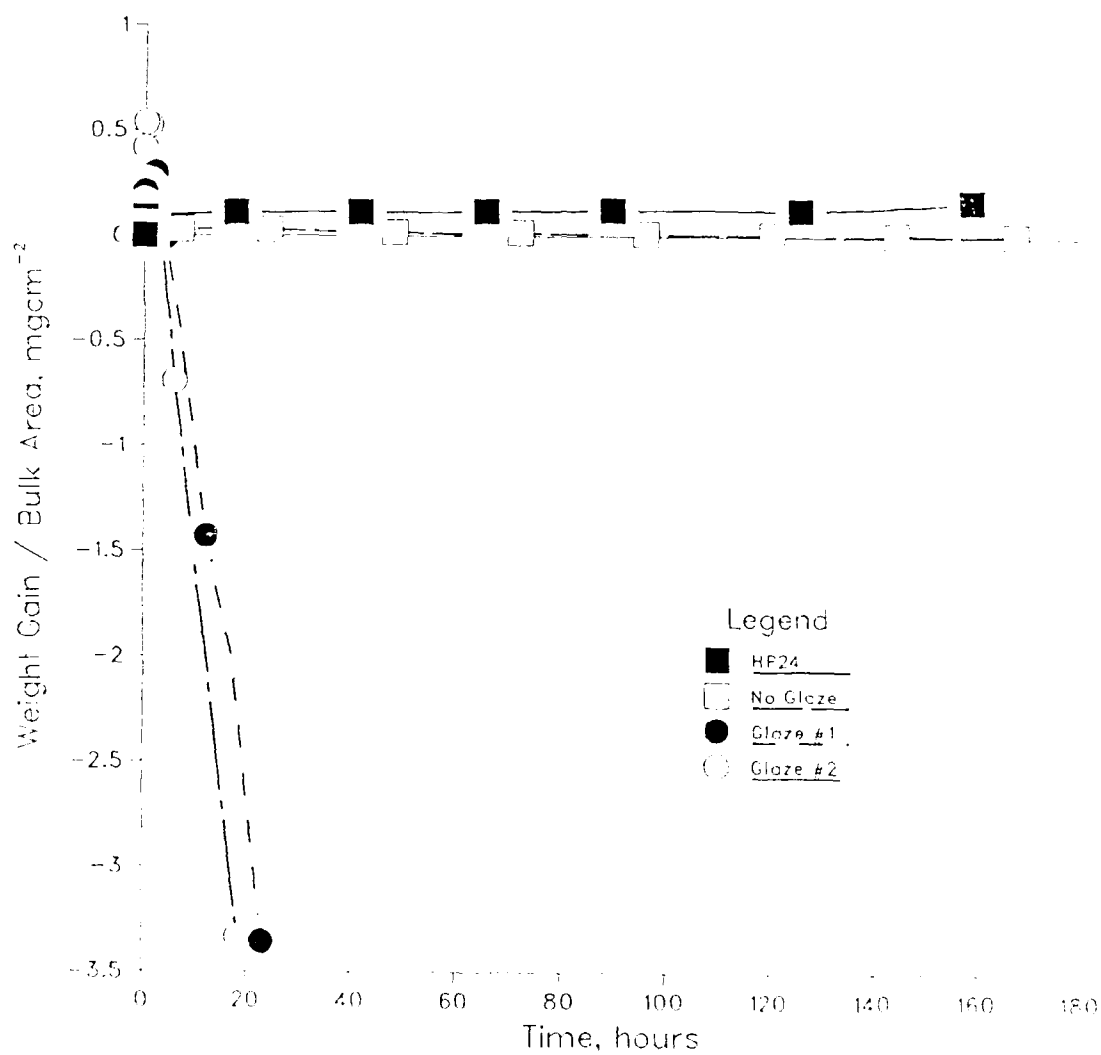


Figure 64. Isothermal oxidation kinetics for the coated systems in flowing oxygen at 1200°C.

# COATED CARBON-CARBON ISOTHERMAL OXIDATION at 1300°C

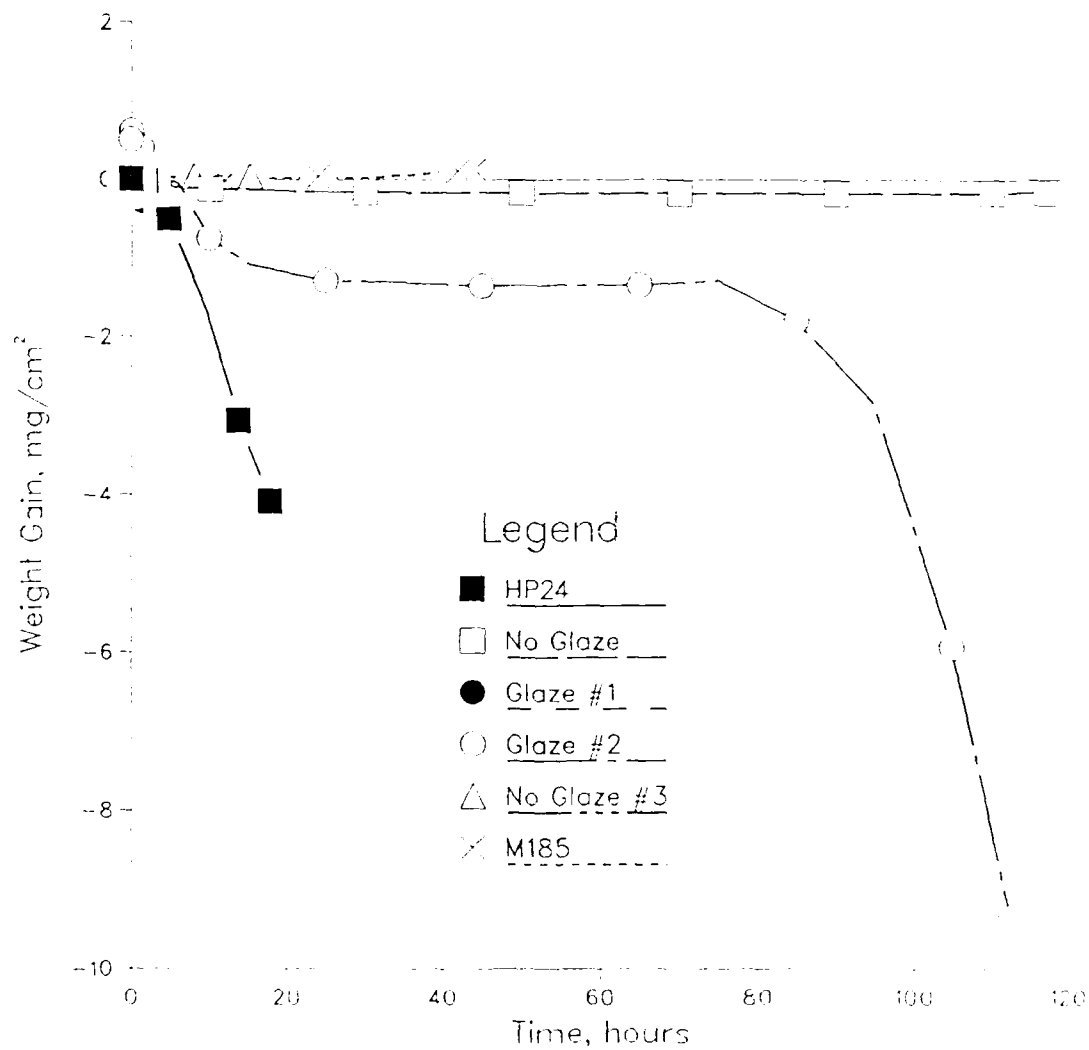


Figure 65. Isothermal oxidation kinetics for the coated systems in flowing oxygen at 1300°C.

# COATED CARBON CARBON ISOTHERMAL OXIDATION at 1400°C.

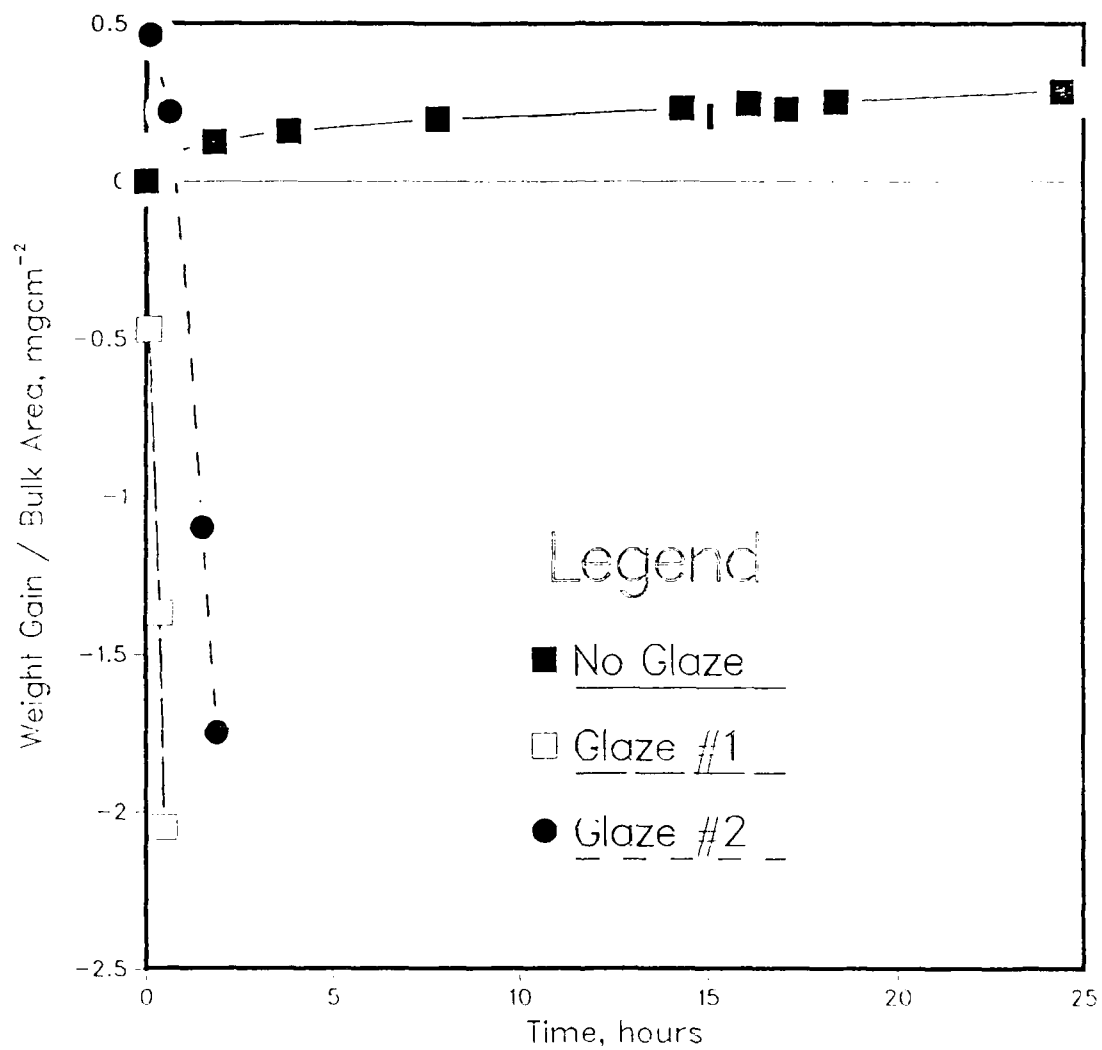


Figure 66. Isothermal oxidation kinetics for the coated systems in flowing oxygen at 1400°C.

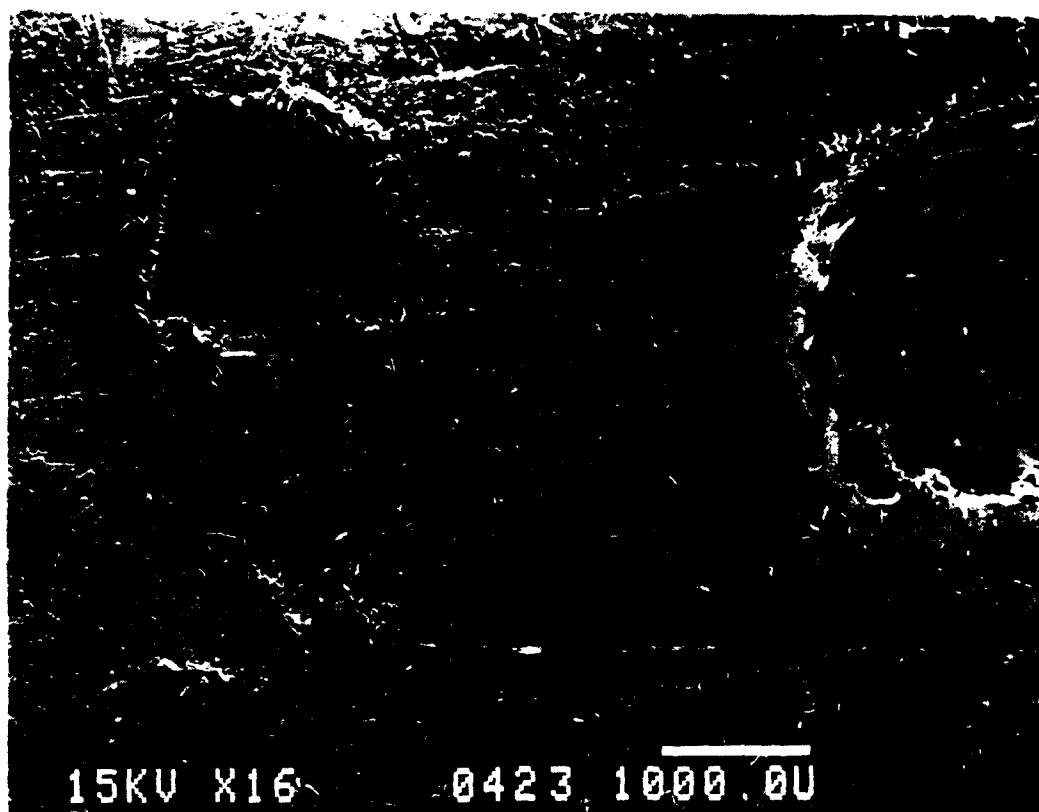


Figure 67. Micrographs of the defects that form on the surface of the HP24 samples after isothermal oxidation at 1100°C.





Figure 68. Cross sections of HP24 after isothermal oxidation at 1200°C. The top micrograph shows B<sub>4</sub>C stringers in the coating. The bottom micrographs show bubbling in the reaction products in cracks.

$B_2O_3$ - $SiO_2$

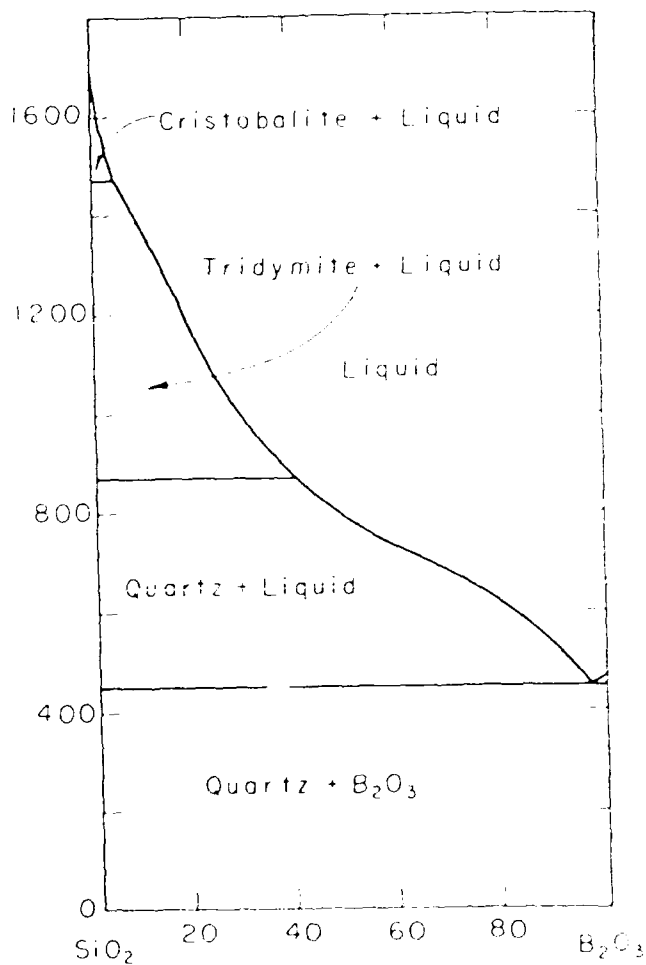


Figure 69. Phase diagram of the  $B_2O_3$  -  $SiO_2$  system.



Figure 70. Optical micrographs show HP24 after oxidation in oxygen at 1100°C for 20 hours. Preferential attack of the bright free Si is observed in each micrograph. Dark particles are  $B_4C$ .

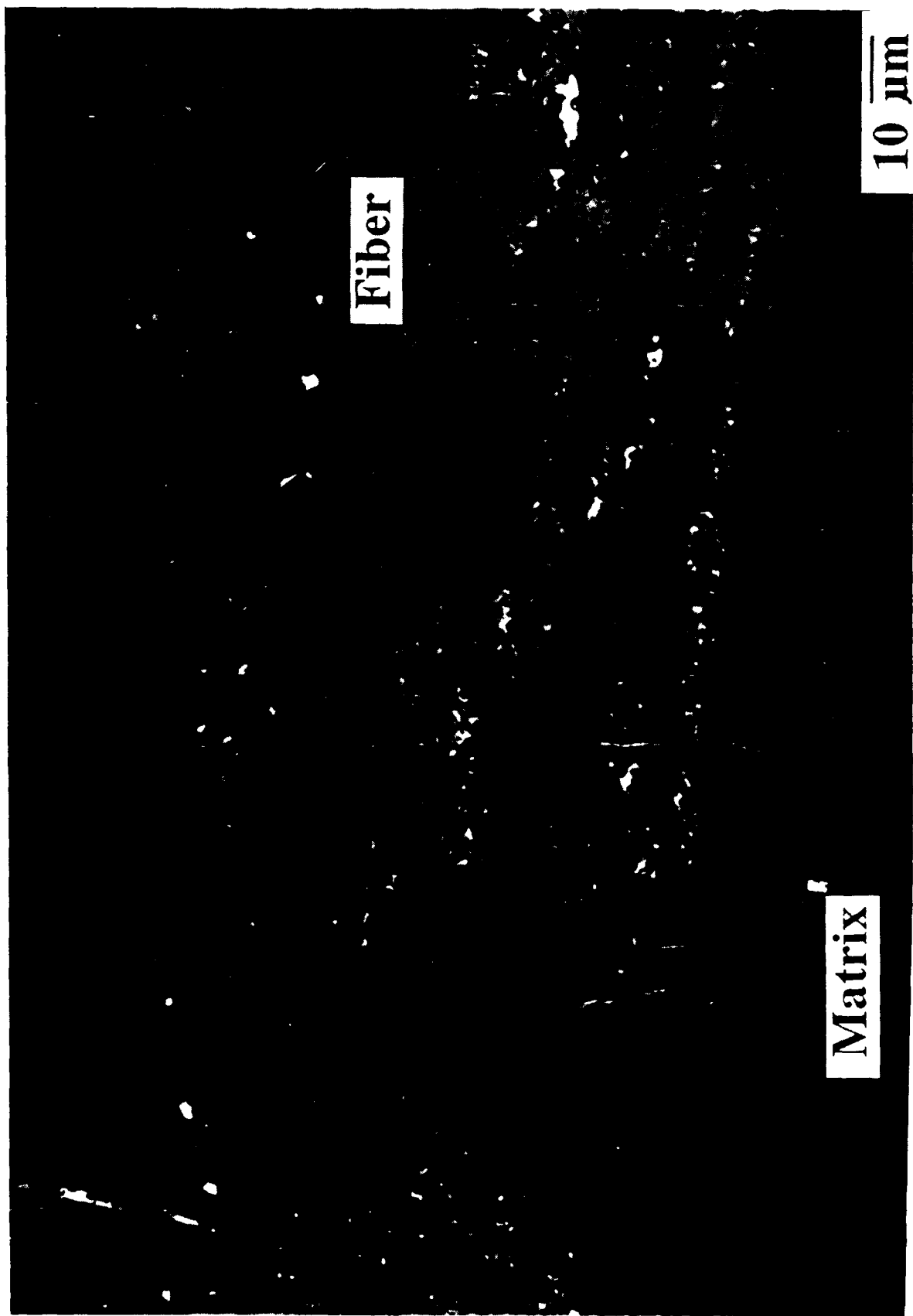


Figure 71. Optical micrograph showing unconverted fibers in a HP24 sample that had been oxidized at 1200°C.

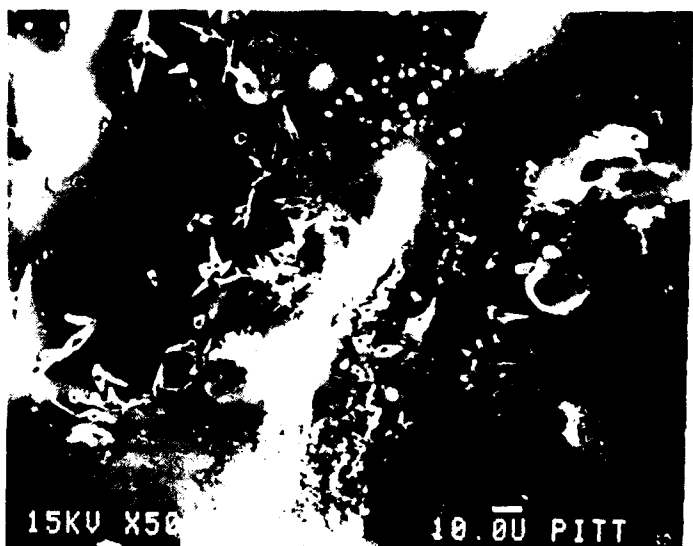
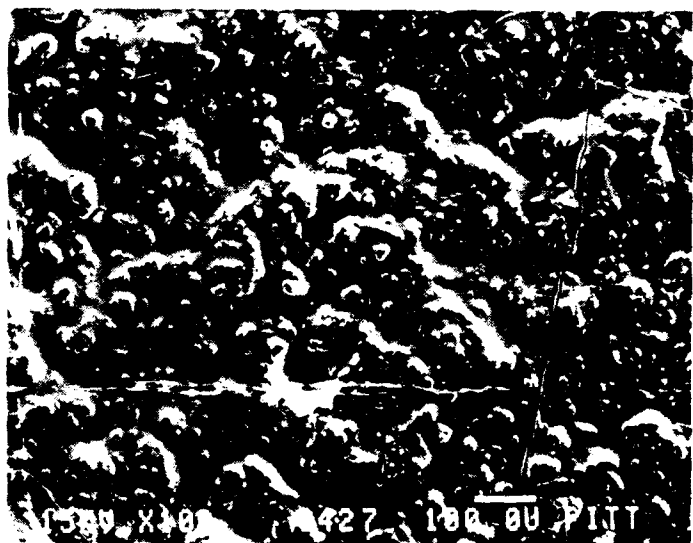


Figure 72. Surface micrographs of the M185 after isothermal oxidation at 1100°C. The top shows a large mound/hole defect, while the other two micrographs show typical surface morphologies.



Figure 73. Micrographs of the M185 sample after isothermal oxidation at 1100°C. The top micrograph is a cross section of the coating and the other micrograph shows the coating/scale interface.

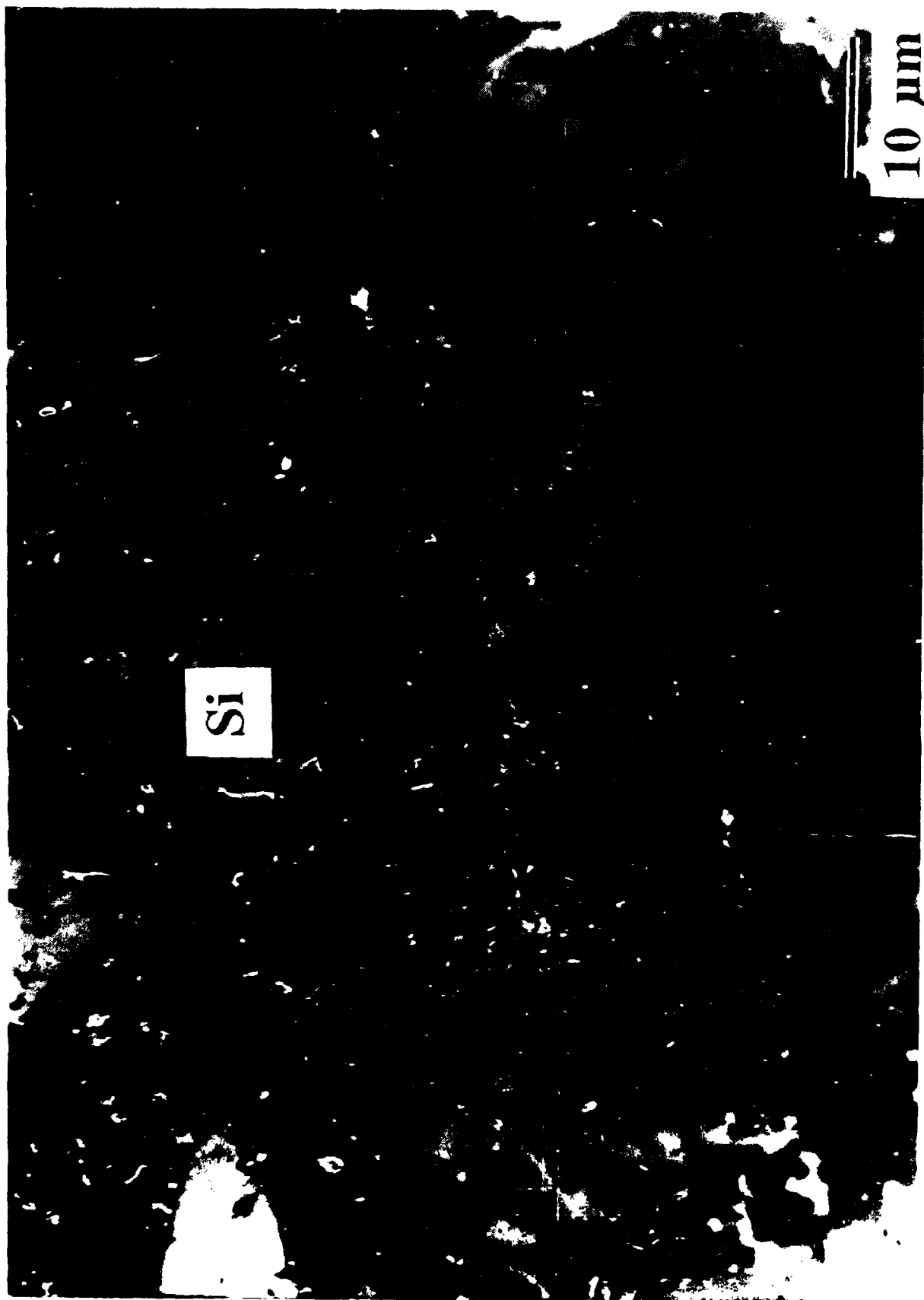


Figure 74. Optical micrographs of particle attack in the  $\text{Al}_2\text{O}_3$  layer after isothermal oxidation. Some particles show formation of another phase, besides  $\text{SiO}_2$ , at their periphery.

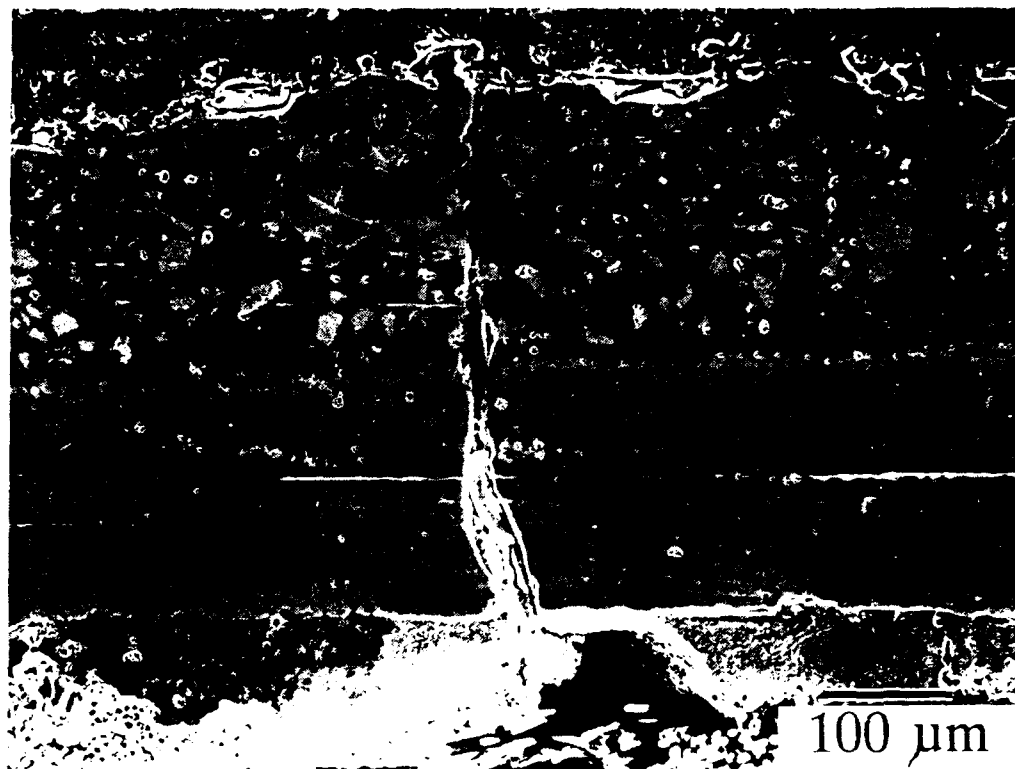


Figure 75. Cross section of the M185 sample after isothermal oxidation in oxygen at 1100°C. The crack is sealed in the top micrograph. The bottom shows a porous crack that is not sealed. The porous crack leads to a mound.



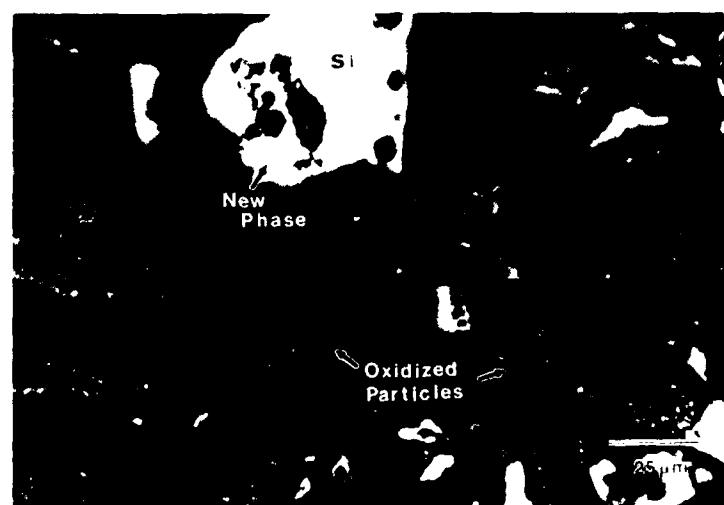
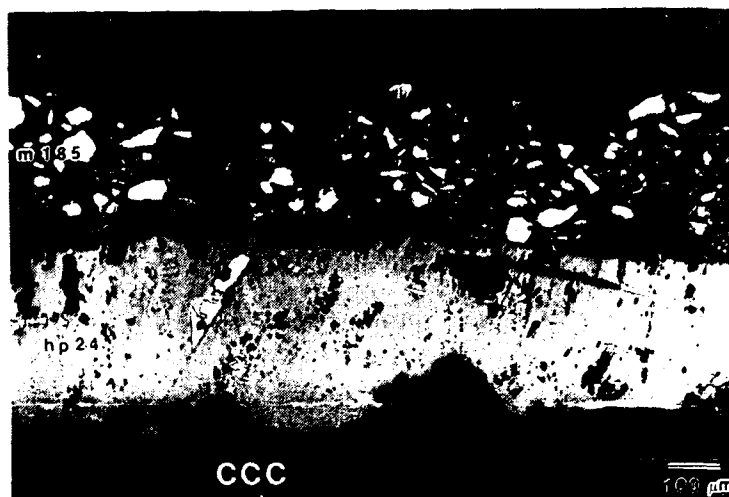


Figure 76. Optical micrographs of the cross section of the M185 coating after oxidation at 1300°C. Particle attack in the M185 glaze and preferential attack of Si in the HP24 are observed.



Figure 77. Surface micrograph of the No Glaze after isothermal oxidation in oxygen at 1100°C. The surface shows cracking and spalling of the silica scale.

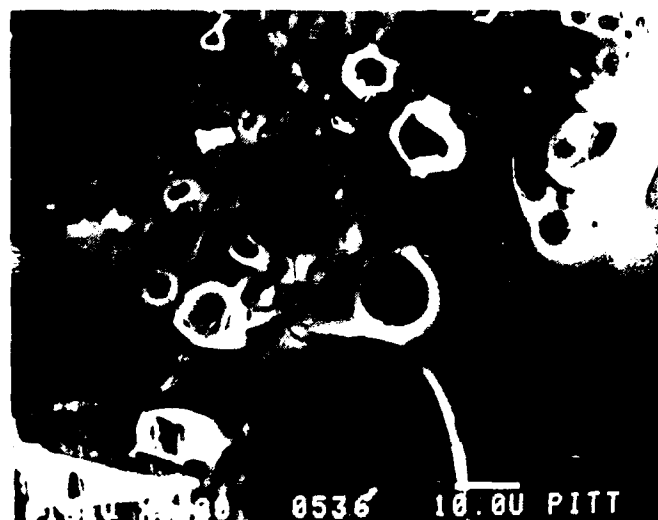
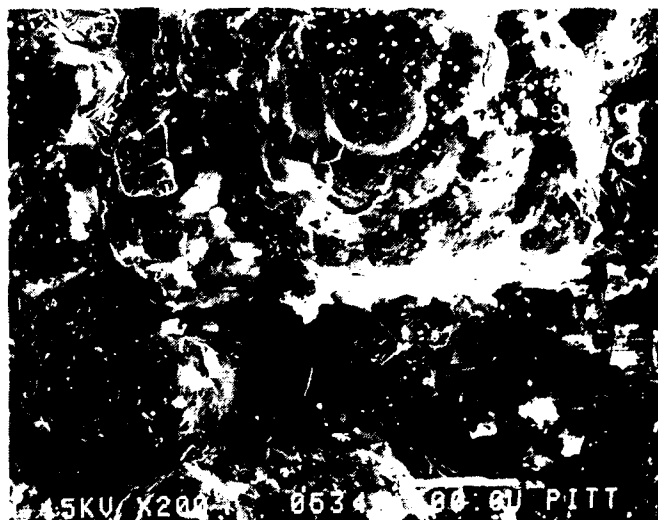


Figure 78. Surface of the No Glaze coating after isothermal oxidation testing at 1300°C.

## Isothermal Oxidation at Various Temperatures

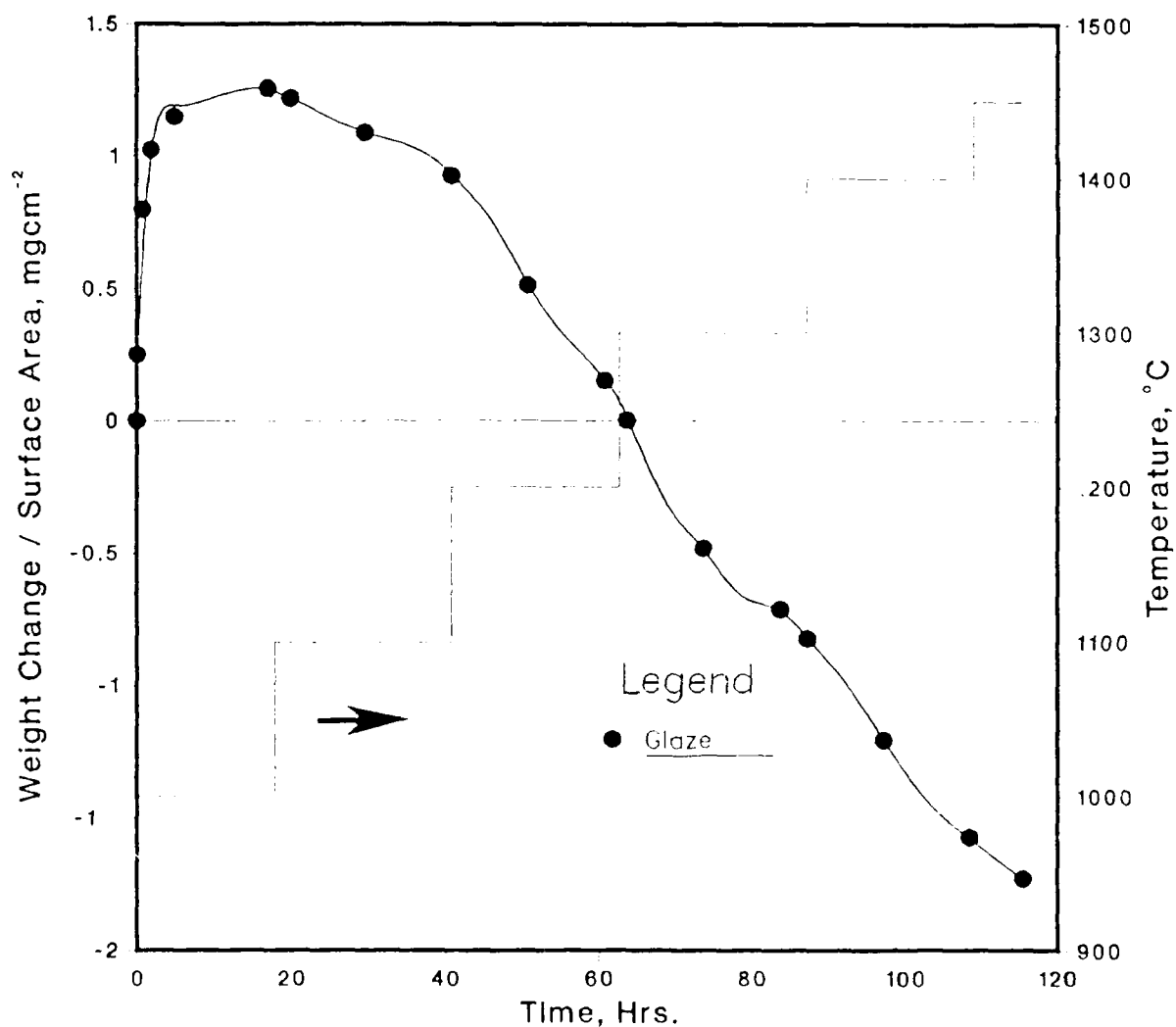


Figure 79. Oxidation kinetics for the Glaze sample when incrementally heated from 1000 to 1450°C in oxygen. No thermal shock of the sample was observed.

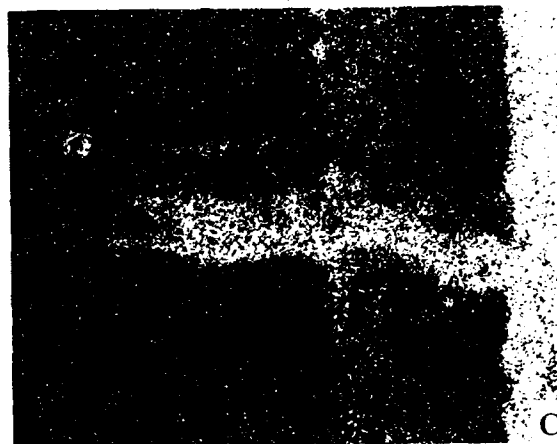
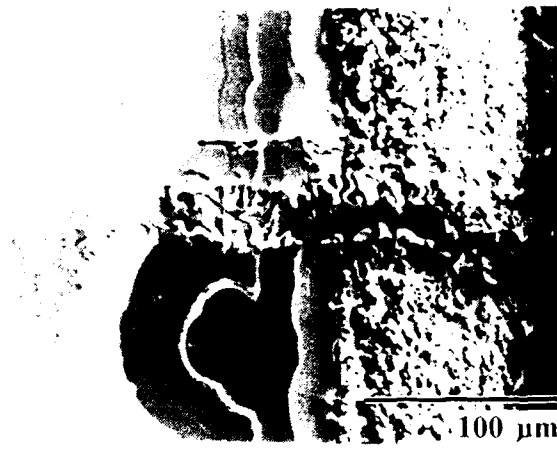


Figure 80. Micrographs and WDS analyses of the glaze sample cross section after oxidation test at 1000 to 1450°C.

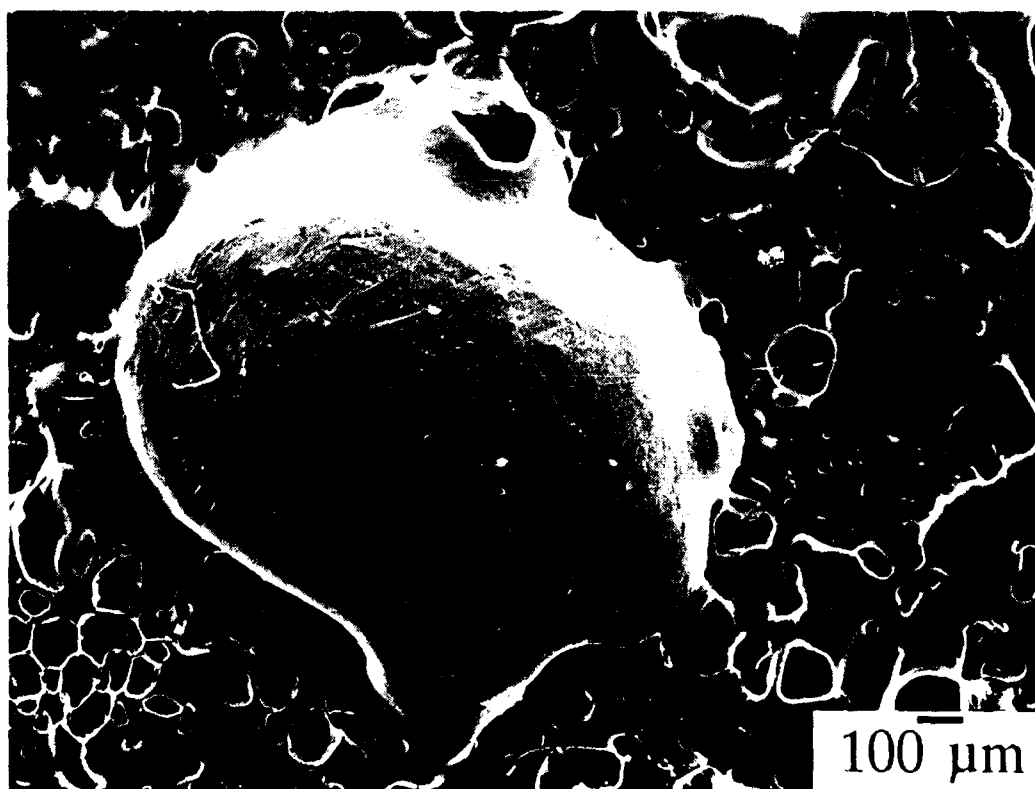
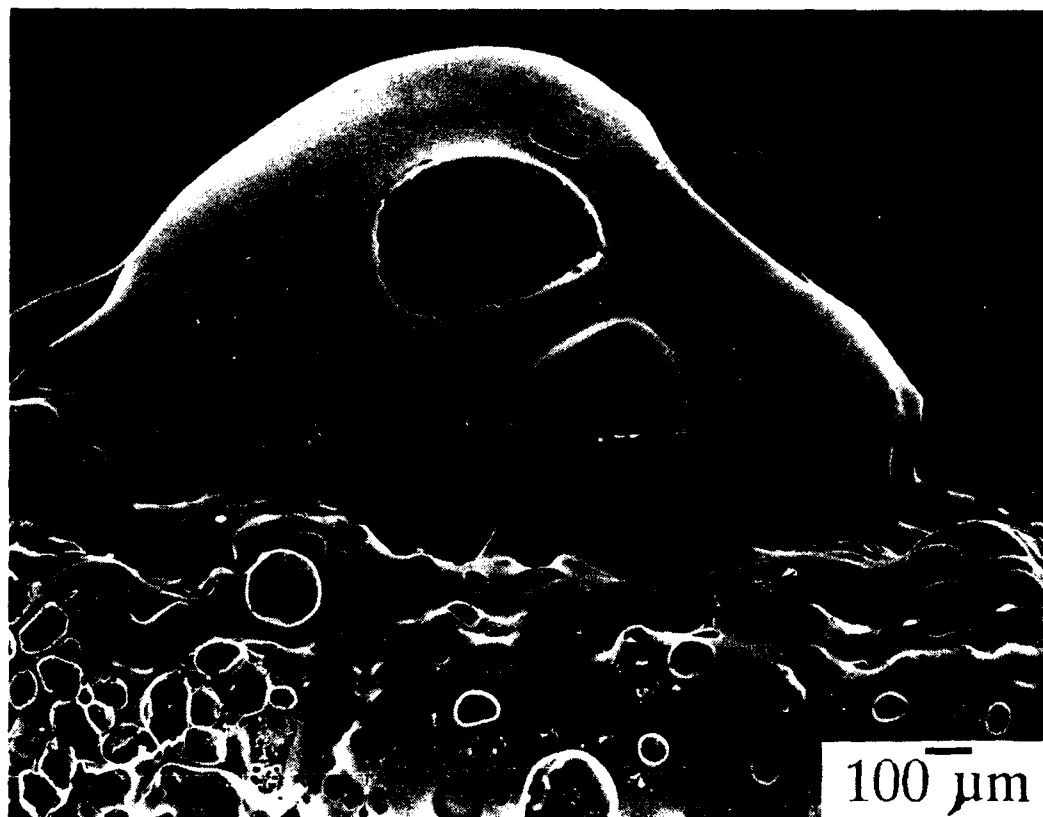


Figure 81. Micrograph of the surface of the Glaze sample after oxidizing at temperatures between 1000 to 1450°C for 120 hours. Surface shows vigorous bubbles occurred on the sample.

# CARBON CARBON CYCLIC OXIDATION in STATIC AIR at 900°C

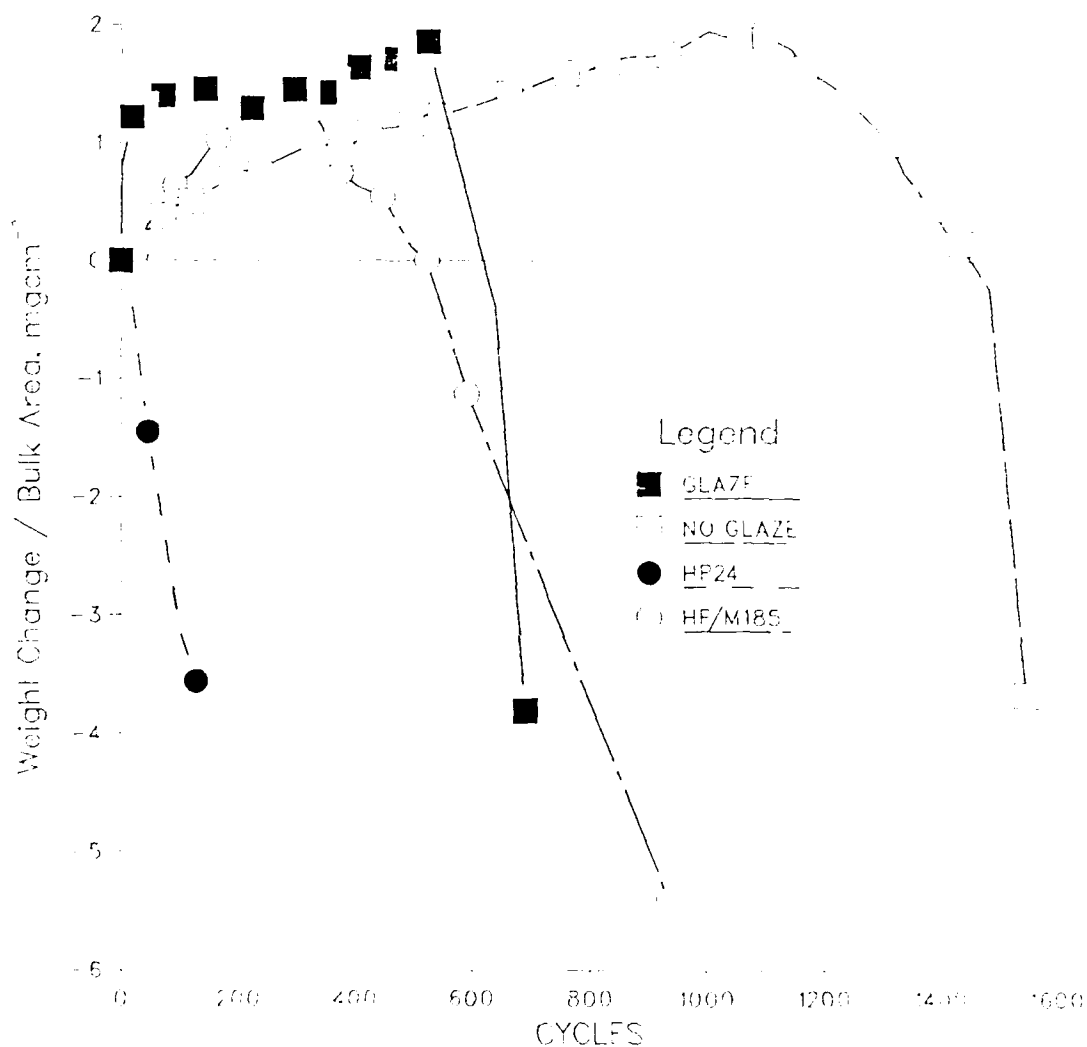


Figure 82. Cyclic oxidation kinetics for the coating system at 900°C in still air.

# CARBON CARBON CYCLIC OXIDATION in STATIC AIR at 1125°C

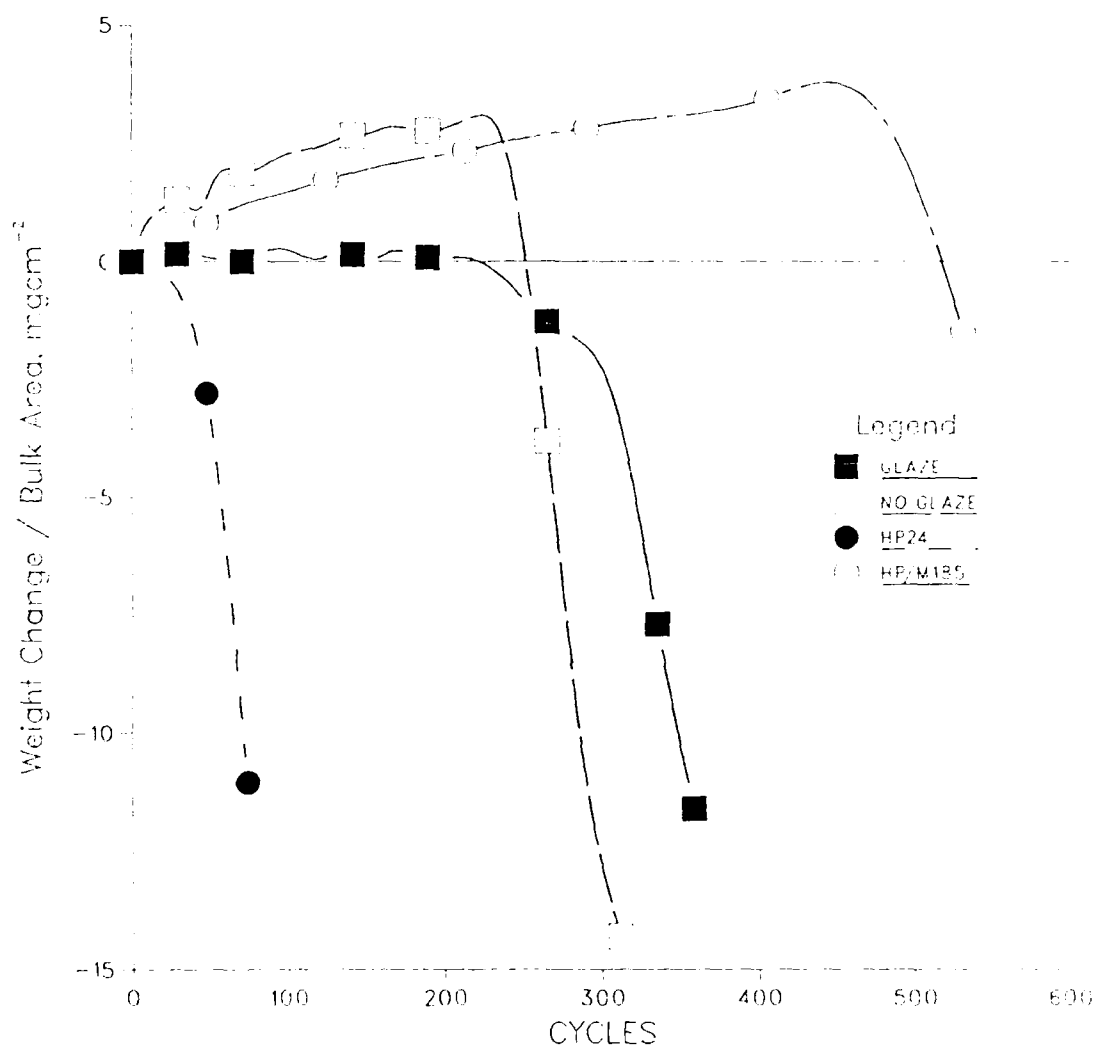


Figure 83. Cyclic oxidation kinetics for the coating system at 1125°C in still air



CARBON CARBON CYCLIC OXIDATION with 30 cc/min  $O_2$  and 1125°C

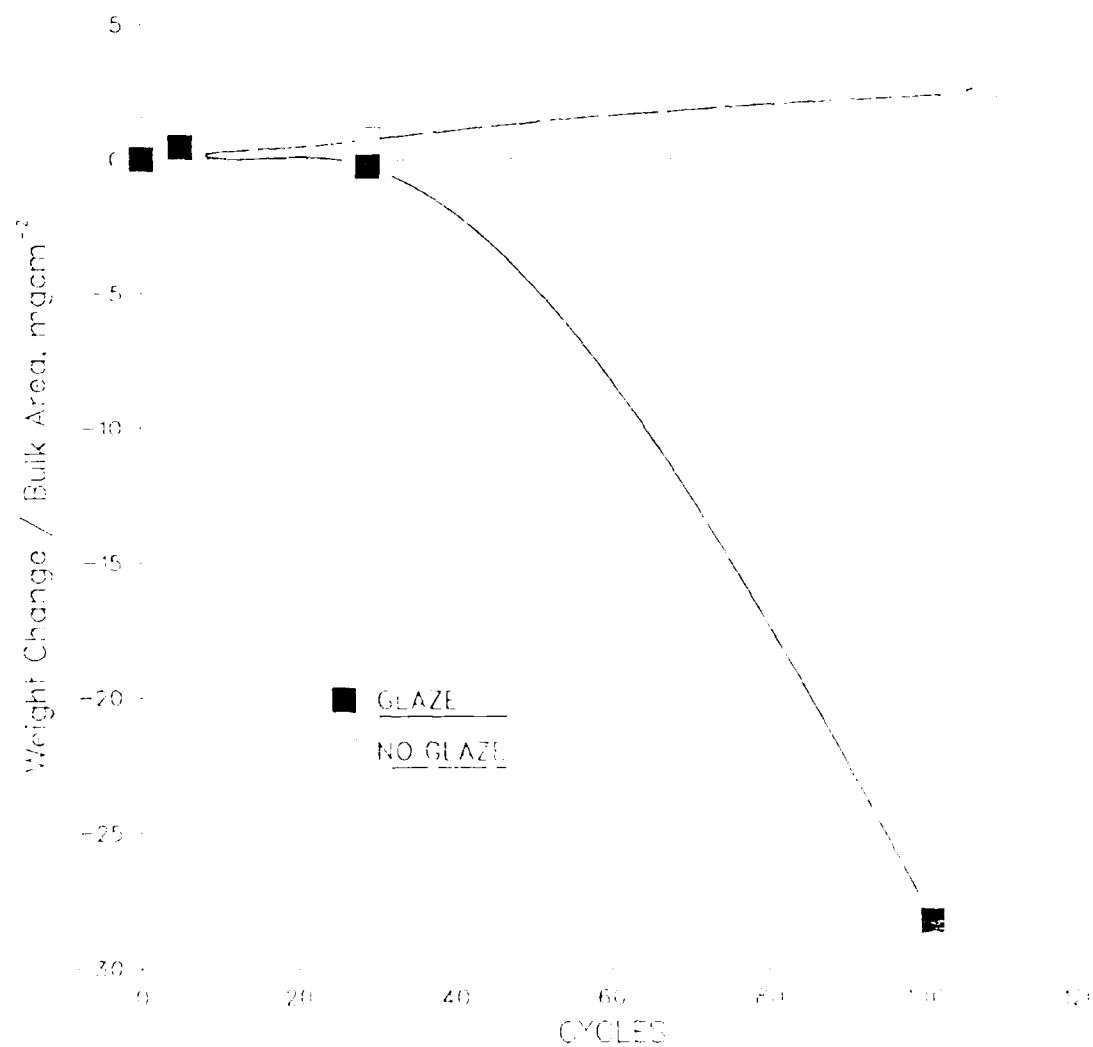


Figure 84. Cyclic oxidation results for the coating systems at 1125°C in flowing oxygen.

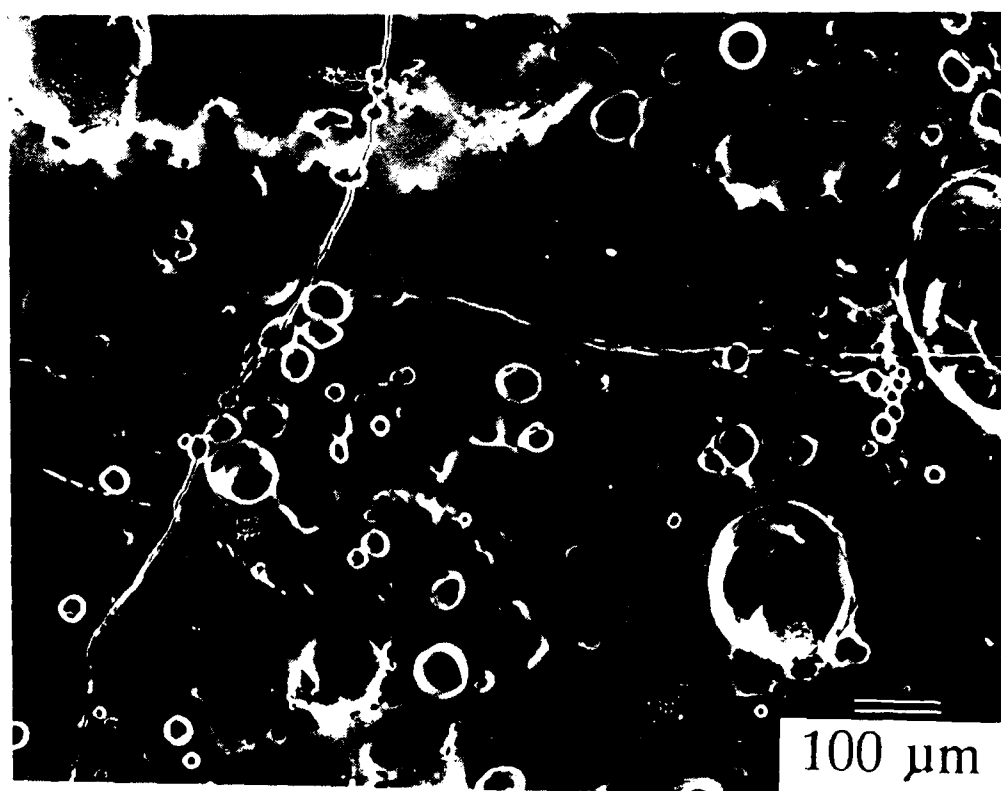
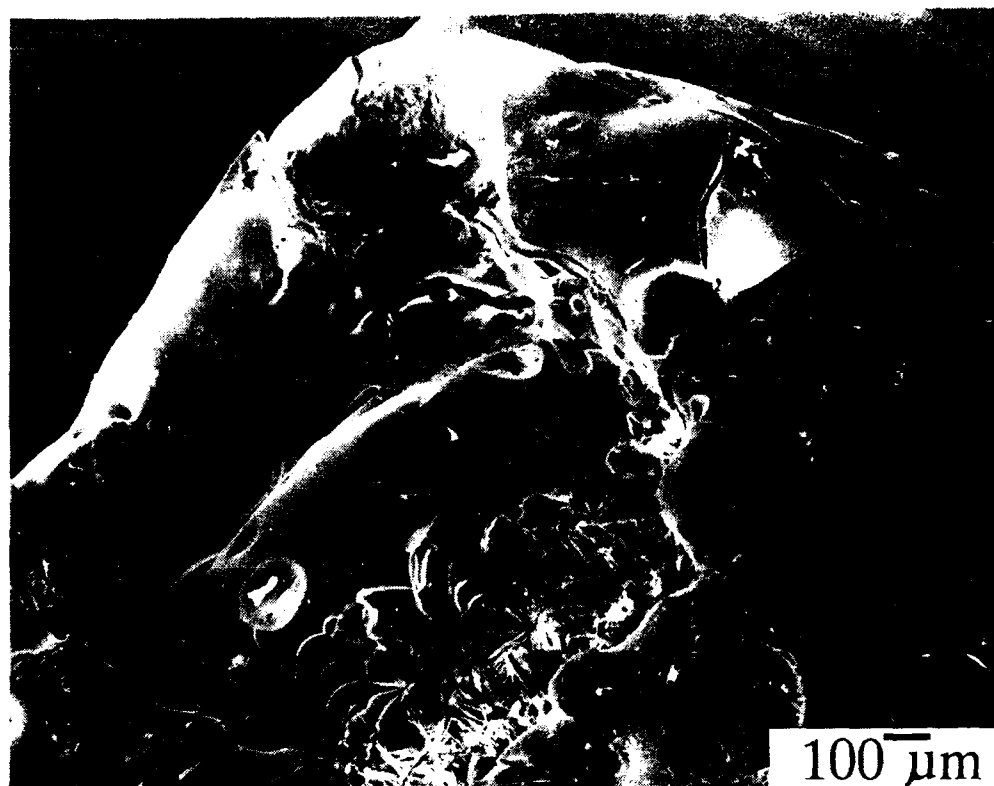


Figure 85. Micrographs showing the surface of the glaze sample after 100 cycles in oxygen at 1125°C. The top micrograph shows a typical large crack at the corner of the sample. The micrograph shows cracks and bubbles near the center of the sample.



Figure 86. Micrographs of the glaze sample after 100 cycles in oxygen at 1125°C. The top micrograph shows a sealed crack. The bottom micrograph shows a cross section of the penetrated coating.

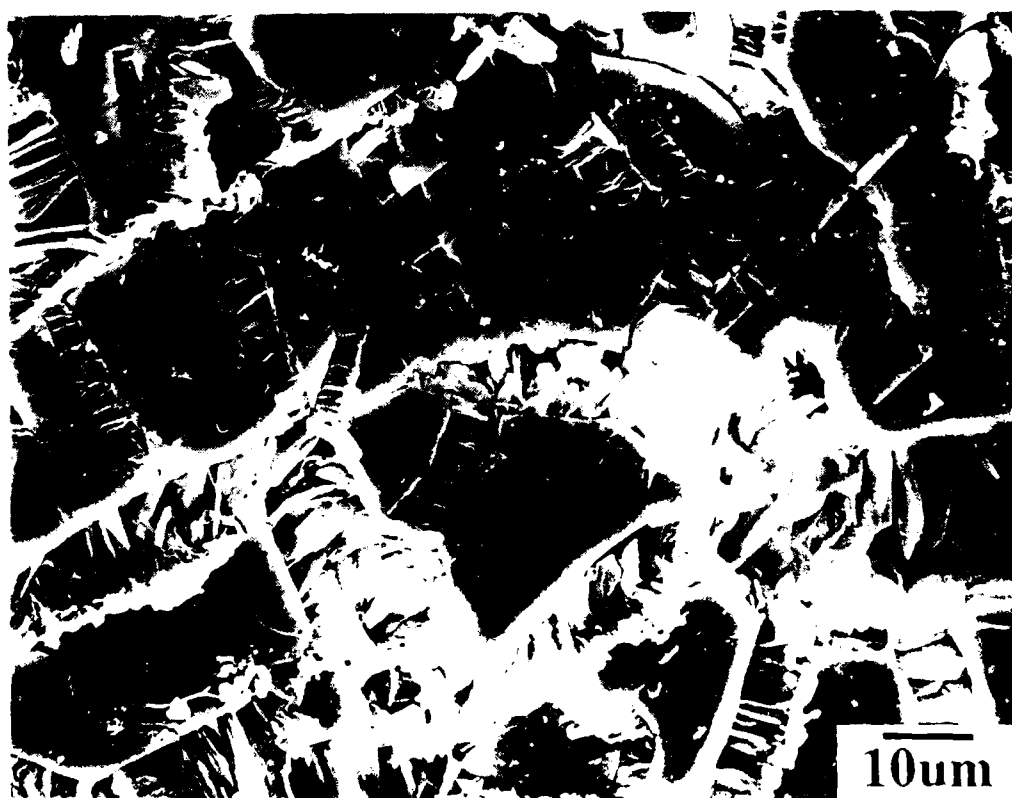


Figure 87. Surface micrograph showing the buckled failure observed in the M185 sample after 975 cycles in air at 900°C. Boron is detected at the rim of the hole. The lower micrograph shows fracturing of the glaze near the hole.

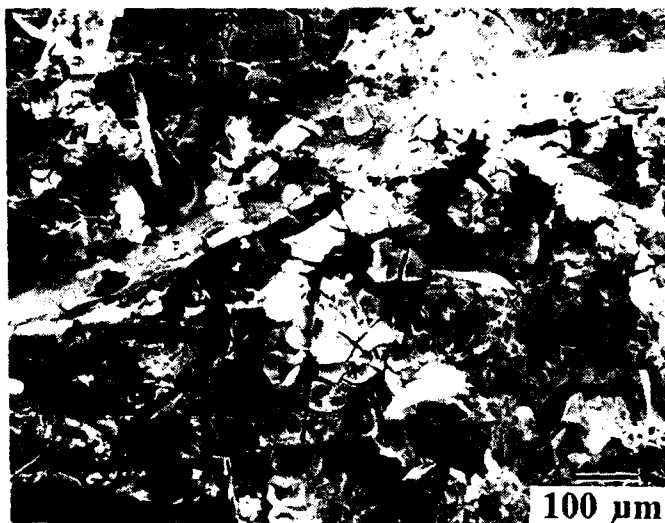
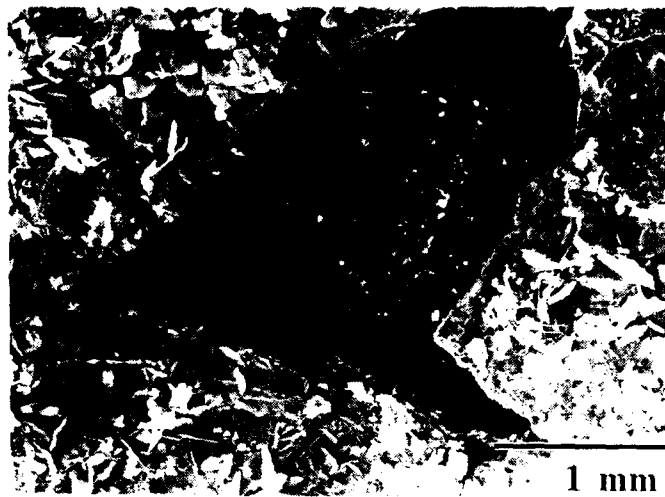


Figure 88. Surface micrographs of the glaze sample after cyclic oxidation at 900°C. The top shows a large failure site. Some boron oxide surrounds the failure site. The other micrographs show cracking and spalling on the surface.

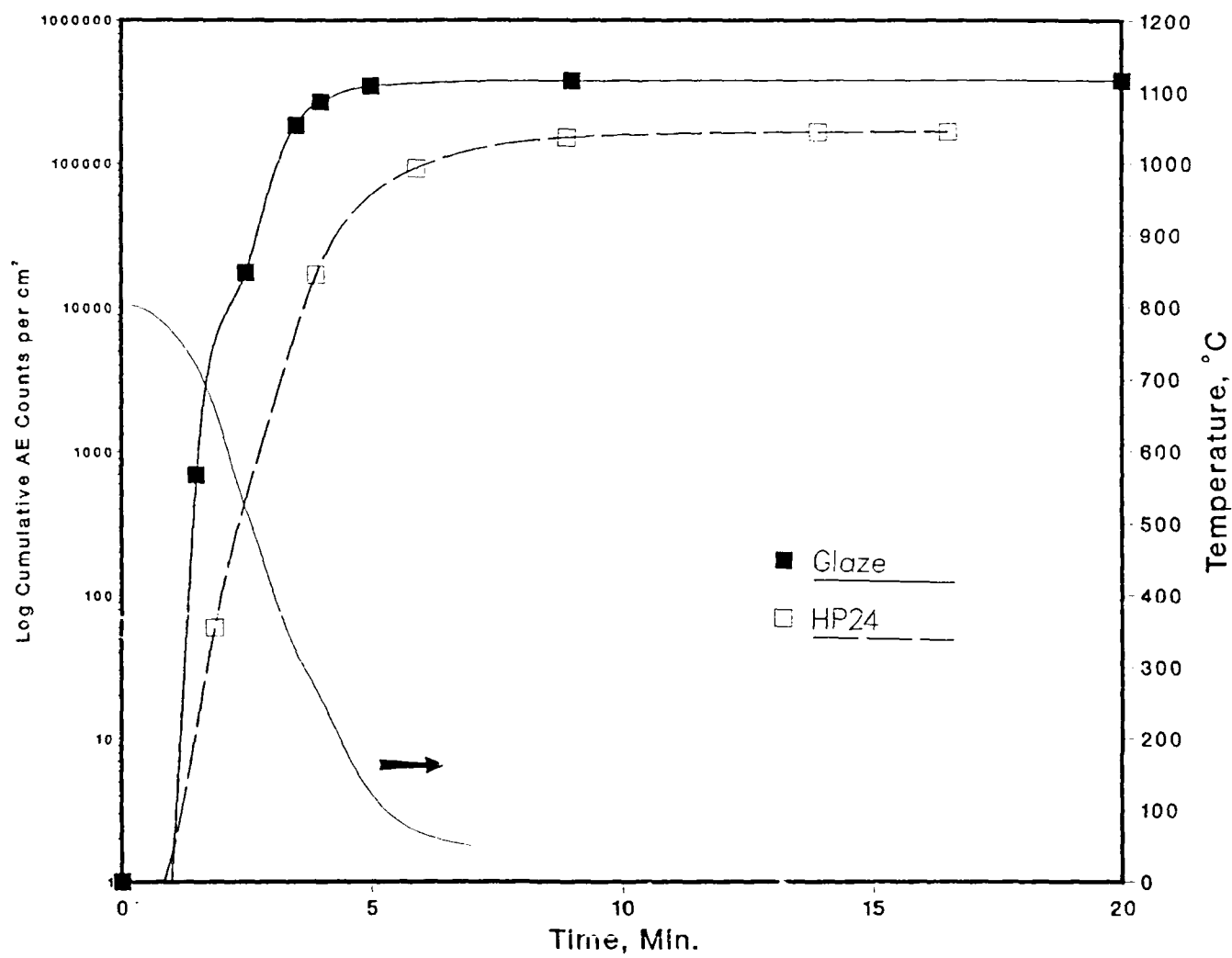


Figure 89. Log cumulative acoustic emission counts vs. time during cool down from 800°C in air.

# Acoustic Emission Counts During Cooling from 1100°C

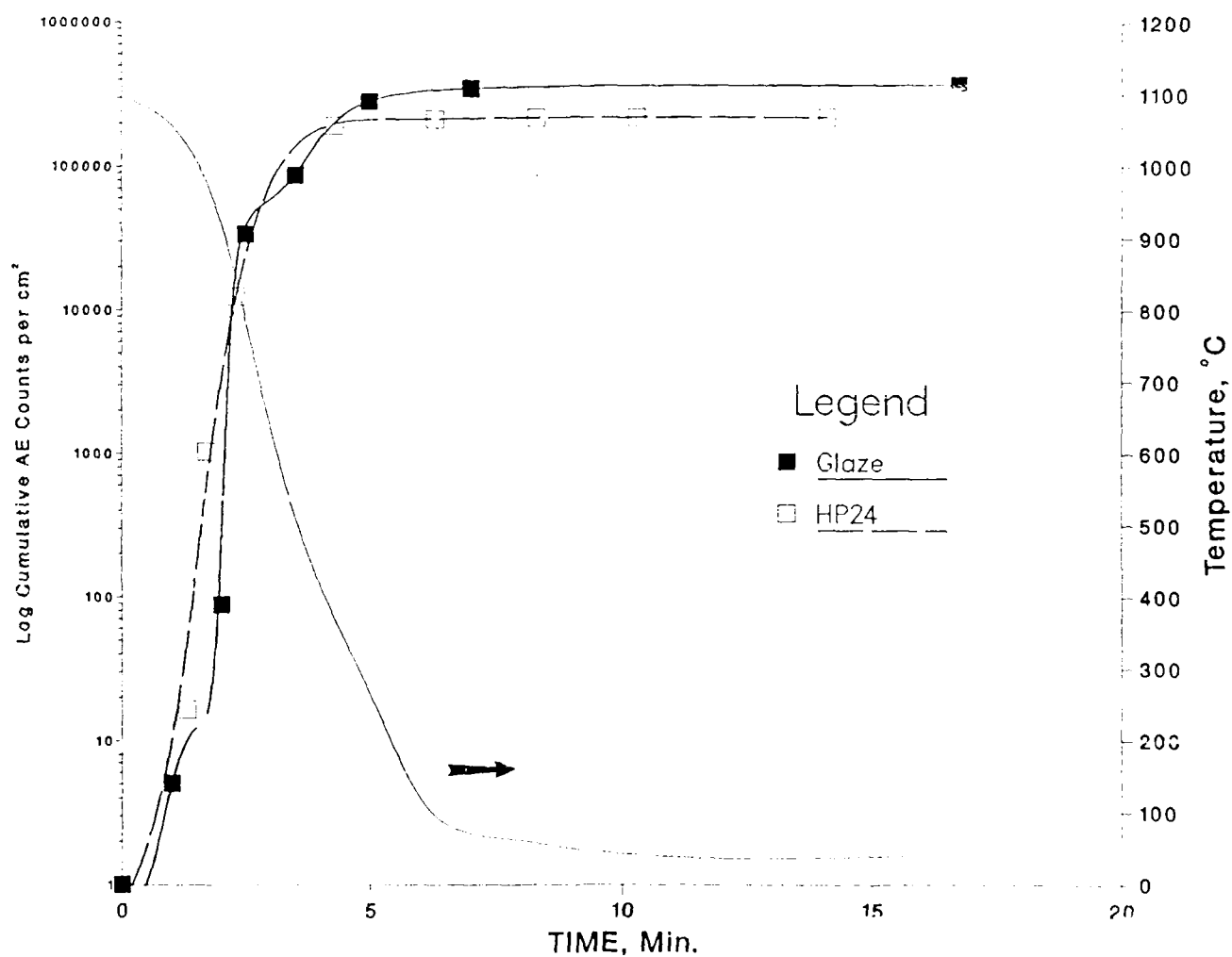


Figure 90. Log cumulative acoustic emission counts vs. time during cool down from 1100°C in air

## APPENDIX A

### THERMODYNAMIC ANALYSES

#### Introduction

Thermochemical analyses use free energy data  $\Delta G_R^\circ$ , equilibrium constant data,  $\log K$ , and equilibrium pressures of volatile species,  $\log P_{M_xO_yH_z}$ , to study the oxidation reactions of carbon-carbon composites with and without boron additions in oxygen and water vapor atmospheres. Table A-1 shows the condensed and gas phases for the two systems of interest, C-O-H and B-O-H.

Table A-2 shows the important chemical reactions which occur at the C(s)/O<sub>2</sub>(g) interface in the gas phase for oxygen gas. Table A-2 also shows the important chemical reactions which occur at the same conditions for water vapor. The direct volatility of carbon vapor is negligible for temperatures of interest here.

Table A-3 shows a similar listing of the important chemical reactions of oxygen and water vapor with boron.

Thermochemical data are available in the 1971 JANAF tables for the temperature range of interest for the several reactions. For the C-O-H system data are presented as logarithms of the equilibrium constant for the reactions assuming the condensed phases are at unit activity. Positive values of  $\log K_R$  for the reaction indicates the reaction is favorable. For precise analyses it is necessary to include pressures of the reactants and products to indicate the course of the particular reaction. Temperature has a major effect on the value of  $\log K_R$  for the several reactions.



For the B-O-H system  $\log p_{B_xO_yH_z}$  vs  $\log p_{O_2}$  and  $\log p_{B_xO_yH_z}$  vs.  $1/T$  plots are used. Where volatile species are formed gas flow, sample size and size of the reaction system have major effects on the equilibria and course of the reaction.

TABLE A-1

Condensed and Gas Phases in the C-O-H and B-C-H systems.

A. C-O-H System

Condensed Phases: C

Gas Phases: CO, CO<sub>2</sub>, H<sub>2</sub>, CH<sub>4</sub>, C

B. B-O-H System

Condensed Phases: B, B<sub>2</sub>O<sub>3</sub>, HBO<sub>2</sub>, H<sub>3</sub>BO<sub>3</sub>,

B<sub>2</sub>H<sub>4</sub>O<sub>2</sub>

Gas Phases: B, B<sub>2</sub>, B<sub>2</sub>O, BO, B<sub>2</sub>O<sub>2</sub>, B<sub>2</sub>O<sub>3</sub>, BHO,

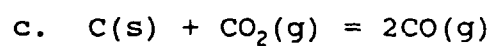
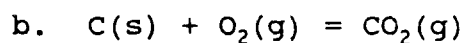
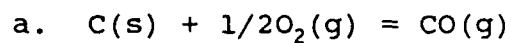
(BHO<sub>2</sub>)<sub>3</sub>, B(OH)<sub>2</sub>, B<sub>2</sub>(OH)<sub>4</sub>, B(OH<sub>3</sub>)

TABLE A-2

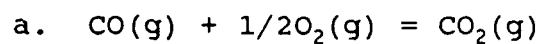
Reactions C + O<sub>2</sub> and C + H<sub>2</sub>O

A. O<sub>2</sub> Atmospheres

1. C(s)/O<sub>2</sub>(g) Interface

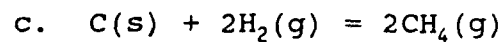
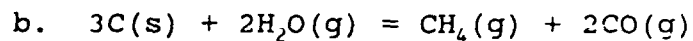
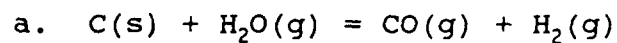


2. Gas Phase



B. H<sub>2</sub>O Atmospheres

1. C(s)/H<sub>2</sub>O(g) Interface



2. Gas Phase

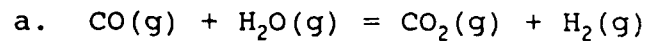
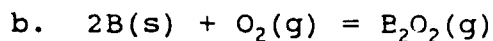
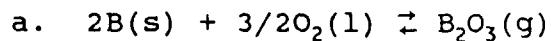


TABLE A-3

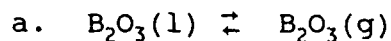
Reactions B + O<sub>2</sub> and B + H<sub>2</sub>O

A. O<sub>2</sub> Atmospheres

1. Interface B(s)/B<sub>2</sub>O<sub>3</sub>(l)

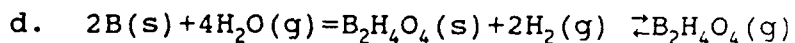
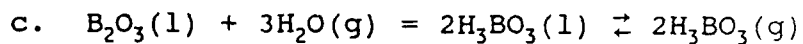
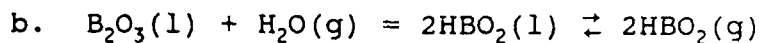
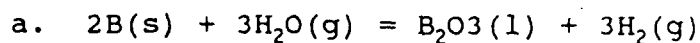


2. Interface B<sub>2</sub>O<sub>3</sub>(l)/O<sub>2</sub>(g)

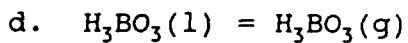
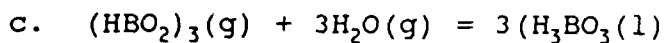
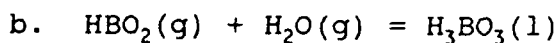
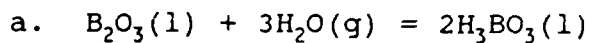


B. H<sub>2</sub>O Atmospheres

1. Interface B(s)/B<sub>2</sub>O<sub>3</sub>(l)



2. Interface B<sub>2</sub>O<sub>3</sub>(l)/H<sub>3</sub>BO<sub>3</sub>(l)



## RESULTS OF THERMOCHEMICAL ANALYSES

### A. Carbon + Oxygen System

Figure A-1 shows a plot of  $\log K_r$  vs.  $1/T$  for the several reactions for the temperature range of 800 to 1600K. The reactions to form  $\text{CO(g)}$  and  $\text{CO}_2\text{(g)}$  are favorable for all temperatures in the plot. The reaction of  $\text{CO}_2\text{(g)}$  with  $\text{C(s)}$  shows a negative  $\log K_r$  below 1000K and a positive  $\log K_r$  above 1000K. The  $\log P_{\text{CO}}$  for reaction Table A-2 (A1c) is given by

$$\log p_{\text{CO}} = 1/2 \log K_r + 1/2 \log p_{\text{CO}_2}$$

The reaction is dependent on  $\log p_{\text{CO}_2}$ .

The reaction in the gas phase of  $\text{CO(g)}$  with  $\text{O}_2\text{(g)}$  is favorable over the temperature range as shown in Figure A-1. The  $\log P_{\text{CO}}$  for reaction Table A-2 (A-2a) is given by

$$\log p_{\text{CO}_2} = \log K_r + \log p_{\text{CO}} + 1/2 \log p_{\text{O}_2}$$

The reaction is favored by high  $\log p_{\text{CO}}$  values and  $\log p_{\text{O}_2}$  values.

### B. Carbon + Water System

Figure A-2 shows a plot of  $\log K_r$  vs.  $1/T$  for the several reactions for the temperatures range of 800 to 1600 K. The reaction of  $\text{H}_2\text{O(g)}$  with  $\text{C(s)}$  to form  $\text{CO(g)}$  and  $\text{H}_2\text{(g)}$  is slightly favorable for temperatures above 1000K. The  $\log p_{\text{CO}}$  for reaction Table A-2 (B1a) is given by

$$\log p_{\text{CO}} = \log K_r + \log p_{\text{H}_2}/p_{\text{H}_2\text{O}}$$

The reaction is favorable for low  $\log p_{\text{H}_2}$  and high  $\log p_{\text{H}_2\text{O}}$  and in gas flow conditions.

The reaction of  $\text{H}_2\text{O}(\text{g})$  with  $\text{C}(\text{s})$  to form  $\text{CH}_4(\text{g})$  and  $\text{CO}(\text{g})$  is favorable for temperatures above 1000K. The  $\log p_{\text{CH}_4}$  for reaction Table A-2 (B1b) is given by  $\log p_{\text{CH}_4} = \log K_r - 2 \log p_{\text{CO}} + 2 \log p_{\text{H}_2\text{O}}$ . The reaction is favorable for high  $\log p_{\text{H}_2\text{O}}$  and low  $\log p_{\text{CO}}$  and in gas flow conditions.

The reaction of  $\text{C}(\text{s})$  with  $\text{H}_2(\text{g})$  to form  $\text{CH}_4(\text{g})$  is unfavorable above 900K as shown in Figure A-2. The  $\log p_{\text{CH}_4}$  for reaction Table A-1 (B1c) is given by

$$p_{\text{CH}_4} = \log K_r + 2 \log p_{\text{H}_2}$$

The reaction is favorable for high  $\log p_{\text{H}_2}$  and under flow.

The gas phase reaction of  $\text{CO}(\text{g})$  with  $\text{H}_2\text{O}(\text{g})$  to form  $\text{CO}_2(\text{g})$  and  $\text{H}_2(\text{g})$  is unfavorable above 1000K as shown in Figure A-2. Equilibrium analyses shows the reaction is favored by high values of  $\log p_{\text{H}_2\text{O}}$  and by removing  $\text{CO}_2(\text{g})$  and  $\text{H}_2(\text{g})$ .

#### C. Boron + Oxygen System

Table A-3 shows the reactions at the  $\text{B}(\text{s})/\text{B}_2\text{O}_3(\text{l})$  and  $\text{B}_2\text{O}_3(\text{l})/\text{O}_2(\text{g})$  interfaces. Volatile gases  $\text{B}_2\text{O}_2(\text{g})$  and  $\text{B}_2\text{O}_3(\text{g})$  are formed. Figure A-3 shows a plot of  $\log p_{\text{B}_x\text{O}_y}$  vs  $\log p_{\text{O}_2}$  where pressures are in atmosphere at 1250K. Figure A-3 also shows the  $\log p_{\text{O}_2}$  for the  $\text{B}(\text{s})/\text{B}_2\text{O}_3(\text{l})$  interface. At 1250 K  $\log p_{\text{O}_2} = -26.8$ . At this interface  $\log p_{\text{B}_2\text{O}_2} = -6.52$  and  $\log p_{\text{B}_2\text{O}_3} = -7.4$ .

$\log K_r$  for reaction Table A-3 (A1a) has a value of 40.202 to form  $\text{B}_2\text{O}_3(\text{l})$  and 32.852 to form  $\text{B}_2\text{O}_3(\text{g})$ . This gives a value of  $\log p_{\text{B}_2\text{O}_3} = -7.4$ .  $\log K_r$  for reaction Table A-3 (A1b) = 20.368 which gives a value of  $\log p_{\text{B}_2\text{O}_2} = -6.52$  for  $\log p_{\text{O}_2} = -26.80$ .

$B_2O_3(l)$  has a melting temperature of 723K. This low melting temperature and high volatility of  $B_2O_2(g)$  and  $B_2O_3(g)$  makes  $B(s)$  a poor oxidation resistant additive to carbon-carbon composites.

Figure A-4 shows a plot of  $\log p_{B_xO_y}$  vs.  $1/T$  of the B - O species at the  $B(s)/B_2O_3(l)$  and  $B_2O_3(l)/O_2(g)$  interfaces. Normal oxidation is proposed for  $\log p_{B_xO_y}$  below -9 and mixed oxidation and volatility above -9.

#### D. Boron + Water System

Table A-3 shows the reactions for the boron - water system. Figure A-5 shows a plot of  $\log p_{B_xO_yH_z}$  vs  $\log p_{H_2O}$  where  $p$  is in atmospheres.  $B_2O_3(l)$  is the condensed phase at 1250K for  $\log p_{H_2O} = 0$ . Here  $\log p_{(HBO_2)_3} = -1.3$ ,  $\log p_{H_3BO_3} = -1.7$  and  $\log p_{HBO_2} = -4.5$ .  $H_3BO_3(l)$  is only formed for  $\log p_{H_2O} > 4.5$ . The volatile species  $(HBO_2)_3$  and  $H_3BO_3$  are very important in the oxidation of  $B(s)$  in  $H_2O(g)$  atmospheres.

Figure A-6 shows a  $\log p_{B_xO_yH_z}$  vs.  $1/T$  plot for the temperature range of 800 to 1500K. Since high pressures of the species  $(HBO_2)_3(g)$  and  $H_3BO_3(g)$  occur gas flow can greatly influence the kinetics of the water-boron reactions.

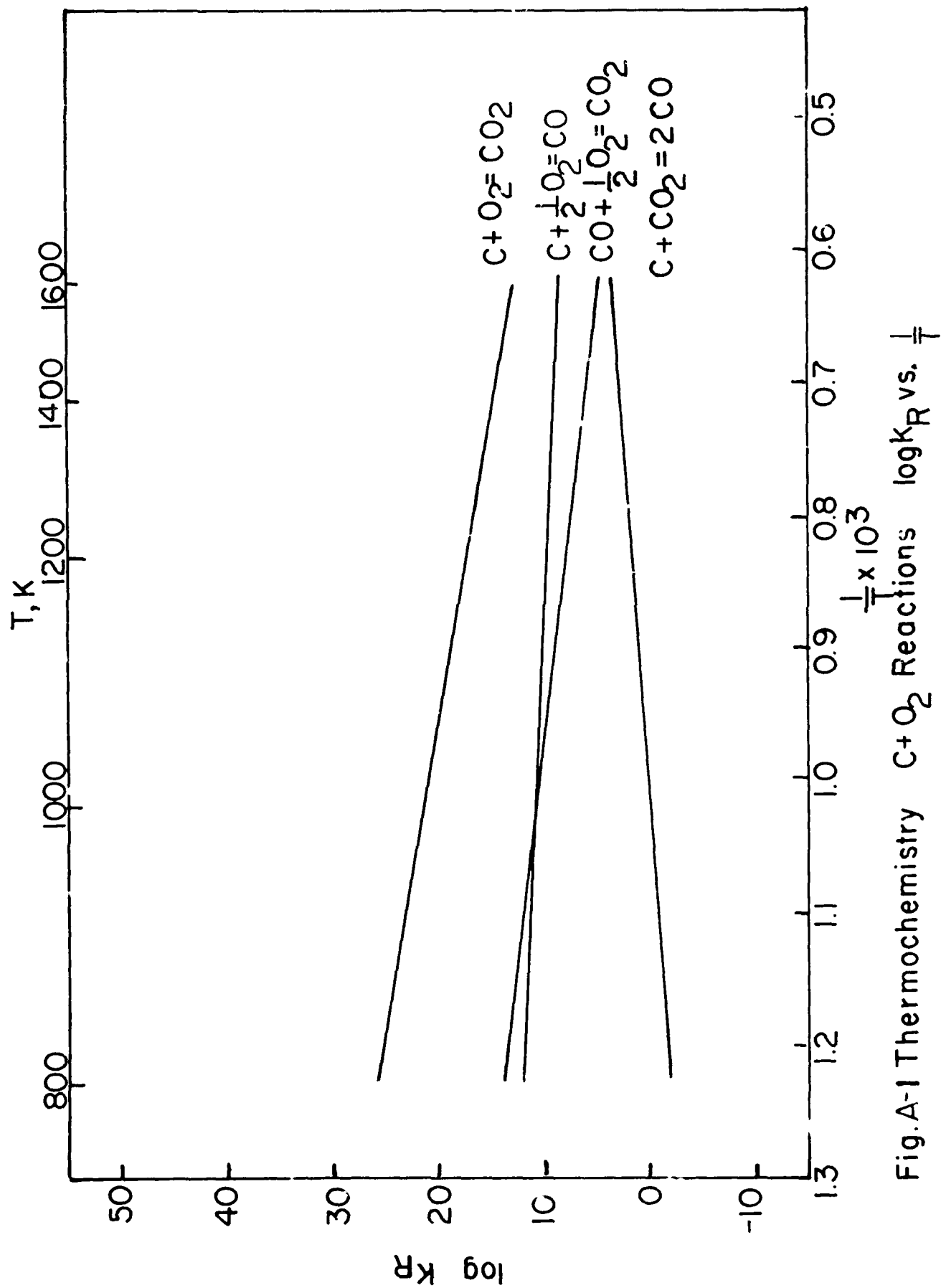


Fig.A-1 Thermochemistry C+O<sub>2</sub> Reactions  $\log K_R$  vs.  $\frac{1}{T}$



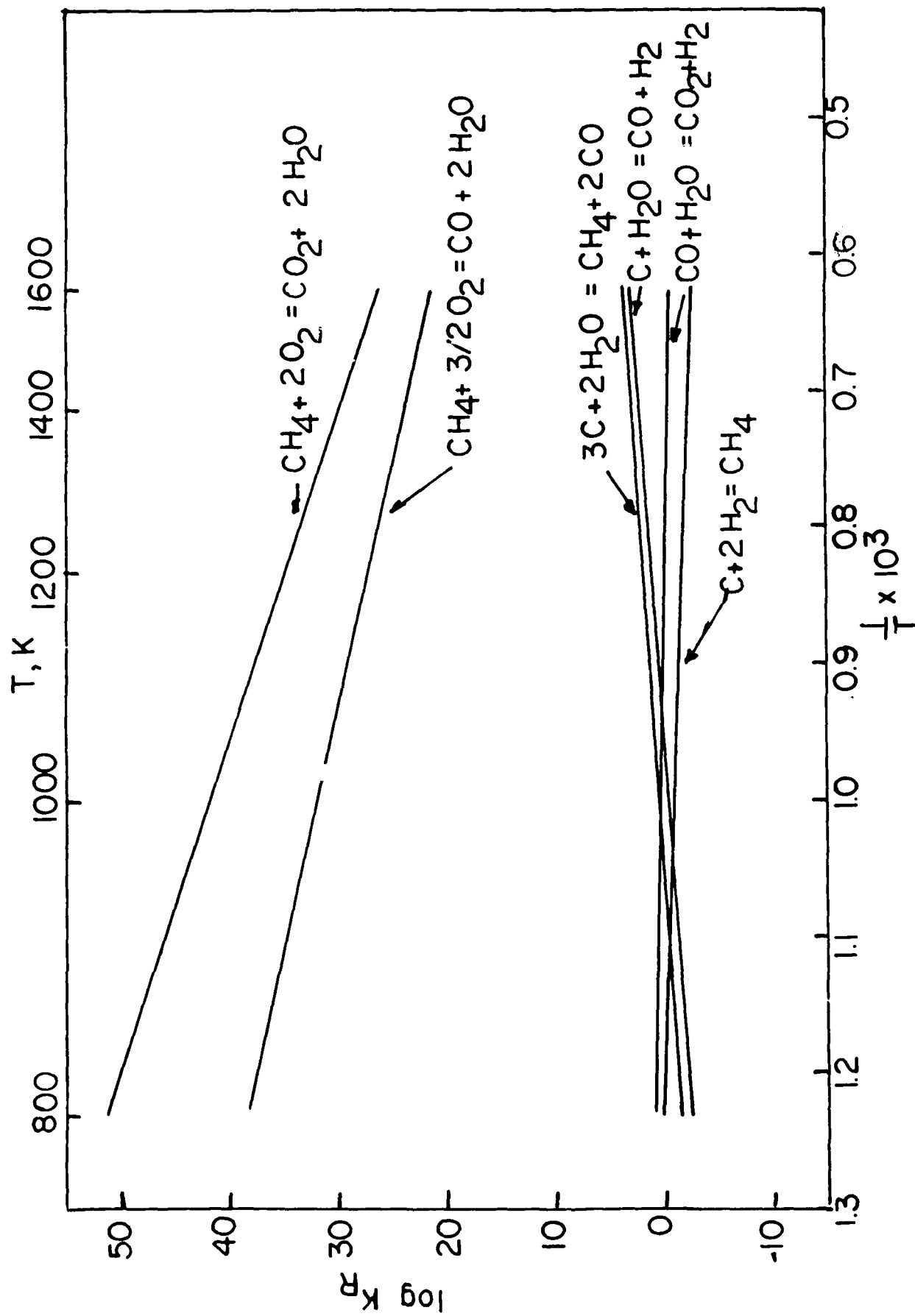


Fig. A-2 Thermochemistry  $\text{C} + \text{H}_2\text{O}$  Reactions  $\log K_R$  vs.  $1/T$

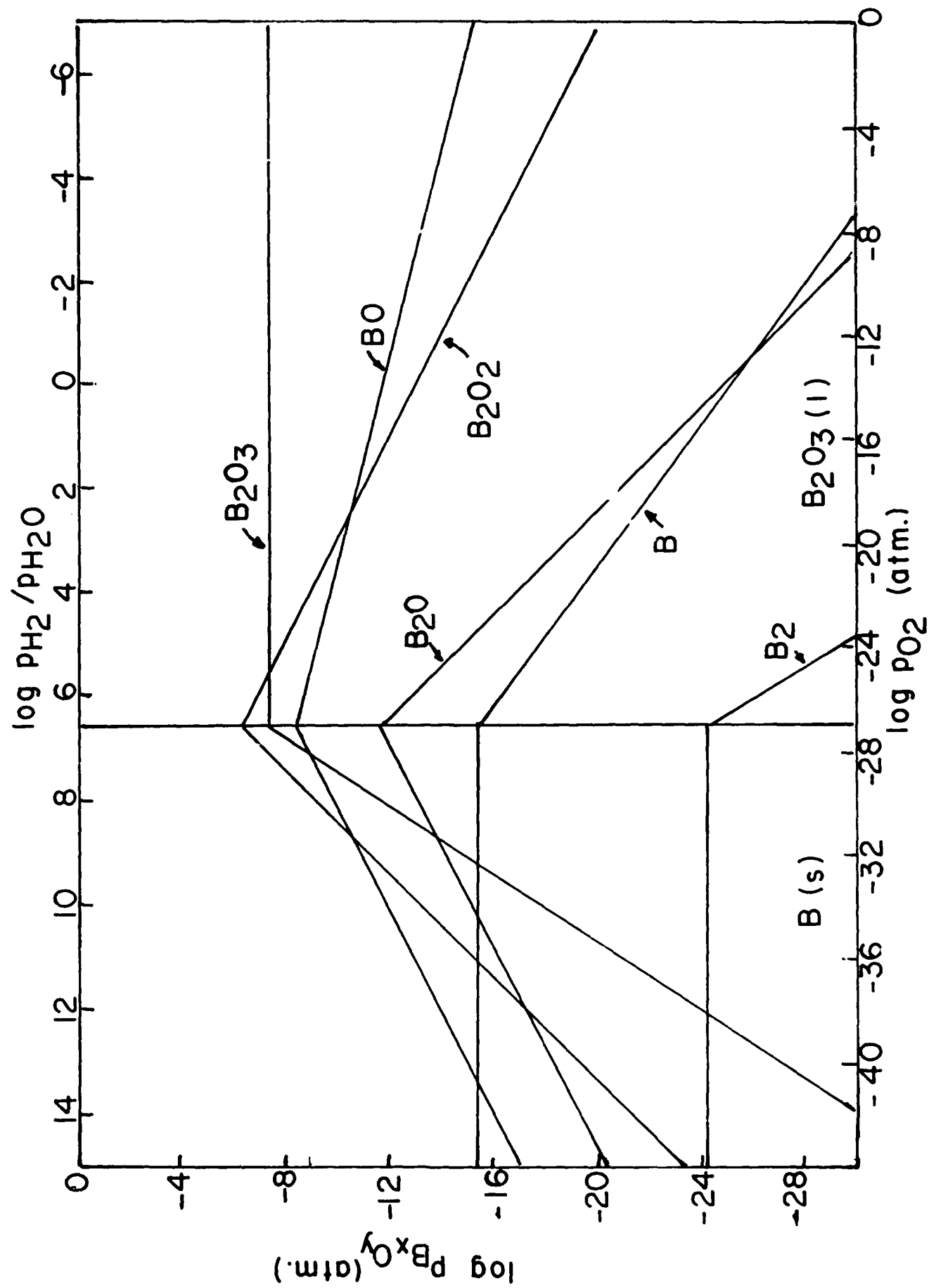


Fig.A3 Volatile Species B-O System 1250 K

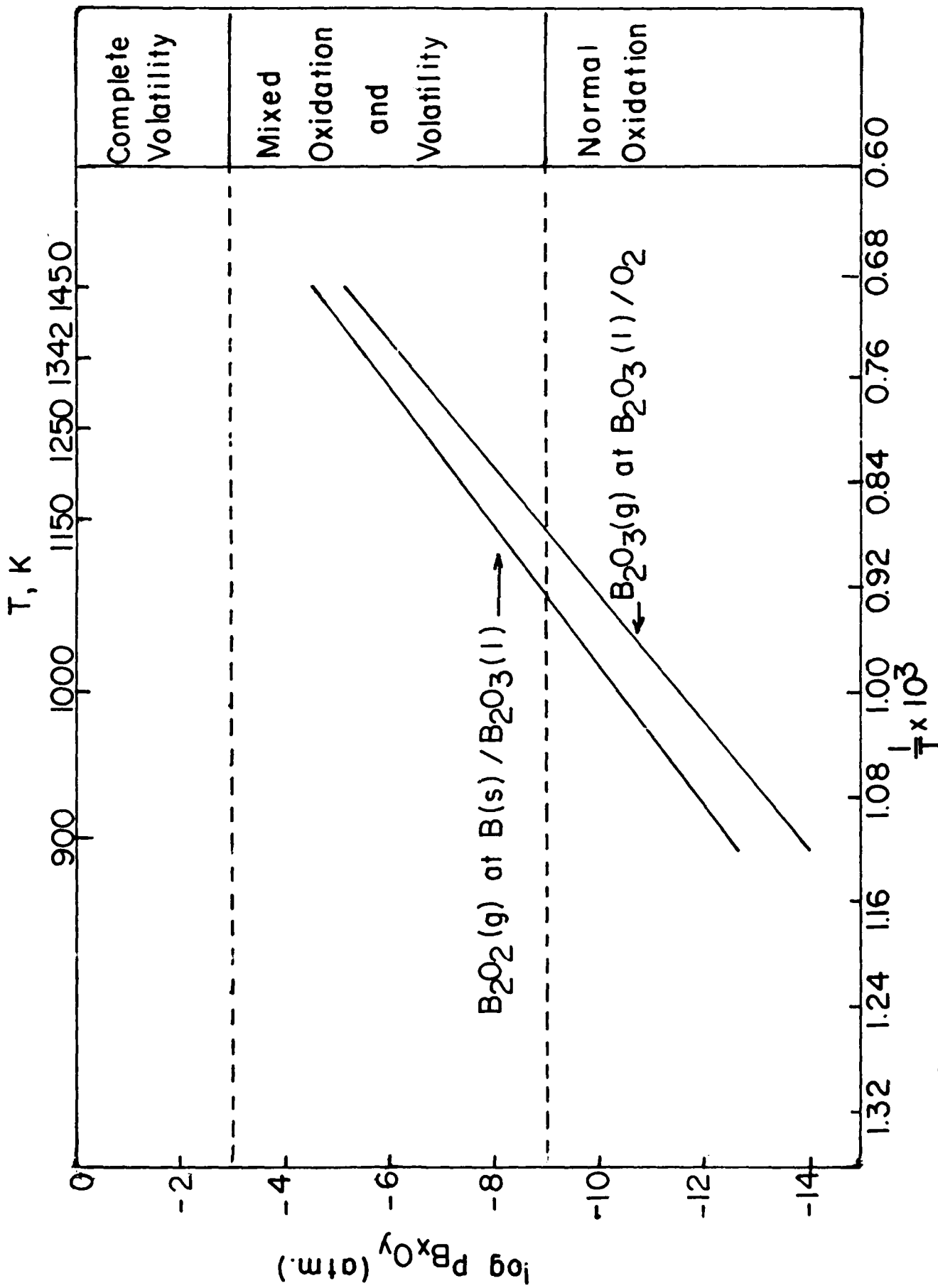


Fig.A4B-O System Volatile Species vs. Temperature

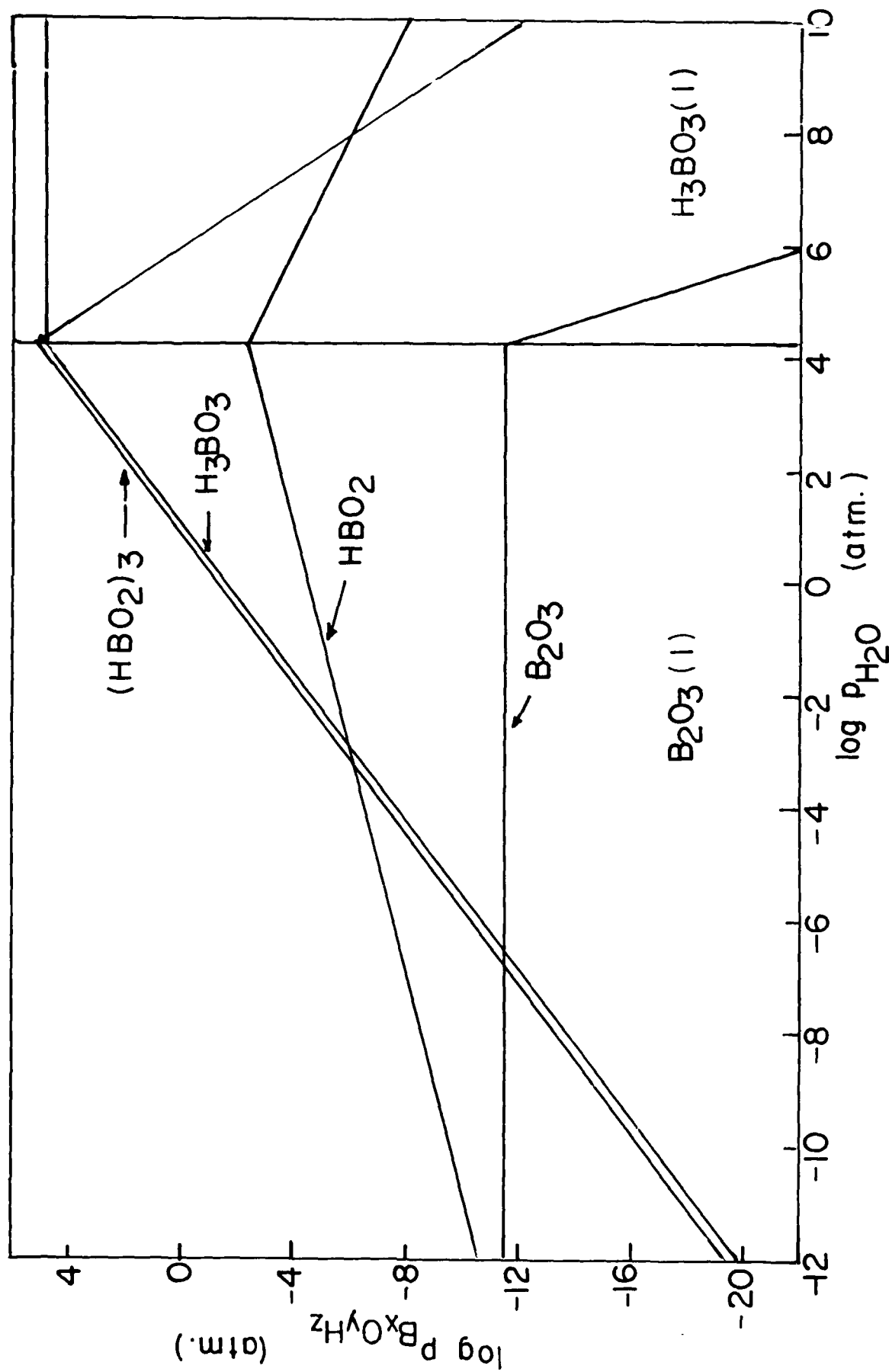


Fig.A-5 B-O-H System Volatile Species 1000 K

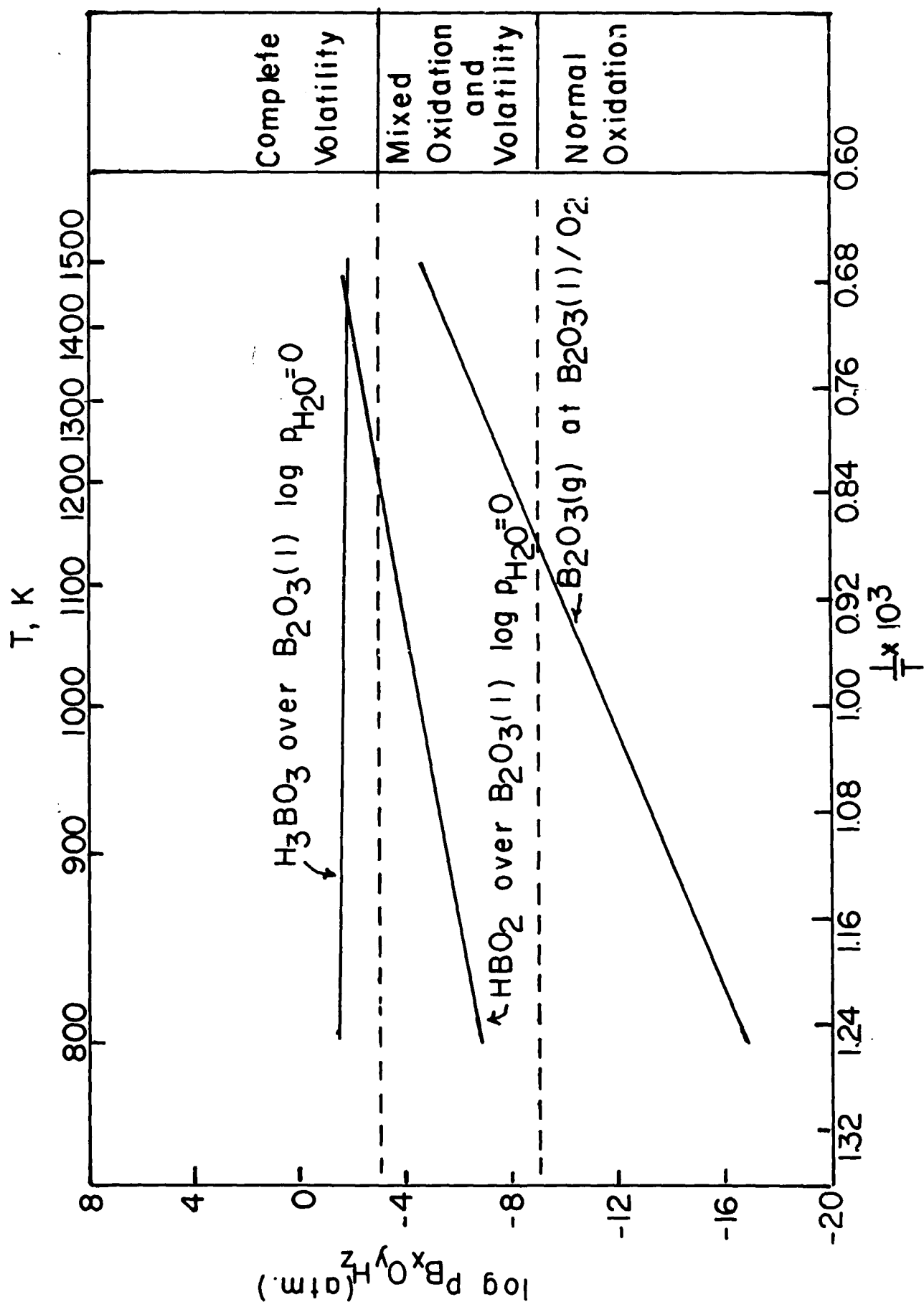


Fig. A6 B-O-H System Volatile Species vs. Temperature